UNIVERSITÀ DEGLI STUDI DI PADOVA

DIPARTIMENTO DI SCIENZE CHIMICHE

CORSO DI LAUREA MAGISTRALE IN CHIMICA

TESI DI LAUREA MAGISTRALE

Evaluation of the Activity and Selectivity of Dinuclear Cu and Ni-NHC/pyrazolato Complexes for the Electrocatalytic CO_2 Reduction

Relatore: Dr. Baron Marco

Correlatore: PD Dr. Pöthig Alexander

Controrelatore: Prof. Dr. Battistutta Roberto

LAUREANDO: NEUBERG SAMUELE

1203013

Anno Accademico 2020/2021

ACKNOWLEDGMENTS

Un immenso ringraziamento ora per i miei genitori, da cui sono stato distante nell'ultimo anno e mezzo. È finto un altro percorso, non poco travagliato e pieno di momenti in cui arrendersi era la scelta più facile da fare. Se sono qui ora è anche grazie a voi, che mi avete sempre sostenuto, appoggiato nelle mie scelte e insegnato a puntare in alto.

Un grazie anche alla famiglia, a cui sono molto legato, che ha sempre creduto in me e si è sempre interessata, anche durante questa lunga parentesi "tedesca".

Nella vita di una persona poi non possono mancare gli amici, quelli di sempre, quelli che, se non li vedi da mesi e mesi, nulla cambia. Loro ci saranno per te, come tu per loro. Grazie per le chiamate serali che hanno alleviato più volte la mia solitudine, grazie per le ritrovate serate in cui si può riprendere a parlare e a scherzare con serenità.

Infine, più di pensiero a *Sara*, per il suo ruolo nell'essere stata al mio fianco in questi quasi tre anni, per aver sopportato tutte le mie insicurezze e paure, per sapere farmi riflettere affinché dia il giusto peso alle cose. Grazie!

ABSTRACT

Calix[4]imidazolylidene[2]pyrazolate is an appealing macrocyclic compound for the selective recognition of H-bonding acceptor molecules and to act as tetra-NHC ligand precursor, affording robust bimetallic complexes. In this study, the Cu(II) derivative has been synthesized from the methylene-bridged ligand employing the *in situ* generated, formal $Cu(PF_6)_2$, upon deprotonation of the four imidazolylidene and two pyrazolate units. As the Bisnickel congener, **Cu_2L^{Me} (PF$_6$)$_2$** assumes a saddle-shaped conformation, with the two metal ions connected by rigid pyrazolate, N-donor, moieties. The GS spin multiplicity of the two Square Planar (SP)-coordinated Cu(II), d^9, metal centres, is the triplet state, as suggested by the typical paramagnetic broadening of the NMR lines and by DFT calculations. UV-Vis, HR-ESI(+) and SC X-ray analysis were also performed. When the same metal precursor was provided to the ethylene-bridged version of the tetraimidazolium ligand, selective recognition of one Cl$^-$ ions was observed, with the formation of the so-called Capsoplex assembly. Such supramolecular aggregate is composed by a central, T_d-coordinated chloride ion, encapsulated by two symmetry-equivalent cationic **$[Cu_2L^{Me}]^{2+}$** units, in a tennis-ball like fashion.

Cu_2L^{Me} (PF$_6$)$_2$ **$[(Cu_2L^{Et})_2Cl]$ (PF$_6$)$_3$**
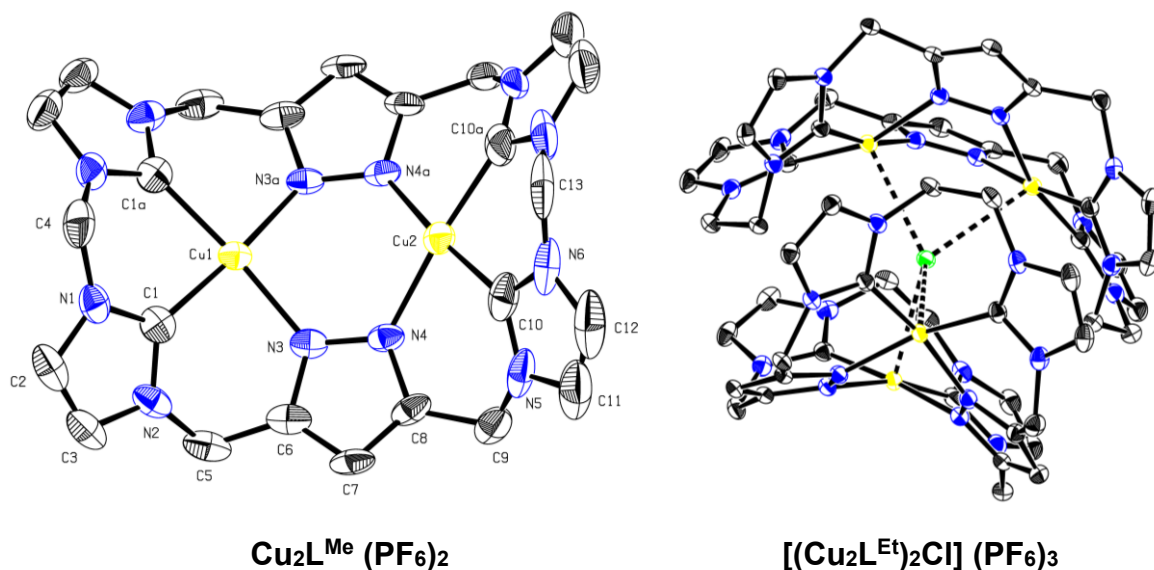
Bimetallic activation of small molecules is a common process in nature, which takes advantage of highly efficient oxidoreductase enzymes possessing bimetallic active sites, redox reservoirs and flexible but robust ligand frameworks. For this reason, calix[4]imidazolylidene[2]pyrazolate Bisnickel(II) complexes, featuring two well-defined coordination pockets with two NHC-donors per metal centre, are envisioned to be active towards CO_2 electroreduction (CO$_2$RR). Therefore, the propylene-bridged Bisnickel(II) complex was synthesized by variation of the established experimental procedure, and its electrochemical behaviour compared with the methylene- and ethylene-bridged congeners. All complexes were active in the cathodic potential window, with irreversible

or quasi-reversible redox features, that DFT calculations attributed being mainly metal-centered reductions, ultimately affording the Ni(I)-Ni(I) species. Remarkably, reversibility and position of the reduction waves are highly dependent on the geometrical features of the metal complexes. **Ni$_2$L^{Pr} (PF)$_6$**, possessing the most flexible ligand platform, shows the highest electrochemical reversibility, resulting from the enhanced capacity of the ligated metal centre to exchange electrons in redox processes which imply electronic configuration and spin state variation. A discrete through-ligand electronic communication was also observed for the three complexes, suggesting favourable overlap of the d-metal orbitals with the π-system of the bridging pyrazole moieties. Subsequently, electrocatalytic CO_2 reductions tests were performed either in aprotic solvent (dry and degassed MeCN), or in presence of small amount of H_2O. The propylene-bridged Bisnickel complex was the only to show an appreciable reactivity towards CO$_2$RR without the addition of any proton source. However, by scanning towards more negative potentials, side phenomena, which affect also the other two complexes, became prominent, resulting in a reduction of the catalytic current. As expected, if small, defined H_2O amounts were added during electrocatalysis, more intense peak-shaped catalytic waves associated to CO$_2$RR were obtained. The selectivity towards CO_2 reduction was markedly higher than for HER, but intense current responses were obtained only in the first electrochemical scans. In fact, the very negative potentials required to trigger these catalytic processes (<-2.5 V vs Fc$^{+/0}$) simultaneously favour unwanted reactions, such as catalyst degradation and/or electrodeposition, which were responsible for the scarce durability and efficiency of these NHC/pyrazolate bimetallic systems. CPE experiments revealed the production, between the gaseous products, of CO and H_2, with current efficiencies that varied according to the employed catalyst and to the applied potential.

TABLE OF CONTENT

ABBREVIATIONS

NOAA   National Oceanographic American Association

IPCC   Intergovernmental Panel on Climate Change

CCS   Carbon Capture & Storage

NHC   N-heterocyclic carbene

Por   porphyrin

NCP   N-confused porphyrin

TPP   tetraphenylporphyrin

TPFPP   tetraperfluorophenylporphyrin

SP   square planar

ET   electron transfer

HS   high spin

NCP   N-confused Porphyrins

NHC   N-heterocyclic carbene

IPr   1,3-bis(2,6-diisopropylphenyl)-imidazol-2-ylidene

FDH   formate dehydrogenase

CODH   carbon monoxide dehydrogenase

PCET   Proton Coupled Electron Transfer

HER   Hydrogen Evolution Reaction

LUMO   lowest unoccupied molecular orbital

HOMO   highest occupied molecular orbital

SOMO   single occupied molecular orbital

TS   transition state

PCP   pincer-type ligand

salen   N,N'-ethylenebis(salicylideneaminato)

bpy   2,2'-bipyridine

TFE   trifluoroethanol

IR-SCE	infrared-spectroelectrochemistry
CRCs	CO_2 reduction catalysts
TFA	trifluoroacetic acid
GS	ground state
NOE	Nuclear Overhauser Effect
CPs	cross peaks
DPs	diagonal peaks
TD-DFT	time-dependant DFT
ICT	intervalence charge transfer
H_{ab}	electronic matrix coupling

Electrochemical notation

$E°_{cat}$	reduction potential of the catalyst
E_{onset}	potential
$E_{1/2}$	half-wave potential
$E_p^{a/c}$	peak potential of an oxidation(a) / reduction(c) event
ΔE_p	peak-to-peak separation (cathodic and anodic scans)
$E_r E_r$	two sequential electron transfer process
GC	glassy carbon
FE	faradaic efficiency
$E_{p,cat}$	potential of the max catalytic current (i_{cat})
$E_{cat/2}$	potential at which the current is equal to $i_{cat}/2$
EC	Electrochemical Chemical process
CPE	Controlled Potential Electrolysis
WE	Working electrode
CE	Counter electrode
RE	Reference electrode

1 INTRODUCTION

1.1 ANTHROPOGENIC CO$_2$ CONTRIBUTION AND CARBON CAPTURE, UTILIZATION AND STORAGE (CCUS).

One of the most important and challenging problems of our time is global warming and climate change. This theme, despite having been introduced far in advance by scientists,[1] belongs to the public opinion and it is object of strong debates since 1997, when the first, world-wide geopolitical accordance was signed, namely the Kyoto Protocol.[2]

For decades environmental physicists, chemists as well geologist have tried to find out the key to correlate the global warming, defined as the increasing of the average temperature on Earth, to the abnormal greenhouse gases concentration registered in the last century. NOAA's (National Oceanic and Atmospheric Administration) analysis found that 2019 global temperatures were 0.95 °C above the 20th century average.[3] To date, there is no reason to think that all the changes the planet is experiencing right now are not of human origin. In 2013, the IPCC's (Intergovernmental Panel on Climate Change) Fifth Assessment Report confirmed the previous statement, claiming that there is a crucial anthropogenic contribution to the increase of the radiative forcing (difference between insolation absorbed by the Earth and energy radiated back to space).[4]

First and major cause of this phenomenon are the renowned greenhouse gases: CO_2, CH_4, N_2O, PF_6, halocarbons (long-lived species) and O_3, CO, NO_x, SO_2 (moderately short-lived species). According to the aforementioned report, carbon dioxide is considered to contribute itself more than 60% to the global warming: being an IR-active molecule (asymmetric stretching of the two double bonds which leads to a strong peak at 2300-2400 cm^{-1}), it can absorb sunlight and consequently trap increasing quantity of energy into the Earth atmosphere.

The principal sources of CO_2 emission are power plants (45%), transport (25%), Steel industry (6%), Refinery and Chemical Industry (5%) and other (19%).[4] The actual concentration of CO_2 in the atmosphere is 419 ppm (relative concentration, May 2022), which is about 100 ppm higher compared to the first direct measure on Earth, dated March 1958 at the hands of C. David Keeling, at Mauna Loa Observatory, Hawaii.

With an estimated quantity of 9.855 Million Tons emitted world-wide every year (2014),[5] carbon dioxide assume a crucial role in the carbon cycle, a series of cyclic absorption/release transformations which CO_2 undergoes in the biosphere and in the atmosphere.
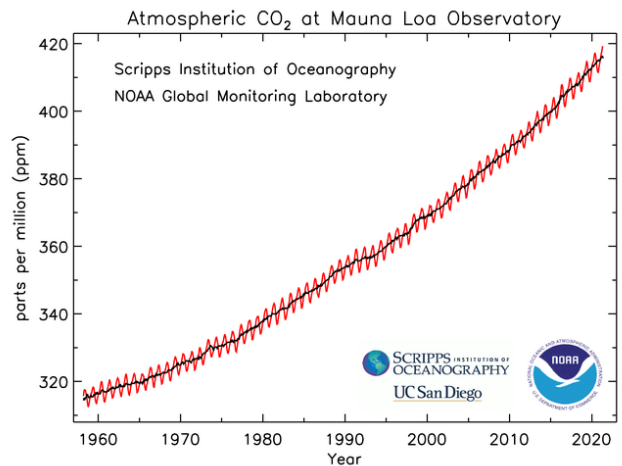
Figure 1.1 | Keeling curve representing the accumulation of CO_2 in the Earth's atmosphere based on continuous measurements taken at the Mauna Loa Observatory (1958 – 2021) day.[6]

The anthropogenic modification of this natural process, despite being of small entity, has attracted more and more interest, with the main idea that our planet need time to adapt to the modifications derived from the human activities. The only problem is the that the time scale of Earth is order of magnitude higher that the time scale for humans, leading to the conclusion that we are running out of time to take serious measures.

Aiming to reduce the carbon footprint of several industrial processes by cutting CO_2 emissions, Carbon Capture and Storage (CCS), which has been outlined some decades ago, is one of the possible solutions. Many approaches have been used to reversibly capture CO_2 from power plants off-gases, mainly based on its absorption in liquid or solid media, made of amines or amino-acid solutions to form ammonium-salts or carbamates ($R_2NH + CO_2 \rightarrow R_2NCO_2H$). The most employed amines are the mono- and diethanolamine, thanks to their high H_2O solubility and to the lower amount of heat need to reverse the CO_2 capture reaction. However, the off gases need to be purified before the capture process from nitrogen and sulphur oxides, to avoid degradation of the amine solution. Other technical solutions are, with different extension, employed to separate and to concentrate CO_2 from off-gases. For diluted CO_2 gas mixtures, one can employ carbonate capture, carbonate looping or lithium silicates to reversibly bind CO_2, whereas, if CO_2 is more concentrated, solvent extraction, membrane separation and activated charcoal adsorption could be exploited.[7] The subsequent on-site carbon dioxide recover and compression are the most energy-demanding steps, even though the development of modern technologies has dramatically contributed to decrease the cost of the whole CO_2 capture process (from 80-100\$ /t to 30 \$/t).[8] Among them, pressurized oxy combustion seems to be a valid alternative to obtain "pure" CO_2 exhaust gases. It is realised by employing pure O_2 to burn coal and hydrocarbons, potentially generating only CO_2 and H_2O, the latest readily separated from CO_2 by condensation at lower temperatures.

2
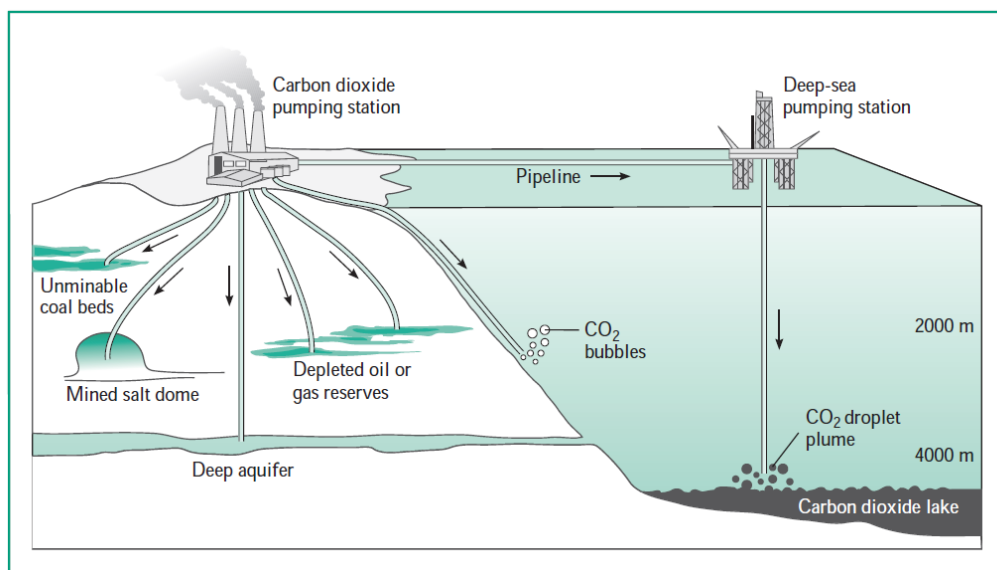
Figure 1.2 | Potential sequestration sites for carbon dioxide in the context of CCS.[7]

Once CO_2 has been isolated, whose detachment is realised through thermal desorption from the absorption matrix, the problem now becomes where and how to store this gas. Again, many hypotheses have been proposed, among which the direct deep-ocean disposal (deep > 3000 m), deep underground storage (depleted oil and gas reservoirs, saline aquifers, *etc.*), and mineral carbonates formation (**Figure 1.2**). However, many doubts surround those storage techniques, resulting in a global scarce application.

Another approach consists in the conversion of the concentrated CO_2 to form value-added chemical species. This strategy, known as Carbon Capture and Utilization (CCU), is attracting more and more endeavours from the scientific community over the last few decades. For example, employing established or new-generation heterogeneous catalyst and "green" H_2, CO_2 could be converted into Methanol (with Cu^0@ZnO/Al_2O_3 catalyst systems),[9] into SNG (synthetic natural gas) via Sabatier-process (utilizing modern transition-metal promoted Ni@Al_2O_3 catalysts)[10] or into Fischer-Tropsch products (still under developing).[11]

In fact, carbon dioxide is an important and appealing C_1 building block in chemical synthesis due to its nontoxicity, abundance, availability, and sustainability. Excellent progress has been achieved in the chemical transformation, incorporation and recycling of CO_2 into high value added organic chemicals, such as bulk chemicals (*vide supra*), but also a series of more sophisticated organic compounds.[12]

However, due to the relative chemical inertness and low reactivity of CO_2, the development of metal-based and non-metal-based catalysts (organocatalysts) has been paramount to achieve the desired reactivity and to access the most diverse classes of chemical compounds using this C_1 synthon. Many recent reviews[13],[14],[15] have outlined the recent progress on this research field.
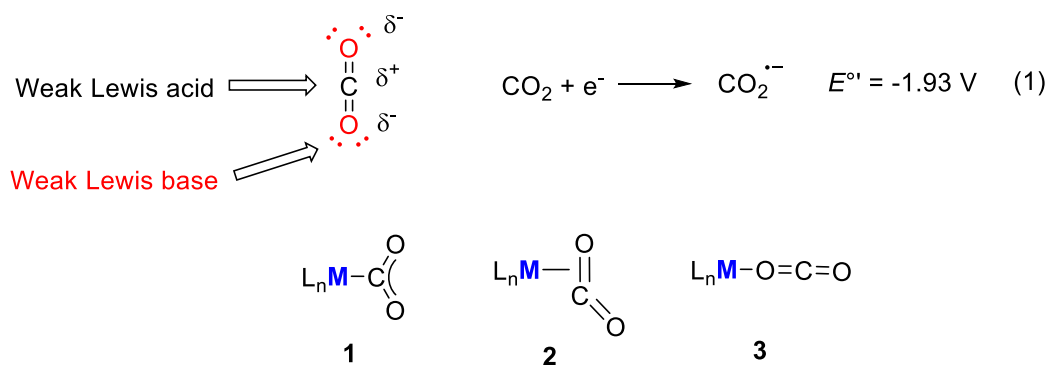
Figure 1.3 | Redox potential for the CO_2 reduction to radical anion formation ($CO_2^{\cdot-}$) and overview of the most common coordination modes of CO_2 to a metal centre: η^1-C (**1**), η^2-(C,O) (**2**) and η^1-O (**3**).

Hence, the key point to expand the scope of CO_2 utilization in several chemical processes is the selective and efficient **activation**, which can be reached with different strategies according to the presence or the absence of metal atom(s) in the employed system. Metal-based catalysts exploit the weak Lewis acidity of the central carbon atom of CO_2, as well as the Lewis basicity of the two terminal oxygens to form "activated" CO_2 adducts (**Figure 1.3**); whereas organic nucleophiles, metal-free systems such as amines, amino acids, N-nucleophiles and N-heterocyclic carbenes (NHCs),[16] can react directly with the CO_2 molecule, forming again reactive adducts.[14],[17]

These "activated" CO_2 adducts can potentially evolve to a plethora of chemical compounds, either for pharmaceutical applications and polymers synthesis or that act as key intermediate for specific chemical processes. It is the case of cyclic carbonates, obtained from CO_2 and epoxides and/or alcohols (**Figure 1.4**: **a, b**); polycarbonate (or polyether carbonate), from CO_2 and epoxides (**c**); methylated and formylated compounds obtained from amines and *in situ* reduced CO_2 (**d**) and finally cyclic (**e**)[18] and acyclic (**f**) carbamates derived from carbon dioxide and propargylic and primary amines under mild conditions.

In addition to the C-O and C-N bond formation presented so far, also the C-C bond formation is another interesting reaction in this context, achieved by the transition metal-promoted CO_2 addition to simple C-H bonds (C–H activation and carboxylation), or to double and triple bonds, both yielding carboxylic acids. Direct C–H carboxylation via carbon dioxide activation is, of course, of great significance. Direct carboxylation of C–H bonds to produce the carboxylic acid is an ideal transformation, for which Cu- and Au-(NHCs) are very active catalysts.[19],[20],[21] These catalytic systems should, however, promote a **chemo**- and **regioselective** addition of CO_2 to double bonds. It is the case, for instance, of the Cp_2TiCl_2 catalyst introduced by *Xi et al.*, which promote the transformation of styrene and its derivatives to α-aryl carboxylic acids (**Figure 1.5**, **a**).[22]
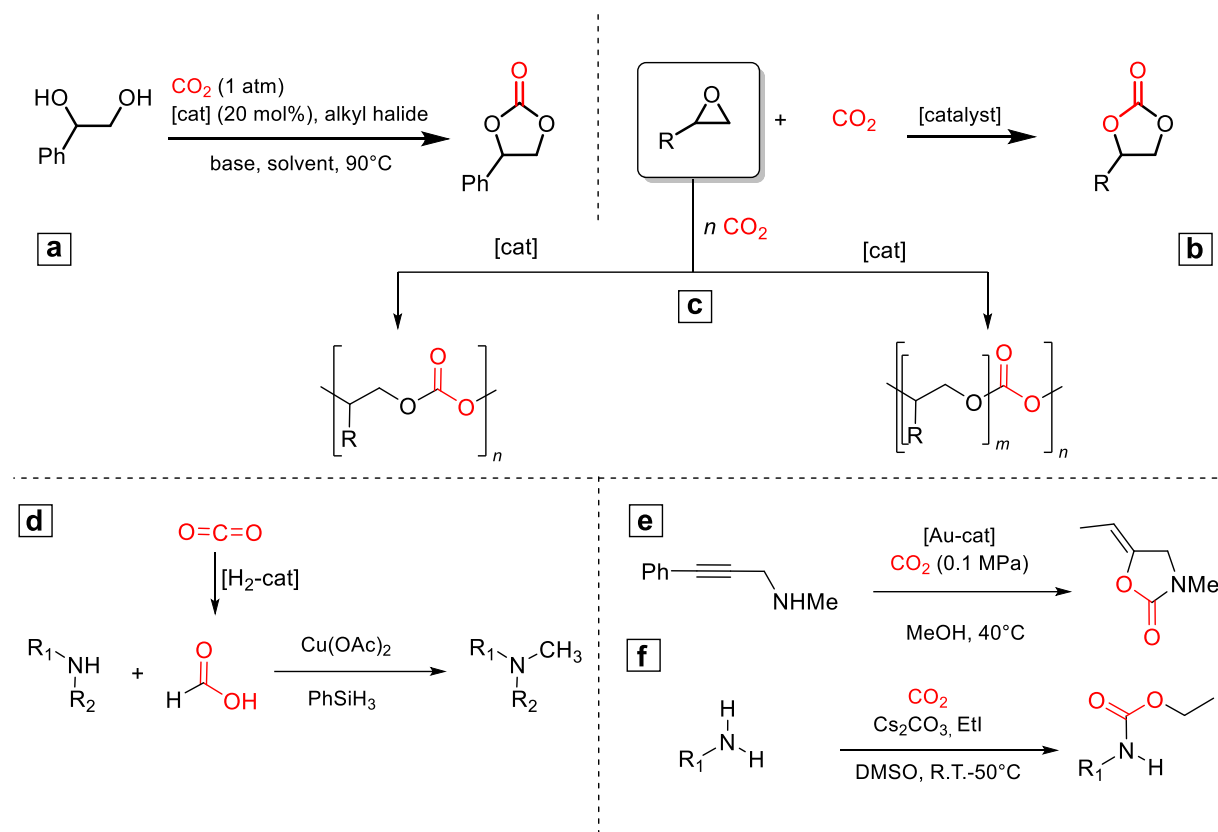
Figure 1.4 | Most relevant classes of compounds obtained from metal-mediated CO_2 activation and conversion.[13]

Another important aspect to considered is the **diastereoselectivity** and the **enantioselectivity** of the carboxylation of unsaturated compounds. To achieve selective asymmetric CO_2 addition to alkenes, however, expensive and often complex chiral ligands have been exploited, such as the recent (S,S)-Ph-BPE ligand (**Figure 1.5**, **c**) used with $Cu(OAc)_2$ catalyst to promote the hydroxymethylation of 1,3-dienes with CO_2 to form chiral quaternary stereocenters.

When, instead, the reactivity of CO_2 with alkynes is considered, Cu-, Ni- and Rh-based catalysts are the systems which have shown the highest performance; as the $NiCl_2$ - 2,9-dimethyl-1,7-diphenyl-1,10-phenanthroline complex introduced by *Martin et al.*, able to catalyse a regioselective hydrocarboxylation of aryl-alkynes (**Figure 1.5**, **b**).[23] Once more, if the target is the enantioselectivity, chiral ligands are used, such as the system introduced by *Tanaka et al.*: (S)-H_8-BINAP – [Rh(cod)$_2$] BF_4 active towards a [2+2+2] asymmetric cycloaddition with CO_2 (**d**).[24]

So far, all the approaches which lead to the fixation of CO_2 and to its utilization as a C_1 synthon in organic synthesis might seem ideal strategies to offer valid carbon sources to produce useful organic compounds and polymer materials, while contributing to solve the environmental challenge to decrease the tropospheric carbon dioxide concentration.
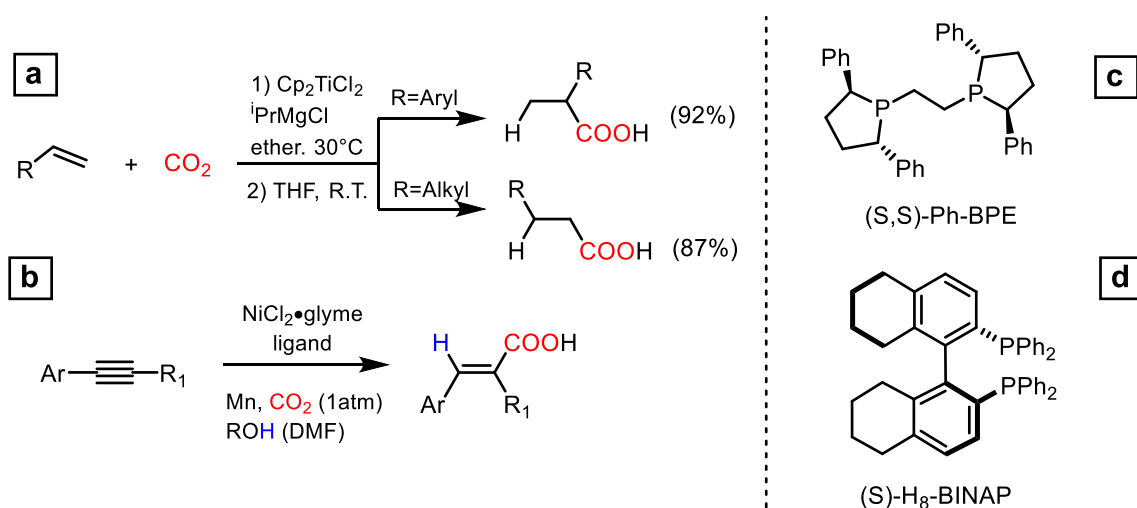
Figure 1.5 | Catalytic carboxylation of unsaturated compounds with CO_2 (**a, b**). (S,S)-Ph-BPE ligand used with $Cu(OAc)_2$ to promote the hydroxymethylation of 1,3-dienes (**c**),[25] and (S)-H_8-BINAP employed in [Rh(cod)$_2$] BF_4 catalyst active towards asymmetric cycloaddition with CO_2 (**d**).[24]

It should be noted, however, that the aforementioned processes are interesting for special organic products and fine chemical synthesis, rather than for a broad use on scales of many tons per year.

On the other hand, heterogeneous catalysis provides a powerful and state-of-the-art solution for the large-scale transformation of CO_2 into basic bulk chemicals, but the processes are not selective enough to achieve value added chemical compounds. In addition, if the selective transformation of CO_2 into more sophisticated molecules with homogeneous catalysis is targeted, the utilization of complex catalytic systems, often made by expensive and non-sustainable ligands, or of stoichiometric reaction partner (Alkyl boranes, Grignard and organolithium reagents), is, to date, the only chance.

A possible approach to avoid stoichiometric reagents is offered by photo- and electrocatalysis and it is likely that future endeavours to convert CO_2 will be provided by the combination of molecular catalysts with the action of electrons and photons.[13] This thesis is situated in this context, trying to provide a contribution to CCU, by exploiting a specific homogeneous catalyst to transform CO_2 into more useful carbon resources. The author's hope is to contribute to develop systems able to reduce the carbon footprint, nowadays extremely important to save the natural endangered equilibrium.

1.2 LESSONS FROM NATURE: CODHs, FDHs AND BIMETALLIC ACTIVATION

In order to understand the main principles which lead the design and optimization of new artificial catalysts, it is vital to know how nature deals with the selective and reversible conversion of CO_2, with a particular focus on the elucidation of the stereoelectronic properties of the extremely efficient natural catalysts, that are, enzymes.

Nature takes advantages of metalloenzymes to interconvert CO_2 and its corresponding reduced species. If carbon dioxide is transformed (not always reversibly) into CO, the interested class of enzymes is called CO dehydrogenases (CODHs); whereas if the product is formate, the enzymes are referred to be formate dehydrogenases (FDHs). They are all metalloenzymes which feature a mono- or multimetallic catalytic active site, as well as some crucial amino acids residues in the outer coordination sphere of the metal(s), to assist reversible CO_2, CO or HCO_2H binding. (**Figure 1.6**).

CODHs are divided in two class: anaerobes [NiFe] CODHs and the air-stable [MoCu] CODHs. They are both characterized by a bimetallic active site, in which the cooperation between the two metals is essential to efficiently promote the desired transformations. It is realised either with a proximity of the two metal ions, or via electronic communication provided by the flexible ligand framework.[26]
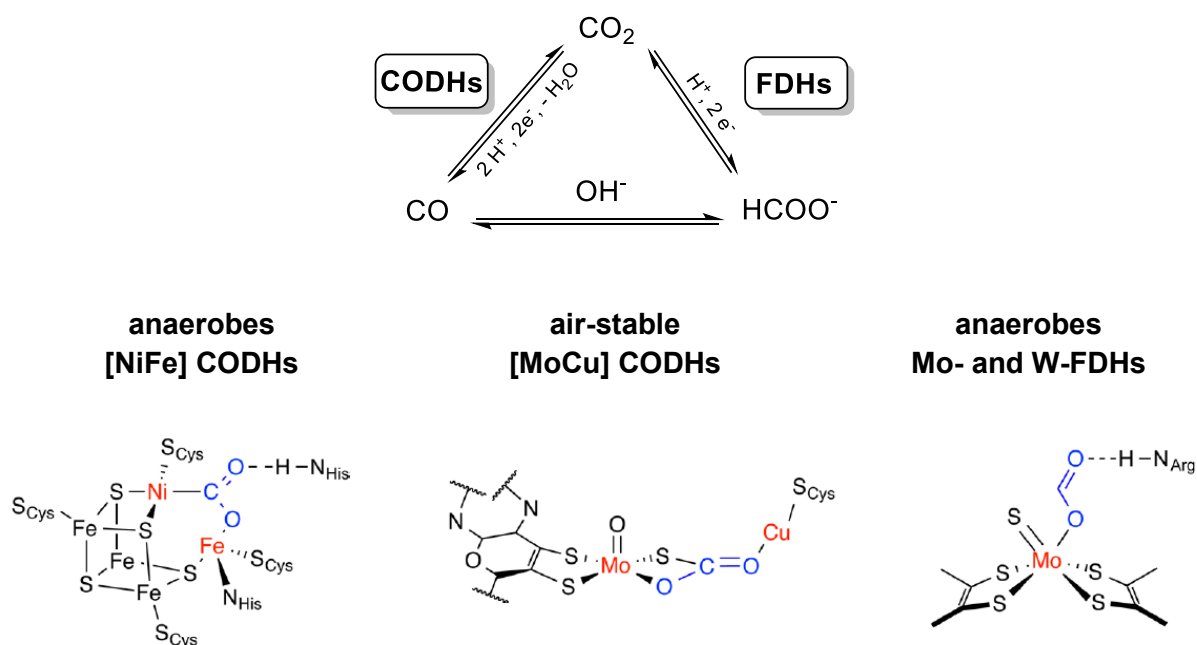
Figure 1.6 | Top: CO_2, CO and HCO_2H reversible interconversion promoted by CODHs and FDHs. Bottom: representation of the active sites of [NiFe] and [MoCu] CODHs; and of Mo-/W-FDHs.[27]

Anaerobes [NiFe] CODHs equilibrate CO and CO_2 near the thermodynamic potential. Their active site is composed by a bridging Fe_3S_4 cluster (of the class of the $[Fe_3S_4](SCys)_3$ iron-sulfur centers) which rigidly places Ni and Fe in close proximity.

$$CO_2 + 2\ H^+ + 2\ e^- \underset{\text{TOF= 40 000 s}^{-1}\ \text{(pH 7.5)}}{\overset{\text{TOF= 45 s}^{-1}}{\rightleftharpoons}} CO + H_2O$$
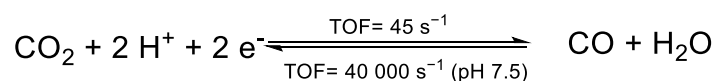
E°= −0.52 V vs the SHE at pH 7

As structure **1** in **Scheme 1.1** denotes, the Ni ion, in the oxidized form, possesses a T-shaped geometry, in which the three Sulfur ligands comes from two S-atoms of the cluster and one from Cys_{526}. The Fe1 atom, instead, possesses a distorted tetrahedral coordination geometry, with His_{261}, Cys_{395}, a μ_3-sulfido ligand from the cluster and a liable H_2O/OH, which is stabilized by H-bonding by Lys_{563}. Detailed studies conducted by *Dobbek et al.* in 2007 on the mechanism associated to the CO oxidation to CO_2 reveal an overall 2-electron process, likely occurring via a ECE mechanism (electrochemical-chemical-electrochemical).[28] When observing the catalytic cycle reported in **Scheme 1.1** in a clockwise direction, the first electrochemical step is the one-electron reduction of the active site to from Ni^I, followed by the CO_2 binding via a coupled ET, to yield the activated $\cdot CO_2^-$ intermediate. Here, the role of the His_{93} is crucial since it can perform H-bonding to the O-atoms of the metallacarboxylate. A local source of protons near the activated CO_2 can, at the same time, increase the stability of the metal-bound intermediate (neutralizing the negative charge) and assist the next protonation steps. At this stage, loss of water from Fe1-OH yield the bridging complex **3**, in which one oxygen of the metallacarboxylate moiety is bound to the Fe1. Again, Lys_{563} helps to stabilize this intermediate, providing H-bonding to the proton of Ni-C(Fe)OOH. Then, the C-O(Fe1) bond is cleaved to form the $Ni^{II}CO$ species, which readily loses CO, recovering the catalytic active site and completing the catalytic cycle.
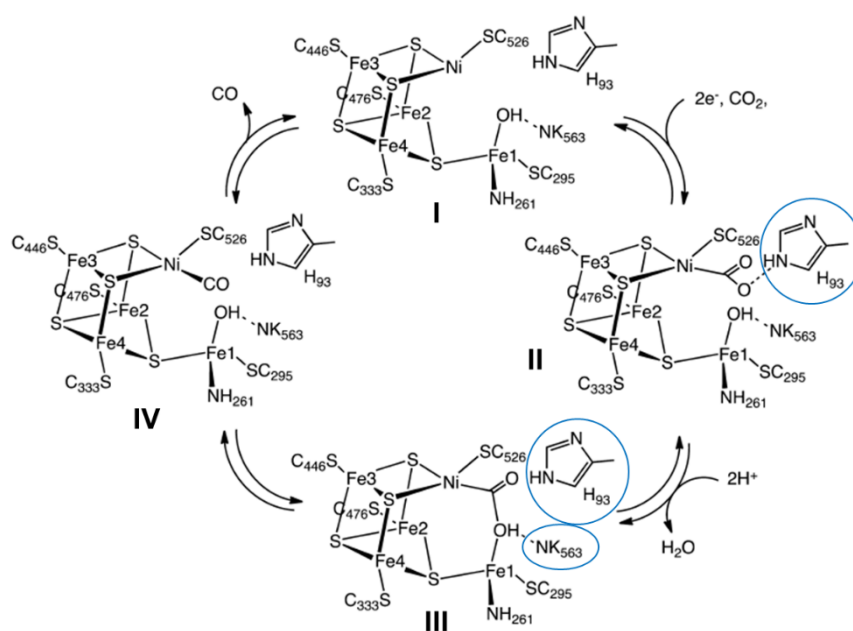
Scheme 1.1 | Proposed mechanism for the Reduction of CO_2 to CO by [NiFe] CODH.[26]

The second class of CODHs features a unique Mo−Cu active site. These air-stable enzymes, that can promote only the oxidation of CO to CO_2, are characterized by a dinuclear [CuSMo(=O)OH] reactive centre which, when in the oxidized form, contains a copper ion bridged via a sulphide ligand to a molybdenum oxo group. The Mo^{IV} centre features a distorted square pyramidal geometry, with an oxo group in the apical position, one μ-S atom, two S of the molybdopterin cytosine dinucleotide of the backbone and one OH group to complete the sphere. The Cu^I ion exhibits a linear two-coordinate geometry with a second sulfur atom from a cysteine residue completing its first coordination sphere.[29] The reduced-state form essentially retains the overall geometry, but with a lengthening of the Cu−Mo distance and of the Mo−O bond distances to the oxo and hydroxy ligands (**VI**, **Figure 1.7**). Regarding the detailed mechanism of the catalytic cycle there are some debates, mainly based on whether the CO coordinates with an end-on fashion to the Cu centre (**VII**),[30] or is inserted into the Cu−S bond (**VIII**).[29] Regardless the two mechanisms, differently from the Ni ion in the [NiFe] CODHs, Mo does not bind CO_2 via a Mo−C bond.
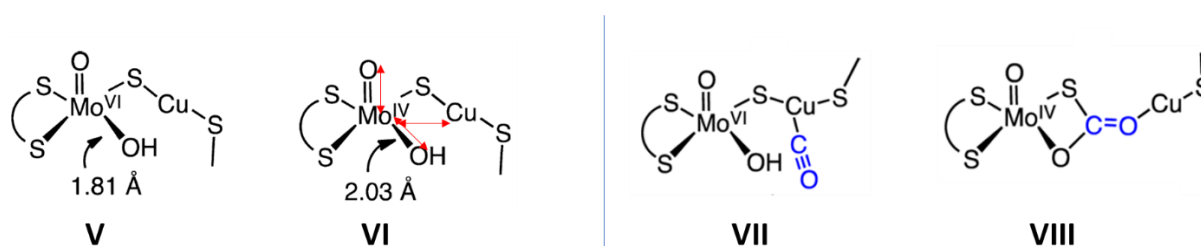
Figure 1.7 | Active site of a [MoCu] CODH in the oxidized (**5**) and reduced state (**6**); possible intermediates in the catalytic cycle: CO via η1-(C) to the Cu centre (**7**) and bridging μ-CO (**8**).[26]

After having analysed the structure-reactivity relationship of the two classes of CODHs, it is possible to draw some conclusions, to understand to which measure these architectural features have inspired the development of artificial molecular systems.

- Both active sites are **bimetallic**, in which a "soft" metal centre (Ni^0, Cu^I) is located in proximity with a "hard" metal (H.S. Fe^{II} and $Mo^{IV/VI}$). Despite this similarity, anaerobes [NiFe] CODHs can interconvert CO_2 and CO with a TON up to 40'000 s^{-1} for CO oxidation and 45 s^{-1} for CO_2 reduction; whereas [MoCu] are unable to promote the CO_2 reduction, probably because Cu(I) is insufficient reducing. However, some common features are found in both mechanisms, such as the bimetallic activation of the substrate and the presence of proximal proton-donating residues, fundamental for the stabilization of the metallacarboxylic intermediates.

- Both CODHs present conserved **redox reservoir**. Mo centres (ranging from +4 to +6 oxidation state) and [Fe₃S₄] supply electrons to the substrate in the catalytic cycle.

- The key point that characterizes these systems and that allows them to be so efficient, is the **minimal reorganization energy** required during the catalytic

cycle. Electron transfer steps, changing the electronic configuration of the metal centre(s), often require a re-arrangement of the ligands in the first coordination sphere. The [FeNi] cluster and the active site of [MoCu] CODHs, for instance, being oxidoreductase enzymes, possesses at least one vacant coordination site, often occupied by a liable ligand which can be easily displaced.

At this stage, it is possible to analyse some core concepts which may lead to a faster and more efficient development of artificial enzymes for CO_2RR.

The first aspect is the **catalyst nuclearity** (mononuclear vs. binuclear). As opposed to single-site catalysis, which can be optimized by changing the identity of the metal and the steric and electronic properties of the ligands, in multimetallic systems more parameters to optimize the catalytic behaviour are available. In fact, when considering multimetallic catalysts, the catalyst nuclearity, tunes the activity and the selectivity of the system. The presence of the second active metal can indeed diversify the reactivity between distinct mononuclear and dinuclear pathways, by issuing selectivity for a specific type of transformation, or specific class of substrates, controlling also the chemoselectivity of the whole process. Furthermore, variation of the **bimetallic pairing** (relative compatibility of two metal sites) can help to expand the scope of reaction pathways, as well as regulate the activity and selectivity (**Figure 1.8**)[31].
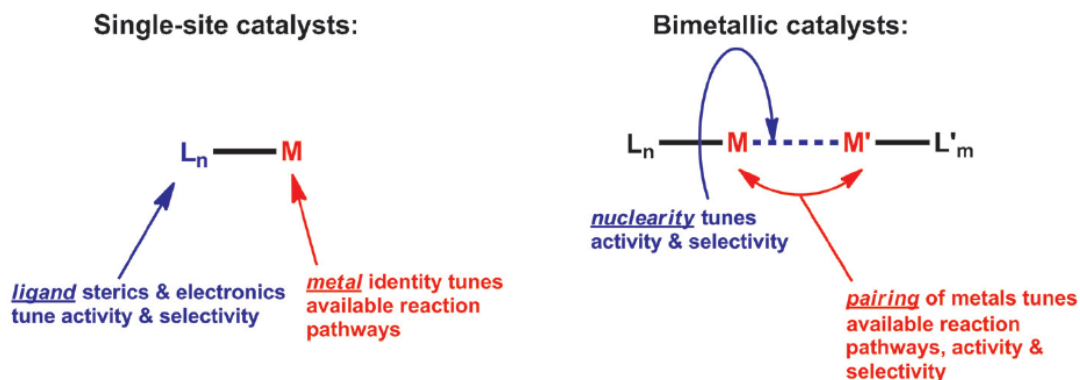
Figure 1.8 | Structure-activity relationships inherent to single-site catalysts (left), and additional optimization parameters available in bimetallic catalysis (right).

In this context, another concept to introduce is the "**cooperativity**" between the metal centres. As discussed above, strong evidence leads to assume that, in the catalytic cycle of the [NiFe] CODHs (**Scheme 1.1**), the two metals cooperate in the activation of CO_2, leading to outstanding catalytic performance (also helped by the internal proton transfer relay). This mechanism of activation is reminiscent of the "frustrated Lewis acid-base pairs", compounds in which a Lewis acid and a Lewis base, because of steric hindrance, cannot combine to form a classical adduct.[26] This concept has been exploited into catalytic systems which require stoichiometric educts to activate CO_2.

The first example of bifunctional activation of CO_2 was reported by the group of *Zanazzi* in 1982.[32] Their systems is based on a nucleophilic cobalt(I), coordinated by a tetradentate salen ligand, and an alkali cation (Li, Na, K, Cs). When the alkali ion was sequestrated by a dicyclohexano-18-crown-6, the fixation rate of CO_2 drops, suggesting a cooperativity between the Lewis pair. Later, in 2014, *Mazzanti et al.* applied the same concept, testing the reactivity of a Uranium(III) siloxide complex, alone or in presence of a Lewis acid towards CO_2 activation.[33] The unique reactivity that the ion pair complex [K(18c6)] [U(OSi-(O^{t}Bu)$_3$)$_4$] showed, *i.e.* the selective reductive disproportionation of CO_2 to yield CO and the mononuclear uranium(IV) carbonate complex, highlights the multimetallic cooperativity that takes place during CO_2RR.

Catalyst nuclearity and metals cooperativity can indeed affect the product selectivity and the catalyst efficiency, and, to date, they have been scarcely considered when developing artificial systems. Nonetheless, there are some systems in which bimetallic cooperativity is shown to play a fundamental role in catalysis. These catalysts will be presented in paragraph 1.5.2.

1.3 PORPHYRINS AND BIMETALLIC SYSTEMS

1.3.1 Porphyrins and metallaporphyrins

Metalloredox enzymes, which constitute approximatively the half of the total enzymes,[34] carry out fundamental roles in biological systems. In fact, they are responsible for the transport and storage of small molecules and ions (like O_2, HCO_3^-, NO_2^-, *etc.*), they enable electron transfer (ET) between substrates and other enzymes, they are also involved in key processes like DNA synthesis and repair, cellular respiration, and even in O_2 evolution (photosynthesis).[35] Sophisticated architectures have evolved to efficiently and selectively incorporate the metal centre(s), protecting it/them from the external environment and to tune its/their reactivity.

Metal containing redox proteins are subdivided in two categories: **electron-carriers** and the **oxido-reductase**. The first class comprises enzymes that possess one or more metal centres found in coordination sites that undergo minimal structural change because of oxidation or reduction. This characteristic, typical of heme-containing proteins, FeS centres and Cu enzymes, minimizes the activation barrier associated with electron exchange and optimizes ET.[36] The second class, namely the oxido-reductase enzymes, is represented by proteins equipped with one or more metal cofactors which possess, in at least one oxidation state, one vacant coordination site for substrate binding. The electronic structure of the cofactor also promotes facile binding and release of substrate and product, respectively. This category comprises square pyramidal or O_h copper sites in different oxidases or reductases (*e.g.* N_2O reductase,[37] CuB centre in cytochrome C oxidase[38]), the high-spin five-coordinate heme centre in cytochrome P450 or the special labile iron in Fe_4S_4 clusters (in aconitase, ferredoxin, endonuclease III).[39]

One prosthetic group (organic or inorganic cofactor that is tightly bound to an enzyme) that, thanks to its robustness and specificity, is present in both class of metal-based enzymes is the heme. Hemes, that are iron-containing **porphyrin** derivates, perhaps represent the archetypal electron-transfer unit.[35] The heme centre is so pervasive in discussion of electro-transfer proteins, to be present in several cytochromes, which are precisely classified according to the types of heme they contain (heme a, b, c and d). Of note, iron-protoporphyrin IX (heme b) is found in haemoglobin, where the {N_4} macrocyclic core that tightly and selectively bounds the Fe ion is responsible for the minimal arrangement required to act as O_2 carrier.

The macrocyclic nature of porphyrins undoubtedly contributes to the exceptional stability of their metal complexes.[40] A macrocycle is defined as a cyclic ligand possessing at least nine atoms in its ring sizes (included the heteroatoms) and three or more donor sites.[41] The fundamental unit of porphyrins is the **porphin**, that is a cyclic aromatic tetrapyrrole ring, possessing a conjugated π-framework[42] and a central {N_4} core (**L1**, **Figure 1.9**). Notably, porphyrins can act as dianionic ligands upon deprotonation of the two "acidic" protons (pKa ≈ 16)[43] at the nitrogen atoms of the pyrrole rings opposite to

each other, to give the respective porphyrinato ions that exhibit remarkable ligation capabilities towards several metals (metalloporphyrins). This feature is ascribable in a larger extent to the macrocyclic effect, first reported by *Hall* and *Amma* in 1969.[44] The nature of the aforementioned effect appears to be related, rather than to the entropic gains seen in the chelate effect,[45] to the solvation and configuration of the metal-free macrocycle. The preorganization of the macrocycle and the related decrease of the enthalpic and entropic costs of the complexation, however, contributes to a lesser extent to the overall stability of the complex.[46] The very relevant player in this context is the solvation, which determines an initial destabilization of the cyclic host molecule, subsequently removed upon complexation.

L1
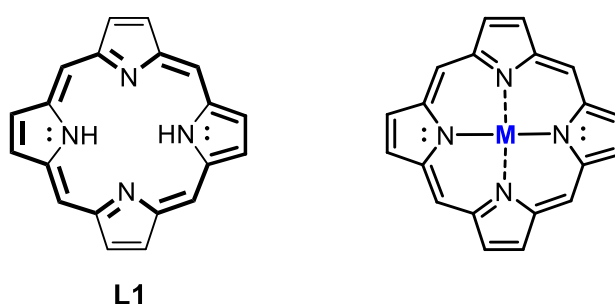
Figure 1.9 | Structure of the porphin ($C_{20}H_{14}N_4$), with the conjugate 18-π electrons system (left) and a metalloporphyrin, which is SP coordinated by the macrocyclic {N_4} core (right).

Modification of the backbone of the porphyrin structure and of the degree of aromaticity has led to the natural development of analogues structures, essential to the same extent as the porphyrin-based systems: the **corrinoids** (found in cobalamins) and **chlorins** (present in chlorophylls).[47]

Synthetic porphyrins and their metalladerivatives have been widely studied in the area of catalysis and mimicking enzymes, such as catalases, peroxidases, C-H activation catalysts (selective oxidations[48] and chemo-/regioselective C-H amination of sp^3 carbon atoms).[49] Because of their unique photochemical properties, they have gained importance also as NMR image enhancement agents, nonlinear optical materials, and DNA binding or cleavage agents. An overview of the most relevant synthetic porphyrins (Porphyrinoids) is given in the **Excursion 1.** Synthetic analogues of the Porphyrins: Porphyrinoid.

Notably, the pioneering studies of *Savéant and coworkers,* dated 1988 revealed that (modified) metalloporphyrins are also active towards CO$_2$RR.[50] They showed how electroreduced Fe("0") tetraphenyl porphyrins (**Fe1**, **Figure 1.10**) outperform all the other catalysts at that time, with a catalytic wave observed over the third, reversible, reduction peak, indicating that the formal $[(tpp)Fe^0]^{2-}$ species is active towards CO$_2$RR. Later, it was found that the activity and catalyst stability is dramatically enhanced when a mono- or divalent Lewis acid is added to the aprotic electrolyte. The employment of Brønsted

acids resulted in an additional increase of reactivity, since H-bonding interactions provided a marked stabilization of the reactive intermediate. Remarkably, the product selectivity is also controlled by the employment of defined amount of a specific Brønsted acids (CF_3CH_2OH, PhOH, TFA, H_2O). When phenolic groups in ortho and ortho' position of the arene substituents of [(tpp)Fe] were installed, a significant improvement of the catalytic performance towards CO_2RR was achieved (**Fe3**).[51] TOF at null overpotential (logTOF^0) for [FeTDHPP] (-4.6 s^{-1}) is four orders of magnitude higher that the respective FeTPP analogue (-8.4 s^{-1}). The same group. In 2016, introduced the most active catalyst along the series: iron tetra(p-N,N,N-trimethylanilinium)porphyrin, Fe-o-TMA (**Fe4**). This catalytic system, having four positively charged groups pointing towards the metal centre, outperforms each previous CRC, showing a CO selectivity of almost 100%, a durability of more than 80 h with an incredibly high activity, expressed in term of logTOF$_{max}$= 6.0 s^{-1} [52]

Ar= Ph **Fe1** - FeTPP
Ar= C_6F_5 **Fe2** - FeTPFPP

Fe3 - FeTDHPP

Fe4 - Fe-o-TMA
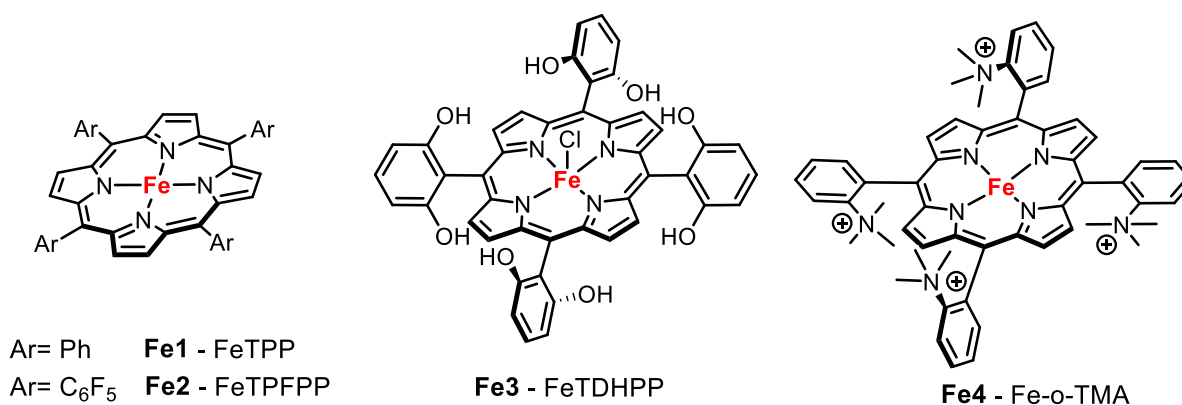
Figure 1.10 | FeTPP (**Fe1**), FeTPFPP (**Fe2**),[52] FeTDHPP (**Fe3**)[51] and the most active homogeneous CRC, Fe-o-TMA (**Fe4**),[52] all introduced by the group of *Savéant*.

Despite showing remarkably efficiency towards CO_2 activation and reduction, Fe-TPP and derivates are extremely selective for CO production, with average current efficiencies reaching almost 100 %. This makes the investigation of alternative catalyst, possessing different nuclearity and metal centre(s), highly interesting to broaden the scope of CO_2 reduction products. Consequently, the need of robust ligand platforms, able to simultaneously ligate defined metal ions, while showing the minimal reorganization energy upon substrate binding, leads to the synthesis of macrocyclic dinuclear complexes.

EXCURSION 1. SYNTHETIC ANALOGUES OF THE PORPHYRINS: PORPHYRINOID

In the last three decades, synthetic chemists have focus lot of efforts to have access to analogues of porphyrins, developing the so-called Porphyrinoid Chemistry. This large class of compounds is attractive because of their spectral, structural, chemical, and physical properties, in comparison with the parent porphyrin systems.

To date, two type of porphyrins isomers have been discovered: they both are characterized by a highly electron conjugation (18-π electrons) and by the formula $C_{20}H_{14}N_4$ representing their macrocyclic core.

The first isomer being introduced by *Vogel et al.* in 1986 is the **porphycene**,[53] followed by the similar *corrphycene*,[54] *hemiporphycene*,[55] and *isoporphycene*,[56] which, despite maintaining the {N4} ligand core, all differ from the natural frames of porphyrins for the pyrrole linking carbons (meso position). The other class, introduced independently by the groups of *Furuta*[57] and *Latos-Grazynski*[58] in 1994, is represented by the so-called inverted or "N-confused" porphyrins (**NCP**), in which one pyrrole subunit is inverted to form a central {N3C} core, maintaining 4 *meso*-carbon atoms. NCP showed from the beginning important characteristics that attracted lots of interests, such as a long wavelength absorption (with applications in photodynamic therapy, PDT),[55] and the ability to generate organometallic derivates.[59]

One of the features of NCP chemistry, which differs from normal porphyrins, is in fact its multivalent nature as a metal ligand. NCP was found to complex either divalent Ni(II)[58] in a square planar fashion or, in the form of trianionic ligand, trivalent Ag(III)[64] to give a redox-stable, distorted SP Ag(III)NCTPP.
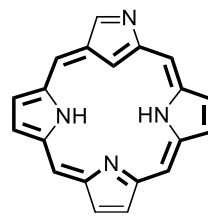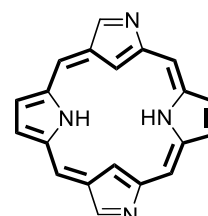
NCP - L2   ***trans*-N₂CP - L3**

To further increase the σ-donor character of the macrocyclic ligand, *Osuka et al.*, in 2000 introduced the doubly N-confused porphyrins (N₂CP), which can stabilize metal centres in higher oxidation states.[65] In particular, the group stated how the cis (Cα,Cβ,N,N) trianionic N₂CP ligand can efficiently form unusual Ag(III) and Cu(III) square-planar complexes with two sets of metal-carbon bonds.

It is worth mentioning the synthesis and study of the "expanded porphyrins", which are large, porphyrin-like macrocycles that contain an increased number of π-electrons, additional coordinating heteroatoms (from, *e.g.*, pyrroles), and/or a larger central binding core compared to their smaller tetrapyrrolic analogue. The first compound of this class was reported by *Woodward* early in 1966,[66] namely a five pyrrole rings structure connected through four *meso*-carbon atoms: *sapphyrin.*

Subsequently, in 1983, *Gossauer et al.* introduced the next higher homologues, *pentaphyrin* and **hexaphyrin**.[60] In particular, the hexaphyrin-derivate here reported, **L4**, achieved by using a Cr^{VI}-based oxidative coupling strategy, showed to be a good hexadentate ligand for lanthanides such as $(UO_2)^{2+}$ and $(NpO_2)^+$.

L4
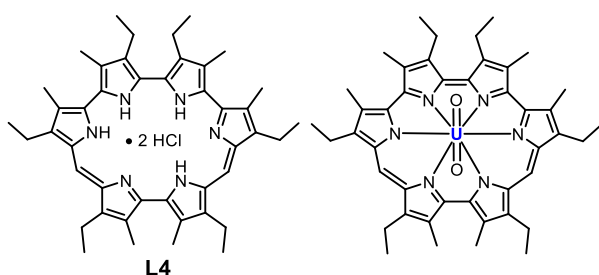
These macrocycles (and the metal derivates) are widely used as anion receptors,[61] sensitizers for PDT,[62] and magnetic resonance imaging (MRI) contrasting agents.

Of note, connected to the last application, it is worth mentioning the three-pyrrole, expanded porphyrinoid, known as **texaphyrin**, introduced by *Sessler et al.* in 1994 (**L5**).[63]

After having synthesized several lanthanide(III) texaphyrin complexes which may serve as photosensitiser for cancer treatment or as adjuvant in radiation therapy,[67] the same group expanded the library of transition metal complexes of texaphyrin by introducing Mn, Cu, Ni, Zn (see below). For Mn(II) and Co(II) they found that the monoanionic macrocyclic ligand provides for a five-coordinate planar arrangement, with the stabilization of the lower oxidation state (+2).

For the Zn(II) complexes, only three nitrogens were found to coordinate the metal centre, which showed one or two ancillary ligands in axial position. Interestingly, the Mn(II) complexes, featuring redox behaviours similar to that showed by lanthanide ones, it is studied as peroxynitrite decomposition catalyst, being a good candidate for the treatment of ROS-related pathologies.[68]

L5 $M^{n+}= Mn^{2+}, Ni^{2+}, Co^{2+}, Zn^{2+}$
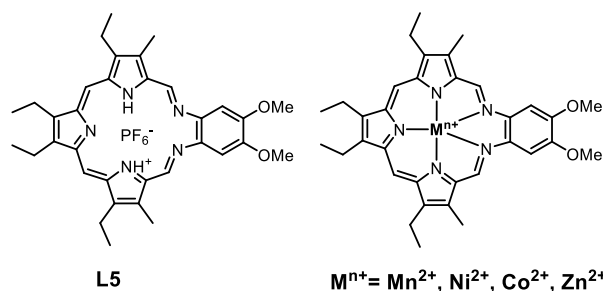
1.3.2 Bimetallic system

With a view to access to bimetallic systems, *hexaphyrins* (porphyrinoids featuring six pyrrole rings, see **Excursion 1.** Synthetic analogues of the Porphyrins: Porphyrinoid) appeared to be good candidates, since some of them were reported to take planar conformation.[69] In this context, in 2003 the group of *Furuta* reported the first doubly N-confused hexaphyrins (**L6**) and square-planar coordinated in-plane bismetal complexes of aromatic porphyrinoid.[59] Those N_2CH porphyrinoids, overcoming the intrinsic difficulty of bimetallic coordination of normal hexaphyrins (that require a selective CH activation of the inner N_2C_2 core), gave rise of flexible bimetallic complexes upon treatment with anhydrous $Cu(OAc)_2$ and $Ni(acac)_2$: **Cu₂1** and **Ni₂1**. Despite the interesting features that defines this class of complexes, *i.e.* presence of two adjacent metal centres surrounded by a 26 π-electron pool, a spontaneous oxidation of the N_2CH macrocyclic core to the amide-form is necessary to stably coordinate the metal centres.

Two years later, the group of *Osuka* reported the synthesis of a homobimetallic Gold (III) complex based on the *meso*-hexakis(pentafluorophenyl)-substituted hexaphyrin (**L7**), a planar and rectangular-shaped, 26π electron macrocyclic ligand.[70] The ligand structure is derived from the doubly NCP (see above), but in this case the nitrogens of the central pyrroles point outwards, determining two fused coordination pocket of the {N_2C_2} type.
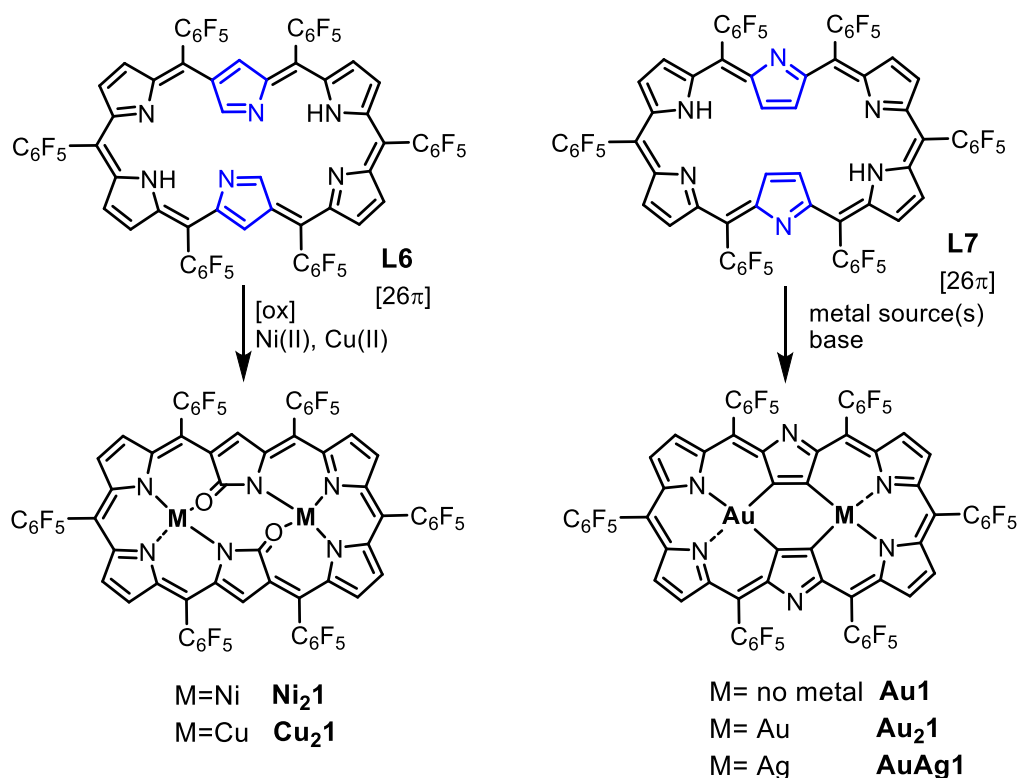

Figure 1.11 | Doubly N-confused hexaphyrins and bismetal complexes reported by *Furuta et al.* (left),[59] and its analogue (with inverted pyrroles) precursor for homo- and heterobimetallic complexes. [70]

The metalation of this ligand has been performed using NaAuCl$_4$ and NaOAc in a 4:1 mixture of CH$_2$Cl$_2$ and methanol, causing the activation of the Cβ-H bonds of the inverted pyrroles, affording the homobimetallic gold complex **Au$_2$1** and the heterobimetallic **AuAg1**. They were also able to isolate the monometallic counterpart, in which only one gold ion was coordinated to two pyrrolic nitrogen atoms and two β-carbon atom. Interestingly, analysing the crystal structures obtained with S.C. XRD, showed that the mono-Au(III) complex exhibits a planar, but twisted structure, whereas **Au$_2$1** adopts a more planar but overall bent structure, because of the decreased congestion between the inner pyrrolic β-protons.

In trying to re-establish the porphyrinic {N$_4$} coordination sites, in 2011 the group of Meyer introduced in the so-called **Siamese Twin Porphyrins**.[71] In these macrocyclic scaffolds, two porphyrin-based structures are efficiently fused together via two pyrazole units (**L8**, **Figure 1.12**). As a result, the aromaticity degree of the ligand platform is decreased respect to the related *hexaphyrins*, resulting in two independent conjugation pathways.[72] This class of porphyrinoids can accommodate two metal centres, giving rise to homobimetallic and heterobimetallic compounds. Among the ligated metals, there are Cu(II), **Cu$_2$2**,[73] Ni(II), **Ni$_2$2**,[73] Pd(II), **Pd$_2$1**,[74] and Pt(II), **Pt$_2$1**.[75] All complexes showed an overall helical twisted conformation, which, in case of **Cu$_2$2**, is responsible for the unique ferromagnetic coupling between the two metal ions arising from the orthogonal disposition of the metal $d_{x^2-y^2}$ orbital, which also minimizes the overlap with the bridging pyrazole unit. In fact, no appreciable electronic communication between the metals was electrochemically detected, since the Siamese Twin Porphyrin framework displays a hidden redox non-innocence, resulting in ligand-based oxidations/reductions. Interestingly, the asymmetrical coordination of metal ions was also achieved, with all the combinations of the previous metal ions reported to date.[75],[76]

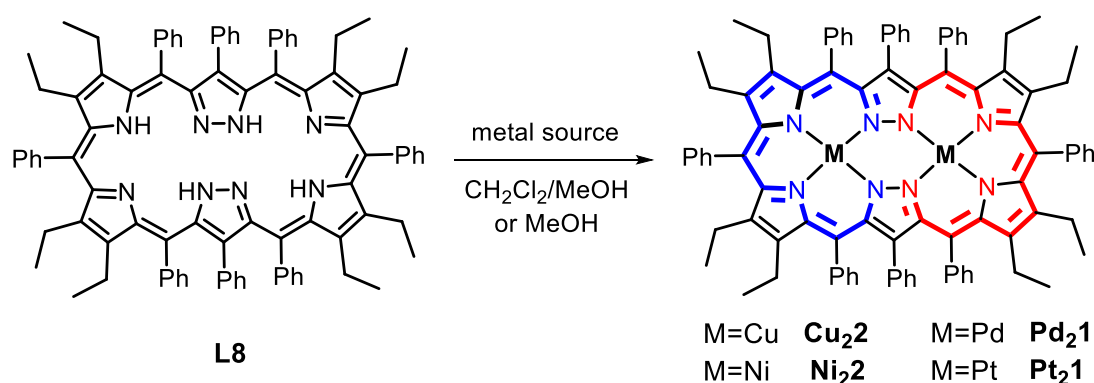| M=Cu | **Cu$_2$2** | M=Pd | **Pd$_2$1** |
| M=Ni | **Ni$_2$2** | M=Pt | **Pt$_2$1** |

Figure 1.12 | Siamese Twin Porphyrins and relative bimetallic complexes.[71],[73]

This last aspect highlights the Siamese-twin porphyrin's potential to serve as an adjustable platform for multielectron redox processes in chemical catalysis and in electronic applications. The nature of bonding between a metal atom and the porphyrin

ligand essentially originates from the presence of two different types of nitrogen donor atoms: two "classical pyridine" type ligands (σ-donor and π-acceptor) and two "unusual" amide- N-ligands (σ- and π-donor). Therefore, electron rich metals can be stabilized due to the π-acceptor character of the amine-type sites, whereas electron poor metals (in high oxidation states) can also be stabilized via electron donation from the amide sites of the ligand.[77] The formal exchange of the heterocyclic building units of the macrocycle from pyrroles to N-alkylated imidazoles results in potential NHC ligand precursors as the resulting donor atom in each heterocycle would be a carbon atom surrounded by two nitrogen neighbours.

In 2015, the group of Pöthig, applying this substitution (four imidazolylidenes instead four pyrazoles), obtained the calix[4]imidazolylidene[2]pyrazolate, which is only topologically reminiscent of the Siamese Twin Porphyrin (**Figure 1.13**).

NHCs replace pyrroles

Siamese-twin porphyrin
Meyer *at al.* 2011

pyrazole/imidazole cyclophane
Pöthig *at al.* 2015
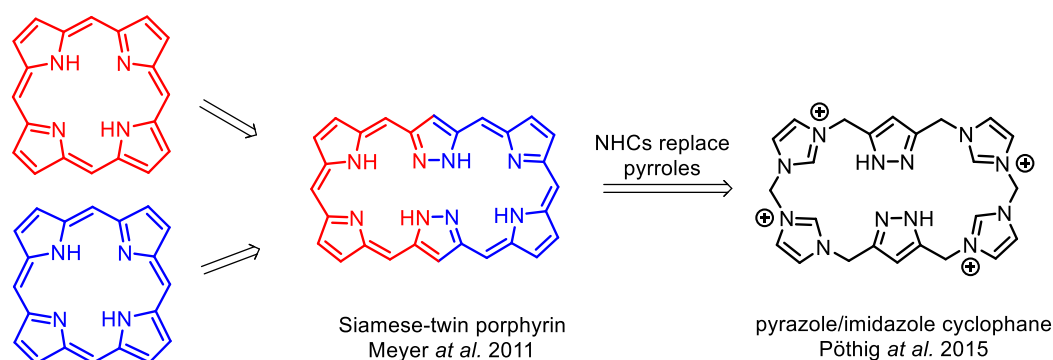
Figure 1.13 | Siamese Twin Porphyrins possess two fused Porphyrin rings connected by pyrazole units. If pyrroles are replaced with imidazoles, a pyrazolate/NHC ligand precursor is obtained.

This hybrid pyrazole/imidazole-based cyclophane, in fact, does not possess any extended electron conjugation, and it can be used, apart for a binucleating ligand precursor, also for hydrogen bond sensor.[78] In fact, the macrocyclic poly-imidazole **H$_6$L^{Me}(PF$_6$)$_4$**, possessing 4 acidic protons pointing towards the inner cavity, can act as a supramolecular host molecule for H-bonding acceptor molecules, such as MeCN. When the NHC-precursor protons are removed and a suitable d^8-metal precursor is provided to the reaction mixture, corresponding dinuclear NHC/pyrazolato Ni, Pd and Pt complexes are obtained.[79] These complexes possess a very attractive solid-state saddle-shaped structure, as X-ray analysis has revealed, whose cavity width slightly depends on the ligated metal (according to its ionic radius) and, to higher extent, to the alkylene bridge that connects the imidazolylidene moieties. When, instead, the *in situ* deprotonated macrocyclic ligand is treated with a d^{10}-metal precursor, an octanuclear Ag(I)- or Au(I)-NHC complexes, with a tubular structure is obtained. Its peculiar well-defined cavity has been employed to incorporate linear molecules and for the development of organometallic rotaxanes (**Figure 1.14**).[80]

Figure 1.14 | Preparation of metal-NHC complexes derived from $H_6L^{Me}(PF_6)_4$.[78],[81]

Considering their bowl-shaped structure, the exceptional stability that characterize the NHC/pyrazolate dinuclear complexes, arising from the strong NHC-metal bonds and from the macrocyclic nature of the ligand, and the overall rigidity of the systems, the evaluation of the small molecules activation potential of the M_2L^R $(PF_6)_2$ is highly attractive. In particular, cons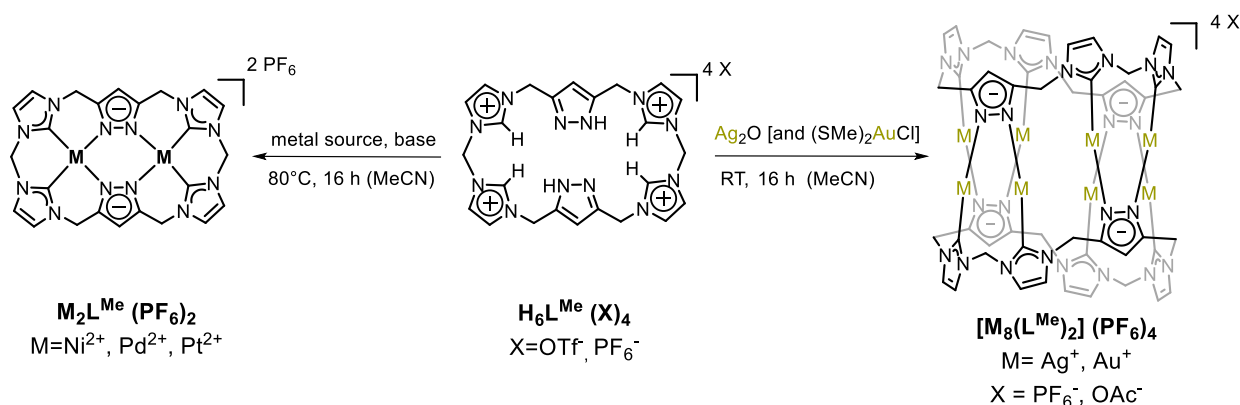idering the increased σ-donation degree in NHC-metal bonds that can increase the nucleophilicity of the metal centre, those metal complexes (especially the Ni-one) are envisioned to be active towards CO_2 reduction.

EXCURSION 2. PYRAZOLATE-LINKED BIMETALLIC SYSTEMS

One phenomenon that renders certain biological catalytic transformations so efficient is metal **cooperativity**, that occurs when the mechanism is influenced by the action of two (or more) metal centre(s), which do not act independently from each other. When aiming at the synthesis of effective bimetallic catalyst, the intermetallic distance, their respective coordination pockets, as well the electronic communication between them are key parameters to take into account (**Figure 1.15**). The employment of pyrazolates, possessing the diazine units, has been largely explored because of its small, planar structure and for the ease of 3,5-difunctionalization.

Figure 1.15 | Representation of a bimetallic metal complex: M1 and M2 are linked through the bridging ligand.

N-heterocyclic carbene donor sites have been added firstly by *Zhou et al.* (for the synthesis of **Ag1** and **Au2**) from the Im-Pyr-Im ligand precursor.[85] The same group reported how the employment of a basic oxide, such as Ag_2O, is sufficient to deprotonate the two NHC precursor protons and to give rise to box-shaped tetranuclear metal complexes.

The same group reported also the bis-Ni(NHC) complex which possesses a 2-

This class of compounds comprises ideal coinage metal complexes to obtain Cu-, Ni-, Pd-, Ru-, Rh- and Ir-complexes.of pyrazole linked NHCs. By varying the wingtip substituent of the imidazole ring and by defining the ligand:precursor ratio, it is possible to control the outcome of the metalation. For example, by employing a bulk picolyl substituent (in the N-wingtip position), bimetallic **Ni₂3**[82] and **Cu₂3**[83] are obtained, while the less bulky methyl group enables the dimerization of the Im-Pyr-Im core around the metals ions, as in **Ni₂4**[82] and **Pd₂2**.[84] Interestingly, **Ni₂3** shows a bridging hydroxy group which coordinates both metal centre, but no electrochemical studies to assess the electronic coupling were performed.

pyridyl N-wingtip donor group instead of the picolyl moiety.[82] Notably, in the latter complex the intermetallic distance is significantly shortened, from 3.873 Å of **Ni₂3** to 3.255 Å.

Building further upon this scaffold, *Herrmann et al.* reported the synthesis of **Ru₂1** and **Rh₂1**, in which the two metals are connected, beyond the diazine unit, by a μ-Cl anion.[86] The complexes, obtained by heating at 110°C the mixture with Ag₂O and the metal precursor, display two O$_h$, coordinatively saturated metal centres. Remarkably, the bis-Ru(NHC) is characterized by a moderate degree of electronic coupling.
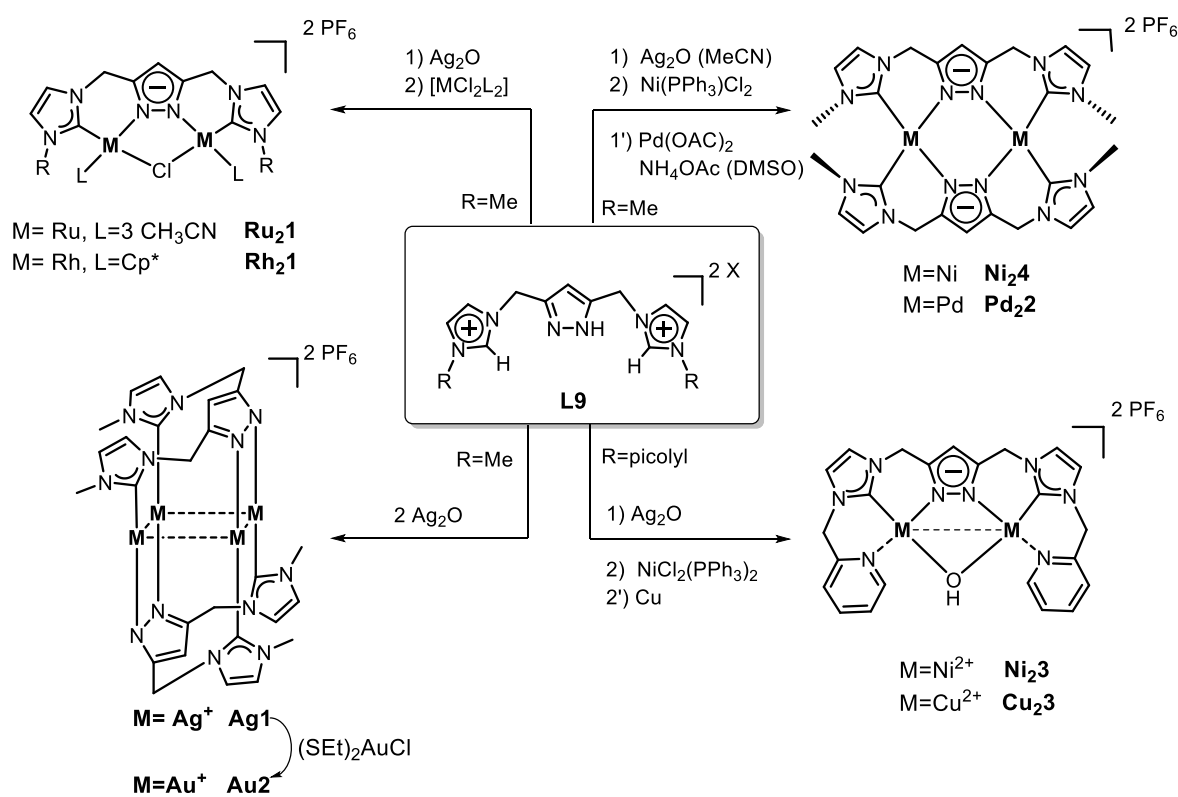

Figure 1.16 | Overview of some of dinuclear pyrazole/NHC-metal complexes obtained from **L9**.

1.4 NHC COMPLEXES: THEORY AND APPLICATIONS

Among all the ligands for transition metals, N-heterocyclic carbenes (NHCs) have experienced an extraordinary development in the last two decades, to the point of attracting much more academic and industrial interest respect to the Fischer and Schrock carbenes.[87] This type of ligands, based on unsaturated carbon atoms with six electrons on their valence shell[88] and at least one nitrogen atom within the ring structure,[89] can act as precursors of the respective NHC-metals complexes. Nowadays, NHCs span a wide range of applications, such as homogeneous catalysis (cross coupling reactions,[90],[91] olefin metathesis,[92] CH activation[93] and many others[94],[95],[96]), material science,[97] as well as metallopharmaceuticals[98]. The utility of the NHCs goes beyond the coordination to transition metal, since complexes of NHCs with p-block elements allow the stabilization of reactive species,[99] providing an useful tool in organic synthesis. Furthermore, the exploitation of NHCs in the young and fast-developing area of organocatalysis has showed to mediate a wide range of different organic transformations, such as polymerizations[100] and transterifications.[101]
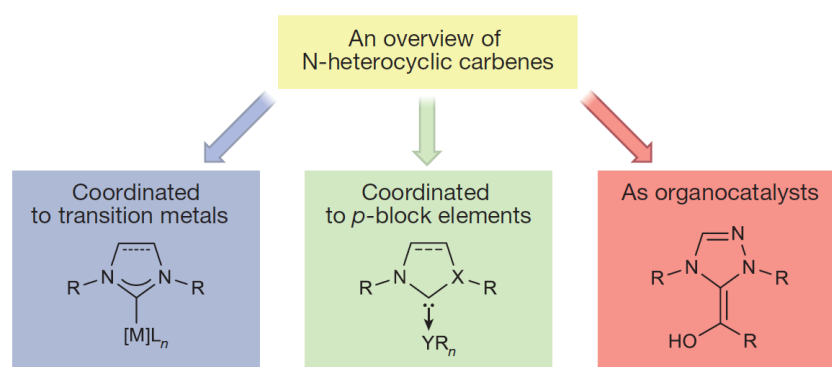
Figure 1.17 | Major applications of NHCs: NHCs can coordinate to metals and p-block elements or they can act as organocatalysts.[88]

Despite the early works of *Wanzlick*[102] and *Öfele*[103] on the synthesis of Hg(II) and Cr(0)-NHC complexes, the turning point in the NHC field is dated in 1991, when *Arduengo et al.*, studying the deprotonation reaction of hindered imidazolium salts, obtained a crystal of the first, stable N-heterocyclic singlet carbene: 1,3-bis(adamantyl)imidazolin-2-ylidene.[104] Thanks to the remarkable stability if the NHC-metal bond, only four year later, the first application of a metal-NHC complex in catalysis was reported. *Herrmann et al.*, in fact, in a seminal work reported how an imidazol-2-ylidenepalladium complexes is highly active towards the Mizoroki–Heck coupling reaction.[105]

To understand the advantages of this class of compounds when employed as ligand precursors, is pivotal to briefly discuss the stereoelectronic properties of NHCs. NHCs, being characterized by a constrained N-C-N bond angle, possess a singlet ground state multiplicity, with the HOMO centered on the sp^2-hybridized carbene lone pair and the

LUMO on its empty p_z orbital (**Figure 1.18**).[88] The main role of the nitrogen atoms is the stabilization of the carbene centre, either *via* inductive effects (lowering the energy of the occupied σ-orbital), or *via* mesomeric effects (π-donation to the carbene empty p_z-orbital).
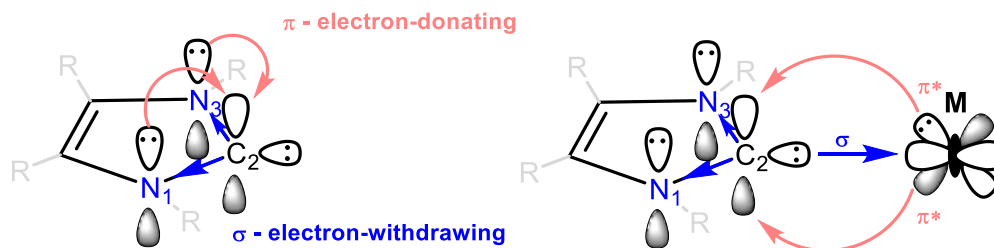
Figure 1.18 | Schematic representation of the stabilization mechanism of imidazol-2-ylidene NHCs (left), and NHC→M σ-donation and π*-backdonation in M-(NHC) bonds.

Different strategies have been reported to date to access the metalation of this unique class of compounds, among which deprotonation of azolium salts, direct oxidative addition and transmetalation.[106] Three are the bonding contribution to the M-(NHC) bond. The most relevant is the NHC→M σ-donation (80% of contribution to the bond), followed by the M→NHC π*-backdonation and the NHC→M π-donation. In this regard, the imidazolylidene moieties, employed in the metal complexes of this study, is expected to possess a reduced π-acceptor ability and a strong σ-donor potential. The **electronic properties** of NHCs are evaluated by the *Tolman electronic parameter* (TEP), [107] which is proportional to the σ-donor strength and span from 2033 cm^{-1} of highly σ-donating mesoionic carbenes to 2058 for the six-membered ring NHCs.[108] Notably, differently from phosphines, electronic properties can be easily tuned by varying ring size and backbone functionalization (altering inductive and mesomeric effects), by the type and number of heteroatoms (N, O, S), and, more elegantly, by the employment of switchable substrates.[109] Furthermore, the **steric properties** assume a relevant role in dictating stability and reactivity of NHCs, because of the kinetic stabilization towards dimerization (Wanzlick equilibrium). Steric properties, which are modulated by the N-wingtip functionalization, are compared with the buried volume (% V_{bur}) value, which is usually comprised between 25-36%.[110]

Hence, NHCs are highly attractive class of compounds because they can provide stronger and more stable NHC-metal bonds, with an increased σ-character and a tunable electron density to the metal centre. For these reasons, a very prominent subgroup of this class of compounds, are the "poly-NHC ligands",[111] and, among them, the attention will be focused on **macrocyclic poly-NHCs**.

1.4.1 Macrocyclic NHC complexes

Macrocyclic poly-NHCs are a versatile class of compounds, employed in molecular[112] or anion recognition[113],[114] and incorporated in supramolecular architectures such as anion-directed mechanically interlocked catenanes[115] and rotaxane structures.[116]

The unique features of macrocyclic imidazolium (and benzimidazolium) salts have made them suitable for being metal NHC precursors. Macrocyclic poly-NHCs can indeed combine the favourable macrocyclic effect to the exceptional stability of M-(NHC) bonds, while possessing a pre-organized cavity to accommodate one or more metal centre(s). Different strategies have been applied for the isolation of this class of compounds, such as an on-site metal template synthesis,[117] photocycloaddition of two linear azolium precursors,[118] ore the most generally applicable transmetalation and the synthesis of macrocyclic poly(azolium) salts followed by their deprotonation to the poly(NHC) derivatives.[119]

The first report of a metallic cyclophan-like, polydentate NHC is dated 2002, when the group of *Baker* introduced a nickel-carbene complex (**Ni1, Figure 1.19**), derived from an Imidazolium-linked *meta*-Cyclophane.[120] The same adaptable ligand platform has been exploited by *Meyer and coworkers* to ligate iron in two different oxidation states,[121] and copper even in three, from +1 to +3.[122] All metal complexes, with the exception of **Cu1**, with Cu(I), possess a saddle-shaped structure, with the nickel ion in **Ni1** characterized by a distorted SP geometry, copper in **Cu1** (Cu^{II} and Cu^{III}) by a distorted square pyramidal coordination, and by an O_h geometry for iron (Fe^{II} and Fe^{III}) in **Fe5**. Fully reversible oxidation waves in the CV, either for the Fe- and Cu-complexes, suggest a relative flexibility of the ligand platform, which, thanks to the linear C^{NHC}-M-C^{NHC} arrangement and to the hemilability of the Pyr donors, allows the ligand to adapt to the different stereoelectronic and coordination requirements of different oxidation states. When a d^{10} metal precursor is added to **L10**, such as [Au(SMe)$_2$Cl], a dinuclear complex is obtained (**Au2**), in which the linearly-coordinated metal centres connect two ligand units, with the pyridines not involved in metal binding.[123]

Figure 1.19 | Pyridine/imidazolylidene macrocyclic ligand precursor (**L10**) and its dinuclear Au complex (left) and mononuclear Ni,[123] as well as Cu^I/Cu^{II}/Cu^{III}[122] and Fe^{II}/Fe^{III} (right).[121]

When the pyridines are replaced by phenyl moieties, the diazolium salt is unable to act as a macrocyclic ligand, and it gives rise to chelate complexes through the NHC donors (with Pd^{II}, Pt^{II}, Rh^{I} and Ir^{I}).[124],[125] The other two ligands, to achieve a SP coordination, arise from two Br⁻ (Pd and Pt) or from a cyclooctadienyl moiety (Rh and Ir).

When the dimension of the size of the macrocycle is expanded and the number of imidazolium units is increased, the tetracoordination of bivalent metal ions becomes very rare. A flexible macrocycle scaffold that is an exception to this trend, and that displays two different metal-dependant coordination modes, is the tetraimidazoluim macrocycle **L11**, introduced by *Hahn et al.* in 2015.[126] If the deprotonation is performed with an external base, and a d^8 metal precursor is added, the mononuclear complexes **Ni2**, **Pd1** and **Pt1** are obtained, whereas if the basic Ag_2O is provided to a solution of **L11**, the tetranuclear octacarbene sandwich **Ag2** is produced (**Figure 1.20**).
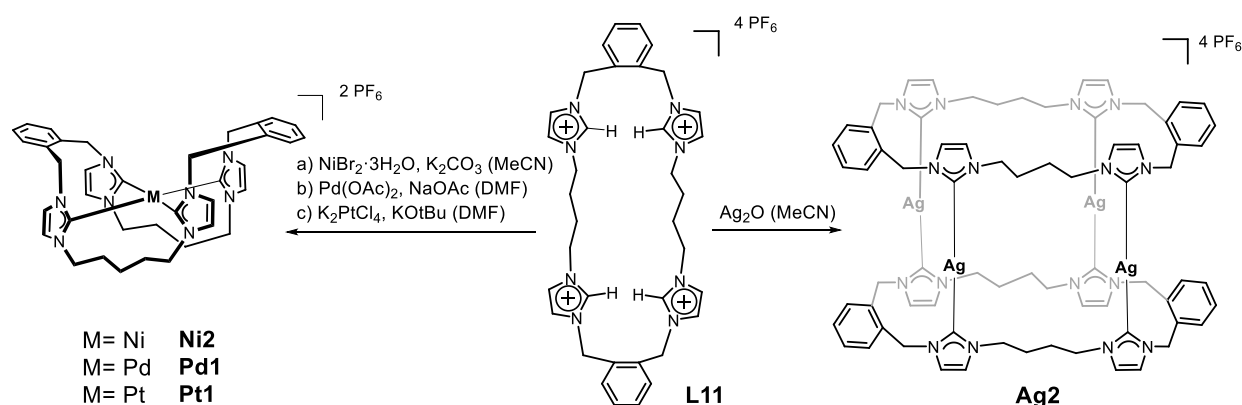

Figure 1.20 | Macrocyclic tetraimidazolium precursor introduced by *Hahn* with metal dependant coordination modes: tetranuclear Ag-NHC complex (right) and mononuclear Ni, Pd and Pt complexes (left).[126]

That study pointed out the fundamental role that the flexibility of the bridging groups in macrocyclic tetra-NHCs have in dictating metal coordination mode and, hence, the overall structure of the complexes. Another very interesting tetraimidazolium macrocycle is **L12**, reported by *Xue et al.* in 2017. Notably, in the flexible macrocyclic structure, there are four benzimidazolium units which serve as NHC precursors and two amines, which can potentially give rise to different metal coordination modes. In fact, adjusting the stoichiometry between the base and the metal precursor, either the all-NHC, mononuclear **Ni3** and **Pd2**, or the binuclear **Ni₂4** and **Pd₂3** are obtained (**Figure 1.21**).[127] The mononuclear complexes possess a distorted SP coordination, whereas **Ni₂5** and **Pd₂3** feature a C_2N_2 coordination pocket, with bridging amine units. Interestingly, the Ni centres in **Ni₂5** are only 2.855 Å apart, with the same complex that is the only redox active among the series, since it shows a fully reversible oxidation feature at 0.23 V, associated to the formation of Ni^{III},Ni^{II}.
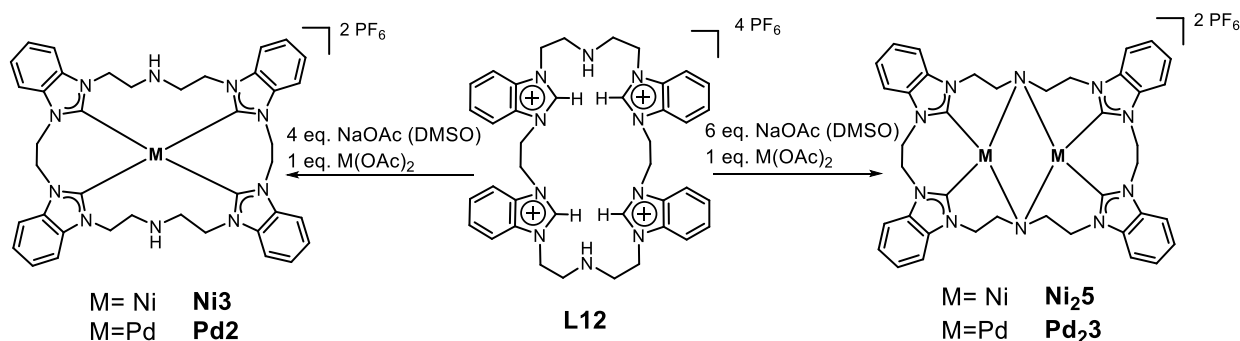
Figure 1.21 | Different NHC and NHC/amine metal complexes obtained from the flexible hexadentate macrocyclic NHC ligand precursor.[127]

The first asymmetrically bridged macrocycle, such as tetra(imidazolium) salt **L13**, was reported by *Jenkins and coworkers* in 2010 (vef)[128] The versatile tetraimidazolium macrocycle possess remarkably coordination potential, being able to form monometallic complexes with Pt(II), Pd(II), Ni(II), Rh(III), Co(II), Ru(II), Cr(II),Au(III) and Fe(II). Of note, the monometallic iron compound has showed promising reactivity towards aziridination of electron-donating aryl azides and a wide variety of substituted aliphatic alkenes in a "$C_2 + N_1$" addition reaction.[129] The group of *Meyer* expanded the application of this Fe(II)-heme analogue by employing it in the electrocatalytic CO_2 reduction (discussed later).[130]

Recently, *Kühn and coworkers* introduced the symmetrical version of **L13**, in which the four imidazolylidene moieties are bridged by methylene groups. The tetraimidazolium precursor, similarly to **L13** gave rise to tubular-shaped complexes with Ag(I)[131] and, upon transmetalation, with Au(I), whereas Cu(III)[132] and Au(III)[133] complexes displayed distorted SP geometries. Furthermore, the same group isolated the Co(II) analogue, which can activate molecular oxygen, resulting in the dicobalt(III) μ_2-peroxo N-heterocyclic carbene **Co1** (**Figure 1.22**). The peroxo moiety can be cleaved upon addition of acetic acid, yielding the corresponding Co^{III} acetate complex, along with H_2O_2 formation. Similar reactivity was shown also the Fe(II) analogue, for which, upon oxidation, a Fe(III)-O-Fe(III) has been isolated.[134] The iron-superoxide compound is highly interesting because of its spontaneous formation upon activation of molecular O_2 in acetone and for its ability to act as an oxidant in epoxidation reactions.[135]
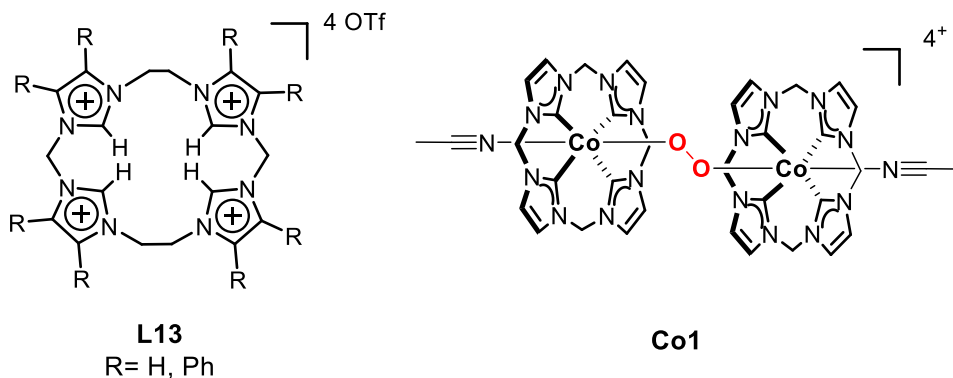
Figure 1.22 | Macrocyclic tetra-imidazolium ligand introduced by *Jenkins et al.* (left),[128] and dicobalt(III) μ₂-peroxo complex reported by *Kühn*.[136]

The field of macrocyclic NHC is way broader than the reported complexes.[106] However, these examples pointed out one of the attractive features of macrocyclic poly-NHCs, that is the potentiality to fine tune the stereoelectronic properties of the coordinated metal centre(s). The latter objective is achieved by optimal ligand design, and it results in the application of this class of compounds in catalytic transformation, among which the young and always more appealing field of small molecules activation.

1.5 ELECTROCATALYTIC CARBON DIOXIDE REDUCTION (CO₂RR)

1.5.1 General considerations regarding CO₂RR

Since the process of making more valuable chemicals from CO_2 involves electron sources, artificial photosynthesis and (photo)electrochemical reduction of CO_2 have attracted more and more interest within the scientific community. Electrocatalysis is the most investigated approach and, therefore, the better understood.

To understand how the latest processes works, it should be noted that each homogeneous electrocatalytic CO_2 reduction process can be divided into three main steps. (**Figure 1.23**) After the first electron transfer (ET) from the electrode surface to the catalyst, which gives rise to the active catalytic species (**i**), interaction between CO_2 and the metal complex takes place (**ii**). Finally, a series of protonation of the catalytic intermediates occur, yielding the reaction products and regenerating the catalyst (**iii**).
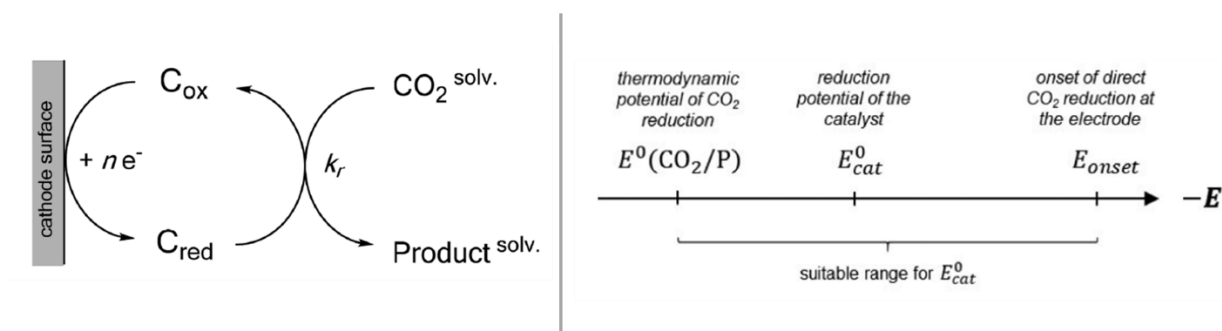

Figure 1.23 | Scheme of the steps involved in homogeneous electrocatalysis (left) and prerequisite for the relative positions of E_{onset}, E^0_{cat}, and $E^0(CO_2/P)$ for establishing a catalytic cycle (right).[137]

(**i**)   For the first step, namely the formation of the active catalytic species, the nature of the catalytic system in terms of reversibility and redox properties is crucial. Clearly, a metal complex which undergoes to rapid and reversible ET with the electrode surface will be a better candidate to promote CO₂RR in solution. Also, the reduction potential of the catalyst (E^0_{cat}) assumes great importance. This value should be in the range between the standard reduction potential of CO_2 ($E^{o'}$, Eq. 2-6, **Figure 1.24**) and, towards more negative potentials, the onset of direct CO_2 reduction at the electrodes (E_{onset}, **Figure 1.23**). In fact, catalysts with $E^0_{cat} > E°(CO_2/P)$ lack of the necessary driving force, since optimal catalytic systems require little overpotential (η) with respect to $E^0(CO_2/P)$; whereas if the CO₂RR takes place to really negative potential, a concomitant direct CO_2 reduction would take place, either at the electrode surface or in solution, which is undesirable. In this context, one of the biggest advantages of homogeneous catalysis, *i.e.* the possibility to fine-tune the E^0_{cat} by modifying the metal centre(s) and the ligand,

comes into play and explain the great efforts made in the last decades aiming at synthesize the "perfect" catalysts.

(ii) The electrocatalytic reduction of CO_2 starts with the interaction between the active (reduced) form of the catalyst and the substrate. Before going to mechanistic discussion of CO_2RR, it is worthwhile pointing out some aspects regarding its molecular properties and coordination chemistry.

Carbon dioxide is a 16 e$^-$ nonpolar linear molecule, with two polarised C-O bonds long 1.17Å that join a central, electrophilic C-atom and two nucleophilic O-atoms.[137] Considering its first ionization energy of 13.8 eV[138] and the slightly negative electron affinity of about −0.6 eV,[139] it can be rationalised how its electrons are tightly bound and how CO_2 is a better electron acceptor than donor. The reactivity of the molecule is hence dominated by the electrophilic character of the carbon atom. A close look to the molecular orbitals (MOs) can support the previous statement. From the qualitative diagram in **Figure 1.24**, it can in fact be noted how the orbitals relevant to the reactivity of CO_2 are the $1\pi_g$ and $2\pi_u$ orbitals, which are the nonbonding highest occupied molecular orbitals (HOMO, localised at the terminal O-atoms) and the lowest unoccupied molecular orbitals (LUMO, mainly carbon-centered), respectively.
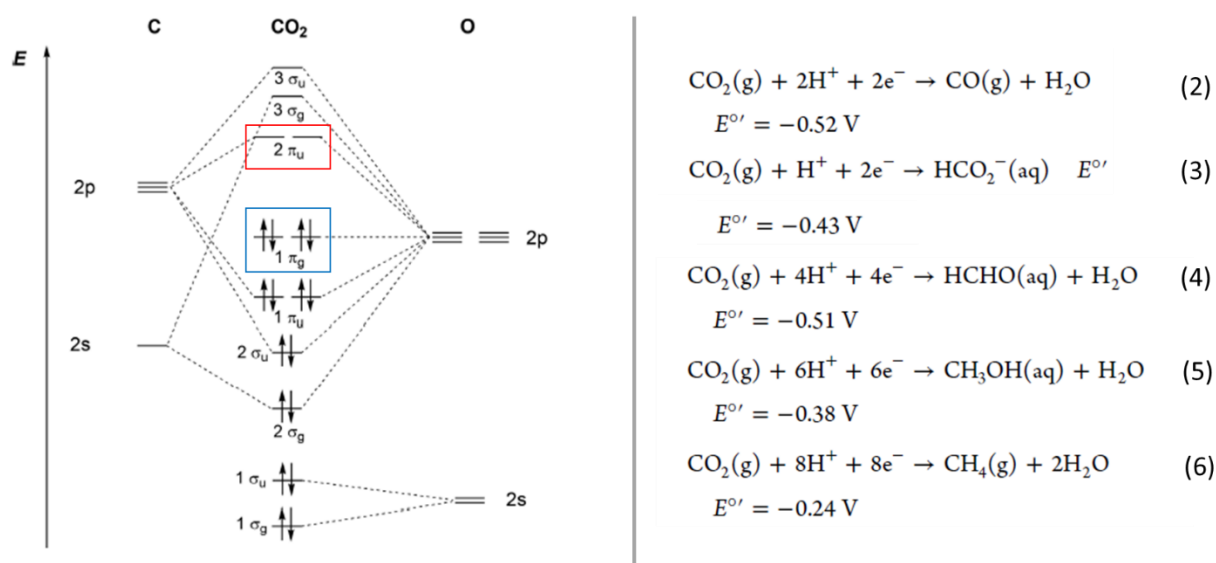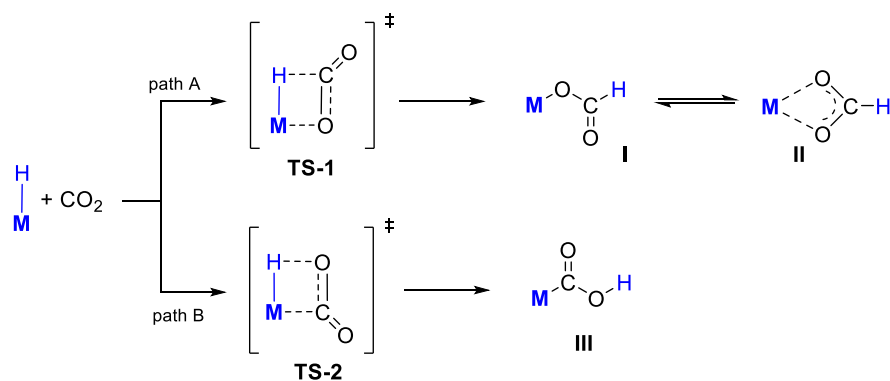

$$CO_2(g) + 2H^+ + 2e^- \rightarrow CO(g) + H_2O \qquad (2)$$
$$E^{\circ\prime} = -0.52 \text{ V}$$
$$CO_2(g) + H^+ + 2e^- \rightarrow HCO_2^-(aq) \quad E^{\circ\prime} \qquad (3)$$
$$E^{\circ\prime} = -0.43 \text{ V}$$
$$CO_2(g) + 4H^+ + 4e^- \rightarrow HCHO(aq) + H_2O \qquad (4)$$
$$E^{\circ\prime} = -0.51 \text{ V}$$
$$CO_2(g) + 6H^+ + 6e^- \rightarrow CH_3OH(aq) + H_2O \qquad (5)$$
$$E^{\circ\prime} = -0.38 \text{ V}$$
$$CO_2(g) + 8H^+ + 8e^- \rightarrow CH_4(g) + 2H_2O \qquad (6)$$
$$E^{\circ\prime} = -0.24 \text{ V}$$

Figure 1.24 | Qualitative molecular orbital diagram of carbon dioxide.[140] and thermodynamic potentials of CO_2 reduction into C_1 building blocks.[26]

The first, crucial, step of any electrocatalytic CO_2RRs is the initial activation of carbon dioxide to the radical intermediate $CO_2^{\cdot-}$ (Eq. 1, **Figure 1.3**), which is characterized by a very negative redox potential E^0: -1.9 V (vs. NHE). In fact, ET into the antibonding LUMOs of CO_2 increases the C−O bond lengths, leading also to a simultaneously geometric distortion of the whole molecule.[141] The very negative potential required to achieve

uncoupled outer-sphere reduction of CO_2 by one electron results from the significant cost in terms of reorganization energy that must be paid during this process. In fact, any interaction of CO_2 with electron-rich metal centres leads to its activation and to a distortion of the O-C-O bond angle, up to 134°.[142] Energy costs that can partly be offset, *e.g.* by a coupling reduction with energetically favourable metal to carbon bond formation. Indeed, in electrocatalysis, CO_2 activation is achieved through an inner-sphere ET to the C-atom, which lead to a stabilization of the radical anion $CO_2^{\cdot-}$, resulting into a less negative redox potential.[143]

Despite the huge number of different reduction pathways, it is possible to elucidate two main mechanism of carbon dioxide activation, which can happen either by binding to a vacant coordination site of the metal centre (**a**), or by CO_2 insertion into a metal-hydride bond (**b**), as depicted in **Scheme 1.2**.[137]

Scheme 1.2 | Competing pathways for CO and HCO_2H formation from CO_2, showing the pivotal role of the metal-hydride in determining product distribution. Oxide (O^{2-} above right) is produced as either CO_3^{2-} or H_2O/OH^-.[144]

(**a**)   If the former mechanism is favoured, the metal-carboxylate species is formed through monodentate C-coordination (η^1 -C), in case of electron-rich metal centres, side on (η^2 -C,O), as in $[Ni(PCy_3)_2(CO_2)]$;[145] and, more rarely, through an end-on O-coordination (η^1 -O) to the electron poor metal centres (**Figure 1.3**).

(**b**)   The other mechanism of carbon dioxide activation is represented by insertion of CO_2 into the M-X bond (M=metal, X= H, O, C, N), as depicted in **Scheme 1.3**. This insertion reaction has been shown to follow two routes, affording either the M−OC(O)H group (TS-1) or the M−C(O)OH moiety (TS-2). In the first case, also called *normal* insertion, the electrostatic attraction between the polarised C-O and M-H bonds favours the optimal orientation of the substrate., bringing in close proximity the electrophilic carbon-atom and the nucleophilic hydride in TS-1, before the generation of the metallaformate species I and II. An example of this type of reactivity is represented by the pincer-based $[Ir(PCP)- H_2]$ complex, introduced by Brookhart in 2012.[146] In this case, the process typically leads to HCO_2H formation (Eq. 3).[147] On the other hand, the *abnormal* insertion of CO_2 via metallacarboxylic TS-2 is less frequently encountered.

Scheme 1.3 | Mechanisms for CO_2 Insertion into a M–H Bond.[137]

(iii) To sum up, after the initial one-electron reduction of the metal centre (eq. 1), the radical anion $CO_2^{\cdot-}$ is formed from the interaction between CO_2 and the reduced metal centre. The electron density flows in this way to the $^{\cdot}CO_2$ ligand, increasing its polarizability and therefore the sensitivity to pH and cation.[148] At this stage, a series of protonation of the catalytic intermediates occur as the final step of the CO_2RR. In fact, in order to enable the electrocatalytic reaction, a suitable proton donor (*e.g.* water, acids or alcohols) is typically provided to the reactive species in small defined quantities. The proton source plays a fundamental role into the observed reactivity, altering thermodynamic and kinetic, as well as determining the selectivity of the whole CO_2RR process.[137]

To understand how Proton-Coupled Electron Transfers (PCET) affect the **kinetic** of CO_2RR, one should distinguish between the two main mechanisms of CO_2 activation: the direct CO_2 binding to a free coordinate site of the metal (**a, Scheme 1.2**) and the CO_2 insertion on a metal-hydride bond (**b**). In the most probable scenario, (case **a**),[149] as depicted in **Scheme 1.4**, protons take part in a synergistic *push-pull mechanism*. The electron density is first conveyed to the $^{\cdot}CO_2$ ligand, while the protons facilitate the electron transfer by pulling out electron density, eventually leading to C–O bond cleavage and liberation of water. This process is often accompanied by the subsequent M-C bond breaking and by formation of CO. In the other case, where HCO_2^-/HCO_2H are preferentially formed during CO_2RR, protons take part in the overall mechanism prior to CO_2 insertion by protonating the electrochemically reduced catalytic intermediate, forming the reactive metal-hydride (**Scheme 1.4**, bottom).

However, the presence of protons (either added protons sources or the employment of protic solvents), may lead to the formation of a radical hydride ($^{\cdot}H^-$), whose role has been pointed out by *Hammes-Schiffer et al.* in 2016.[150] For this reason, the **selectivity** of the catalyst, that is controlled, besides from the ligand, by the pH, electrolyte and proton source, plays a crucial role in determining the reaction products.
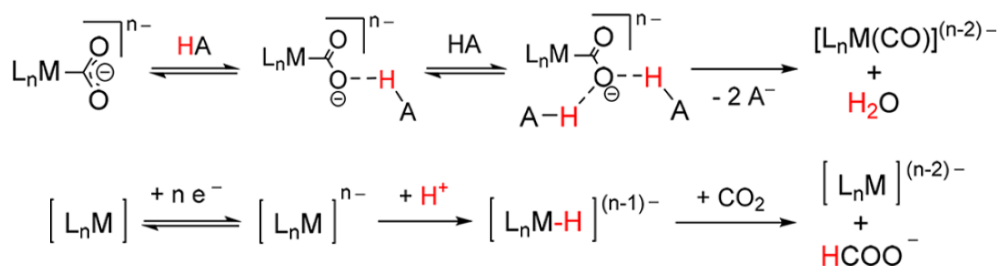
Scheme 1.4 | Possible roles of protons in CO_2 reduction by further activation of M-CO_2 intermediate (top) and formation of an active M-hydride species (bottom).[137]

The electrochemically generated radical hydride, may, indeed, promote undesired catalytic reactions or influence the stability of the catalyst itself. Thus, the outcome of the reaction will be carbon-derivates (in case of ˙H⁻ preference to react with ˙CO_2), or H_2 if the reactivity towards H⁺ dominates. The latter reaction, which can limit the selectivity towards CO_2RR, is also known as HER (**Hydrogen Evolution Reaction**) and it should be minimized, *e.g.* by choosing the correct cathode material (preferring Hg electrodes or GC instead of Pt-based ones), or working strictly within controlled pH window.[137]

In any case, catalysed PCETs provide new reaction pathways to achieve a single-electron reduction/protonation which, without PCET, would be characterized by a high energy charged transition state (S⁻, **Figure 1.25**).

The discussion of the possible mechanisms in CO_2RR are limited to CO/HCOO⁻ formation, since homogeneous catalytic systems able to reduce CO_2 beyond those products are still rare. The Latimer-Frost diagram in **Figure 1.26**, that indicates an increase of relative free energy of the products as the number of electrons added rises, gives a comprehensive explanation of this phenomenon.
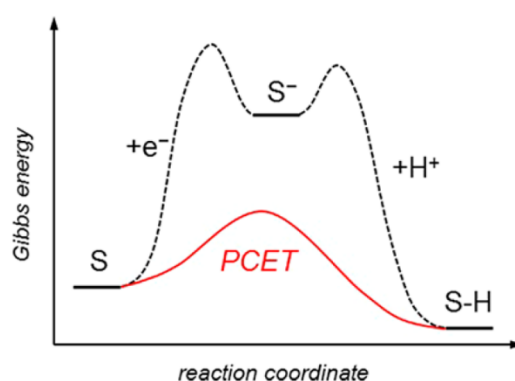
Figure 1.25 | Typical energy profile of a proton-coupled electron transfer (PCET). The two displayed energy profiles correspond to different reaction coordinates.[144]

32
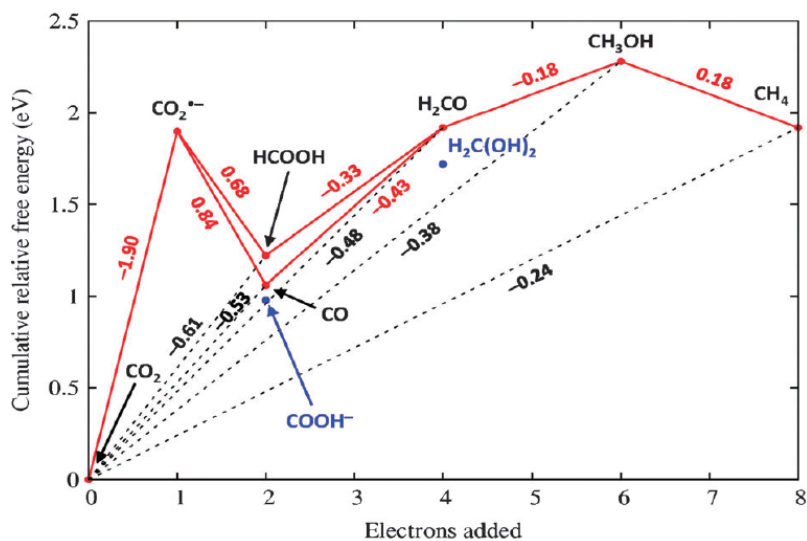
Figure 1.26 | Latimer–Frost diagram for the multi-electron, multi-proton reduction of CO_2 in homogeneous aqueous solution at pH 7 based on the potentials in eq. 2-6. Any species lying above the straight line joining two adjacent points (e.g., CO_2^{-} between CO_2 and HCOOH) is thermodynamically unstable with respect to disproportionation.[151]

In this regards, the heterogenized CuTDHPP (**Cu2**), introduced by *Wang et al.* in 2016, is a great exception, since it can electroreduce CO_2 in water to yield methane and ethylene with TOFs of 4.3 and 1.8 molecule site^{-1} s^{-1}, respectively, and with an overall Faradaic Efficiency (FE) of 44% for hydrocarbons.[152] A close look to the molecular structure will reveal the presence of eight hydroxyl groups in the second coordination sphere of the copper centre, which assist the multi-electron, multi proton coupled reactions, boosting the selectivity towards hydrocarbons.[153] Furthermore, ethylene production represent the only example to date, together with **Cu₂4** (Bouwman, 2010)[154] and **Cu₂5** (Maverik, 2014)[155] of the formation of C_2 product via reductive dimerization of $^{.}CO_2^{-}$ (**Figure 1.29**). In the two dinuclear Cu-complexes, however, PCET are not involved, since an aprotic environment is necessary to produce oxalate, recovered by quantitative addition of a lithium salt to recover $Li_2(C_2O_4)$.

Cu2

33
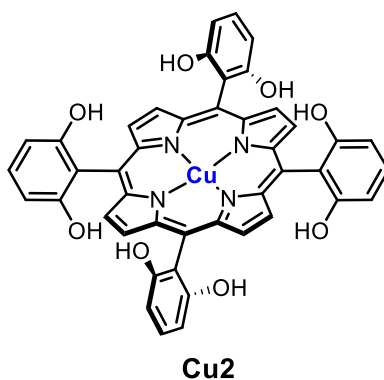
1.5.2 Multimetallic CRCs: providing alternative reaction pathways.

Bimetallic catalysts possess several advantages over the respective single-site systems. Firstly, catalyst nuclearity is an alternative optimization parameter that modulates catalyst selectivity in a way that is complementary to ligand design. Secondly, bimetallic cooperativity, as in the case of many enzymes, can contribute to improve the activity towards a specific class of reactions.

For these reasons, also in the field of CO_2RR, some bi- and multimetallic catalysts have been prepared and tested with a view to broadening the scope of the formed products. The most relevant examples are described hereafter. Multi- and bimetallic systems could be achieved by ligand design, in which two or more metal centres are forced to stay in close proximity by occupying the available coordination sites, or by non-covalent interactions which held together two monomeric units whose association can be controlled by varying the external conditions.

The first strategy led the group of the Nobel laureate J.P. Sauvage to the synthesis of first binuclear Ni-cyclam (**Ni₂6**) in 1988 (cyclam=1,4,8,11-tetra-azacyclotetradecane). The same group previously reported, how a monometallic Ni(II)-cyclam (**Ni4**) is an excellent and selective electrocatalyst for the reduction of CO_2 to CO, even in pure H_2O, using a Hg electrode, KNO_3 as electrolyte and pH of 4.1.[156] In order to access to C−C coupled products, they linked together two nickel cyclam units developing the dimeric **Ni₂6** (**Figure 1.27**).[157] Surprisingly, **Ni₂6** acted as an excellent catalyst for HER in aqueous media (Hg pool as WE), probably because of the formation of a dihydride intermediates of the Ni(H)-Ni(H) type, enhanced by the cooperativity of the two closed Ni centres. Catalytic activity towards CO_2RR was detected only in $DMF/NaClO_4$ (0.1 M H_2O), with HCO_2H becoming the major product. CPE at E_{appl} = −1.4 V vs SCE with **Ni₂6** showed formate selectivity of 81%. In 2000, the group of *Tsymbal* studied a series of bis Ni(cyclam), with the single macrocyclic units separated by an increasing alkyl length.[158] The envisioned increase of reactivity was not observed, also due to partial absorption to the Hg-plated Ag electrode. Therefore, they tried to increase the steric bulkiness around the Ni centres in an analogue series of heptaaza macrocyclic complexes. Once more, no net catalytic improvement respect to **Ni4** was observed. *Suh and colleagues* took a step further, designing the trimeric congener of the Ni heptaaza macrocyclic complexes, **Ni₃1**.[159] Cyclic voltammetry studies in $MeCN:H_2O$ (9:1) showed that, despite the flexible tren bridge which links together the three macrocyclic units, the respective Ni ions are electrochemically independent. The CV is in fact characterized by a single, three-electron cathodic wave, whose intensity is more than doubled when CO_2 was purged into the MeCN solution, but the overall catalytic efficiency of **Ni₃1** is lower than that of $[Ni(cyclam)]^{2+}$, since it produces less CO per nickel centre.
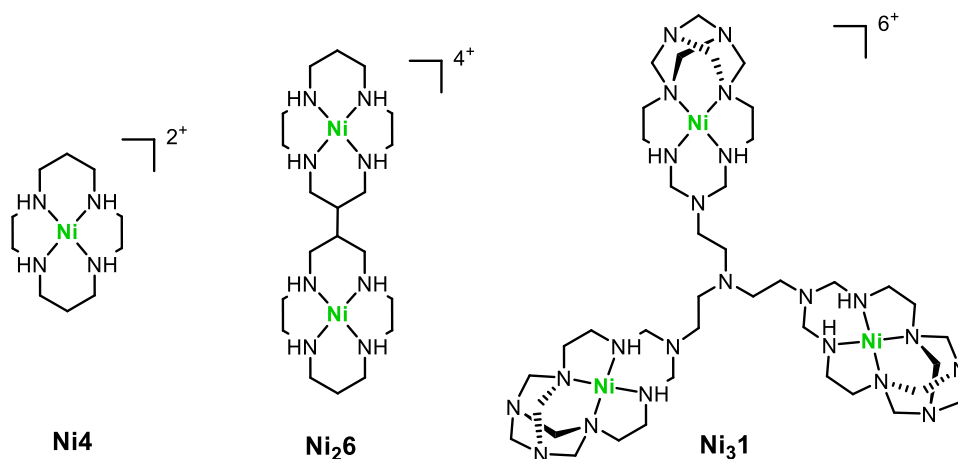
Figure 1.27 | Very active, parent compound of all Ni-cyclams **Ni4**, introduced by *Savéant et al.*,[156] dimeric version **Ni₂6**, and trimeric, heptaaza macrocyclic **Ni₃1**, reported by *Suh et al.*[159]

Another category of CRCs are the phosphine-based systems, for whose development the group of *DuBois* gave exceptional contributes. In 1994, to overcome some limitations affecting monometallic Pd(II) complexes bearing tridentate phosphine ligands,[160] they reported the synthesis of a series of the bimetallic Pd complexes, two of which possessing a methylene (**Pd₂4**) and a 1,3-phenylene linker (**Pd₂5**) connecting two monometallic moieties (**Figure 1.28**). Whereas the methylene-linked dimer showed remarkable activity towards CO_2 reduction, the complex bearing the 1,3-phenylene linker, despite having a TON that exceed 200 (because of the improved stability arising from the bulky Cy groups), did not show a cooperation between the two metal centres.[161] **Pd₂4**, in fact, is the only successful example, in a series of di-, tetra-, and pentanuclear[162] Pd tridentate phosphine complexes, in which a bimetallic cooperativity takes place, which is essential to achieve notable high activity ($k > 10^4$ M^{-1} s^{-1}).[163] The intermetallic distance in **Pd₂5** is speculated to be too high to retain bimetallic cooperation, resulting in two independent Pd atoms.[161] The authors, nearly a decade before the structure of the active site of [Ni,Fe] CODHs was revealed (**Figure 1.6**), suggested one possible TS, **9** , in which one Pd atom is connected to the C atom of carbon dioxide, whereas the other to one oxygen in a process that precisely involves both Pd atoms. Unfortunately, the stability of the catalyst remains low, as it showed only 10 turnovers in DMF/NEt₄BF₄ electrolyte.

An outstanding case of products selectivity dictated by catalyst nuclearity was reported in 2010 by the group of *Bouwman*, namely a dinuclear copper(II) complex, **Cu₂4**, which is able to catalyse the reductive dimerization of CO_2 to oxalate in quantitative yield (FE= 96%).[154] Two characteristics render this complex a milestone for CO_2 reduction and conversion: it is able to capture the highly diluted carbon dioxide directly from air and, more important, the catalytic cycle is established at +0.03 V vs NHE (almost 2 V more positive than $E^0_{CO_2/CO_2^{.-}}$).
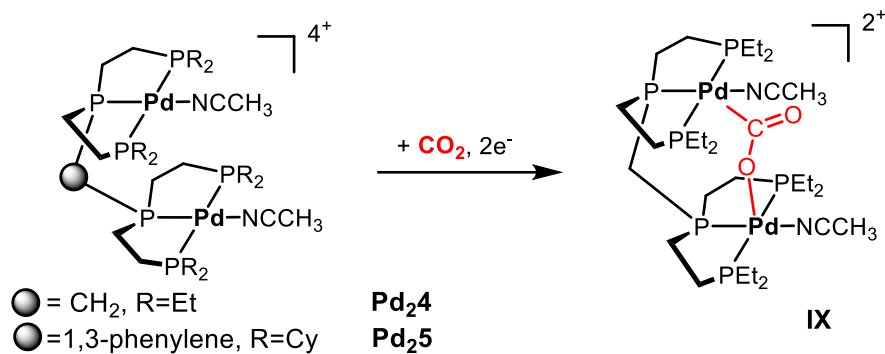
Figure 1.28 | Bimetallic Pd-P$_3$ complexes active towards CO$_2$RR and proposed intermediate in which one molecule of CO$_2$ bridges two Pd ions.[163]

During the catalytic cycle, **Cu$_2$4** is reduced via a 2e$^-$ reduction to a Cu(I)-Cu(I) intermediate, which rapidly reacts with two CO$_2$ molecules, forming two radical Cu(II)-$^\bullet$CO$_2^-$ adducts per complex. Subsequent intermolecular dimerization of two $^\bullet$CO$_2^-$ leads to the formation of a bridging oxalate complex. The catalytic cycle can only be sustained by constant removal of oxalate through precipitation of the Li salt, from the LiClO$_4$ electrolyte. The system shows 6 turnovers upon 7 h electrolysis in CH$_3$CN, thereafter the rate of the reaction gradually decreased as the crystallized lithium oxalate starts to cover the electrode surface, thereby hampering electron transfer.

Another interesting complex was reported in 2014 by *Maverick et al.*: a dimeric Cu(II) macrocycle, **Cu$_2$5** (**Figure 1.29**), which is able to react with atmospheric CO$_2$ in 96% yield over several days, giving a species in which oxalate bridges intramolecularly the two copper centres.[155]. Reduction of the copper atoms can be easily realised either chemically with sodium ascorbate, or electrochemically with a semi-reversible process at -0.27 V vs Fc$^+$/Fc. UV-Vis and IR spectroscopy suggest that the reduced Cu(I) centres react with atmospheric CO$_2$ to form the Cu(II)-O$_2$C$_2$O$_2$-Cu(II) adduct. In fact, after 128 h, the appearance of the dd transition band of d^9-Cu(II) centres and the isolation of a green compound, analysed by SC- Xray diffraction, confirm the formation of oxalate-bridged the complex.

Cu$_2$4   **Cu$_2$5**   **X**
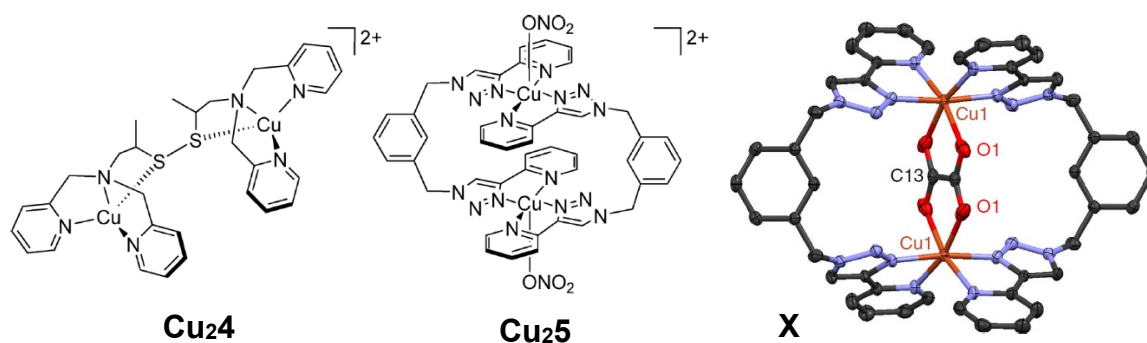
Figure 1.29 | Cu-tripodal complexes introduced by *Bouwman* (**Cu$_2$4**)[154] and bpy-based Cu(I) complex **Cu$_2$5** by *Maverik*.[155] Crystal structure of the oxalate-**Cu$_2$5** adduct (**X**), with the bridging C$_2$O$_4^{2-}$ ion being formed by CO$_2$ reduction, and the two Cu atoms separated by 5.4213(7) Å.[155]

Nevertheless, these results illustrate how a metal-organic supramolecular system can be designed and tuned to act as selective CO_2 sequester, exploiting cooperative interactions between two proximal metal centres which can optimally promote direct coupling of CO_2 into higher molecular weight products containing C–C bonds.[137]

By exploiting the robust macrocyclic N_4 ligand platform, and the remarkable activity that some TPP have shown towards CO_2RR, *Naruta and coworkers* reported the synthesis of **Fe₂1** and **Fe₂2**, two iron complexes featuring covalently-linked cofacial porphyrin macrocycles as ligands which keep the iron centres at 3.4 - 4 Å from each other (**Figure 1.30**).[164] The fully reduced dimeric species is assigned to possess a [Fe^0Fe^0] core. Both cofacial systems are efficient CO_2RR, with catalytic performances that are almost one order of magnitude higher than the monometallic counterpart, with a calculated k_{cat} of $2.0 \cdot 10^4$ and $1.6 \cdot 10^4$ s^{-1} and logTOF$_{max}$ of 4.3 and 4.2 s^{-1} for Fe₂DTPP and Fe₂DTPFPP, respectively. The position of the catalytic wave can provide some keys to understand this remarkable reactivity towards CO_2 reduction. In fact, its appearance over the $Fe^I,Fe^I/Fe^I,Fe^0$ redox couple under Ar (-1.4 V in **Fe₂1** and -1.25 V in **Fe₂2**, vs NHE) indicates the starting of the catalytic process once the Fe^IFe^0 porphyrin species is electrochemically generated (**Figure 1.30** for **Fe₂2**). This observation led the authors to speculate that the Fe^I/Fe^0 intermediate acts as a **Lewis pair** in which the activation of CO_2 is extremely favored. In monomeric FeTPFPP, the onset is observed over the third reduction peak, namely the Fe^I/Fe^0 redox process, indicating that active species in catalysis is Fe^0TPFPP.[165] Regarding the selectivity of the process, CPE experiment (-1.25 V, η=0.56 V in DMF/10% H_2O solution) revealed a FE$_{CO}$ of 92 % for **Fe₂2**, indicating that the dimer is an efficient and selective electrocatalysts for the reduction of CO_2 to CO over HER. **Fe₂1** showed the same, or even higher selectivity but with slightly higher overpotential, the latter being significantly higher for the monometallic **Fe1** and **Fe2**, despite showing the same selectivity.[166]
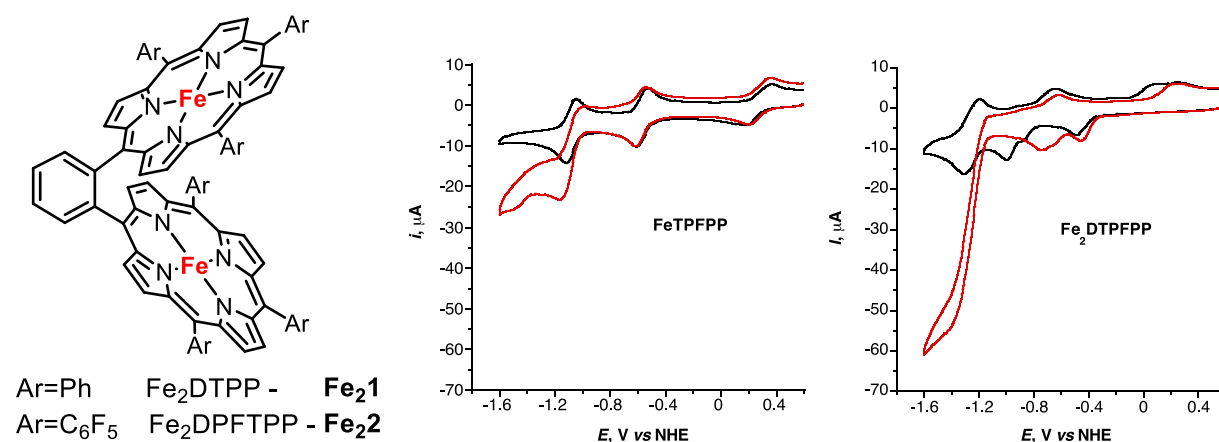
Figure 1.30 | 1,3-Phenylene linked cofacial TPP (**Fe₂1**) and PFTPP (**Fe₂2**), introduced by the group of *Naruta*.[167] Comparison between CV of monometallic FeTPFPP (**Fe2**, 1 mM) and **Fe₂2** (0.5 mM) in DMF/10% H_2O at 50 mV/s scan rate under Ar (black lines) and CO_2 (red lines).[164] The benchmark highlights the large catalytic current of the dinuclear complex, over the third, reversible reduction peak, symptom of electrocatalysis.

These results clearly prove that the high performance of the CO_2 to CO conversion catalysts is due to the presence of binuclear Fe centres at suitable Fe−Fe separation distance, provided by a 1,3-phenylene bridged Fe porphyrin dimer, which can provide a suitable framework for the cooperation of the two Fe centres during catalysis. However, no effect of catalyst nuclearity on product selectivity was observed, since the outcome of the reduction was still the 2-e⁻ reduced CO.

Ability, that of influencing the mechanistic pathways of CO_2RR by the presence of two metal centres, showed instead by the dimeric Re-based catalyst **Re2**, introduced by *Kubiak et al.* in 2014.[168] Studying the reactivity of the well-known [Re(bpy)(CO)₃Cl] class of catalysts, introduced in the 80s by Lehn and coworkers,[169] they realised that the catalytic performance could be notably enhanced by increasing the bulkiness of the substituent in the 4,4'position of the bipyridine ligand, introducing [Re(bpy-^{t}Bu)(CO)₃Cl].[170] The unwanted Re-Re bond formation, which hampers CO_2 binding in **Re1** (**Figure 1.31**)[171] was also avoided, reaching FE$_{CO}$ up to 99% (± 2%) in MeCN solution and a second order rate constant of 650 M^{-1} s^{-1}. More interestingly, by replacing the ^{t}Bu moieties with two methyl acetamidomethyl groups in **Re2**, they observed an uncommon electrochemical behaviour, consistent with a noncovalent dimerization process. In fact, the current response of **Re2** varied according to the chosen solvent (either MeCN or *N,N*-DMF), suggesting that H-bonding could be involved in that process. Furthermore, by purging the solution with CO_2, the electrocatalytic mechanism for the unimolecular 2e⁻ reduction of CO_2 (which applies, for instance, to **Re1**) was not encountered. Further spectroelectrochemical (SEC) studies confirm the H-bond-driven dimerization of the reduced [Re⁰(bpy˙⁻)(CO)₃]⁻ *via* the two methyl acetamidomethyl moieties (**XI**), whose main implication is the unique catalytic product distribution. In fact, differently from the parent **Re1**, **Re2**, operates at milder potentials and selectively catalyses the reductive disproportionation of CO_2 into CO + CO_3^{2-} in MeCN, with a TOF$_{max}$ of 57 s^{-1} under CO_2-saturation conditions (with added TFE, 0.795 M) and a FE$_{CO}$ of 54 ± 8%.
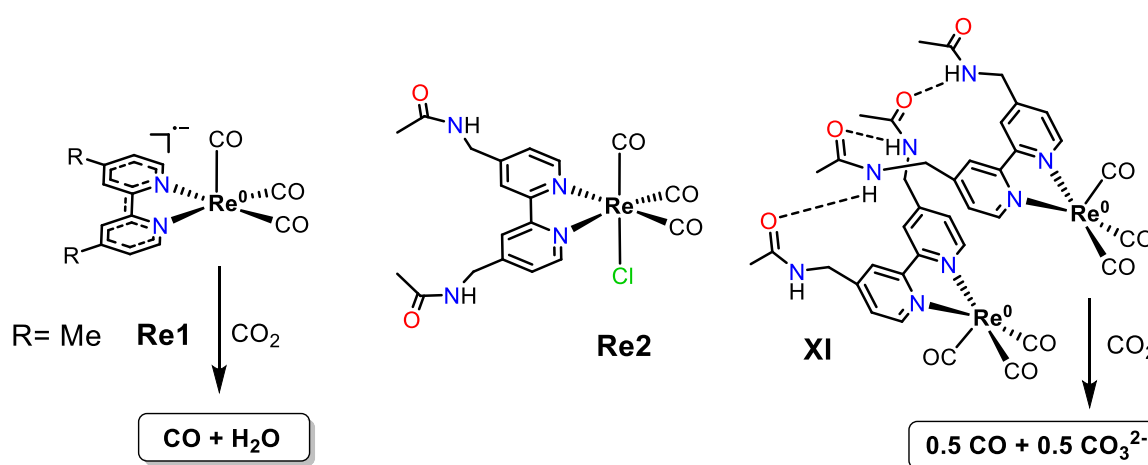
Figure 1.31 | Left: doubly reduced form of the [Re^I(bpy-Me)(CO)₃Cl] (**Re1**) catalyst, selective for 2-e-reduction of CO_2 to CO and H_2O with a FE$_{CO}$ of 90 ± 5 %.[172] Middle: **Re2** and its H-bonding driven dimerization process (right), responsible for the selectivity of the CO_2RR process.[168]

These findings demonstrate that noncovalent self-assembly (**XI**, **Figure 1.31**) can modulate the catalytic properties of metal complexes by favouring alternate catalytic pathways. With this study, the group was able to prove the effect of **catalyst nuclearity** in dictating product selectivity during two-electron CO_2 reduction.

Recently, *Jurss et al.* developed another exceptional system which allowed for the further elucidation of the role of bimetallic cooperativity in CO_2RR. In this complex (***cis*-Re₂1**, **Figure 1.32**), the spatial proximity of the two $[Re^I(bpy')(CO)_3Cl]$ units is achieved by the rigid anthracene-bridging group.[173] Notably, the complex has been isolated in two conformations: ***cis*-Re1** and the *trans* conformer (in which the two Re-centres are opposite to the anthracene moiety), both being active towards CO_2RR. However, only if the Re-ions are at optimal distance, they can act cooperatively during electrocatalytic CO_2 reduction. In fact, from mechanistic studies, a pathway involving bimetallic CO_2 activation and conversion was identified for ***cis*-Re₂1**. Structure **XII** represents the proposed TS, in which activated CO_2, similarly to **Pd₂4**, **Cu₂5** and [NiFe] CODHs, binds the two metal centres in a bridging fashion. While the average activity of ***cis*-Re₂1** is higher than the trans conformer (TOF$_{max}$= 11 s^{-1} vs 4.4 s^{-1}), the catalytic behaviour is shown to vary according to the potential applied in the CPE experiments. At low overpotential, in fact, ***trans*-Re₂1**, which acts with a monometallic mechanism, promotes the reductive disproportionation of CO_2 into $CO + CO_3^{2-}$. The same product selectivity, albeit with higher efficiency, is reached at higher overpotential with ***cis*-Re₂1** (FE$_{CO}$=81 % at E_{appl} = -2.5 V *vs* Fc$^+$/Fc).

The development of bimetallic systems, though providing alternative reaction pathways and allowing the formation of products unreachable with the monometallic counterparts, is not always associated to outstanding catalytic activity. Some well-established monometallic systems, such as Fe tetraphenylporphyrins (**Fe1**-**Fe4** and derivates) and unsaturated Ni cyclams (**Ni5**), possess outstanding performances that are still used as a benchmark for CRCs. There are plenty of other catalysts which shows remarkably activity towards CO_2 reduction, whose complete description has been recently made by excellent reviews.[137],[144],[174] Nevertheless, only two of the different classes of catalysts, among those not discussed until now, possess an extremely active complex.
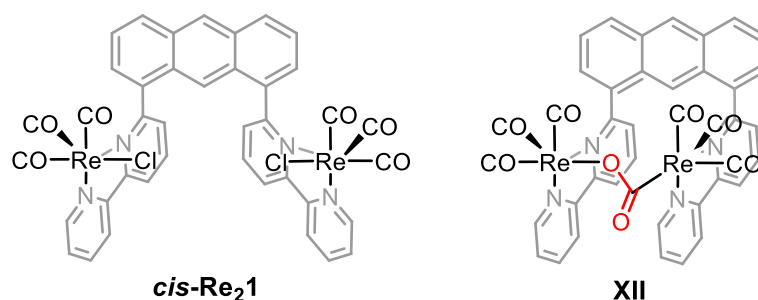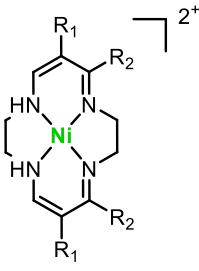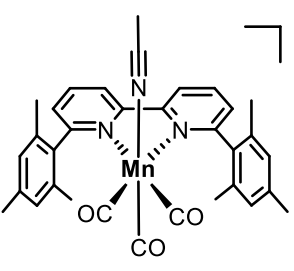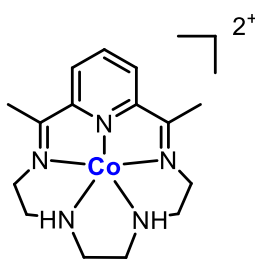
Figure 1.32 | *Cis*-conformers of the rigid dinuclear Rhenium Complex **Re₂1**, introduced by *Jurss and coworkers*. The complex allows for the cooperative, bimetallic CO_2 activation.[173]

High activity that was reached after decades of ligand optimization, based on detailed studies of the mechanistic implications of CO₂RR. These improvement can be related to the addition of bulky substituents to avoid dimerization and degradation processes, as in the case of the Mn(bpy)(CO)₃Cl derivative **Mn1**,[175] or which concern the implementation of H-bonding donor groups in the outer coordination sphere of the metal centre, as in **Co2**, which features an unsaturated N_5 macrocyclic ligand.[176]

Table 1.1 | Ni5, **Mn1** and **Co2** with relative product selectivity, activity and catalytic conditions.

Ni5[177]	Mn1[175]	Co2[176]
R₁= COOEt, R₂= Me		
HCOOH (90%) + CO (5%) -2.15 V vs Fc⁺/Fc	CO (98%) -2,2 V (vs. Fc⁺/Fc)	CO (82%) η=0.56 V -1.5 V (vs SCE)
TON= 750	TOF= 5000 s⁻¹ (1.4 M TFE)	-
MeCN, NBu₄ClO₄ Hg pool	MeCN, NBu₄BF₄ GC electrode	DMF, NBu₄BF₄ GC electrode

1.5.3 Benchmark of monometallic NHC-based homogeneous catalysts.

Following the pioneering works in the early 70s, the field of CO_2 activation and conversion has attracted raising interest, with a net outbreak in the last two-three decades. In 1971, *Tsay et al.* reported the first complex in which one molecule of carbon dioxide is linearly coordinated with the two C=O bonds to two Ni centres,[178] and, in the same year, the group of *Volpin* reported the first metallacycle formation involving CO_2 and a dicyclopentadienyldiphenyltitanium.[179] For the first time, exploiting a transition-metal complex, it was possible to activate the stable and nonpolar CO_2 molecule, paving the way to its conversion to more useful C-feedstock. Then, considered the parallel development of active homogeneous metal complexes and **heterogeneous systems**, a strong debate broke out among the scientific community. If, on one side, solid-state material catalysts are often stable, extremely efficient and allow the formation of species beyond two-electron transfer from CO_2, they may exhibit low product selectivity, giving mixtures of low carbon-based products owing to an intrinsic variety of the catalytic active sites in their surfaces.[137] On the other hand, synthetic **molecular catalysts**, though being less robust and durable than heterogenous systems, can achieve excellent product selectivity under milder and more monitorable conditions. The optimization of the selectivity with homogeneous systems is often easier to realise and to tune, since the structure-activity relationship, that can be monitored by *in situ* coupled SEC techniques, is controlled by rational **ligand design** (macrocycle vs. acyclic, EWG vs. EDG, steric hindrance, *etc.*) and variation of the metal.

Ligand design, which, only in the last decade, has expanded to include **NHCs**, the robust and highly attractive class of C-donors compounds presented in chapter 1.4. NHC ligands, being strong σ-donor groups, can efficiently increase the electron density in the metal centre, via increased σ-donation to the metal empty d-orbitals. Electron-rich metal centres can, in turns, strength CO_2 binding and promote C-O bond cleavage.

This concept was clearly proved by the study of the group of *Lloret-Fillol* in 2018 on the well-known class of [Mn(bpy')(CO)$_3$(X)] CRCs. They replaced the bpy unit first with a mixed py-^{Me}NHC group (**Figure 1.33**, **Mn2**), and then with the doubly NHC, bis-^{Me}NHC (**Mn3**).[180] Notably, an increase of selectivity and activity for **Mn3** was observed with respect to **Mn2** and to the parent bpy-based Mn compounds. The author reported how the electron density after two subsequent reduction is strongly localised in the Mn-centre (as opposed to the classical bpy-based CRCs),[181] entailing a redox-innocence of the bis-NHC ligand and a more available metal-centered HOMO to perform nucleophilic attack to CO_2. Consequently, **Mn3**, during CPE studies shows a selectivity for CO production of 92% over 4 h, with 56 turnovers and a TOF of 2100 s^{-1}. With the addition of small concentration of H_2O, the catalytic activity was further increased, to reach unprecedent performances: $TOF_{max} = 3.2 \cdot 10^5$ s^{-1} and $TON_{CO} = 98\%$.
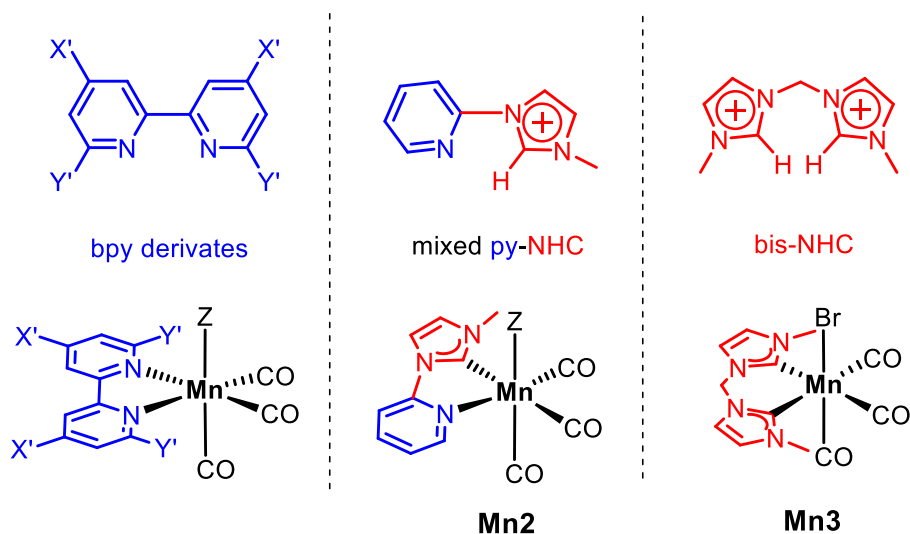
Figure 1.33 | Selected Mn(I) catalysts for electrocatalytic CO_2-to-CO reduction with of [Mn(bpy')(CO)$_3$(X)] reported in the literature, **Mn2** and the highly performant, bis-NHC **Mn3**.[180]

These Mn-complexes, however, were not the first NHC-based complexes employed as CRCs. Some years before, indeed, *Chang and coworkers* reported the synthesis and characterization of a series of Ni bis(pyridine-imidazolyidene-NHC) compounds: **Ni6**, **Ni7**, **Ni8**.[182] These complexes, which differs from each other from the alkylene spacer which connect the imidazolylidene moieties, are characterized by a geometry- and structure-dependant CVs. The authors report how a less rigid structure (propylene-bridge, **Ni8**) is associated with an increase of reversibility and to less cathodic potential required to reduce the Ni centre. Nevertheless, all three complexes showed electrocatalytic CO_2 reduction activity over the second reduction peak and CPE conduced in wet (5% H_2O) MeCN at -1.5 V (vs. SCE) revealed selective CO formation with 12 turnovers, albeit with moderate rates (TOF$_{Ni8}$= 5.9 h^{-1}). Later, in 2013, the same group took a step further by replacing the pyridine units with the **more π-acceptor** isoquinoline ligand, giving **Ni9**.[183] The onset potential for CO_2RR was thus reduced to −1.20 V vs SCE, 200 mV more positive than **Ni8**, while the observed FE$_{CO}$ was 90% for the first 0.5 h, to give a TON$_{CO}$ = 35 (in H_2O-free MeCN, GC WE).[183]

n=1 **Ni6**
n=2 **Ni7**
n=3 **Ni8**

Ni9
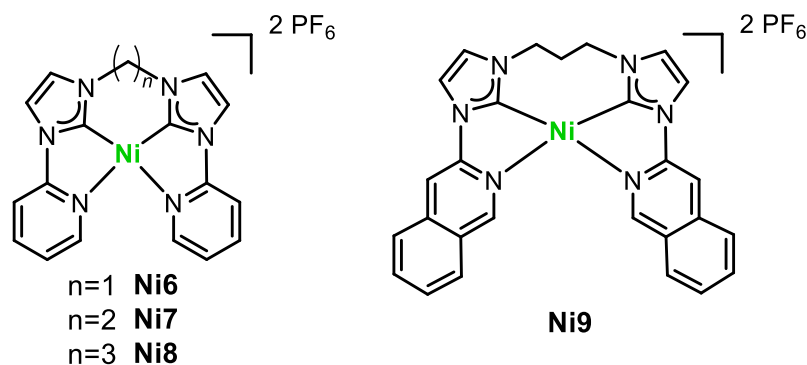
Figure 1.34 | Bis(pyridine-imidazolyidene-NHC) complexes **Ni6-Ni8**[182] reported by *Chang et al.* and the isoquinoline derivate **Ni9**. [183]

If, instead, the conjugation is extended on the imidazole-based N-heterocyclic carbene donors (with benzimidazole units, **Ni10**), the overpotential associated to CO_2 reduction is increased, *i.e.* it is shifted towards more negative potentials. The peak positions in the CV, however, are positively-shifted respect to **Ni8**, meaning that the benzimidazolylidene acts as better π-acceptor with regard to the imidazolylidene ligand.[183] Building further upon this scaffold, it was found that **breaking the conjugation** between the NHCs and the pyridine donors also shifts the onset potential of CO_2 reduction to more negative values. The CV of **Ni11**, in fact, displays only a slight current enhancement under CO_2, with an onset potential of -1.45 V. With these data in hands, it can be stated that the extended conjugation at the appropriate location on the ligand platform is favourable for catalytic CO_2 reduction.
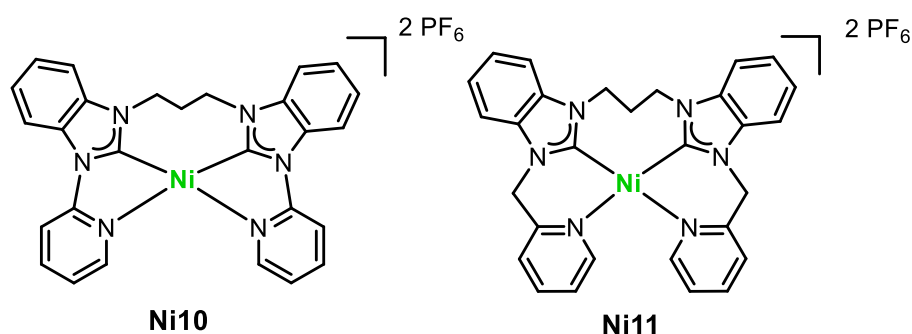
Figure 1.35 | Chang's mixed benzimidazolium/pyridine **Ni10** and **Ni11**, in which the electronic conjugation between the donors has been removed by the insertion of a methylene bridge.[183]

More efficient catalytic systems have been obtaining exploiting the so-called **pincer-type** bis-NHC ligands. These compounds feature a tridentate ligand consisting of one central pyridine (N-donor), or benzene (C-donor), which joins two imidazolylidenes or benzimidazolylidenes donor groups. In this ligand framework, the steric bulkiness (% V_{bur}) can be easily tuned by varying the N-wingtip substituents. Furthermore, the tridentate nature of these ligands has been designed to leave the fourth coordination site available for CO_2 binding, which should replace the coordinated solvent molecule. Selective and efficient CO_2-to-CO reduction was observed for **Ni12** (**Figure 1.36**), introduced by *Sun et al.* in 2012.[184] Notably, the highest activity has been registered in wet MeCN (max 0.8 mM H_2O), with a TOF as high as 90 s^{-1}, several times higher than the tetradentate Ni pyridine-imidazolylidene **Ni8**. The **extended conjugation** that characterizes the whole C^N^C pincer complex is also found in **Ni13**, in which the central Py-unit has been replaced by the 1,3-aryl-substituted moiety, realising the more electron-donor (ED) C^C^C coordination motif.[185] *Hollis and coworkers*, by inserting in the N-wingtip positions more ED butyl groups, reported how **Ni13**, being characterized by cathodic shifted reduction features (see, *e.g.* **Ni10**), promotes CO_2RR with a calculated TOF of 30 s^{-1} (75 times higher than **Ni8**).

$+2/0$

X=N, R=Me, L=MeCN   **Ni12**
X=C, R=Bu, L=Cl⁻   **Ni13**
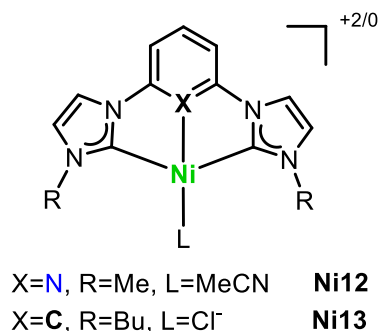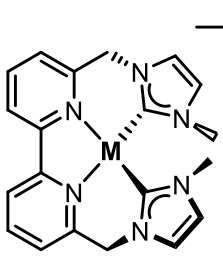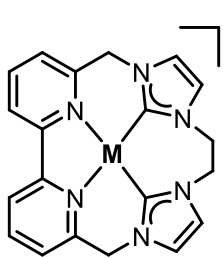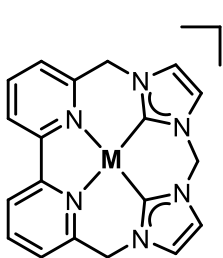
Figure 1.36 | Ni-NHC pincer complexes featuring a central pyridine donor (**Ni12**)[184] or a 1,3-phenylene moiety (**Ni13**)[185].

However, with the C^C^C ligand, the selectivity for CO_2 is significantly lower than **Ni12**, and the reported current efficiencies are FE_{CO}= 34% and FE_{HCOOH}= 47%, observed in MeCN / 2M H_2O solution. Once more, breaking the conjugation has revealed to be detrimental for CO_2RR, as demonstrated by *Patrick and coworkers* with pincer-type benzimidazole-based complexes.[186] Between those compounds, the Ni-based shows only marginal CO production, possessing a net preference for HER over CO_2RR.

The influence of a macrocyclic ligand platform on CO_2RR efficiency has been clearly highlighted by *Jurss and coworkers*, by comparing the activities of acyclic bipyridyl-NHC complexes with two correlated macrocyclic versions. They introduced **Ni14-Ni16,** [187] and **Co3-Co5**,[188] in which each metal centre, either Ni(II) or Co(II) is tetracoordinated by redox-active N^N^C^C ligand motif. The authors, with the support of DFT calculation, carried out an extensive Structure-Activity Relationship study, from which it emerged that more rigid and constrained macrocycles (**Ni16** and **Co5**), being characterized by metal-based reductions, better perform in the catalytic reduction of CO_2. Thanks to their limited flexibility, macrocyclic complexes also showed higher selectivity towards CO_2RR over HER, as the CPE-data reported in **Table 1.2** suggest. A general increase of current efficiency for CO production in the Co-series is observed, due to the tendency of Ni(I)-hydrides formation, maximized in **Ni14**. The overpotential (η) associated to CO_2 reduction is generally reduced for **Co3-Co5**, respect to the Ni-series (**Table 1.2**). These results demonstrate that increasing the **rigidity of the ligand framework** enhances catalytic activity and selectivity for CO_2 reduction over the competing H_2 evolution reaction. The most corroborated hypothesis is that the more the ligand is constrained, the greater the electron-density localised in the metal-centre, thus facilitating CO_2 binding and reduction. This effect is further emphasised in the macrocyclic tetracarbene-iron(II) complex (**Fe6**, **Figure 1.37**), in which a "supernucleophilic"[152] iron centre is electrochemically generated, whose electrons mainly occupy the d_{z^2} orbital, rather than the $d_{x^2-y^2}$ or ligand-based orbitals. This complex, recently introduced by *Meyer et al.,* features the macrocyclic **L13** (**Figure 1.22**) as ligand platform and two apical MeCN ligands.[130]

Table 1.2 | Acyclic Ni and Co complexes supported by redox-active bipyridyl-NHC donors (**Ni14** and **Co3**), 16- and 15-membered ring macrocyclic versions (**Ni15**, **Co4** and **Ni16**, **Co5**). [187],[188]

| M= Ni **Ni14** | | M= Ni **Ni15** | | M= Ni **Ni16** | |
| M=Co **Co3** | | M=Co **Co4** | | M=Co **Co5** | |

	Ni	**Co**	**Ni**	**Co**	**Ni**	**Co**
FE$_{CO}$ (%)	5	78	56	91	87	**98**
FE$_{H2}$ (%)	**93**	20	43	7	11	-
TOF (s^{-1})	-	66	21.7	186	47.5	**570**
η$_{CO2RR}$ (V)	-	0.55	0.93	0.78	0.92	0.72

It is an organometallic heme analogues which outperforms all the other first row transition metal CRCs, including Jurss's Ni- and Co-based complexes. Remarkably, peak-current analysis[189] reveal TOFs of 3300 s^{-1} and 3100 s^{-1} for **Fe6** and **Fe7**, respectively, bringing even more evidence of the increased activity of macrocyclic NHC complexes. These outstanding catalytic efficiencies have been reached without adding any proton source, establishing a catalytic cycle in which two formal $CO_2^{\bullet-}$ radical anion disproportionate into CO and carbonates (FE$_{CO}$=92% for **Fe6**). The substitution of one apical MeCN ligand with one CO in **Fe7** enabled the minimization of side phenomena that, affecting **Fe6**, limited its activity to only 4 turnovers.

$L_1=L_2$=MeCN **Fe6**
L_1=CO, L_2=MeCN **Fe7**
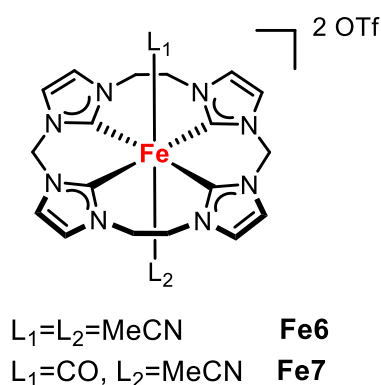
Figure 1.37 | Heme analogues introduced by *Meyer et al.*, highly active towards CO_2RR.

The profound **macrocyclic effect** on catalytic performance observed by the group of *Jurss*[187],[188] and *Meyer*[130] can pave the way to the investigation and to the optimization of NHC-based catalyst, still too little examined, notwithstanding the incredible potentiality of this class of compounds.

2 OBJECTIVES

Alkylene-bridged calix[4]imidazolylidene[2]pyrazolate framework have proved to be excellent ligands for the isolation of dinuclear nickel(II) complexes.[190],[78] The square-planar coordination of each metal centre is realised via two NHC-donors (imidazolylidenes) and two pyrazolate units, which are also responsible for the electronic communication between the ions.[86] Pöthig et al. reported how the dinuclear nickel complex possess a solid-state bowl-shaped structure, with the cavity dimensions being influenced by the length of the alkylene-bridge between the imidazolyidene moieties. This peculiarity is responsible for the unique host-guest chemistry of this organometallic compound, which, when possessing the ethylene-bridging group, can selectively recognize chloride and bromide ions in solution. The resulting supramolecular assembly is characterized by a tennis ball-like structure, in which one anion is encapsulated by two cationic dinuclear nickel complexes. The nature of the interactions which stabilize the host-guest complex has been assigned to be mainly electrostatic (between the metal ions and the halide), with a contribution of multiple hydrogen-bonding interaction, arising from the CH_2 groups of the ligand that point towards the Ni-Ni moiety.

In this context, it is interesting to evaluate how the host-guest properties vary by extending the alkylene-bridge, or by replacing the ligated metal ions. To accomplish this task, the propylene-bridged H_6L^{Pr} $(PF_6)_4$ ligand will be synthesized by adjusting the reported experimental procedure,[78] to then be used to isolate the bimetallic nickel complex Ni_2L^{Pr} $(PF_6)_2$. Furthermore, the poly-NHC ligand precursors H_6L^R $(PF_6)_4$ will be exploited to expand the scope of 3d transition metals to copper and elucidate their structural properties. The synthesis of Cu_2L^{Me} $(PF_6)_2$ has already been reported, albeit an indirect strategy was employed, with the inconvenient halogen-abstraction step required to extract the encapsulated chloride from the stable Capsoplex assembly.[191] The obtained compounds (of Ni and Cu) will be characterized by NMR Spectroscopy (in case of diamagnetic complexes), ESI-MS, UV-Vis and IR Spectroscopy. Computational studies will be performed to investigate the stereo-electronic properties of the binuclear complexes.

Ni_2L^R $(PF_6)_2$

n= 1, 2 Pöthig 2015, 2016
n= 3 **This work**

H_6L^R $(PF_6)_4$
n= 1,2,3

Cu_2L^R $(PF_6)_2$
n= 1, 2 **This work**
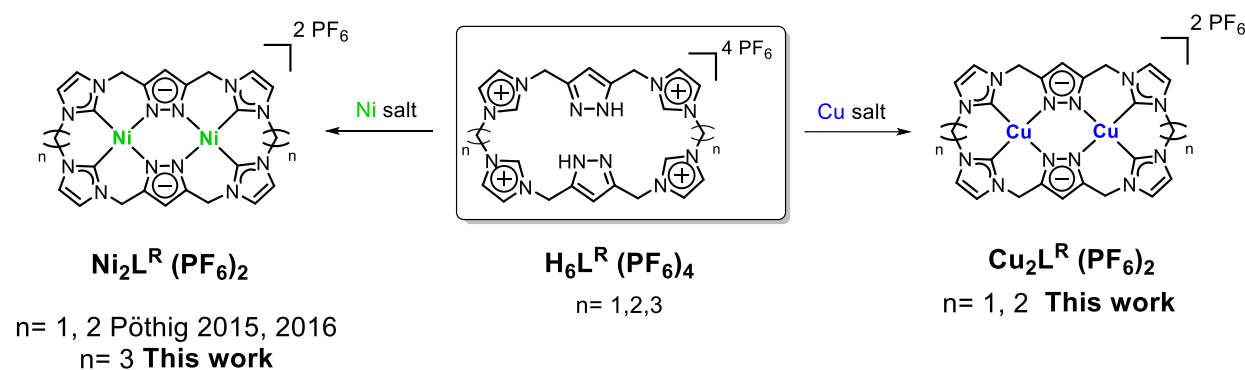
The unique arrangement of the metal centres and the hydrogen bond donors pointing into the cavity makes these complexes highly promising systems for the activation of small molecules via substrate recognition, encapsulation, and catalytic transformation. Consequently, the activity of these complexes to act as CRCs will be electrochemically evaluated. Homogeneous (photo)electrochemistry is a promising strategy to transform the inert CO_2 molecule into value-added chemicals, which can be realised either by incorporating CO_2 into organic scaffolds, or by reducing it into C_1-C_2 building blocks (CO, CH_3OH, $HCOO^-$, $C_2O_4^{2-}$). The presence of two metal centres and of a redox reservoir in the series of bimetallic **Ni_2L^R (PF$_6$)$_2$** complexes, could potentially favour the transfer of more than two electrons to the substrate. To date, most of the reported catalytic cycles show how CO_2 is activated by binding to the monometallic active site and transformed with a series of PCET into different product. Despite the electronic properties of homogeneous catalysts can be fine-tuned with ligand modifications, the transfer of more than two electrons to the reactive intermediate remains a challenging task.[137] Furthermore, the anion-binding capacity of **Ni_2L^R (PF$_6$)$_2$** and the subsequent Capsoplex formation can be exploited to simultaneously bound two molecules of CO_2, promoting the formation of dimerization products, such as oxalate. This type of reactivity was achieved with completely different catalysts, such as the dinuclear Cu(I) complex featuring a tripodal thiolate/pyridine-based ligand,[154] or the pyridyltriazole chelated bimetallic Cu(II) complex, introduced by *Maverik and coworkers*.[155]

Prior to the evaluation of the activity of the Ni-complexes towards CO_2RR, their full electrochemical characterization will be performed, involving the study of electron-transfer kinetics, stability of the reduced species, behaviour in solution and electronic communication between the metal centres. Particular relevance will be attributed to the influence of the geometry and flexibility of the complexes in the electrochemical response. Consequently, the reactivity towards CO_2 will be assessed, and, considering the well-known scenario in which the presence of a proton source boosts CO_2 conversion, the reactivity towards H_2O will the investigated. If no intense activity towards hydrogen evolution is detected, CO_2 reduction studies will be conducted in aprotic organic solvents with small, defined H_2O additions.
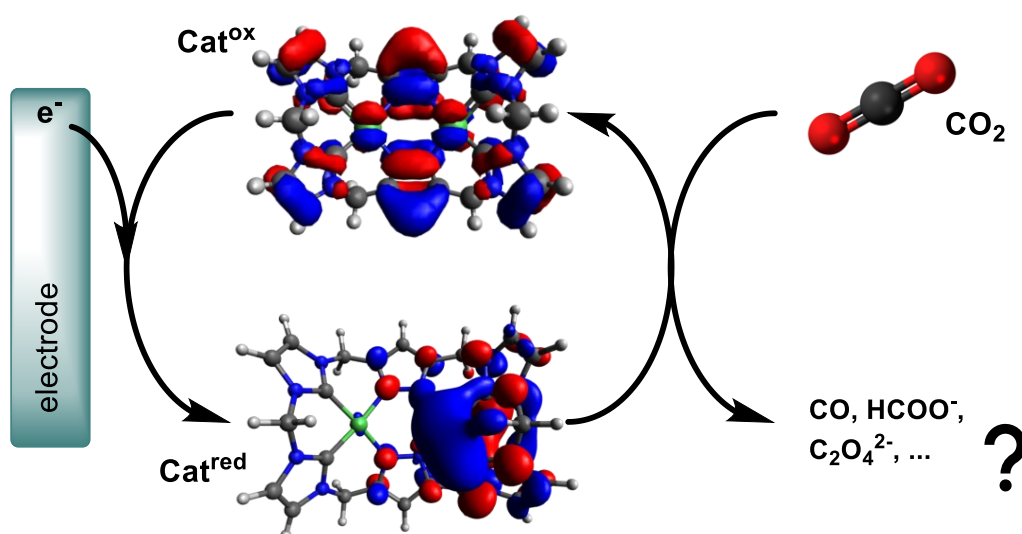
Finally, in the case that homogeneous catalysis will be detected, chronoamperometric experiments will be coupled to GC analysis of the produced gaseous products, to evaluate the extension and the selectivity of **Ni₂Lᴿ (PF₆)₂** towards CO_2RR. Here, the choice of the applied potential in the CPE will be crucial. If, one hand, by choosing a more negative potential one can aim to the best catalytic performances, side reactions and degradation processes are favored at more cathodic potentials. Furthermore, HER should also be minimized in CRCs, and a strategy to do that is the precise determination of the onset potentials of both catalytic waves (HER and CO_2RR).

3 RESULTS AND DISCUSSION

3.1 PROLIGANDS SYNTHESIS

The synthesis and of methylene- and ethylene-bridged calix[4]imidazolium[2]pyrazole cyclophanes, **H₆L^Me(X)₄** and **H₆L^Et(X)₄** (X=OTf⁻ or PF₆⁻) has recently been reported by the group of Pöthig.[78],[190] The propylene-bridged macrocycle, **H₆L^Pr(X)₄**, was successfully synthesized following the well-established cyclization strategy, optimized for the Me- and the Et-bridged proligands by the same group. This approach, namely 3+3 ring-closing, where 3+3 is related to the number of heterocycles contained in the coupling partners, consists of a cyclization reaction between 3,5-bis(imidazol-1-ylmethyl)-1-(tetrahydropyran-2-yl)-1*H*-pyrazole **7** and suitable C1-C3 building units bearing two leaving groups X (**Scheme 3.1**). The crucial intermediate **7** is achieved with a six-steps synthesis, from the commercially available 3,5-dimethyl pyrazole. Initially, the latter compound was oxidized in a buffered aqueous solution containing an excess of the strong oxidant KMnO₄, to yield dimethyl pyrazole-3,5-dicarboxylate (**1**) in 75% yield, which is then transformed in 3,5-Bis(hydroxymethyl)pyrazole hydrochloride (**2**). The esterification reaction was conducted using a large excess of SOCl₂, to form the intermediate acyl-chloride, which was subsequentially substituted via treatment with cold MeOH, to form **2**. A reduction of **2** was then performed employing LiAlH₄ in refluxing Et₂O and subsequent treatment with concentrated hydrochloric acid, to form the chloride salt **3** in 82 % yield, in good agreement with that reported in the literature.[78] Then, dimethyl pyrazole-3,5-dicarboxylate (**3**) was treated at 95°C with an excess of SOCl₂, to afford 3,5-Bis(hydroxymethyl)pyrazole hydrochloride (**4**) in 74 % yield, which is slightly lower than that reported for the same synthesis. The pyrazole moiety of compound **4** was hence protected at r.t. in DCM with 3,4-dihydro-2*H*-pyran. Recrystallization from hot hexane gave 3,5-Bis(chloromethyl)-1-(tetrahydropyran-2-yl)-1H-pyrazole (**5**) with good purity and in 88 % yield. Reaction of **5** with the freshly prepared, nucleophilic sodium imidazolide (**6**) in MeCN gave the protected, key intermediate half ligand, *i.e.* bis(imidazol-1-ylmethyl)-1-(tetrahydropyran-2-yl)-1*H*-pyrazole in excellent purity and yield: 92%. The presence of the protecting group in 1-position of the pyrazole moiety is essential to avoid, during the next delicate cyclization step, the formation of higher and smaller-size macrocyclic molecules. The concomitant presence of two imidazole groups and of the protecting tetrahydro-4*H*-pyrane (thp) increases the complexity of the behaviour of **7** in solution, as demonstrate by the ¹H-NMR spectrum (reported in the Appendix). In fact, the highly asymmetry character of the molecule imparted by the bulky thp group, as well the presence of one stereogenic centre in the same protecting group, is responsible for the magnetic inequivalence of almost all the -CH₂ protons of **7**. Of note, the signal of only one of the two bridging methylene groups is splitted up and therefore coupled with each other, whereas the analogue protons on the other side of the pyrazole

ring are magnetically equivalent. Hence, a rotational hindrance of one imidazole ring caused by the bulky thp group was suggested.[192] At this stage, to efficiently perform the cyclization step, a suitable C1-C3 bridging group was synthesized. Following the procedure employed by Altmann and coworkers, the unstable methylene-bis(trifluoromethanesulfonate) (**8**) was obtained from cleavage of paraformaldehyde with trifluoromethanesulfonic anhydride (Tf_2O) at high temperature. After a column purification, the resulting compound was isolated in 23% yield, which is comparable to the reported one. The intrinsic reactivity of the compound required the storage of **8** at low temperature under Ar. For the ethylene counterpart, the reaction conditions were milder, the starting material was ethylene glycol and the final yield was 74%, slightly lower than that reported in literature. Propylene-bis(trifluoromethanesulfonate) **10** was taken from a previous batch and not prepared during this project.

The cyclization to the proligands **H_6L^R (OTf)$_4$** (R= Me, Et, Pr) turned out to be the most crucial step, performed with the slow addition of the alkyl-bis(trifluoromethanesulfonate) to a solution of **7** (over 1 h) at low temperature (-40°C). These conditions are essential to favour the formation of the desired macrocycles, which were in any case obtained with a yield not exceeding 29% for **H_6L^{Me} (OTf)$_4$**, 22% for **H_6L^{Et} (OTf)$_4$** and 18% **H_6L^{Pr} (OTf)$_4$**. For the methylene and the ethylene-bridged macrocyclic compounds, these values are in accordance with the one reported in the literature,[78] whereas for the propylene-bridged the yield was comparable to that of the smaller ring size-analogues. The last step of the proligand synthesis is the anion exchange, from the OTf^- counterion to more hydrophobic PF_6^-, achieved by dissolving the triflate proligands in a basic aqueous solution and subsequent addition to a solution containing an excess of NH_4PF_6. The yield of this anion-scrambling reaction, by which the PF_6-proligands were obtained, was 45% for **$H_6L^{Me}(PF_6)_4$**, 86% for **$H_6L^{Et}(PF_6)_4$** and 92% **$H_6L^{Pr}(PF_6)_4$**. As suggested by the low yield related to the methylene-bridged calix[4]imidazolium[2]pyrazole, this reaction was found to be not as straight-forward as it was reported in the literature. In fact, when the re-dissolution of the obtained **H_6L^{Me} (PF$_6$)$_4$** in MeCN was attempted to eliminate all the H_2O traces, it was only partially soluble. Some possible reasons for the non-optimal solubility of the latter compound in acetonitrile could be either that there were still traces of water molecules coordinated inside the pocket of the macrocyclic ligand, or that the anion exchange was only partially successful. An intense water peak at δ= 3.43 ppm in the ^{1}H-NMR spectrum of the MeCN insoluble fraction suggest the reliability of the first hypothesis, whereas the presence of some unassignable peaks in the ESI(+)-MS spectrum at m/z: 282.28 and 563.55, supports the second claim. Hypothesis, however, that is not corroborated by the presence of the triflate signal in the ESI(-)-MS spectrum. In fact, the latter spectrum shows only the intense peak at m/z: 144.87, that is related purely to the PF_6^- counterion. However, one should note that the triflate and the hexafluorophosphate counterions have different volumes (86.9 Å and 73 Å, respectively). This property, together with the higher tendency to structure dissociation typical of OTf^-, could reflect a complete different behaviour during the ionization phase of the mass analysis, with the OTf- being destroyed and hence not detectable.[193] Nevertheless, only the fraction of **H_6L^{Me} (PF$_6$)$_4$** which showed high solubility in MeCN revealed to be of high

purity and it was used for the complexation with Ni and Cu. The same reaction, *i.e.,* the anion-exchange conducted for H_6L^{Et} **(PF₆)₄** and H_6L^{Pr} **(PF₆)₄**, did not show the same problems, and their purification lead to the final product in good yield and purity. As a result of the last step, namely the dissolution in MeCN, precipitation with Et₂O and the consequent *in vacuo* drying, all three macrocyclic proligands were found to coordinate one acetonitrile molecule, in accordance with their ability to act as H-bonding sensors.[78] Indeed, their NHC precursor protons of all four imidazolium moieties are selectively pointing towards the nitrogen atom of an acetonitrile molecule hosted in the coordination pocket provided by the macrocyclic structure.
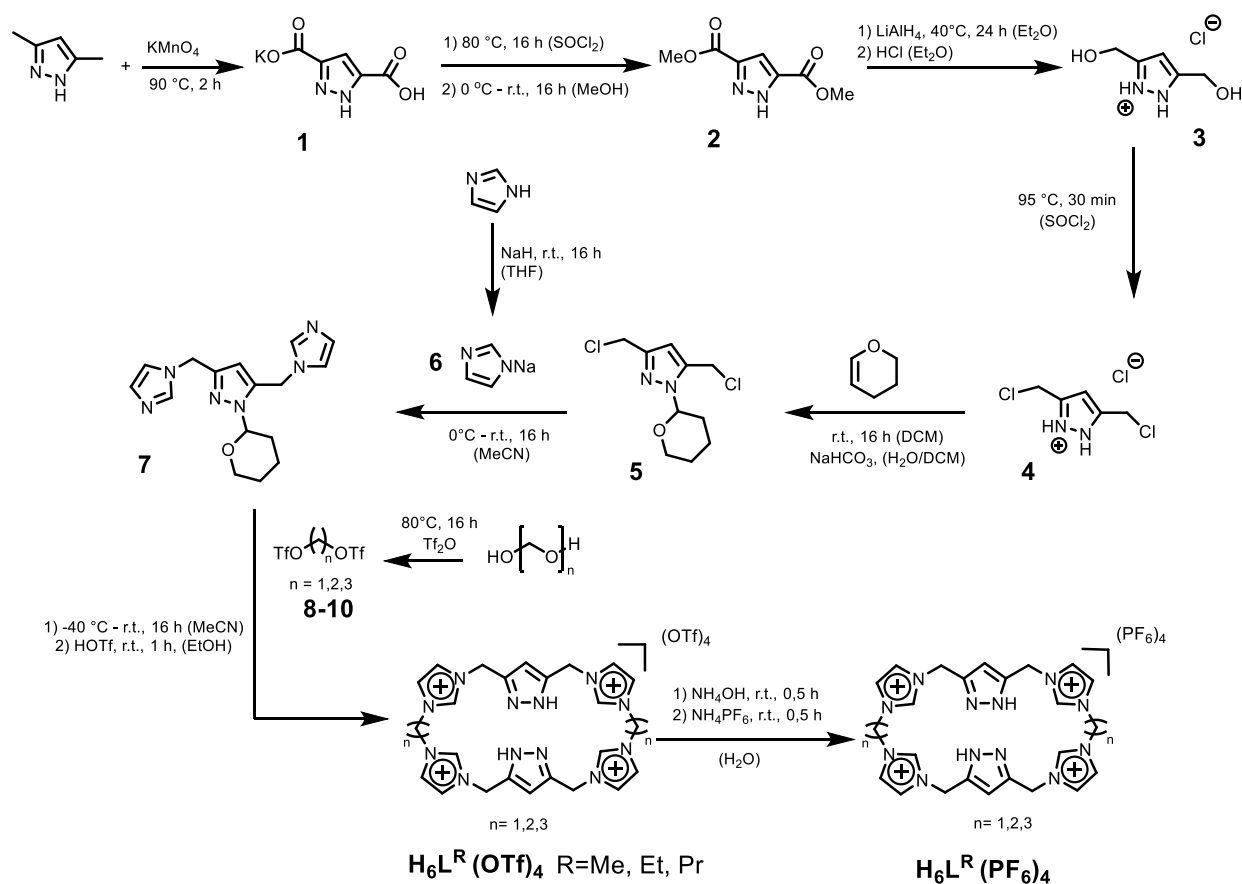
Scheme 3.1 | Synthesis of proligand H_6L^{Me} **(PF₆)₄,**[78] H_6L^{Et} **(PF₆)₄,**[190] and H_6L^{Pr} **(PF₆)₄** (this work).

The ¹H-NMR spectra of H_6L^{Me}**(PF₆)** and H_6L^{Et}**(PF₆)₄**, as well as their spectra obtained with mass spectrometry (MS), were employed as analytical data to compare with those reported in the literature and to verify the purity of the synthesized compounds.

When H_6L^{Et} **(PF₆)₄** is considered, a variable-temperature ¹H-NMR experiment was performed to acquire more knowledge of the fluxional behaviour of the ethylene-bridging protons (**Figure 3.2**). In DMSO-d₆, in the low-field region, at 13.15 ppm, one can find the broad singlet relative to the NH proton of the pyrazole moiety, which is broadened and slightly shifted towards lower ppm upon heating to 80°C. In the final spectrum, obtained

after cooling to r.t. the sample, that signal can be described more as a doublet (*virt.*), with a coupling constant of 13.5 Hz. The coupling partners are not easily assigned, since a ^4J with H_A or H_B (in **Figure 3.1**) would also entail a splitting in the signal of the coupling partner. Unlikely, both H_A and H_B show two singlets, respectively at δ = 6.02 and 4.73 ppm, excluding a possible coupling with NH_{Py}. Consequently, another coupling partner should be hypothesized: with the help of the SC structure of **H₆L^Et (PF₆)₄**, reported by Pöthig *et al.* in 2016,[190] one can observe that the NH_{Py} are directed outwards the macrocyclic cavity and they are not involved with the complexation of the MeCN molecule (blue circles in **Figure 3.1**). Another important aspect to consider is that in the ^1H-NMR spectrum of **H₆L^Et (PF₆)₄** recorded in CD₃CN the signal relative to NH_{Py} is located at significantly lower chemical shift then the same signal in DMSO-d₆ (δ = 11.49 ppm vs. 13.16 ppm). In fact, it is not unsurprising that a strong H-bonding acceptor solvent, like DMSO-d₆, cause a shift towards lower field of the signals of H-bonding donor groups, the latter being instead less deshielded in a weaker H-bonding acceptor solvent, like CD₃CN. On this basis, the most probable explanation for the apparent "splitting" of the two peaks is that the two NH_{Py} possess different chemical environments, in which the H-bonding competition between water and DMSO-d₆ determines a slightly difference on the chemical shift of NH_{Py}.

At δ = 8.88 ppm the multiplet related to H_L is present. These series of peaks, as well as the multiplet centered at 7.63 ppm relative to H_C and H_D, become one broad singlet when the temperature is raised, with the narrowest band obtained at 80°C. When the sample is cooled down, the protons connected to the NHC precursor carbon are characterized by a splitting pattern which resembles one doublet of doublets. However, the excessively high *J*-value leads to the same conclusion of the NH_{Py} protons, namely that different chemical environment caused by the coordinated MeCN molecule causes the splitting of H_L protons. Conversely, when CD₃CN was chosen as solvent, the protons of the imidazolide backbone are two distinct broad singlets at 7.43 and 7.48 ppm (spectrum in the Appendix).

Whereas the signal relative to the pyrazole backbone (H_A) and the methylene-bridging protons (H_B) remain unchanged upon heating to 80°C, the flexible ethylene-bridging protons merge together in a broad signal upon heating (δ = 5.40 ppm). This is in accordance with the initial assumption, according to which the molecule has a certain flexibility and rotation freedom, with H_E and H_F than can assume different orientations in the space. The final spectrum in DMSO-d₆ show again a splitting pattern reminiscent of a doublet of doublets (dd), whereas in CD₃CN these protons (H_E and H_F) appear as a singlet at δ = 5.36 ppm. The dd pattern of the ethylene-bridging protons comprises a geminal coupling (^2J = 31.5 Hz) and a vicinal coupling (^3J = 8.1 Hz).

Figure 3.1 | Left: Molecular structure of part of **H₆L^{Et} (PF₆)₄**, showing in detail the protons whose signals are discussed in the V.T.-NMR spectrum. Right: Solid-state structure of **H₆L^{Et} (PF₆)₄** reported by Altmann and coworkers.[190] The macrocycle cavity is clearly found with one MeCN molecule coordinated inside the pocket, with the N-atom acting like a H-bonding acceptor of the four NHC precursor protons H$_L$. The non-coordinating PF₆⁻ counterions are omitted for clarity.
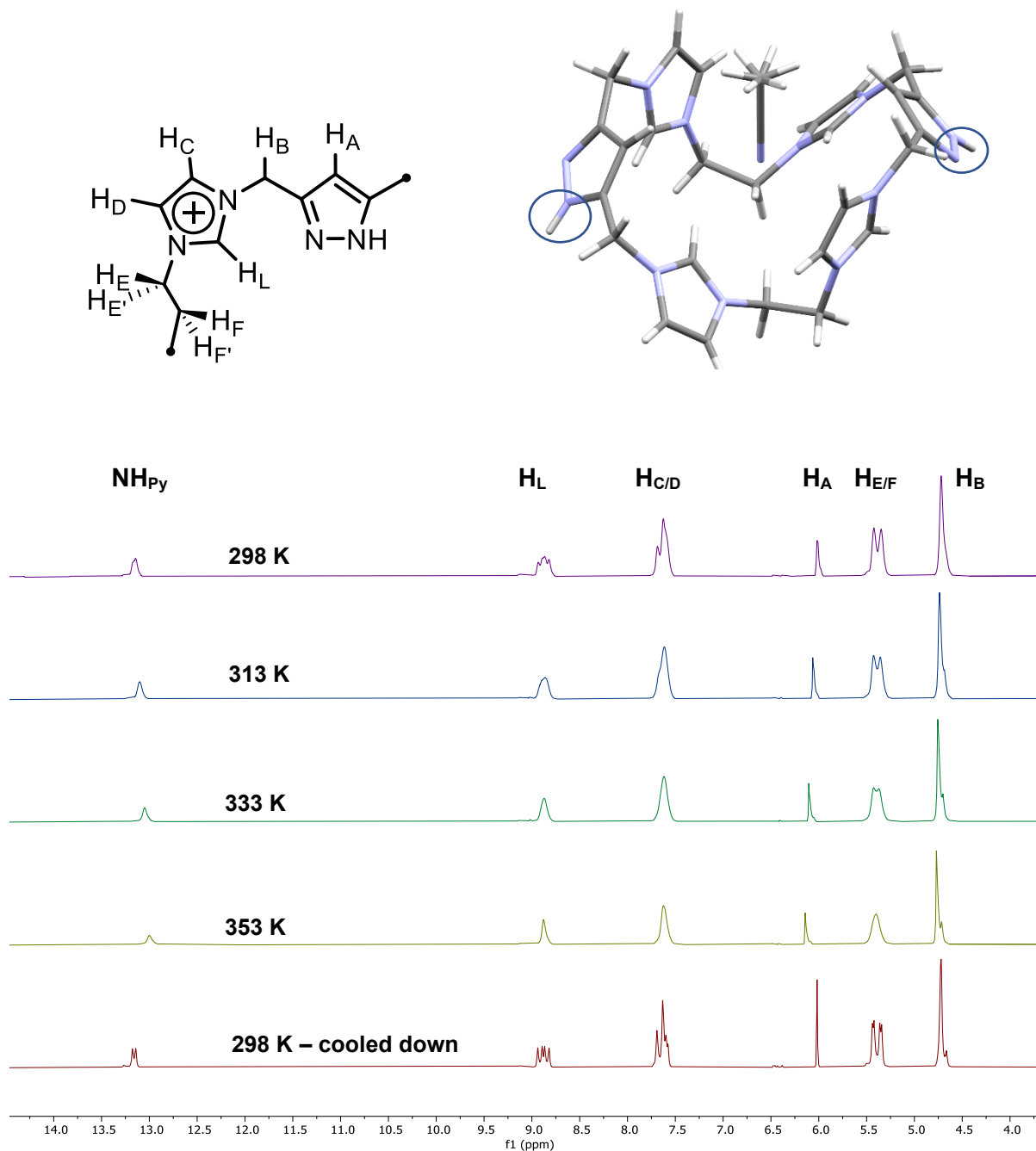
Figure 3.2 | V.T. ¹H-NMR of **H₆L^{Et} (PF₆)₄** at r.t., 40°C, 60°C, 80°C and again at r.t. after cooling, solvent: DMSO-d₆.

The third proligand synthesized was the propylene-bridged calix[4]imidazolylidene[2]pyrazolate, H_6L^{Pr} **(PF$_6$)$_4$**. Interestingly, it possesses the same splitting of the backbone protons of the imidazolide moieties as H_6L^{Me} **(PF$_6$)$_4$**: they are found as two triplets with a ^3J of 2.0 Hz. Regarding the propylene bridge, it turns out the H_E and H_G (**Figure 3.3**) are magnetically equivalent, and their signal is a triplet with a ^3J of 7.5 Hz. Their coupling partner is the central methylene group, H_F, which is thus a quintet, characterized by the same coupling constant. Considered the complex behaviour that H_6L^{Et} **(PF$_6$)$_4$** shows in solution, to get more knowledge of the spatial disposition of the propylene-bridged macrocycle, as well as to assign the respective signals for H_C and H_D, a ^1H ^1H NOESY NMR experiment was conducted. This technique exploits the NOE effect, through which two nuclei that are in spatial proximity (<5 Å) can, with a process called dipolar coupling, exchange magnetization through space.[194]

The spectrum reported in **Figure 3.3** has indeed allowed the assignment of the imidazolylidenes backbone protons, being H_C in spatial proximity with H_B, but not with the propylene-bridging group $H_{E/G}$ and H_F. Another interesting feature is that the NHC precursor protons, H_L, are spatially closer to $H_{E/G}$ than to the central methylene groups H_F of the propylene bridge. This observation is more likely addressable to the increased mobility of the macrocycle molecule, which also coordinates one molecule of MeCN. Since the acetonitrile molecule is coordinated via the NHC precursor protons, it is reasonable to assume the central H_F point outwards the macrocyclic cavity. The dipolar coupling between $H_{E/G}$ and H_F is also observed, but not reported in **Figure 3.3**.
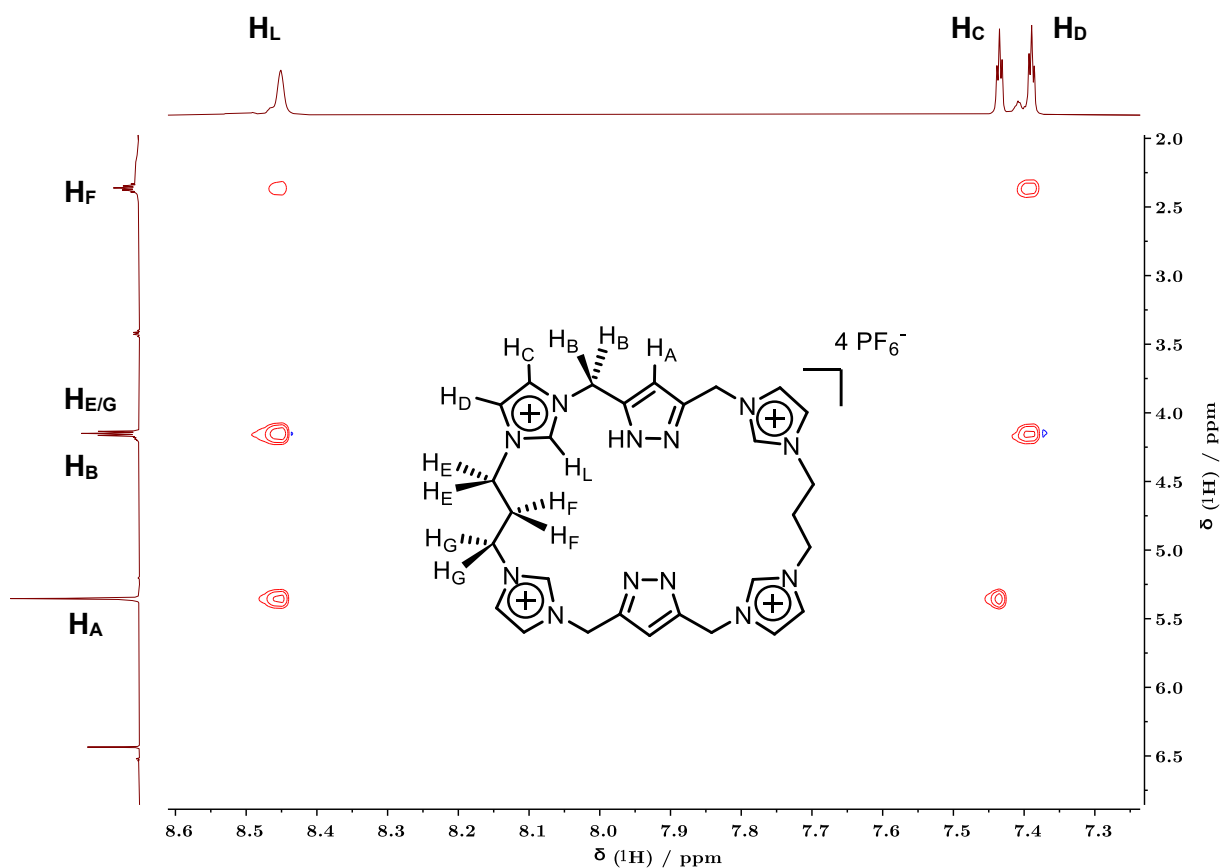
Figure 3.3 | Cutout of the ^{1}H-^{1}H NOESY spectrum of **H$_6$L^{Pr} (PF$_6$)$_4$** in CD$_3$CN showing through-space coupling between the NHC precursor H$_L$ with H$_B$ and H$_{E/G}$, and, to a lower extent, with H$_F$. Positive NOE is observed in this spectrum, since the CPs have opposite sign respect to the DPs. For this reason, spin diffusion limitations are excluded.

3.2 Calix[4]imidazolylidene[2]pyrazolate Bisnickel(II) Complexes
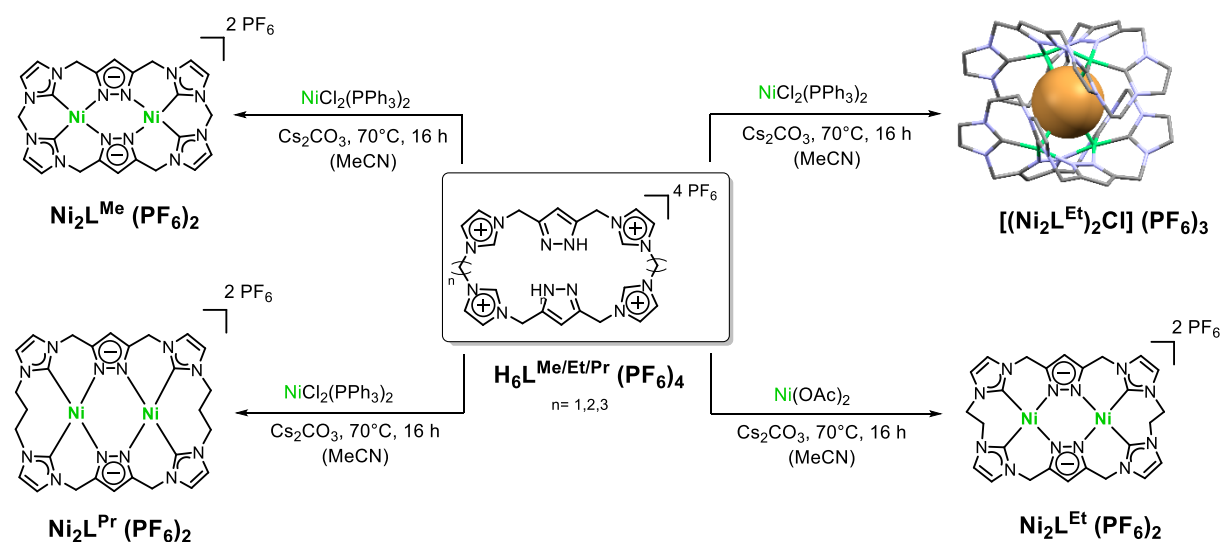
Scheme 3.2 | Synthesis of **Ni₂Lᴿ (PF₆)₂** (R=Me, Et, Pr) from proligand **H₆Lᴿ (PF₆)₄**. Employment of NiCl₂(PPh₃)₂ as metal precursor from **H₆Lᴱᵗ (PF₆)₄** leads to chloride encapsulation by two **Ni₂Lᴱᵗ** moieties, forming Capsoplex.[190]

The compounds **H₆Lᴿ (PF₆)₄** (R=Me, Et, Pr) have been used as ligand precursors for the synthesis of the corresponding bimetallic nickel(II) complexes. **Ni₂Lᴹᵉ (PF₆)₂** and **Ni₂Lᴱᵗ (PF₆)₂** have been already reported by *Pöthig et al.*,[78],[190] whereas **Ni₂Lᴾʳ (PF₆)₂** was synthesized following the same procedure used for the methylene bridged Ni-complex. There are different approaches for the synthesis of NHC complexes, including the employment of free carbenes, the use of an internal or external base, oxidative addition and transmetalation from Ag-NHC complexes. For the studied ligand system, the external base-approach has demonstrated to be efficient and reproducible. The chosen base was Cs₂CO₃ which, if provided to the macrocyclic imidazolium salt in large excess (10 eq.), favours the deprotonation of the four imidazolylidene and of the two pyrazole protons, leading to the metal NHC complex. Caesium carbonate is, in addition, easily removable from the acetonitrile solution containing the Nickel complex by washing it with water.

Applying the conditions as shown in **Scheme 3.2**, all the three nickel complexes were obtained as light-yellow solids after workup in a yield of 28% for **Ni₂Lᴹᵉ (PF₆)₂**, 74% for **Ni₂Lᴱʳ (PF₆)₂** and of 29% for **Ni₂Lᴾʳ (PF₆)₂**. Although the yield for the methylene-bridged complex is lower than the reported one, its purity was confirmed by ¹H, ¹³C-NMR spectroscopy and with ESI(+)-MS analysis. ¹H NMR resonances relative to the macrocyclic ligand protons were observed in the region between 5 and 8 ppm (see spectrum in the Appendix). The most deshielded signals are attributed to the backbone of the imidazolylidene moieties (H$_C$ and H$_D$ in **Figure 3.5**), which show two doublets with a ³J of 2.0 Hz, followed, at more negative chemical shifts, by the singlet of the pyrazole

proton (H$_A$). The pattern of the signal of the methylene bridge between the imidazolylidenes units (H$_{E/E'}$), at first glance, resembles a quartet, centered at 6.10 ppm. Interestingly, a closer look to the chemical systems, with the support of ^{1}H-^{1}H NOESY, as well of the bidimensional HSQC and HMBC spectra, reveals that the signal at 6.10 ppm is caused by a non-first order coupling. In fact, it is described more precisely as two doublets affected from strong coupling. In this assignment, coupling between the geminal protons H$_E$ and H$_{E'}$ gives the large splitting of 12.9 Hz, and a chemical shift difference of 17.4 Hz for the two geminal protons leads to strong coupling that distorts the multiplet intensities so that the "outer" lines are reduced in intensity while the "inner" lines are increased. For the signal of H$_B$ and H$_{B'}$ the same second-order phenomenon was observed, with ^2J (H$_B$-H$_{B'}$) being 15.6 Hz and the difference in chemical shift 21.8 Hz. The fact that the methylene-bridging protons are no longer magnetically equivalent is a consequence of the non-planar structure which **Ni$_2$L^{Me} (PF$_6$)$_2$** assumes, which has been described in great detail by Altmann and coworkers.[78] In addition to the literature report, ^{1}H-^{13}C HSQC and HMBC spectroscopy, conducted in this study, have allowed the precise assignment of all the carbon resonances in **Ni$_2$L^{Me} (PF$_6$)$_2$**, with the carbene resonance being at 159.8 ppm. The latter frequency is comparable with other carbene frequencies reported for Ni-NHC macrocycles. **Ni16**, reported by *Jurss and coworkers*, is characterized by a chemical shift of 155.9 ppm,[187] whereas in the imidazolium-cyclophane **Ni1** (**Figure 1.19**) of *Williams et al.* the carbene is found at 165.3 ppm.[120]
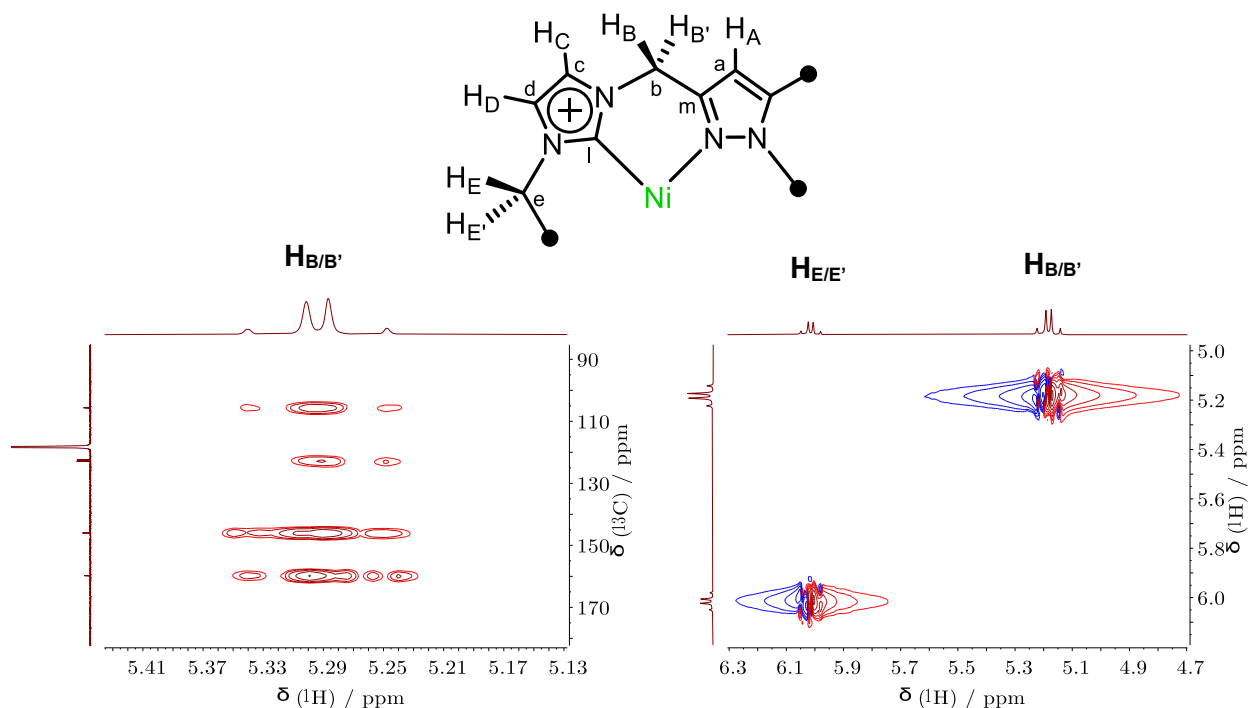
Figure 3.5 | Cutouts of the ^{1}H-^{13}C HMBC (left) and ^{1}H–^{1}H NOESY (right) of **Ni$_2$L^{Me} (PF$_6$)$_2$** in CD$_3$CN. The left spectrum clearly indicates that the virtual quartet centered at 5.29 ppm can be deconvoluted in two contributions, arising from the magnetically inequivalence of H$_{B/B'}$.

By increasing the length of the alkyl-bridge from methylene to ethylene, no change in the electronic properties of the carbenic carbon is appreciable, since a very similar carbon resonance is observed in the ^{13}C-NMR spectrum (158.4 ppm vs. 159.8 ppm). However, the ^{1}H-NMR spectrum of **Ni₂L^Et (PF₆)₂** differs from the methylene-bridged analogous since the second-order effect, which characterized the methylene bridging protons in **Ni₂L^Me (PF₆)₂**, is no longer existing. In fact, the two magnetically inequivalent protons H$_B$ and H$_{B'}$ (**Figure 3.6**) result in two distinct doublets at 5.50 and 5.10 ppm, with a geminal coupling constant of 15.4Hz. The singlet at 5.36 ppm in the proligand, representative of the protons of the ethylene-bridge, is splitted in two multiplets in **Ni₂L^Et (PF₆)₂**, because of the magnetic inequivalence of H$_{E/E'}$ and H$_{F/F'}$, caused by the saddle-shape structure that the complex assumes, as demonstrated by the crystal structure reported by Altmann and coworkers.[190]

The propylene-bridged **Ni₂L^Pr (PF₆)₂** was obtained with a similar procedure as the methylene-bridged calix[4]imidazolylidene[2]pyrazolate Bisnickel(II) complex, namely the addition of 2 eq. of NiCl₂(PPh₃)₂ and 10 eq. of Cs₂CO₃ to a proligand solution in MeCN at 80°C. Fractional precipitation from MeCN:Et₂O leads to pure **Ni₂L^Pr (PF₆)₂**, which has been fully characterized with mono and bi-dimensional NMR experiments, mass spectrometry, elementary analysis and UV-Vis Spectrophotometry.
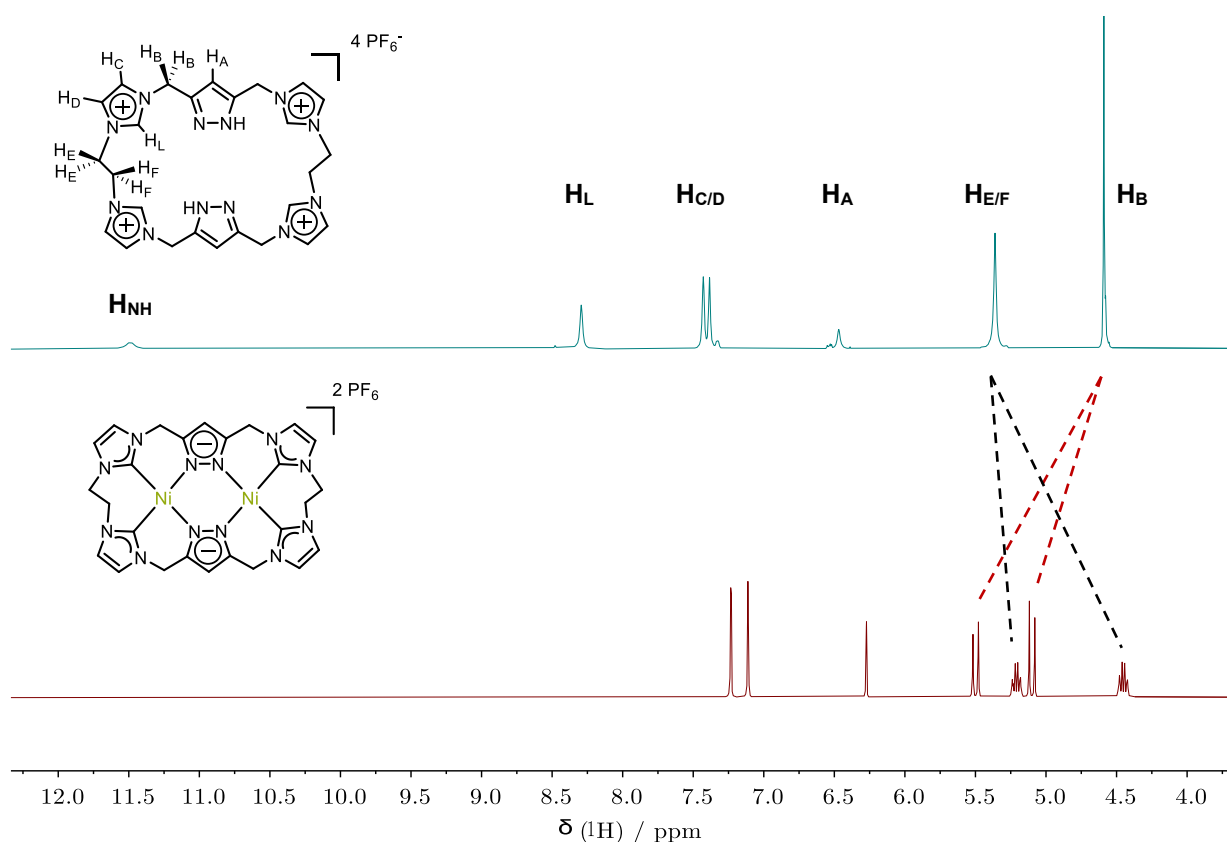
Figure 3.6 | Comparison of the ^{1}H-NMR spectrum of **H₆L^Et (PF₆)₄** (top), and **Ni₂L^Et (PF₆)** (bottom) in CD₃CN. The spectrum of the metal complex is characterized by the splitting of the methylene (H$_B$) and ethylene (H$_{E/F}$) protons, due to the decreased mobility upon metal complexation.

The first interesting aspect arising from ^{1}H-NMR analysis is the complex splitting pattern of the propylene-bridging protons. In fact, in **Ni$_2$L^{Pr} (PF$_6$)$_2$**, the H$_{E/E'}$ and H$_{G/G'}$ protons (**Figure 3.7**) becomes magnetically inequivalent and they are splitted in two multiplets, centred at 4.66 and 3.60 ppm, whereas H$_{F/F'}$ is shifted to lower ppm (2.23 ppm) compared to **H$_6$L^{Pr} (PF$_6$)$_4$**. Despite the superimposition of the latest signal to the water peak (2.13 ppm), arising from H$_2$O present in the sample itself (traces) or in the NMR solvent (CD$_3$CN), ^{1}H-^{13}C HSQC spectrum gives some indications that the signal of H$_F$ and H$_{F'}$ may be splitted in two peaks, in accordance with the other magnetically inequivalent -CH$_2$ bridging protons. In addition, ^{1}H-^{13}C HSQC allowed the assignment of the high-fielded carbon resonance of C$_f$ (29.8 ppm), whereas the ^{1}H-^{1}H NOESY give confirmation of spatial proximity between H$_{F/F'}$ and H$_{E/E'}$ - H$_{G/G'}$ (**Figure 3.7**).

Previous to the start of this project, single crystals suitable for SC-XRD were grown from slow diffusion of diethyl ether into a solution of **Ni$_2$L^{Pr} (PF$_6$)$_2$** in MeCN at ambient temperature. The Ni atoms, as in the other two bimetallic complexes, are coordinated with a pseudo-square planar geometry in the two coordination pockets. In contrast to **Ni$_2$L^{Me} (PF$_6$)$_2$** and **Ni$_2$L^{Et} (PF$_6$)$_2$**, it possesses smaller N$_{Pyr}$–M–C$_{NHC}$ (*cis*) and N$_{Pyr}$–M–N$_{Pyr}$ angles (**Table 3.1**) of 87.34° and 89.6°, respectively.
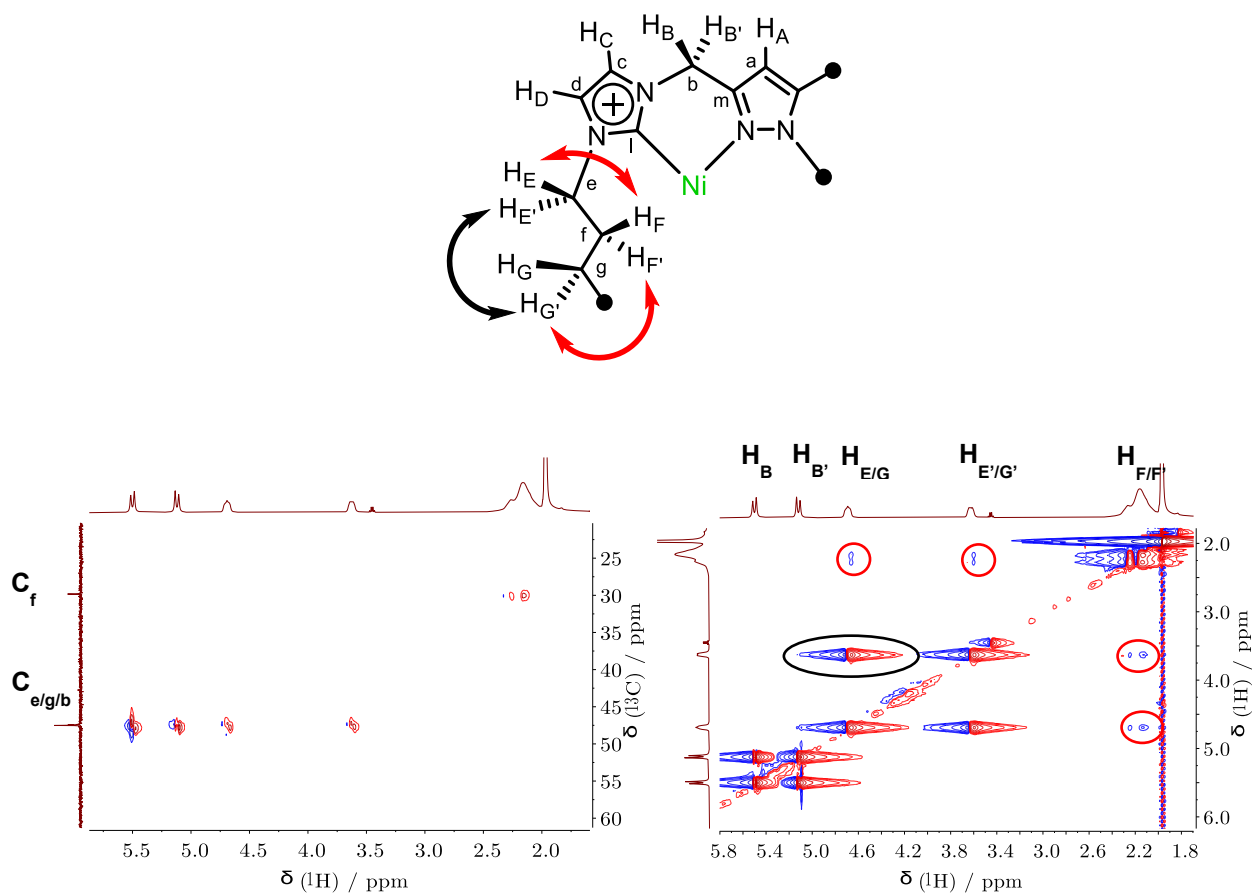
Figure 3.7 | Cutouts of the ^{1}H-^{13}C HSQC (left) and ^{1}H–^{1}H NOESY (right) of **Ni$_2$L^{Pr} (PF$_6$)$_2$** in CD$_3$CN. Both spectra confirm the presence of the H$_{F/F'}$ signal at 2.23 ppm, that is fused with the peak of the residual water.

Consequently, the pyrazolate units are closer to each other and the complex is more squashed in the middle (see trend in γ / °) and wider in correspondence of the imidazolylidene moieties. This feature is not so unexpected, since the propylene bridge is more steric demanding and hence it forces the imidazolylidenes to assume less relaxed conformations. Therefore, the C_{NHC}–M–C_{NHC} angle is increasing along the series, from 86.2° of Ni_2L^{Me} (PF$_6$)$_2$ to 96.2° of Ni_2L^{Pr} (PF$_6$)$_2$ and the θ angle (defined by the intersection between the planes passing through the imidazolylidene moiety and the metal centre of each cavity) is decreasing. The θ value is representative of the "tension" of the imidazolylidenes, caused by the bulkiness of the alkyl bridge. A smaller value of this angle means that the NHC moieties are far from being in a flat conformation (**Figure 7.1**). The θ angle assumes values of 136.6° in Ni_2L^{Me} (PF$_6$)$_2$, 125.8° in Ni_2L^{Et} (PF$_6$)$_2$ and 118.1° in Ni_2L^{Pr} (PF$_6$)$_2$. In the latter compound, in fact, the imidazolylidenes are directed more towards the cavity of the complex, whereas in the methylene-bridged complex, they assume a more relaxed conformation, being closer to each other. No significant variation was observed for the other relevant angle, φ, (see **Table 3.1** for its definition) which describes the "squeezing" of the cavity. In the propylene bridged complex the intermetallic distance resulted increased respect to the other two complexes. Its value, 3.654 Å, is slightly lower than the sum of the van der Waals radii of Ni (1.89 Å). The average metal - carbene bond length is also increased in Ni_2L^{Pr} (PF$_6$)$_2$ (1.899 Å), whereas the average M-N_{Pyr} bond length is slightly reduced along the series, reaching 1.898 Å. Of note, the overall symmetry of the complex is lower in Ni_2L^{Pr} (PF$_6$)$_2$, with significant variation on bond lengths and angles from one cavity to the other, most likely for the molecular hindrance induced by the propylene bridges.
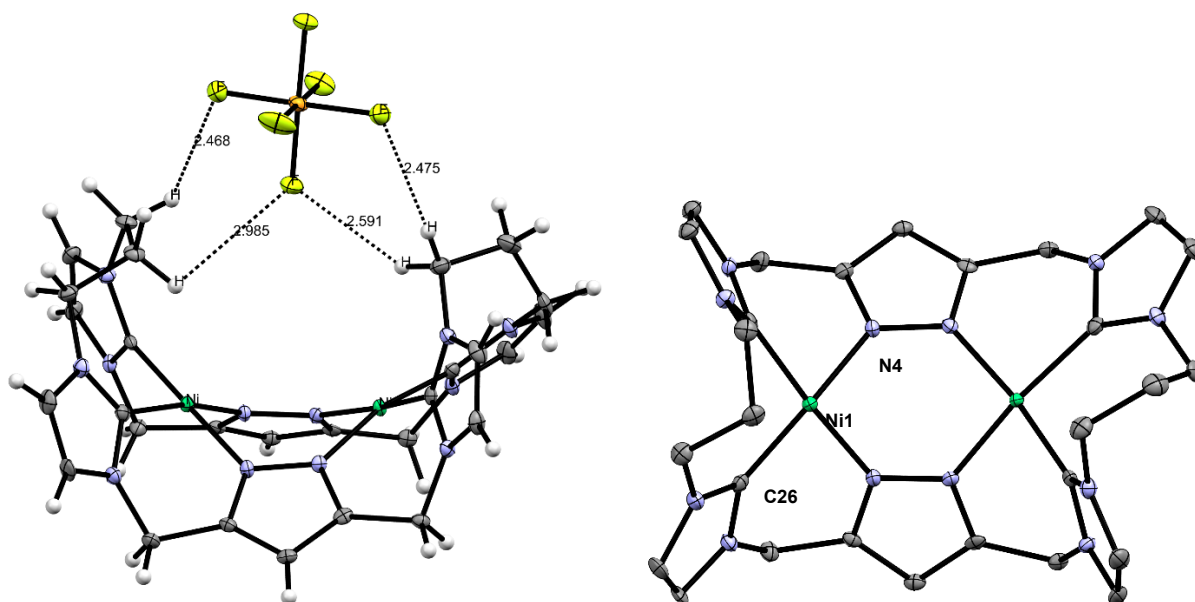
Figure 3.8 | ORTEP-representation of the single-crystal molecular structure of Ni_2L^{Pr}(PF$_6$)$_2$. Thermal ellipsoids are at the 50% probability level. Left: Side-view highlighting the C–H --- F contacts to one of the PF$_6$ ions by dashed lines; Right: Top-view of the solid-state structure with solvent molecules, PF$_6$ ions, and hydrogen atoms omitted for clarity.

Table 3.1 | Selected mean bond distances, bond angles for **Ni$_2$L^R (PF$_6$)$_2$**, (R = Me, Et, Pr). **θ** (°) is the average angle of intersection between the planes containing the imidazolide backbone atoms and the metal centre, for each cavity; whereas the "squeezing" angle **φ** (°) is calculated between two planes that are defined by the metal center and the four coordinating atoms. *γ* is calculated by the intersections of the planes containing the two pyrazole moieties. For a visualization of these angles refer to **Figure 7.1** The same parameters obtained from DFT calculations are also reported, obtained using **ωB97xD/6-31(+)G** and **ωB97x-D/6-31(+)G(d,p)** theory level, that are split-valence, diffuse double ξ basis sets.

structural parameter	Ni$_2$L^{Me} (PF$_6$)$_2$	Ni$_2$L^{Et} (PF$_6$)$_2$	Ni$_2$L^{Pr} (PF$_6$)$_2$	Ni$_2$L^{Pr} (PF$_6$)$_2$ ωB97xD/ 6-31(+)G	Ni$_2$L^{Pr} (PF$_6$)$_2$ ωB97xD/ 6-31(+)G(d,p)
M–M / Å	3.600	3.645	3.654	3.658 (0.11)	3.649 (0.14)
M–C$_{NHC}$ / Å	1.860	1.883	1.899	1.916 (0.89)	1.919 (1.05)
M–N$_{Pyr}$ / Å	1.903	1.901	1.898	1.905 (0.37)	1.911 (0.68)
N$_{Pyr}$–M–C$_{NHC}$ / ° (*cis*)	89.5	88.2	87.3	87.6 (0.30)	87.4 (0.11)
N$_{Pyr}$–M–C$_{NHC}$ / ° (*trans*)	175.2	175.1	170.0	168.8 (0.71)	169.1 (0.53)
N$_{Pyr}$–M–N$_{Pyr}$ / °	94.7	90.7	89.6	89.7 (0.11)	89.7 (0.11)
C$_{NHC}$–M–C$_{NHC}$ / °	86.2	92.5	96.2	96.4 (0.21)	96.5 (0.31)
θ / °	136.1	125.8	118.1	116.6 (1.24)	116.4 (1.44)
γ / °	143.7	118.1	114.0	114.1 (0.09)	114.3 (0.26)
φ / °	123.3	123.4	122.6	121.0 (1.31)	121.5 (0.90)

Eventually, excited states UV-Vis absorption properties were analysed in MeCN for all the three Ni-complexes. In **Figure 3.9** the relative spectra are reported, in which one can notice that the higher energy transition, centered at 217 nm for all complexes, is a ligand-based excitation, since it is the only detectable band for the proligands **H$_6$L^R (PF$_6$)$_4$** (R= Me, Et, Pr). Its nature is most likely attributable to a $\pi - \pi^*$ transition involving the pyrazolate aromatic units. The metal complexes are also characterized by an intense charge transfer transition (most likely a LMCT). Regarding this last band, going from **Ni$_2$L^{Me} (PF$_6$)$_2$** to **Ni$_2$L^{Et} (PF$_6$)$_2$**, a blue shift can be observed on the maximum absorption (303 and 291 nm, respectively). This specific excitation is broadened in **Ni$_2$L^{Pr} (PF$_6$)$_2$**, that also possesses another, less intense, band in the 370-410 nm region. This weak band could be attributed either to the forbidden $d - d$ transitions involving the empty $x^2 - y^2$ orbitals of the Ni atoms.[184] **Ni$_2$L^{Me} (PF$_6$)$_2$** and **Ni$_2$L^{Et} (PF$_6$)$_2$** also possess another weak band centered at 360 nm, whose nature is most likely a metal centered $d - d$ transitions, in which mixed atomic orbital functions (p, d) contribute to the overall MO and allow a partial lifting of the Laporte selection rule. This last, broad band is the responsible of the slight yellow colour that the complexes assume when dissolved in polar solvents, like MeCN or *N,N'* DMF.
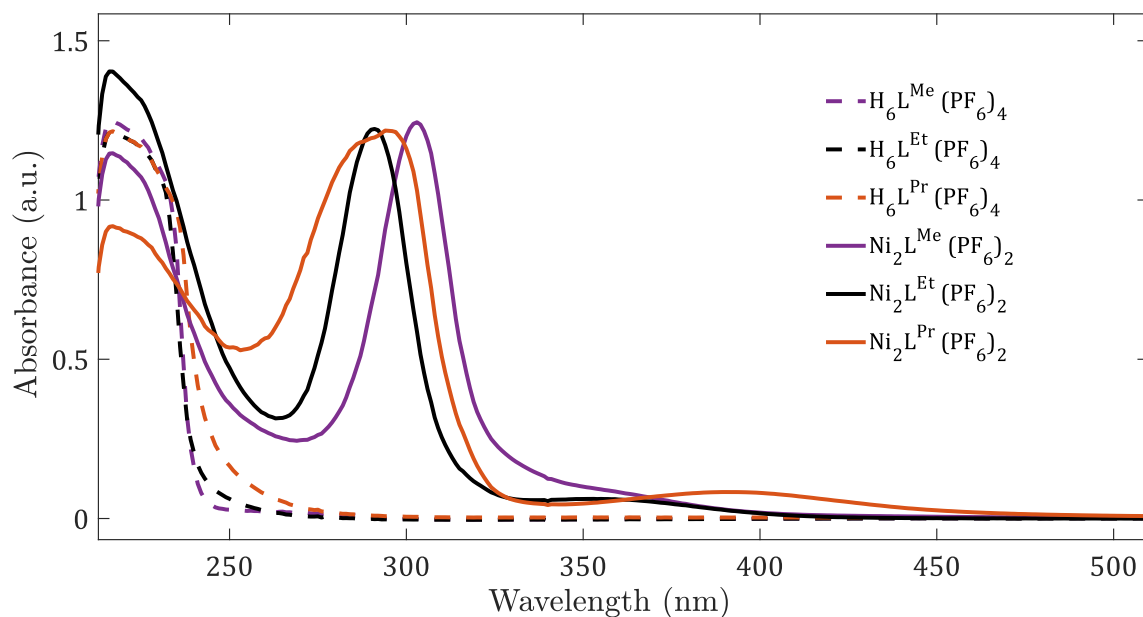
Figure 3.9 | UV-Vis spectra of the Ni complexes and their relative proligands. The intensities are normalised to the metal-centered band.

In **Figure 3.10** the frontier orbitals of **Ni₂L^{Pr} (PF₆)₂** are reported, obtained from TD-DFT calculation. The employed basis set was a split-valence, triple ξ **6-311(+)G(3df,pd),** implemented with polarized and diffuse functions. The calculation was performed in solution, employing the Conductor-like Polarizable Continuum Model (CPCM, solvent: MeCN)[195] in order to best reproduce the behaviour of the complex in "real" conditions during spectrophotochemical studies. Interestingly, one can observe how the HOMO of the Ni-complex is mainly located on the π system of the pyrazolate and of the imidazolylidene moieties of the ligand, as well as over the d_{z^2} orbitals of the metals, whereas the LUMO and LUMO+1 are delocalised over one (or both) metal centre(s).
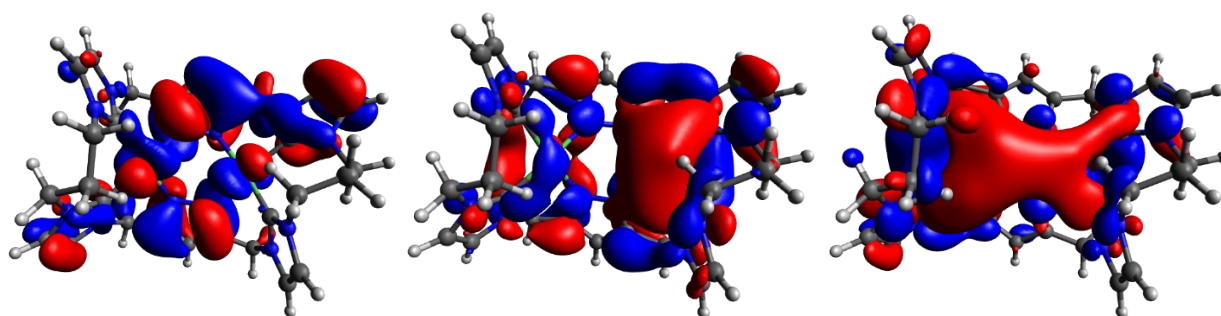
Figure 3.10 | HOMO (left), LUMO (middle) and LUMO+1 (right) of ¹[Ni₂L^{Pr}]²⁺ (plotted in *Avogadro,* isosurface value of 0.02).

3.3 CALIX[4]IMIDAZOLYLIDENE[2]PYRAZOLATE BISCOPPER(II) COMPLEXES

3.3.1 Synthesis and characterization of Cu_2L^{Me} $(PF_6)_2$
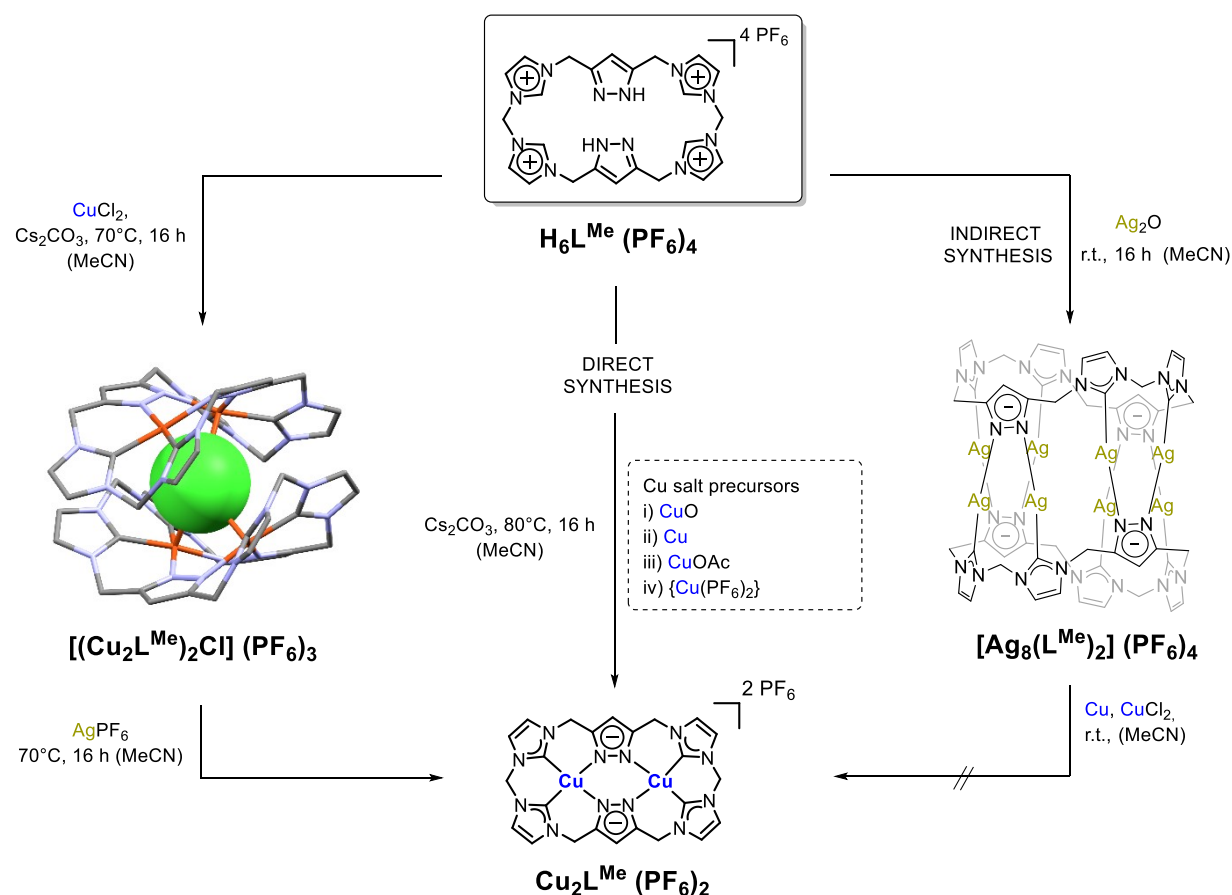
Scheme 3.3 | Synthesis of Cu_2L^{Me} $(PF_6)_2$ via Capsoplex formation (previous to this study),[191] via direct synthesis screening different metal precursors and attempted synthesis via transmetalation from $[Ag_8(L^{Me})_2]$ $(PF_6)_4$.

Another 3d-metal interesting for its CO_2 reduction activity is copper. There are only a few literature-know macrocyclic NHC-Cu complexes; if then one considers only the systems possessing square planarly coordinated copper, in the +2/+3 oxidation state, they are even more rare. The first report is dated 2018, when *Kühn and coworkers* developed a tetra calix[4]imidazolylidene copper complex, with the metal being a formal Cu^{3+} centre.[132] It was obtained in high yield from the reaction of the proligand with copper(II) acetate under air. While reacting, the copper centre undergoes to a disproportionation reaction and yields the Cu(III) complex and Cu(I)OAc as byproduct. More interestingly, an adaptable N-heterocyclic carbene hosting copper in three different oxidation states was synthesized by *Meyer et al.* in 2020.[122] The ligand system was obtained by replacing two *trans*-positioned imidazolylidenes with two pyridine, providing a C^N^C^N

cavity. This peculiarity, namely the hemilability of the pyridine moieties, allow the overall system to be flexible enough to maintain the coordinated copper ion upon oxidation from Cu^+ to Cu^{2+} and then from Cu^{2+} to Cu^{3+}. The Cu^{2+} congener was obtained by selective oxidation employing ferrocenium cation (Fc^+) from the Cu^+ complex in MeCN solution, and the metal centre was shown to be strongly coordinated to one MeCN molecule in the apical site.

As showed in **Scheme 3.3**, calix[4]imidazolylidene[2]pyrazolate biscopper(II) complexes was successfully synthesized *via* the chloride-encapsulated supramolecular complex **[Cu$_2$(L^{Me})$_2$Cl] (PF$_6$)$_3$** and subsequent halide abstraction in MeCN (not published).[191] Notably, the same reaction conditions employing $Ni_2Cl_2(PPh_3)_2$ instead of $CuCl_2$ in the reaction with the methylene-bridged proligand, didn't lead to the encapsulation of one Cl^- ions, but to **Ni$_2$L^{Me} (PF$_6$)$_2$**. This difference is attributable to the peculiar structure of **Cu$_2$L^{Me} (PF$_6$)$_2$**, which is able to better stabilise the "Capsoplex" adduct through a combination of multiple hydrogen bonding and attractive Coulomb interactions between the guest and the metal centres.[190] Nevertheless, this two-steps approach is affected by a low overall yield (13%) associated with the possible Ag-contamination of the final products.[191] During halide abstraction, in fact, a stoichiometric amount of $AgPF_6$ is required to force the disruption of the supramolecular assembly and favour the isolation of the single, saddle-shape, complex. Despite the latter reaction is thermodynamically driven by the precipitation of AgCl, it revealed not to be robust and reproducible, with silver contamination easily detectable with mass spectrometry analysis of the final product.

Another "indirect" approach, largely used in the literature to synthesize a variety of metal-NHC complexes is transmetalation (**Scheme 3.3**, right). This strategy consists in the preparation of the Ag(I), Au(I) or, more rarely, Cu(I) NHC complex, that are characterized by the coinage metals being bound in a linear fashion, forming molecular box-type complexes.[196],[131],[197],[198] For the ligand system considered in this study, a fully characterized octanuclear Ag(I) complex was introduced by *Pöthig and coworkers*, named Pillarplex.[81] Hence, after having isolated the pure **[Ag$_8$(L^{Me})$_2$] (PF$_6$)$_4$** complex, synthesized following the literature known procedure, different Cu(II) sources were tested with a view to obtain the pure **Cu$_2$L^{Me} (PF$_6$)$_2$** *via* transmetalation.

First, inspired by the work of *Chen and coworkers*,[83] powdered Cu^0 was provided to a MeCN solution of Pillarplex either at r.t. or at elevated temperatures. With no conditions traces of dinuclear copper complex were observed, demonstrating that the oxidation of metallic copper observed by Chen and coworkers when reacting with an hexanuclear Ag-NHC complex didn't took place. Hence, as second attempts, a stoichiometric amount of $CuCl_2$ was employed, to force the removal of the eight Ag^+ ions via AgCl precipitation. Despite a strong change in colour was observed even at room temperature (from the pale yellow of **[Ag$_8$(L^{Me})$_2$] (PF$_6$)$_4$** and greenish of $CuCl_2$ in MeCN to the intense blue of the final mixture), MS analysis of the reaction mixture didn't reveal any characteristic peak of the target **Cu$_2$L^{Me} (PF$_6$)$_2$**.

Considered the failure of the transmetalation route, the efforts have been tailored to the most convenient, but less straight-forward, "direct" synthesis. The first attempt was based on a strategy employed by *Chen and coworkers*,[83] namely the addition of an excess of Cu powder (8.5 eq.) to a proligand solution in MeCN under air. After stirring of the reaction mixture at room temperature and then at 80°C, no clear evidence of **Cu_2L^{Me} (PF$_6$)$_2$** formation arises from MS analysis. Hence, the "internal base" strategy was applied: an excess of the basic CuO (3 eq.) was provided to **H_6L^{Me} (PF$_6$)$_4$**. One would expect, as in the case of Ag$_2$O, that the basicity of the oxo anion is sufficient for the deprotonation of the ligand, ultimately yielding water as the only by-product. In practise, after stirring at r.t. the suspension in MeCN, mass spectroscopy analysis revealed that only the starting proligand was present, and no intermediates or products were formed. Consequently, a more basic ligand was needed, and Cu(OAc)$_2$ was chosen. The Cu-salt was added in slightly excess (2.3 eq.) to a proligand solution under inert conditions and an external base was added to further booster the deprotonation of the four NHCs and the two pyrazolate protons. NaOAc (10 eq.) was employed to limit the variety of anions in the solutions, which can replace the PF$_6$-counterion of the proligand. During stirring at 80°C, the mixture assumes first a yellow colour, and then a dark green tonality. For the first time, after washing and fractional precipitation, a green solid was obtained. MS analysis revealed no isotopic pattern relative to the bimetallic Cu-complex (discussed in detail later), whereas it was possible to note the formation of a mixed PF$_6$-OAc ligand species (m/z= 257.38, 659.12, 701.04, 763.85), probably originated from the undesired anion scrambling process.

At this stage, the necessity to avoid direct use of chloride and acetate anions with **H_6L^{Me} (PF$_6$)$_4$**, leads to the employment of the "naked" Cu^{2+} ion present in {Cu(PF$_6$)$_2$}. This chemical species, exploited as metal precursor by *Schiemann et al.* for the synthesis of a bis(terpyridine)-copper(II) complex,[199] is formed in solution, by mixing a stoichiometric amount of CuCl$_2$ and AgPF$_6$ (2 eq.). The immediate precipitation of AgCl took place and the supernatant assumed an intense green tonality. After filtering the white solid off, the methylene-bridged proligand and an excess of Cs$_2$CO$_3$ were added to the supernatant, containing [Cu(NCCH$_3$)$_4$] (PF$_6$)$_2$, and the mixture was stirred at 80°C overnight. From the resulting red suspension, a green/yellow solid was obtained after fractional precipitation with MeCN : Et$_2$O. NMR spectroscopy revealed the presence of broad and not defined bands, suggesting the presence of a paramagnetic species, as one would expect from a Cu^{2+} (d^9) complex. Mass spectroscopy was therefore chosen as preferred analytical technique. Considered the natural abundance of ^{65}Cu (30.85 %) and ^{63}Cu (69.15 %), for a bimetallic copper complex one would expect three intense peaks in the mass spectrum (M, M+2, M+4), with relative intensity 100 : 89 : 20. Indeed, the molecular peak at m/z = 893.93, the peak at m/z = 748.97, relative to the loss of one PF$_6$ anion and the peak at m/z = 302.37 [Cu$_2$L^{Me}]$^{2+}$, all possess the correct isotope pattern relative to the dinuclear complex. In addition, the mass spectrum, reported in the Appendix, does not show contaminations of silver, deriving from AgPF$_6$ and any peaks at higher m/z, that could have been an indication of the formation of supramolecular assemblies (Capsoplex).
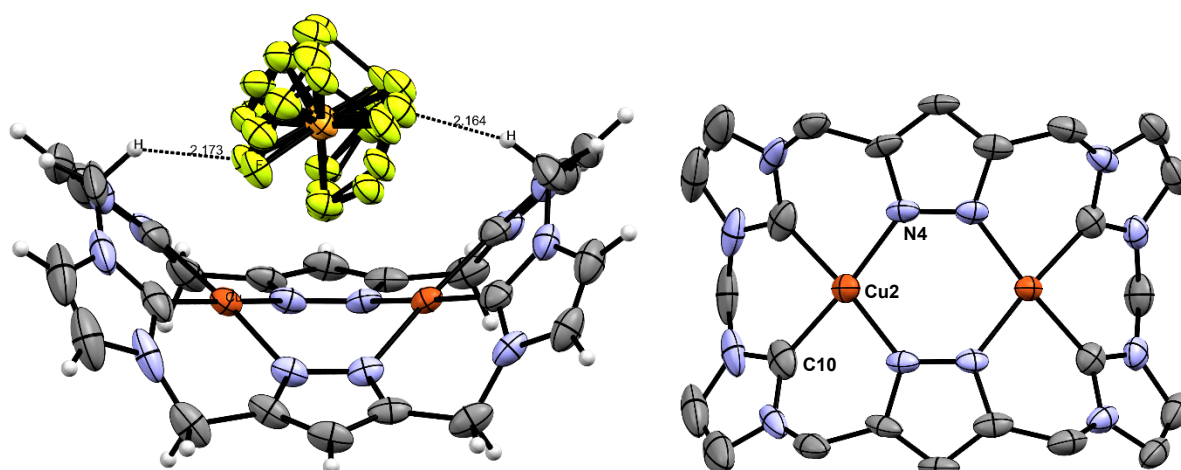
Figure 3.11 | ORTEP-representation of the single-crystal molecular structure of **Cu$_2$L^{Pr}(PF$_6$)$_2$**. Thermal ellipsoids are at the 50% probability level. Left: Side-view highlighting the C–H --- F interactions to one of the PF$_6$ ions by dashed lines; Right: Top-view of the solid-state structure with solvent molecules, PF$_6$ ions, and hydrogen atoms omitted for clarity.

Single crystals of **Cu$_2$L^{Me} (PF$_6$)$_2$** suitable for X-ray crystallography were obtained by slow diffusion of diethyl ether into a concentrated solution of the copper complex in dimethyl formamide at room temperature. The molecular structure in the solid state was solved and refined properly and the resulting crystal structure is illustrated in **Figure 3.11**. The complex, as in the case of **Ni$_2$L^{Me} (PF$_6$)$_2$**, assumes a saddle-shape conformation, with the two Cu-centres coordinated in a square planar fashion. As shown also in **Table 3.2**, despite the metal-to-metal distance is essentially the same of the Ni-congener, the metal-NHC and the metal-pyrazolate bonds are slightly longer, as a consequence of the decreased ionic radii of the two copper centres. Accordingly, the N$_{Pyr}$–M–N$_{Pyr}$ angle, as well as the C$_{NHC}$-M-C$_{NHC}$ one, are wider in the Cu-complex, with the C$_{NHC}$–M–N$_{Pyr}$ angle that is slightly reduced. The "squeezing" angle ϕ is also reduced, compared to the Ni-complex (119.1° vs. 123.3°), meaning an overall more flattened structure, with a wider cavity. The other relevant difference is the value of the angle described by the planes containing the two pyrazole moieties, γ, that is significantly higher respect to the Ni-counterpart (163.5° vs. 143.7°). These structural parameters indicate that **Cu$_2$L^{Me} (PF$_6$)$_2$** assumes a more relaxed conformation, with the "bowl" structure being less pronounced than **Ni$_2$L^{Me} (PF$_6$)$_2$** (**Figure 3.12**), proving that the methylene-bridged calix[4]imidazolium[2]pyrazole ligand is relative flexible in accommodating different metals in its cavities.

To gain further insight into the electronic structure, as well as the spin states, DFT calculations have been conducted and compared to results from UV-Vis spectroscopy and cyclic voltammetry measurements. First of all, when considering a Cu^{2+} complex, which possess an electronic configuration of {Ar}3d^9, it is important to assess if the complex has a spin multiplicity of S=+1, being in the triplet state, or S=0, being in the singlet state.
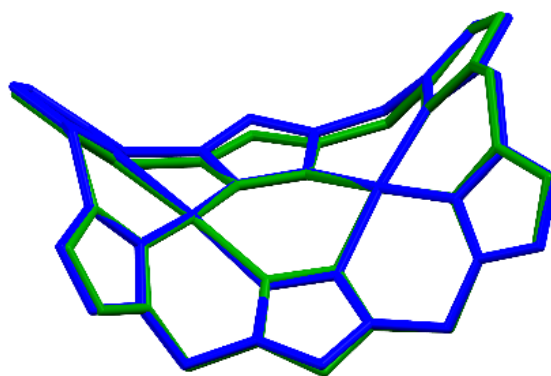
Figure 3.12 | Structural overlay of **Ni₂L^Me (PF₆)₂** (green) and **Cu₂L^Me (PF₆)₂** (blue). Solvent molecules, PF₆ ions, and hydrogen atoms are omitted for clarity. RMS: 0.0974.

Broadening of the NMR lines, as already discussed, leads to think about a preferred triplet state, in which the two singularly occupied $d_{x^2-y^2}$ orbitals of the copper centres (with SP geometry) are not interacting to each other to realise an antiferromagnetic coupling.

Table 3.2 | Selected mean bond distances, bond angles, and indicator angles for **M₂L^Me (PF₆)₂**, (**M** = **Cu**, **Ni**). For a description of θ, γ, ϕ value, refer to **Table 3.1**.The same parameters obtained from DFT calculations are reported, derived using split-valence double ξ, **ωB97x-D/6-31(+)G** and triple ξ **6-311(+)G(3df,pd)** basis set, as well as **B3lyp/6-31+G(d,p)**. The highest accuracy was shown by the former functional/basis set combination.

structural parameter	Ni₂L^Me (PF₆)₂	Cu₂L^Me (PF₆)₂	Cu₂L^Me (PF₆)₂ ωB97x-D/ 6-31(+)G	Cu₂L^Me (PF₆)₂ ωB97x-D/ 6-311(+)G(3df,pd)	Cu₂L^Me (PF₆)₂ B3lyp/ 6-31+G(d,p)
M–M / Å	3.600	3.615	3.747	3.752	3.778
M–C_NHC / Å	1.860	1.975	2.003	2.011	2.018
M–N_Pyr / Å	1.903	1.990	1.998	2.012	2.025
N_Pyr–M–C_NHC / ° (*cis*)	89.5	87.0	88.21	88.33	88.35
N_Pyr–M–C_NHC / ° (*trans*)	175.2	175.1	173.81	173.82	174.02
N_Pyr–M–N_Pyr / °	94.7	96.3	97.28	97.21	96.96
C_NHC–M–C_NHC / °	86.2	87.6	86.16	86.01	86.24
θ / °	136.1	141.8	137.41	139.2	137.25
γ / °	143.7	163.5	153.29	155.72	155.25
ϕ / °	123.3	119.1	132.07	133.13	132.24

Under the latest condition, in fact, the complex would behave as a diamagnetic species, with a null spin magnetic moment, and an overall singlet spin state. To support this claim, DFT calculation were conducted to the cation fragment, **[Cu₂L^Me]²⁺**, using ωB97x-D/6-31(+)G(d,p) level theory (which is a split-valence double ξ basis set, supplemented by diffuse and polarized functions).[200] The results showed that the triplet state is 198.09 kJ mol⁻¹ more stable than the singlet one, and a plot of the spin density is found in **Figure 7.3**. The reported spin density is the difference of the α- and the β-spin population. It can be clearly seen that these α-electrons are mainly located in the $d_{x^2-y^2}$ orbitals of the Cu^{2+} ions, but they are also partially delocalised along the metal-heteroatom σ-bonds, since there is a substantial contribution of the σ-orbitals of the NHC atoms and of the nitrogen of the pyrazolate moieties.

Electrochemical studies of **Cu₂L^Me (PF₆)₂** were conducted to investigate the redox behaviour of the complex, as well as to test if the pyrazolate-linker can provide electronic communication between the two metal centres. The cyclic voltammogram, recorded in dry acetonitrile under Ar atmosphere (+ 0.1 M TBAPF₆ to ensure electrical conductivity of the solution and to minimize diffusion and migration processes) showed that, despite the complex is highly stable against reduction in the whole cathodic window of the solvent (**Figure 7.13**, appendix), it is easily oxidized upon scanning towards positive potentials. A fully reversible event at +0.02 V (vs. Fc⁺/Fc redox couple) is observed, with a peak-to-peak separation (ΔE_p) of 94.8 mV, followed by another reversible event at +0.31 V (ΔE_p = 158.7 mV) and a third, quasi-reversible oxidation at E_p^a= +0.93 V. A summary of the electrochemical data is shown in **Table 3.3**. The ΔE_p of $E_{1/2}$ (1) and $E_{1/2}$ (2) are significantly larger than a sequential two-electron transfer process (E_rE_r), which should be of 57 mV. Higher peak-to-peak separation are indicative of processes with a less favoured electron-transfer step from the electrode to the analyte, that could arise from a greater degree of rearrangement prior to electron transfer, or because the molecule is strongly adsorbed on the electrode, blocking fast electron transfer.[158]

According to DFT calculation, with ωB97x-D/6-31(+)G(d,p) theory level, the first redox process matches with a metal-based oxidation, with the atomic partial charge relative to copper (derived from the atomic polarization tensor) changing from +0.909 (**Figure 7.3**), to +1.098 for the mono-oxidised species. The removal of one electron from **³[Cu₂L^Me]²⁺** (where the prefix ³ indicates the spin multiplicity), give rise to **²[Cu₂L^Me]³⁺**, which is shown to be 100.72 kJ more stable than the quartet state, meaning that there is only one unpaired electron left. A plot of the spin density and of the SOMO of **²[Cu₂L^Me]³⁺** (**Figure 7.4**) suggests, as in the case of the starting complex, that the electron density is delocalised over the $d_{x^2-y^2}$ orbitals of the Cu^{2+} ions, as well as on the M-C_NHC and M-N_Pyr bonds. Equal values for both Cu centres of the atomic partial charge (+1.098) can exclude the presence of a valence-mixed species. Further oxidation, $E_{1/2}$ (2), which takes place +0.312 V, leads to **¹[Cu₂L^Me]⁴⁺**, which possesses a null spin multiplicity and hence no unpaired electrons. Of note, the singlet state is 179.15 kJ mol⁻¹ more stable than the triplet state.
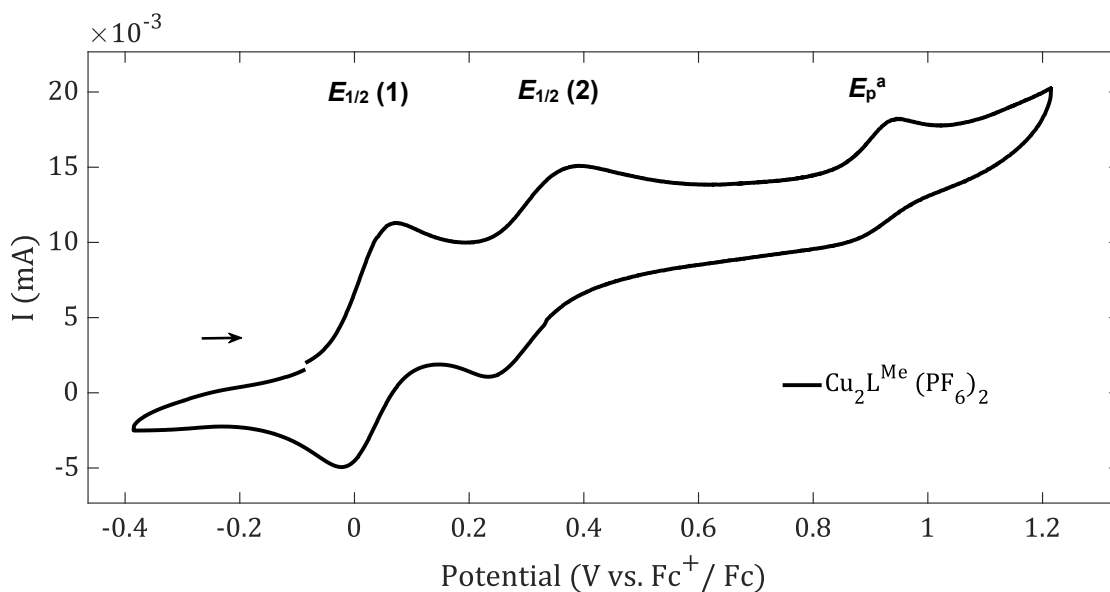
Figure 3.13 | Cyclic voltammetry of **Cu₂Lᴹᵉ(PF₆)₂** in a range of -0.3 V to +1.3 V, scan rate: 100 mV s⁻¹, solvent: MeCN (+TBAPF₆ 0.1 M). CV recorded in the whole solvent window is reported in **Figure 7.13**.

The two copper ions are characterized by a decrease of the partial atomic charge: from +1.098 to +0.720. A reduction of the partial atomic charge upon oxidation is counterintuitive, and, in fact, the Mulliken population analysis has revealed to be a rather inaccurate technique when employing large basis set. Nevertheless, comparing the HOMOs of ^{2}[**Cu₂Lᴹ͏ᵉ**]$^{3+}$ and ^{1}[**Cu₂Lᴹᵉ**]$^{4+}$ (**Figure 7.5**), one can point out that, upon oxidation, the electron density is more localised on the π orbitals of the NHC imidazolylidene donors. Hence, it is possible to assume that there is an increased π-donation to the d-orbitals of the metals in the case of ^{2}[**Cu₂Lᴹᵉ**]$^{3+}$, resulting in a decreased partial atomic charge. The last observable oxidation ($E_p{}^a$: +0.93 V) yields ^{2}[**Cu₂Lᴹᵉ**]$^{5+}$, in which the electron density is located mainly in one of the pyrazolate unit (**Figure 7.6**). The fully occupied HOMO is still delocalised mostly over the π systems of the redox-innocent imidazolylidenes backbone, as well as on the $d_{x^2-y^2}$ orbitals of the Cu^{3+} ions and on the π system of one pyrazole. Surprisingly, the unpaired electron is localized in HOMO-11, which is delocalised over the π systems of one pyrazolate moiety, as well as over the two adjacent NHC donor groups (**Figure 7.6**). The partial atomic charge, in accordance to ligand-based oxidation, is not significatively affected: +0.70 for both Cu^{3+} centres.

Concerning electronic communications between the metal centres, cyclic voltammetry is known to be a powerful technique to estimate the intermetallic electronic coupling. In fact, Robin and Day introduced a classification system to categorize bimetallic complexes according to the intensity of the electronic coupling, assessed by the difference of the two subsequent redox events in the CV.[201]

Table 3.3 | Summarized peak potentials of the CV of **Cu₂L^Me (PF₆)₂** and the proposed oxidation states, based on Spin population analysis from DFT calculation.

Peak	E (V vs Fc⁺/Fc)	ΔE_p, mV	Oxidation state
$E_{1/2}$ (1)	0.024	94.8	Cu^{III}/Cu^{II} (L^{2-})
$E_{1/2}$ (2)	0.312	158.7	Cu^{III}/Cu^{III} (L^{2-})
$E_p{}^a$	0.934	-	Cu^{III}/Cu^{III} ($L^{\cdot}$)⁻

Despite a Cu(II) complex featuring a pyrazolato-bridged bis-NHC ligand has been reported by Chen *et al.*,[83] no electrochemical characterization was presented. Nevertheless, Gervasio and coworkers reported the synthesis of a related copper-coordinated pyrazolato-bridged complex. The bimetallic systems featured two reversible, one-electron oxidations separated by 230 mV, indicating strong intermetallic communication between the metals.[202] In **Cu₂L^Me (PF₆)₂**, the difference between $E_{1/2}$ (1) and $E_{1/2}$ (2) is 288 mV, suggesting even a stronger electronic coupling between the metal centres. Nevertheless, an accurate allocation of the homo-binuclear Cu complex into one of the classes of Robin and Day's system is not possible only on the basis of electrochemical data, since it would require also spectrochemical investigation for the detection of intervalence charge transfer (ICT) for the evaluation of electronic matrix coupling (H_{ab}).[203] The visualization of the HOMO-1 (SOMO) in **Figure 3.15**, gives clear evidence of the π character of the N-N bonds of the pyrazolate moieties that, in turns, are responsible for the bonding interaction with the metals through their partially occupied $x^2 - y^2$ orbitals.

Finally, to investigate the excited state properties of **Cu₂L^Me (PF₆)₂**, UV-Vis spectra of the copper complex, as well of the methylene-bridged proligand have been recorded in solution (solvent: acetonitrile) and compared to that of **Ni₂L^Me (PF₆)₂**. As shown in **Figure 3.14**, the copper complex is characterized by an intense transition centered at 232 nm, as opposed to the nickel complex that possess two transitions at 217 and 303 nm. The fact that the intense band for **Cu₂L^Me (PF₆)₂** at 232 nm is shifted towards higher wavelengths respect to the Ni-complex and to the pure ligand, leads to assume that the metal centres are somehow involved in this transition, for instance via a LMCT from the pyrazolate moiety to the Cu^{2+} centres. However, some authors, dealing with similar complexes, claim that the transitions below 300 nm are mainly ligand-centered, which involve the π and π^* orbitals of the pyrazolate moieties.[202],[204],[205] In **Cu₂L^Me (PF₆)₂** a weak additional band, with maximum at 423 nm is present, whose nature could be related to the Laporte-forbidden $d - d$ transition involving the semi-occupied $x^2 - y^2$ orbitals of the Cu atoms. The intensity of these type of bands, which usually are responsible for the colour of the complexes, is low, with extinction coefficients (ε_{max}) that rarely exceed 10 m⁻¹ s⁻¹. To support these claims, TD-DFT calculations were conducted to get more insights of the nature of the observed transitions, employing the CPCM solvation mode (implicit model) with ωB97xD/6-311(+)G(3df,pd) level theory.
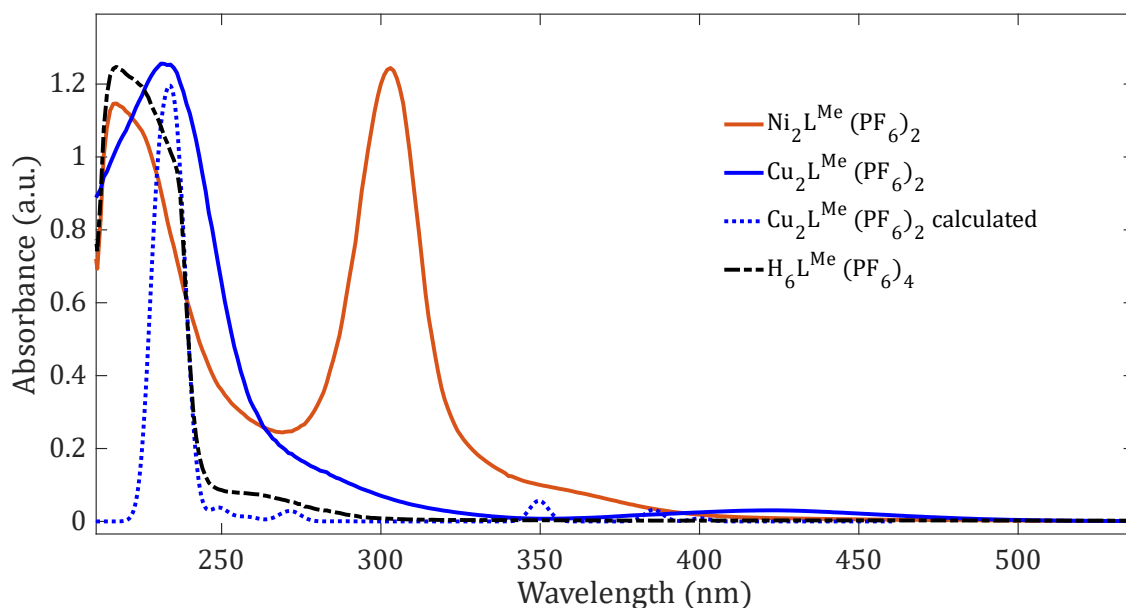
Figure 3.14 | Benchmark of the UV-Vis spectra of **Cu_2L^{Me} (PF₆)₂** (experimental and computed, *vide supra*), **Ni_2L^{Me} (PF₆)₂** and **H_6L^{Me} (PF₆)₄** in the 200-550 nm region.

The simulated spectrum is reported with the dotted blue trace in **Figure 3.14**, whose most intense band is centered at 230-240 nm. Both the single vertical transitions that give rise to that band (located at 229 and 235 nm) involves β-electron transition and the excitations occur from HOMO-4 to HOMO/HOMO-1. As observed from **Figure 3.15**, ligand-centred orbitals are highly involved in these transitions, corroborating the hypothesis of a mixed-character excitation: pyrazole π- π* transitions and LMCT. Finally, the weak band at 349 nm of the computed spectrum would instead originate from α-electron transitions, more in detail from HOMO-1 to LUMO+1 and HOMO to LUMO, with a significant metal-orbitals contribution (**Figure 3.15**).
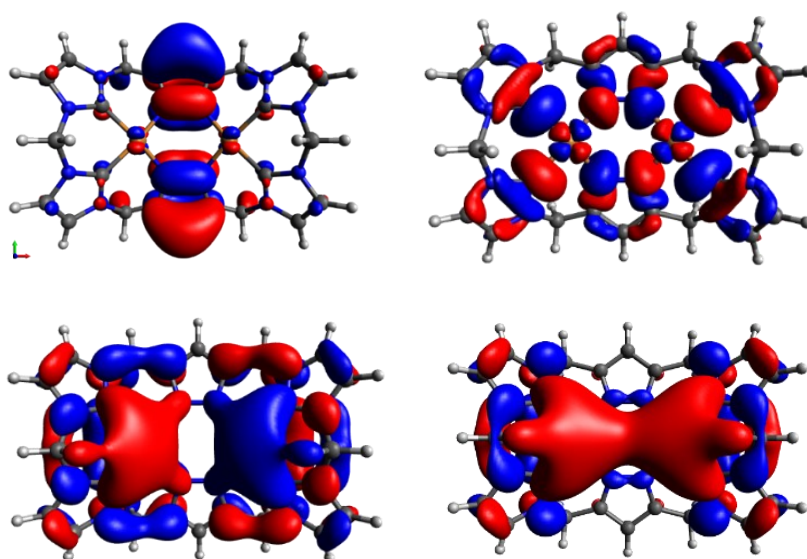
Figure 3.15 | Visualization of the HOMO-4 (top left), SOMO (HOMO, top right), LUMO (bottom left) and LUMO+1 (bottom right) of ³**[Cu_2L^{Me}]²⁺** (plotted in *Avogadro,* isosurface value of 0.02).

73

3.3.2 Towards the synthesis of Cu$_2$L^{Et} (PF$_6$)$_2$
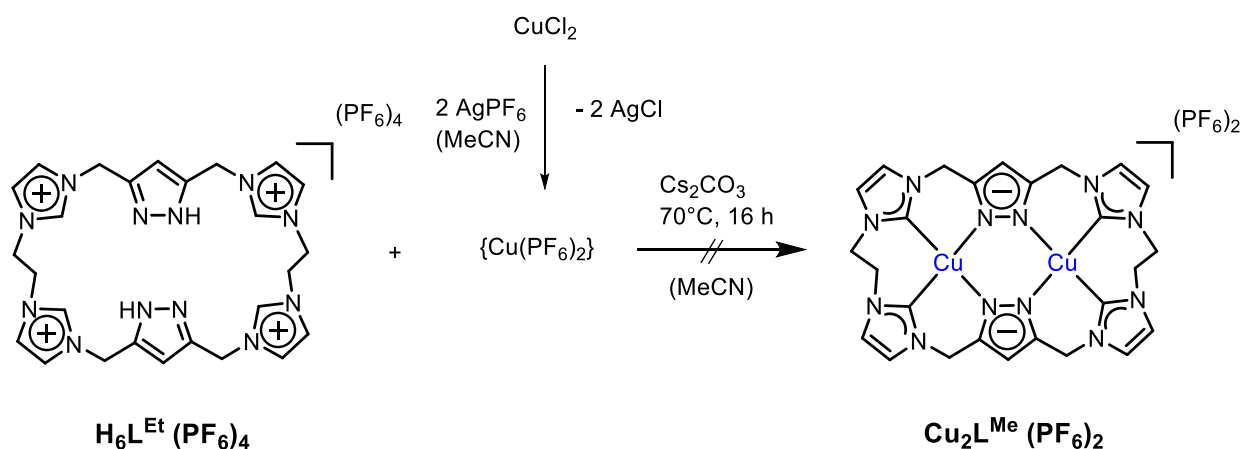
Scheme 3.4 | Attempted synthesis of **Cu$_2$L^{Et} (PF$_6$)$_2$** using the same procedure of the methylene-bridged analogous.

Considered the success of the employment of *in situ* synthesized {Cu(PF$_6$)$_2$}, the same procedure has been used also to access to the ethylene-bridged analogue, from **H$_6$L^{Et}(PF$_6$)$_4$**. Hence, after stirring the reaction mixture in MeCN overnight at 80°C (red/orange tonality), washing with H$_2$O and drying, a brownish powder was obtained. In order to remove the possible Ag contaminations deriving from the non-complete reaction of AgPF$_6$, the solid was dissolved in MeCN and filtered through a Celite® pad. Then, from the resulting filtrate, fractional precipitation (MeCN : Et$_2$O) was performed and the different fractions analysed via mass spectroscopy. The result didn't provide clear indication of the obtaining of pure **Cu$_2$L^{Et} (PF$_6$)$_2$**. If, on one side, the peak at m/z= 777.1, with the M, M+2 and M+4 peaks having an intensity ratio of 100:89:20, could indicate the presence of the pure bimetallic Cu complex, another intense peak at m/z= 667.1, that possesses an isotopic pattern of 75:100:44, can be related to the formation of a species containing three Cu ions. At this stage, one may think that the choice of the solvent mixture for the purification mixture, *i.e.* fractional precipitation, was not ideal. Therefore, from the solid product of the reaction, several crystallization attempts were performed. The successful method was found to be slow diffusion of Et$_2$O in DMF at r.t., which yield small orange needles deposited on a dark green layer of impurities. Eventually, SC X-ray analysis of those coloured needles reveals that the product of the reaction was the chloride encapsulation complex **[(Cu$_2$L^{Et})$_2$Cl] (PF$_6$)$_3$**, rather than the bimetallic, saddle-shaped complex. Its molecular structure, solved and refined, is reported in **Figure 3.16**.
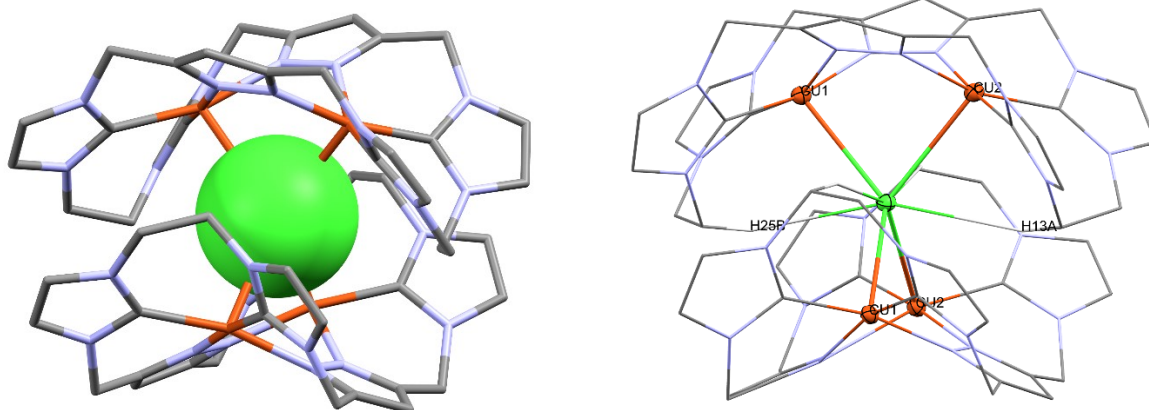
Figure 3.16 | Molecular structures of **[(Cu₂Lᴱᵗ)₂Cl] (PF₆)₃**. Non-encapsulated counter anions and solvent molecules are omitted for clarity. Left: the dinuclear complexes are shown as capped sticks, the encapsulated anion in the space filling model, emphasising the different demand in volume of the anion. Right: Coordination environment around the halide (Cl⁻) including hydrogen bonding to the ethylene bridges.

As in the case of the Ni-ethylene-bridged complex, the tendency to encapsulate and to stabilize one chloride ions appears to be evident.[81] The central chloride ions is tetracoordinated in a distorted tetrahedron fashion by four copper ions, each of which is, in turns, square-pyramidally coordinated with the four in-plane coordination atoms being two NHC carbons and two pyrazolate nitrogens of the ligand. The M-Cl-M angle, of 78.80°, is slightly higher than in **[(Ni₂Lᴱᵗ)₂Cl] (PF₆)₃** (75.70°), with the squeezing of the single crisp complexes being less marked in the case of the copper encapsulation complex (122.6° vs. 124.6°). Further evidence of the more flattened structure of the latter compound is the γ value (angle between the pyrazolate units, **Figure 7.1**), that is significantly larger in the case of the Cu-complex compared to the Ni-one, meaning that in the Ni-capsoplex the tennis-ball shape is even more evident. One possible explanation for this phenomenon is that, when one compares the Cu-complex with the Ni-one, copper ions are better accommodated into the coordination pocket of the ethylene-bridged ligand, as shorter $M\text{-}N_{Pyr}$ and $M\text{-}C_{NHC}$ bond distances suggests. This in turns, implies a less structural distortion of the ligand framework upon coordination. As **Table 3.4** shows, the metal-Cl distances are on average smaller than in the analogous Ni-capsoplex, but higher than the sum of the ionic radii of the ions, suggesting a favourable electrostatic interaction between Cu^{2+} and Cl⁻. On the contrary, the H-bonding interaction between the central encapsulated chloride and the protons of the ethylene-bridged complex are weaker in the copper case, since their distance is, in average 0.25 Å longer.

Table 3.4 | Selected geometrical parameters of **[(Cu₂L^{Et})₂Cl] (PF₆)₃** compared to **[(Ni₂L^{Et})₂Cl](PF₆)₃**.[190] ϕ is the squeezing angle of the single saddle-shape complex.

structural parameter	[(Ni₂L^{Et})₂Cl] (PF₆)₃	[(Cu₂L^{Et})₂Cl] (PF₆)₃
M‑M / Å	3.5790	3.605
M-C$_{NHC}$ / Å	1.885	2.003
M-N$_{Pyr}$ / Å	1.912	2.006
M1–Cl / Å	2.9217	2.782
M2–Cl / Å	2.9116	2.886
H25B-Cl / Å	2.616	2.819
H13A-Cl / Å	2.616	2.884
M1-Cl-M2 / ° (*cis*)	75.70	78.80
ϕ / °	124.6	122.8
γ / °	122.27	131.1

With a view to obtain the single bimetallic Cu complex, following the "direct" synthesis approach (discussed in paragraph 3.3.1), one should keep in mind that if, on one side, the tendency to encapsulate anions is higher for the Cu-series in comparison to the Ni-counterpart,[191] the source of Cl⁻ in this study is mainly ascribable to the unreacted CuCl₂ starting material, not quantitatively reacted with AgPF₆. Either a little excess of CuCl₂ in reaction reported in **Scheme 3.4**, or the employment of impure AgPF₆ could have been the source for the presence of free Cl⁻ ions in the reaction mixture, which have led to the formation of **[(Cu₂L^{Et})₂Cl] (PF₆)₃**. Hence, if the same reaction, with exact stoichiometric amounts of extremely pure reagents (CuCl₂, AgPF₆ and Cs₂CO₃) will be conduct again, it is likely that the single, crisp-shaped **Cu₂L^{Et} (PF₆)₂** will be obtained in high purity, applying the same isolation procedure employed for **Cu₂L^{Me} (PF₆)₂**.

3.4 REACTIVITY TOWARDS CO$_2$ REDUCTION – ELECTROCHEMICAL CHARACTERIZATION AND CATALYSIS

3.4.1 Electrochemical characterization of Ni$_2$L^R (PF$_6$)$_2$ (R= Me, Et, Pr)

As discussed in Paragraph 1.5.1, a metal complex, in order to be an efficient catalyst for CO$_2$ electroreduction, must fulfil some electrochemical requirement. The velocity of the ET with the electrode surface, the reversibility of the redox processes and the value of reduction potential of the catalyst (E^0_{cat}) are crucial (**Figure 1.23**). Before testing the ability of the Ni complexes to act as homogeneous electrocatalyst for CO$_2$RR, a detailed electrochemical study was performed on the pure complexes. Acetonitrile and ^{n}Bu$_4$N (PF$_6$)$_2$ (TBAPF$_6$, 0.1 M) were chosen as solvent and supporting electrolyte because of the high solubility of the three Ni complexes in MeCN and the broad potential window of the solvent. The PF$_6$ version of TBA was used to avoid unwanted anion scrambling reactions which can change the properties of the measured complexes (*e.g.* solubility, redox potential). Concerning the choice of the working electrode (WE) and the counter electrode (CE), glassy carbon electrodes (3 mm diameter) were employed because of their relative chemical inertness in a broad potential window. The pseudo-reference electrode (RE) was the common AgNO$_3$/Ag electrode. All potentials are reported *vs.* the Fc$^+$/Fc^0 (ferrocenium/ferrocene) couple. If not otherwise specified, the CVs are acquired with a scan rate of 100 mV s^{-1}, with a metal complex concentration of 1.0 mM.

The cyclic voltammogram of **Ni$_2$L^{Me} (PF$_6$)$_2$** is shown in **Figure 3.17**. The complex, as opposed to **Cu$_2$L^{Me} (PF$_6$)$_2$**, is active only in the cathodic region, with two irreversible reductions observed at -2.41 V and -2.57 V. Scanning towards the anodic region, with potential as high as 1.0 V, no oxidation event ascribable to the Ni-complex was detected. The potential at which the two reduction events occur is significantly negatively shifted in comparison to the monometallic NHC-Ni complexes discussed in the Introduction. In particular, the macrocyclic monometallic **Ni15** and **Ni16** complexes, studied by *Jurss and coworkers*, possess a reversible first reduction event at -1.36 V, followed by another reversible couple at $E_{1/2}$ = -1.85 V,[187] whereas the acyclic, monometallic N^C^C^N coordinated **Ni6** shows an irreversible cathodic peak at -0.84 V and a reversible one, at E_p^c= -1.70 V.[182] Those potentials were associated to the Ni^{II}/Ni^I redox couple. When the redox properties of **Ni$_2$L^{Me} (PF$_6$)$_2$** are compared to reported pyrazole-bridged bimetallic Ni complexes (**Ni$_2$2, Ni$_2$7**), only slightly less cathodic redox features are observed. The Siamese-Twin Porphyrins Bisnickel compound, introduced by *Meyer and coworkers* (**Ni$_2$2, Figure 1.12**),[76] shows a reversible reduction at $E_{1/2}$ = -1.79 V, followed by an irreversible redox event at -2.10 V. Recently, the group of *Meyer* introduced a pyrazolate-linked bimetallic Ni complex (**Ni$_2$7**), characterized by one pseudo-reversible reduction at -2.30 V and one additional irreversible feature at -2.75 V in THF.
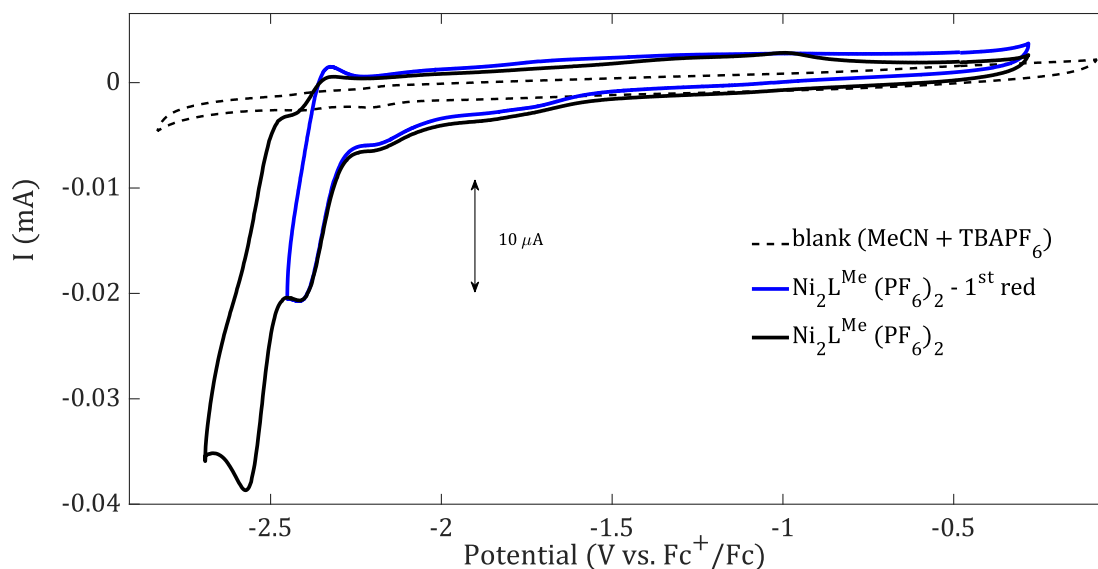
Figure 3.17 | Cyclic voltammetry of **Ni₂Lᴹᵉ (PF₆)₂** in a range of -0.3 V to -2.7 V, scan rate: 100 mV s⁻¹, solvent: MeCN (+ TBAPF₆ 0.1 M).

The shape of its CV, in which the redox features are associated to the metal-centered reductions, is similar to **Ni₂Lᴹᵉ (PF₆)₂**, even though **Ni₂7** doesn't possess NHC moieties, which were replaced by N-Aryl substituted β-diketiminato (nacnac) ligands.[206] This comparison brings even more evidence of the redox-inactivity of the imidazolylidenes moieties, when employed as NHC ligands in a metal complex.[130, 207]

Ni₂7
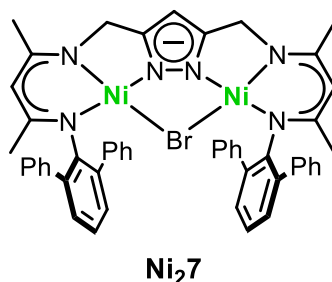
Figure 3.18 | Ni-nacnac complex reported by *Meyer et al.*, active toward selective CH activation.[208]

To further explore the electrochemical behaviour of **Ni₂Lᴹᵉ (PF₆)₂**, the first reduction peak, centered at E_p^c (1), has been isolated (blue line), since electrochemical processes promoted at lower potentials could affect the reversibility of the first reduction. The limited increase in reversibility suggests the presence of a coupled chemical reaction following the electrochemical step, which is also in part reflected by the high peak-to-peak separation of the reduction event at -2.41 (97 mV). This value exceeds the one expected for an electrochemically reversbile one-electron redox couple (59 mV), but it can be related to non-optimal experimental conditions, such as not polished electrode surfaces, or relative areas betwenn WE and CE.[209] To get more insights on the electrochemical reversibility of the two observed redox features, scan rate-dependant CVs of the first

reduction (**Figure 7.15**), and of the whole potential window (**Figure 7.14**) were acquired. When increasing the scan rate from 50 mV s^{-1} to 500 mV s^{-1}, the redox event at E_p^c (2)= -2.57 V remained irreversible, whereas the first reduction, E_p^c (1)= -2.41 V, showed an increased reversibility. Despite the net growth of anodic current at -0.94 V may lead to think of a coupled oxidation event, electrodeposited species could have played a role in the increase of i_p^a at that potential. As expected, the peak position of E_p^c (2) shifts towards more negative potentials when the scan rate is increased (45 mV from 50 to 500 mV s^{-1}), further suggesting competitve chemical reactions, which most likely are responsible for the absence of electrochemical reversibility. The peak-to-peak separation (ΔE) of the first reduction event is decreasing with higer scan rates: from 97 of 100 mV s^{-1}, to 80 mV s^{-1}. With these data in hands, it is possible to affirm that the coupled chemical reactions, which are competitive with the electrochemical time scale, mainly affect the mono-reduced species, whereas the second reduction showed no reversibility (neither scarce), making any interpretation difficult.

As already discussed in the Paragraph 3.3.1, electrochemical data can be employed to investigate the electronic communication between the two Ni-centres. In fact, the pyrazolate moiety has already shown the ability to promote the electronic coupling between two ligated metal centres.[86],[202] On this basis, it is reasonable to assume that the two redox features observed in **Ni$_2$L^{Me} (PF$_6$)$_2$** describes two subsequent one-electron reductions of the metal centres, eventually forming a Ni^I/Ni^I species. If the two Ni centres would have been electrochemical independent, the CV should show one two-electron reduction, such as in the Ni$_2$(biscyclam)$^{4+}$ (**Ni$_2$5**) of *Sauvage*,[157] and in the series of structural-related bis(polyazamacrocyclic) nickel complexes introduced by *Tsymball* and coworkers.[158]

The difference between the two peak potentials, E_p^c (1) - E_p^c (2), is 159 mV, lower than **Cu$_2$L^{Me} (PF$_6$)$_2$** (288 mV) and the Ru−bis(NHC) complex introduced by *Kühn et. al.* (380mV),[86] suggesting a scarce electronic coupling between the Ni-centres. A precise evaluation of the comproportionation constant (K_C) has not been performed, since the waves didn't show full reversibility.[203] Furthermore, in absence of SEC characterizations, it was not possible to estimate the electronic coupling matrix H_{ab}, necessary to classify the compound in one of the three Robin and Day's classes.

When the alkyl spacer between the imidazolylidene moieties is increased of one carbon atom as in **Ni$_2$L^{Et} (PF$_6$)$_2$**, the reversibility of the first reduction peak is slightly increased. The ethylene-bridged Ni-complex is characterized by one quasi-reversible reduction event at -2.37 V, followed by a subsequent irreversible reduction at -2.58 V. When the first reduction peak is isolated (blue line, **Figure 3.19**), its reversibility does not increase, but the peak-to-peak separation decreases from 141 mV (black trace) to 105 mV (blue line). By increasing the scan rate, a net increase of reversibility is observed for the first reduction peak, whereas the most cathodic one remains irreversible.
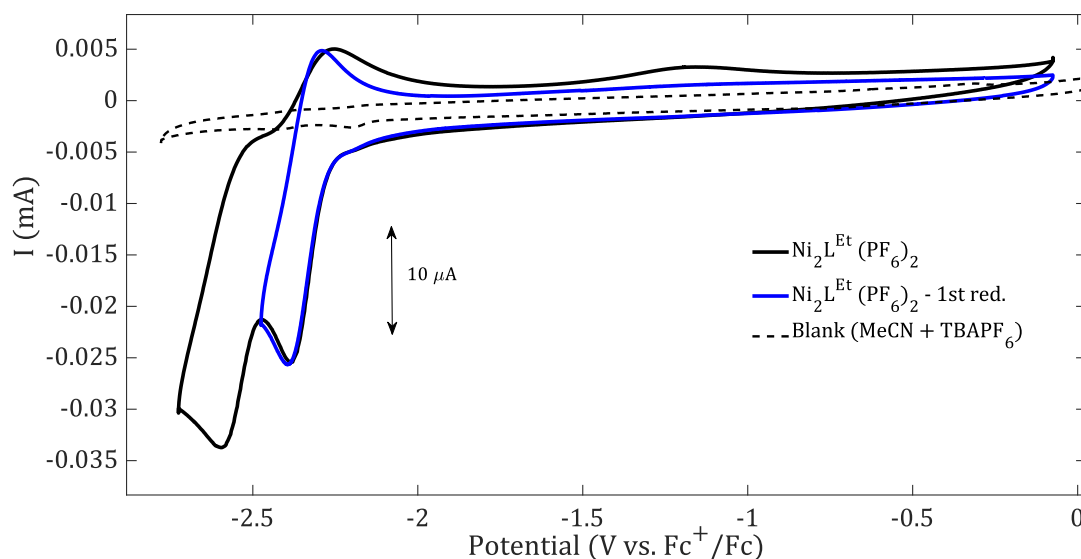
Figure 3.19 | Cyclic voltammetry of **Ni₂L^Et (PF₆)₂** in a range of -0.3 V to -2.7 V, scan rate: 100 mV s⁻¹, solvent: MeCN (+ TBAPF₆ 0.1 M), GC disk as WE.

As for the methylene-bridged congener, E_p^c (2) shifts towards a more negavite potential when the scan rate is increased (**Figure 7.21**), suggesting coupled chemical reactions which limit the reversibility of the electrchemical steps.As expected, when the CVs aquired with scan rate of 10 and 50 mV s⁻¹ (**Figure 7.22**), the reversibility of the first event, at -2.37 V is completely lost, therefore the two subsequent reduction events are hardly detectable. This phenomenon leads to an uncommon response in the peak current (i_p) - $v^{1/2}$ plot (**Figure 7.23**). In fact, at smaller scan rates (v< 200mV s⁻¹), the two linear fits are superimposable, whereas they start to drift as soon as i_p^c (1) and i_p^c (2) becomes well resolved, and the reversibility of the first reduction slightly increases.

The current response of the coupled oxidation to the first reduction event with increasing scan rate is linear, even though its slope is smaller than the reductive processes. The Randles-Sevcik equation (eq. 8), valid for electrochemically reversible processes, states that a freely diffusing species in solution is characterized by a linear relationship between those two parameters and that deviations could be related either to electrochemical quasi-reversibility, or to surface-adsorbed species. The latter scenario, however, cannot be completely excluded since the peak-to-peak separation of the first reduction event is not shifting with increasing the scan rate and it lies between 170-180 mV, suggesting sluggish ET and, arguably, an overlap of two redox events.[209] A further prove of the scarce degree of reversibility arises from the observation of the behaviour of the reductive peak potentials upon increase of the scan rate. If, on one side, E_p^c (1) is cathodically shifted only of 23 mV from 50 mV s⁻¹ to 2 V s⁻¹, E_p^c (2) is varying by a 73 mV with the same scan rate variation. In the case of **Ni₂L^Et (PF₆)₂**, the difference between E_p^c (1) and E_p^c (2), a parameter that is related to electronic coupling between the two metals centres, is 211 mV. Slightly more separated cathodic peak suggests a higher electronic communication between the two Ni-atoms, in comparison to **Ni₂L^Me (PF₆)₂**.
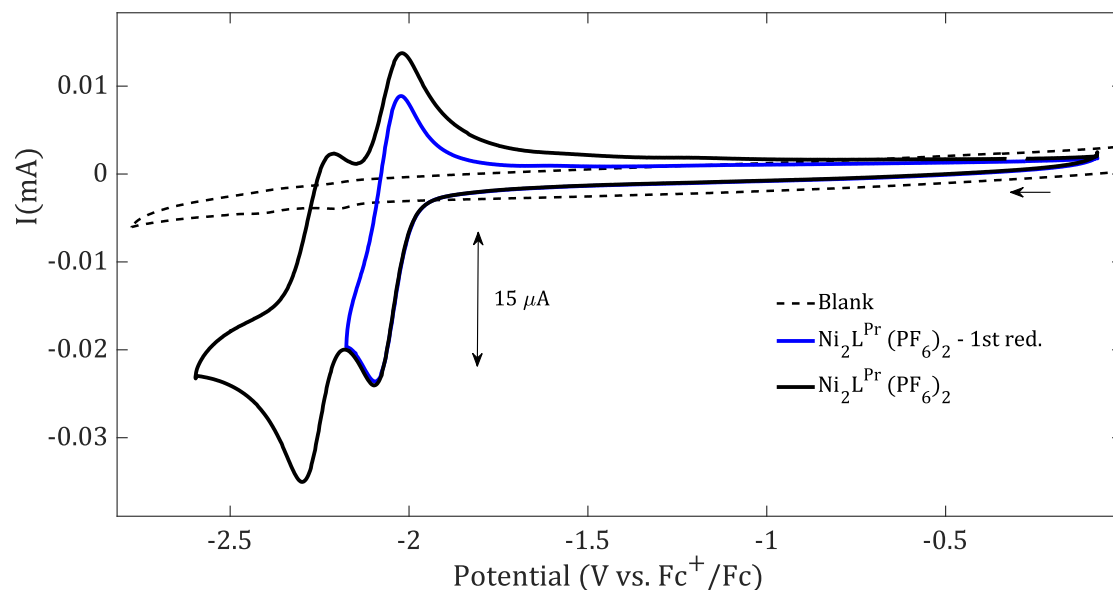
Figure 3.20 | Cyclic voltammetry of **Ni₂Lᴾʳ (PF₆)₂** in a range of 0 V to -2.55 V, scan rate: 100 mV s⁻¹, solvent: MeCN (+ TBAPF₆ 0.1 M), GC disk as WE.

An increased electrochemical reversibility was observed for **Ni₂Lᴾʳ (PF₆)₂**. The voltammetric response for the propylene-bridged Ni complex shows two quasi-reversible oxidation/reduction processes in the potential range between 0 and -2.6 V (**Figure 3.20**). The first aspect to consider is that the two reduction processes in **Ni₂Lᴾʳ(PF₆)₂**, namely $E_p{}^c$ (1) at -2.10 V and $E_p{}^c$ (2) at -2.30 V, occur at less negative potentials compared with the other binuclear Ni-complexes, as the direct comparison reported in **Figure 3.21** clearly shows.

In addition, precious information regarding the reversibility can be extrapolated by observing the electrochemical behaviour depending on the scan rate (**Figure 7.26**). Firstly, in contrast to the ethylene-bridged complex, **Ni₂Lᴾʳ (PF₆)₂** shows a perfect linear trend of both reduction and oxidation peak currents i_p vs $v^{1/2}$ (**Figure 7.29**), suggesting free diffusion in solution.

Surprisingly, if, for the second reduction event the peak potential, $E_p{}^c$ (2), is significantly shifted with increasing scan rates (53 mV more negative from 50 mV s⁻¹ to 1 V s⁻¹), the position of $E_p{}^c$ (1) is less affected by higher scan rates. Scan rate-independent peak potentials are typical of reversible electrochemical processes, which, however, should also be corroborated by scan rate-independent peak-to-peak separation (ΔE) of the same redox feature (59 mV) and a $i_p{}^c$/ $i_p{}^a$ ratio equal to 1.[189] On this basis, it is possible to conclusively affirm that the second redox processes that characterize **Ni₂Lᴾʳ (PF₆)₂**, is not fully reversible, since, upon scan rate increase, ΔE also increases, from 58 mV with the slower scan rate, to 106 mV with the higher one.

As far the electronic communication between the two metal centres is concerned, the difference between the subsequent reduction events is 200 mV, and this value is in the

same order of magnitude of that found in the ethylene-bridged complex. This suggests that the further increase of the alkylene bridge does not lead to an increase of the electronic coupling between the two Ni-centres, as well as of the intermetallic distance (**Table 3.1**). There are two major contributions to electronic coupling between two metals centres: direct through-space coupling (in systems with a short metal-to-metal distance) and ligand-mediated electronic communications.[203],[86] Of course, these factors are not always independent to each other, and they can simultaneously contribute to intermetallic coupling. The trend in the intermetallic distance, which increases from **Ni₂L^Me (PF₆)₂** to **Ni₂L^Pr (PF₆)₂**, (from 3.600 Å to 3.654 Å), would not explain by itself an increase of the electronic coupling matrix H_{ab} and, hence, of electronic communications between the two metals. A second, important, consideration concerns the overall geometry of the complexes. Despite the squeezing of the cavity (expressed by the **φ**-value) is not affected by the larger alkyl group of **Ni₂L^Pr (PF₆)₂**, the "bending" of the pyrazole moieties, given by the angle γ, is significantly increased from **Ni₂L^Me (PF₆)₂**, to **Ni₂L^Et (PF₆)₂** and **Ni₂L^Pr (PF₆)₂** (from 143.7°, 118.1° and 114.0°; **Table 3.1** and **Figure 7.1**). This structural peculiarity may be related to a more pronounced delocalisation of electron density between the two metals, as well as to a more favoured overlap of the d_{z^2}, d_{xz} and d_{yz} orbitals of the metal centres with the π-systems of the pyrazole moieties, facilitating the electronic coupling between the two Ni-ions (see Appendix, **Figure 7.7** and **Figure 7.8**).

Well-defined redox waves for the propylene-bridged complex also allowed the estimation of the comproportionation constant K_C from electrochemical data, following well-known approaches.[210] The comproportionation constant, calculated from eq. 7 , is a measure of the thermodynamic stability of the mixed valence (MV) state (Ni^II,Ni^I). In fact, in bimetallic systems that are not electronically communicating ($H_{ab} \sim 0$), the following equilibrium could be established, in which the charge introduced by, *e.g.,* electrochemical reduction, is localised in one defined metal ion.

$$[Ni^{II},Ni^{II}] + [Ni^{I},Ni^{I}] \quad \overset{K_C}{\rightleftharpoons} \quad 2\ [Ni^{II},Ni^{I}]$$
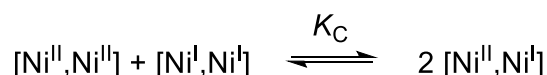
Increasing the communication ($H_{ab} \geq \lambda/2$), the charge starts to be delocalized in both metal centres, with the fully delocalization observed for the class III compounds (Robin and Day's system).[201] K_C is indeed a measure of the extension of the electronic coupling and, hence, of H_{ab}.[210]

$$K_C = 10^{\Delta E_p/59mV} \;\rightarrow\; K_C = 10^{200mV/59mV} = 2.1 \cdot 10^3 \;\rightarrow\; log_{K_c} = 3.32 \qquad\qquad \text{eq. 7}$$

Since the comproportionation constant is a measure of a chemical equilibrium, it is reasonable to extrapolate this parameter from reversible redox waves, and, hence, only for **Ni₂L^Pr (PF₆)₂**. The resulting logarithmic value, 3.32, is smaller than other pyrazolate-bridged complexes, such as the Ru–bis(NHC) complex (**Ru₂1**) introduced by *Kühn and coworkers* ($log_{K_c} = 4.0 - 6.4$),[86] or the bimetallic Ni^III,Ni^II species bearing a Siamese Twin porphyrin as ligand platform (**Ni₂2**, $log_{K_c} = 7.0$),[75] but high enough to assert that

the MV Ni^I,Ni^{II} species (obtained with electrochemical reduction at -2.10 V) is stable enough to be potentially isolated and spectroscopically investigated.

In **Figure 3.21** the direct comparison of the electrochemical behaviour of the three Ni-complexes is presented. The most striking evidence is the increase of reversibility and the less negative potential required to add electrons into **Ni_2L^{Pr} (PF$_6$)$_2$**. The only difference between the presented complexes is the alkylene spacer, that, as seen before, imparts distortions and structural changes in the overall geometry of the bowl-shaped compounds. Notably, the influence of structural and geometric parameters in the electrochemical behaviour of one metal complex has already been reported for the series of analogous monometallic Ni-NHC complexes (**Ni6-Ni8, Figure 1.34**), introduced by *Chang et al.*[182] In particular, they reported how the flexibility of the ligand platform is crucial to render the metal centre more prone to exchange electrons with reversible redox processes.

Since, going from **Ni_2L^R (PF$_6$)$_2$** to the 1-e$^-$ (and 2-e$^-$) reduced counterparts, the electronic configuration, as well as the spin multiplicity of the complexes changes, a less rigid and "distorted" SP coordination motif of the metal centre could be beneficial for the redox properties.
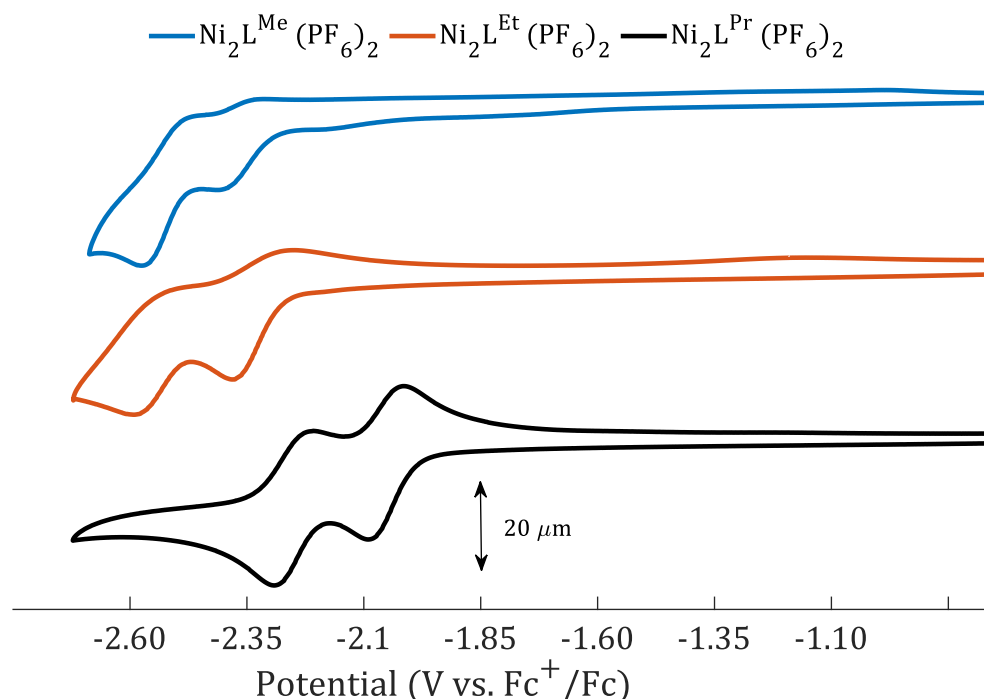
Figure 3.21 | Comparison between the CVs of the three Ni-complexes. Whereas **$Ni_2L^{Me,Et}$(PF$_6$)$_2$** possess irreversible reduction peaks, **Ni_2L^{Pr} (PF$_6$)$_2$** is characterized by reversible and positively-shifted redox features.

As reported in **Table 3.5**, the deviation from the ideal SP geometry is more pronounced in the propylene-bridged complex, with the τ_4' value that is significantly higher than in the other two complexes ($\tau_4' = 0$ in the SP geometry and $\tau_4' = 1$ in the T$_d$ case).[211] This observation leads strong evidence that the geometrical distortion dictated by the propylene-bridge strongly affects the coordination geometry of the Ni centres, enhancing the flexibility of the whole ligand which, in turns, results in an higher stability degree of the reduced species.

In trying to explain the different electrochemical responses of the three complexes, many other considerations can be done. One of the most meaningful concerns the width of the bimetallic cavity. As **Table 3.5** and **Figure 7.2** indicate, **Ni₂L^{Pr} (PF₆)₂** possesses the most squeezed cavity, as opposed to **Ni₂L^{Me} (PF₆)₂**, where the H$_{endo}$ protons are 6.578 Å apart.[212] Consequently, a wider cavity potentially exposes the bimetallic core to the external environment, favouring side reactions and/or decompositions that limit the electrochemical reversibility. Wider cavity, that, as expected, is also responsible of the very little distortion from the ideal SP geometry shown by **Ni₂L^{Me} (PF₆)₂**.

Table 3.5 | Selected geometrical parameters of **Ni₂L^{R} (PF₆)₂**, (**R = Me, Et, Pr**) indicating the geometrical differences between the complexes. For the "squeezing" angle ϕ and for γ, refer to **Figure 7.1**. For the τ_4' parameter, to the reference [211]. The bimetallic pocket in **Ni₂L^{Pr} (PF₆)₂** possesses asymmetrical coordination geometries, as different values of τ_4' suggest.

Complex	Ni₂L^{Me} (PF₆)₂	Ni₂L^{Et} (PF₆)₂	Ni₂L^{Pr} (PF₆)₂
γ / °	143.7	118.1	114.0
ϕ / °	123.3	123.4	122.6
H$_{endo}$-H$_{endo}$ (Å)	6.578	5.036	4.348
N$_{py}$-Ni-C$_{NHC}$ − N$_{py}$'-Ni-C$_{NHC}$' /°	3.33	6.78	10.87/14.43
τ_4' / °	**0.070**	**0.072**	**0.135/0.104**

Considered the limited electrochemical reversibility and the possible formation of electrodeposited species at very cathodic potentials, more in-depth analysis has been performed on the solution properties of the three Ni-complexes. Therefore, from the scan-rate dependance of the reduction events, the estimated diffusion coefficients of **Ni₂L^{R} (PF₆)₂** were calculated using the Randles-Sevcik equation:

$$i_p = 0.4463 n F A C^0 \left(\frac{nFvD_0}{RT}\right)^{1/2} \qquad eq.\,8$$

Where *n* is the number of electrons transferred in the redox event, A (cm^2) is the electrode surface area, D_0 is the diffusion coefficient of the oxidized analyte (cm^2 s^{-1}) and C^0 (mol cm^{-3}) is the bulk concentration of the analyte.

In almost all cases, CVs at different scan rates show the anodic and cathodic peak currents varying linearly with the square root of the scan rate from 0.10 to 1.0 V s^{-1} (**Figure 7.16**, **Figure 7.23** and **Figure 7.29**), consistent with diffusion-controlled redox processes.[189] The calculated D_0 coefficients are reported in **Table 3.6**, and they are in the same order of magnitude of the spectroscopically (DOSY) determined for **Ni$_2$L^{Et} (PF$_6$)$_2$**, which is $1.0 \cdot 10^{-5}$ cm^2 s^{-1}.[190]

Table 3.6 | Electrochemical data from the CVs of **Ni$_2$L^R (PF$_6$)$_2$** (R=Me, Et, Pr) reported in **Figure 3.21**. E_p^c is the reductive peak potential, for **Ni$_2$L^{Pr} (PF$_6$)$_2$** also the ΔE_p is reported in brackets, because of the pseudo-reversibility. $\Delta[E_p^c (1) - E_p^c (2)]$ is the difference between the two subsequent reductions. D_0 (cm^2 s^{-1}) is the diffusion coefficient of the oxidized form of the Ni-complexes calculated by the linear fit from the Randle-Sevcik equation.

Complex	$E_p^c (1)$ (V)	$E_p^c (2)$ (V)	$\Delta[E_p^c (1) - E_p^c (2)]$ (mV)	D_0 (cm^2 s^{-1})
Ni$_2$L^{Me} (PF$_6$)$_2$	-2.414	-2.573	159	$3.174 \cdot 10^{-5}$
Ni$_2$L^{Et} (PF$_6$)$_2$	-2.370	-2.581	211	$2.669 \cdot 10^{-5}$
Ni$_2$L^{Pr} (PF$_6$)$_2$	-2.096 (77)	-2.296 (85)	200	$1.219 \cdot 10^{-5}$

Furthermore, in order to resolve potential overlapping peaks in the CV, Square Wave Voltammetry (SWV) was employed to get more insights on the electrochemical behaviour of **Ni$_2$L^R (PF$_6$)$_2$** (R= Me, Et, Pr). No overlapping peaks were detected in **Figure 3.22**, where the higher reversibility of the propylene-bridged ligand is once more highlighted.
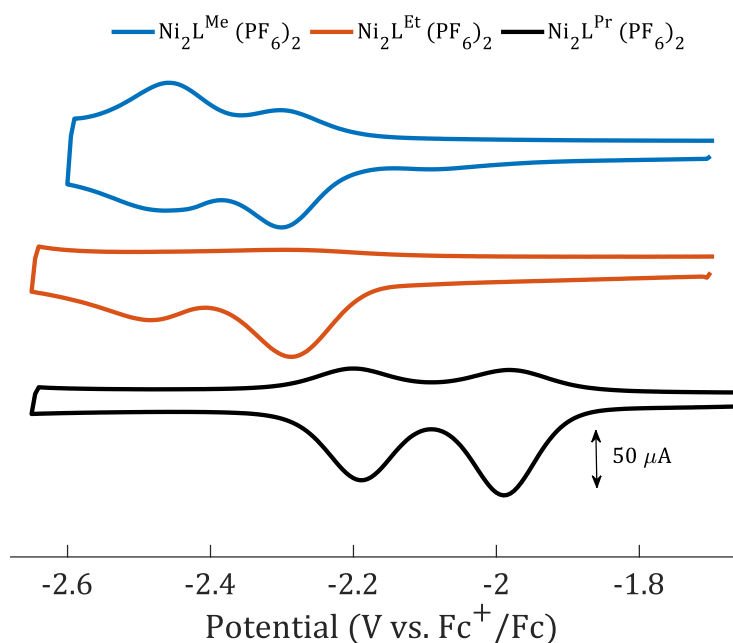
Figure 3.22 | SWV of the three Ni-complexes in reduction and oxidation. E_{step}: 5 mV; E_{ampl}: 20 mV, f= 25 Hz.

To acquire greater knowledge on the nature of the mixed valence species (MV), as well as to investigate the electronic distribution in the reduced species, electrochemical data were combined with computational studies. DFT calculations were performed to the mono-reduced **[Ni$_2$L^R]$^{1+}$**, as well as to the doubly reduced **[Ni$_2$L^R]^0**. The employed functional and basis set were uωB97x-D/6-31(+)G, and the calculations were run in solution, using the SMD approach (solvent: acetonitrile, dielectric constant, ε = 35.688).[213]

In all the three Ni-complexes the first reduction is computed to be mainly metal-based, as the plot of the spin population for the one-electron reduced species indicates (**Figure 7.9**). The reduced **[Ni$_2$L^R]$^{1+}$** compounds are computed to possess a doublet state, with the unpaired electron occupying one orbital that results from the linear combination of metal-based d-orbitals with the π-system of the pyrazoles and of the imidazolyidenes (**Figure 7.10**). No other spin states are computationally accessible. Therefore, the mixed valence species are formally written as ^{2}[Ni^{I}Ni^{II}(L^{2-})]$^+$. The atomic charges, deriving from the atomic polar tensors (APT),[214] are consistent to the reduction of one of the two metal centres (**Table 3.7**). When the second electron is added to the reduced Ni-complexes, to form the overall neutral **[Ni$_2$L^R]^0** species, two spin multiplicity are computationally conceivable. They are singlet (if the same SOMO accepts the additional electron, to form a ^{1}[Ni^{II}Ni^0(L^{2-})]^0 species) or if it adds to another orbital and is antiferromagnetically coupled with other electron, and triplet (if the added electron goes to another orbital, with the same spin than the unpaired one, forming ^{3}[Ni^{I}Ni^I(L^{2-})]^0 species). It turns out that the triplet state is 368 kJ mol^{-1} (for **^{3}[Ni$_2$L^{Me}]^0**) and 124 kJ mol^{-1} (for **^{3}[Ni$_2$L^{Pr}]^0**) more stable than the singlet state, corroborating the hypothesis that the two subsequent reductions yield a Ni^I/Ni^I species. Plots of the spin density, reported in **Figure 7.11**, show the population of d-metal orbitals for both Ni-centres.

To provide a clear explanation of the previous discussion, related to ligand flexibility and structural change upon reductions, the τ'_4 parameters for each calculated intermediate are reported in **Table 3.7**. Interestingly, during the first reduction, which is associated to a spin change of the whole complex, the geometry of the first coordination sphere of the two Ni-ions is asymmetrically altered. In fact, the computed relative change in the value of τ'_4 represents the distortion of the coordinated ligands following the change in the electronic configuration of that defined Ni-centre. The extension of this variation, which is more pronounced for **Ni$_2$L^{Pr} (PF$_6$)$_2$**, is related to the flexibility of the ligand scaffold. The solution-state structure of the reduced **[Ni$_2$L^R]^0** complexes, possessing the Ni-ions in the d^9 electronic configuration, significantly differs from the ideal SP geometry. In this context, the remarkably high τ'_4 value for the fully reduced propylene-bridged complex (0.416), suggests a marked distortion towards the tetrahedral coordination.

"[Ni$_2$L]$^{2+}$"		"[Ni$_2$L]$^{+}$"		"[Ni$_2$L]^{0}"
^{1}[Ni^{II}Ni^{II}(L^{2-})]$^{2+}$	$\xrightarrow[E_p^c(1)]{+ 1\ e^-}$	^{2}[Ni^{II}Ni^{I}(L^{2-})]$^{+}$	$\xrightarrow[E_p^c(2)]{+ 1\ e^-}$	^{3}[Ni^{I}Ni^{I}(L^{2-})]^{0}
		^{2}[Ni^{II}Ni^{II}(L$^{\bullet-}$)]$^{+}$		^{1}[Ni^{II}Ni^{0}(L^{2-})]^{0}
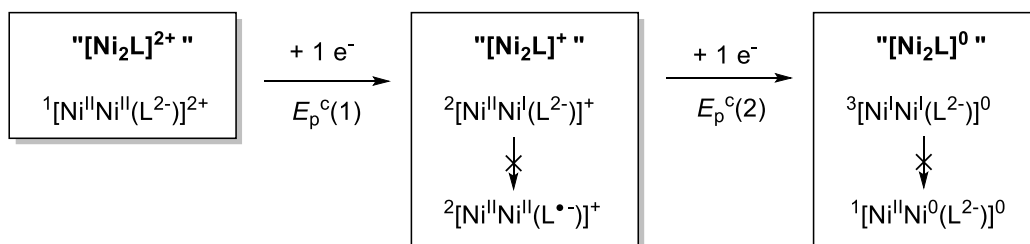
Having a closer look to the electronic distribution and to the MOs characterizing the reduced **[Ni$_2$L^R]^0** complexes (**Figure 7.12**), one can realise that electron-rich systems with a d_{z^2}-based nucleophile could provide a promising platform for activating CO_2 as an electrophile in a multi-electron, multi-proton fashion.[182]

Table 3.7 | Atomic charges deriving from APT for the 1-e$^-$ reduced and 2-e$^-$ reduced species and geometrical parameter τ_4'. [211]

	R= Me			R= Et			R= Pr		
	Ni1	Ni2	τ_4' / °	Ni1	Ni2	τ_4' / °	Ni1	Ni2	τ_4' / °
^{1}[Ni$_2$L^R]$^{2+}$	0.50	0.50	0.070	0.53	0.53	0.060	0.58	0.59	0.159/0.105
^{2}[Ni$_2$L^R]$^{+}$	0.55	0.05	0.070/0.082	0.58	0.12	0.040/0.145	0.62	0.10	0.263/0.095
^{1}[Ni$_2$L^R]^{0}	0.50	0.72	-	-	-	-	0.60	1.10	-
^{3}[Ni$_2$L^R]^{0}	0.10	0.10	0.117	0.20	0.20	0.138	0.26	0.06	0.416/ -

3.4.2 CO₂ electroreduction studies

Electrocatalytic CO_2 reduction with the three nickel complexes was then investigated by CV in CO_2-saturated dry MeCN solutions. The 5 mL electrolyte solution was purged with pure CO_2 for 10-15 min, to realise a saturation concentration of 0.23 M. Whilst in case of of **Ni₂L^R (PF₆)₂** (R= Me, Et), no net catalytic peak was detected in the scanned potential window, **Ni₂L^{Pr} (PF₆)₂** shows a defined current increased over the first redox event, at $E_{p,cat}$ = -2.05 V (**Figure 3.23**). However, the intensity of the irreversible catalytic peak decreases upon repeated scans, suggesting competing side phenomena such as electrode deposition, substrate depletion or catalyst degradation. Notably, these drawbacks seem to be markedly reduced when the scan is stopped at -2.20 V (**Figure 7.31**), with the catalytic peak current that is stable upon several cycles ($E_{cat/2}$ = -1.97, E_{onset} = -1,87 V, $i_{p,cat}$ / i_p^0 = 2.0). Since a shift of $E_{p,cat}$ respect to E_p^c (1) was not observed, the most probable scenario is the reaction of CO_2 with the newly formed MV Ni^{II},Ni^I species, resulting in its activation in the metal-bound "bent" COO$^{\bullet-}$ radical anion. To provide an explanation of the observed reactivity, in absence of any proton source, one possible mechanism that has been reported for bimetallic systems, is the reductive disproportionation of CO_2 into CO and CO_3^{2-}.[168],[173] According to that mechanism, the reactive $CO_2^{\bullet-}$ radical, that is (η^1-C) coordinated to one electron rich metal centre, reacts with a second molecule of CO_2, forming CO and carbonate. Regrettably, no chronoamperometric analysis has been performed to elucidate the produced chemical species. The hydrogen atoms of the flexible propylene-bridge that point towards the bimetallic cavity (H$_{endo}$, **Figure 7.2**) could have a role in the stabilization of defined intermediates formed in this catalytic process. It is known, indeed, that macrocyclic complexes featuring pendant amines[215] or acidic groups[216] in close proximity to active metal active metal centre have a beneficial role in catalysis since they can establish a hydrogen bonding network which assists CO_2 bonding and promotes its transformation. Going back to the methylene- and the ethylene-bridged species, a pronounced reduction of the cathodic current is detected, that goes along with the complete loss of resolution of the two subsequent reduction events. Again, electrode deposition and irreversible chemical reactions could explain the observed reactivity.

To evaluate the ability of **Ni₂L^R (PF₆)₂** (R= Me, Et, Pr) to act as CRCs, their reactivity in presence of CO_2 and of a proton source has been investigated. The necessity of a protic environment, provided by adding defined amount of a specific proton source (H_2O, acids or alcohols) to the chosen aprotic solvent, is clarified when the key role of PCET (discussed in the introduction) is considered. PCET reactions, in fact, altering thermodynamic and kinetic of CO_2RR, provide an alternative pathway to the high energetic one-electron, one-proton reduction of CO_2.[151] The choose of the proton source is crucial, since its chemical nature, including acidity and reactivity towards the CRC, determines the selectivity of the whole CO_2RR. [137]
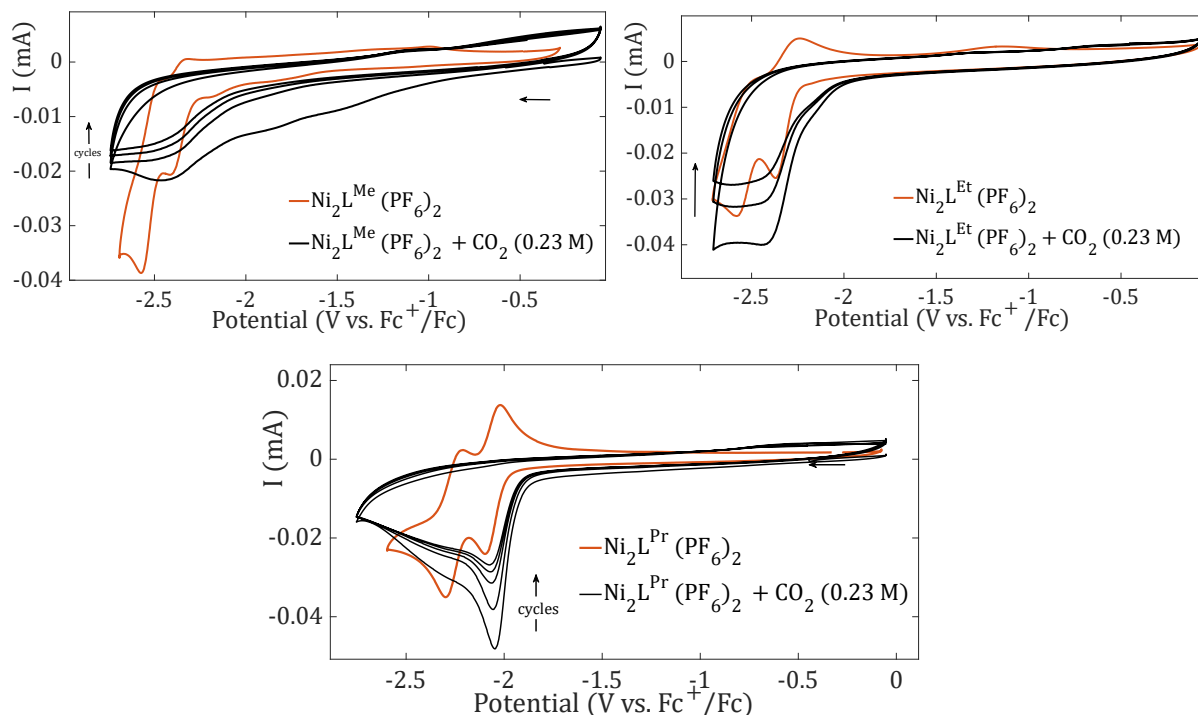
Figure 3.23 | CVs of **Ni₂Lᴿ (PF₆)₂** (R= Me, Et, Pr) at 1 mM concentrations in MeCN/0.1 M TBAPF₆ (scan rate = 100 mV s⁻¹, glassy carbon WE) under N₂ (red) and with CO₂ saturation (0.23 M, black).

Therefore, the reactivity of the three nickel complexes towards a 1 M H_2O solution in the electrolyte (MeCN + 0.1 M TBAPF₆) has been tested by CVs. The main drawback, when studying CO₂RR in presence of a proton source, is the concomitant activity of the catalyst towards hydrogen evolution reaction (HER). This process, which should be avoided, produces H_2 via metal-bound hydride intermediates, decreasing the selectivity and the efficiency of CO_2 reduction. In this context, Ni-complexes, featuring protons relays and mono/bidentate phosphine ligands (DuBois-type), as well as polypyridine donors or cyclam ligating framework, are known to effectively promote HER.[217],[218],[219]

Ni₂Lᴹᵉ (PF₆)₂ did not show marked reactivity towards water, with no catalytic peak arising in the scanned potential window (0 / -2.7 V, **Figure 7.18**). This feature suggest that H_2O can be a suitable proton source in the CO₂RR studies employing the methylene-bridged complex as a catalyst. In the case of **Ni₂Lᴱᵗ (PF₆)₂**, however, a peak-shaped response was obtained, with $E_{p,cat}$ = -2.56 V, and an onset potential of -2.23 V (**Figure 3.26**). Furthermore, two weak oxidation features are detected at E_p^a = -1.39 V and -1.14 V, whose intensity is reduced almost entirely when the cathodic scan is stopped at -2.43 V, after the first reduction peak. The presence of these anodic features, whose intensity is maintained constant upon different several cycles, is ascribable to the oxidation of chemical species produced by scanning the potential at more negative potentials (*e.g.* Ni Hydroxo intermediates). Therefore, for the ethylene-bridged complex is possible to affirm that the activity towards HER is not completely absent, even though an $i_{p,cat}$ / i_p^0 ratio of 3.4 denotes a scarce reactivity for H_2 production.
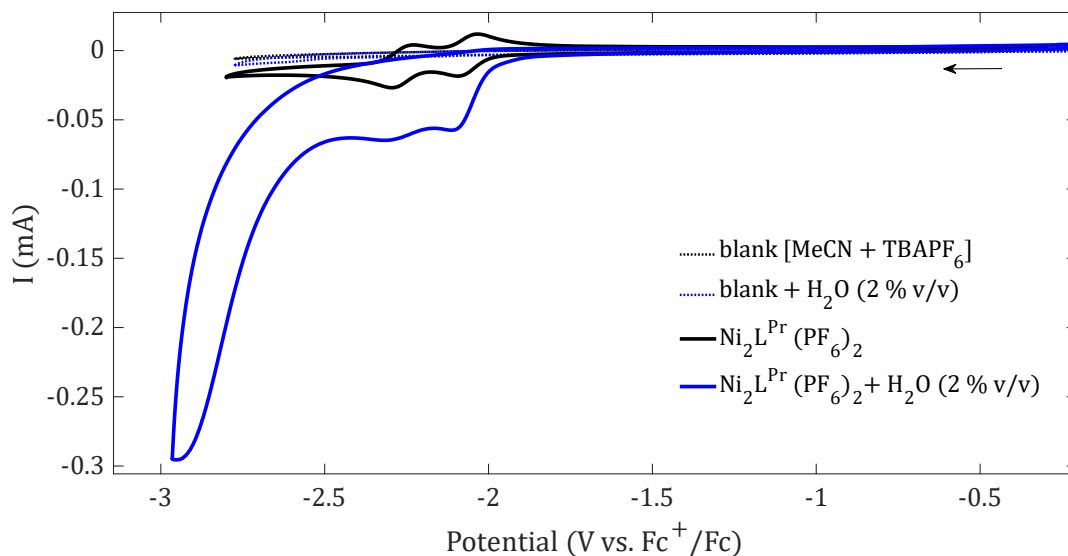
Figure 3.24 | CV of **Ni$_2$L^{Pr} (PF$_6$)$_2$** under a N$_2$ (black) or N$_2$ + 1.0 M H$_2$O (blue) atmosphere in MeCN + 0.1 M TBAPF$_6$ scanning toward cathodic potentials at 0.1 V s^{-1} with a GC disk WE.

Finally, **Ni$_2$L^{Pr} (PF$_6$)$_2$**, showed an increase of the two reduction peaks that characterize the Ni-complexes, and a sharp, peak-shaped catalytic wave $E_{cat/2}$= -2.75 V. The net increase of cathodic current is indicative of HER activity, which is maintained upon several cycles. Despite this unwanted reactivity, $E_{cat/2}$ for direct reduction of CO$_2$ with the propylene-bridged complex was -1.97 V, which is at far less negative potential respect to HER, meaning that H$_2$O can still be used as proton source for CO$_2$RR at milder potentials (<2.5 V).

At this stage, H$_2$O-promoted CO$_2$ reduction was investigated by CV by adding a small amount of milliQ H$_2$O (100 μL, conductivity <0.1 μS·cm^{-1}) to the CO$_2$-saturated solution, containing 1 mM of the Ni-complex.

In the case of **Ni$_2$L^{Me} (PF$_6$)$_2$** a strong peak-shaped catalytic curve appears at $E_{cat/2}$= -2.30 V, with onset potential of -1.60 V. This reduction peak, which is a clear hint for catalytic reactions occurring between the Ni-complex, H$_2$O and CO$_2$, is accompanied with weak oxidation peaks at -1.02 V and -0.44 V (better visible in **Figure 7.18**), whose intensity increases upon several scans. The presence of these anodic features suggests the oxidation of electrode-deposited chemical species that are formed electrochemically (or *via* competitive chemical reactions) during the cathodic scan. The fact that the catalytic peak is preceded by a pre-wave, that $i_{p,cat}$ significantly decreases upon consecutive electrochemical cycles, and that the reaction mechanism is, so far, unknown, does not enable the evaluation of catalytic parameters (such as k_{cat}, TOF, TON) from the established foot-of-the wave analysis (FOWA).[216] Furthermore, when the stability of the detected catalytic peak is considered, **Figure 7.19** shows how this wave is markedly reduced as several scans are acquired.
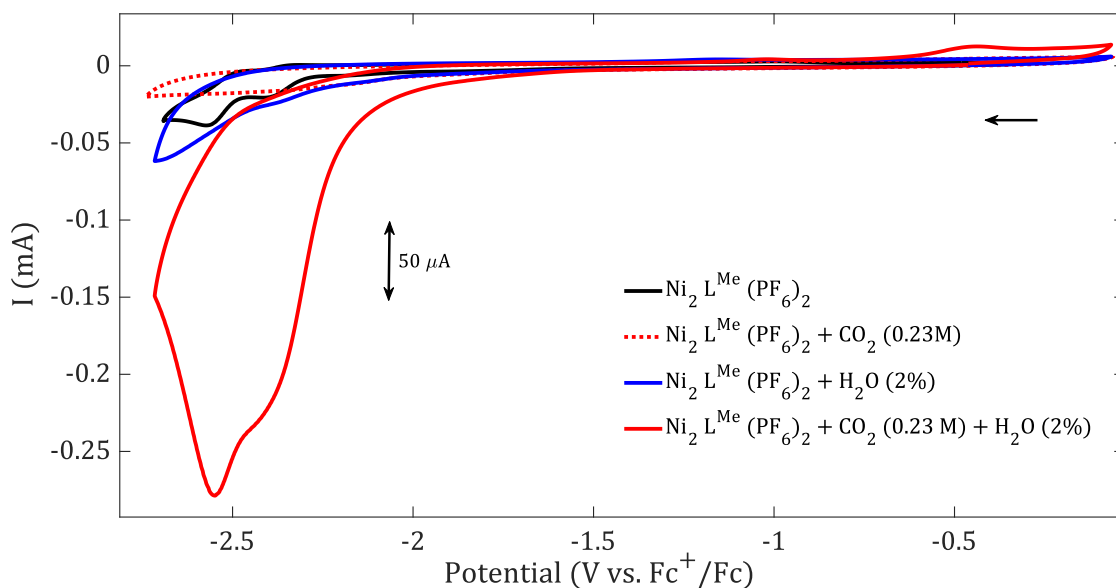
Figure 3.25 | CV of **Ni₂L^Me (PF₆)₂** under N₂ (black), CO₂ (dotted red), N₂ + 1.0 M H₂O (blue) and CO₂ + 1.0 M H₂O (red) in MeCN + 0.1 M TBAPF₆ scanning toward cathodic potentials at 0.1 V s⁻¹ with a glassy carbon disk WE.

Taking into account the scarce electrochemical reversibility that characterized **Ni₂L^Me (PF₆)₂**, and the limited reactivity that the same complex shows towards CO₂ (**Figure 3.23**), one can tentatively affirm that the observed peak-shaped behaviour is more related to side phenomena such as catalyst degradation or inhibition (which lead to electrode deposition), more than defined activity towards CO₂RR of the Ni-complex. Bulk electrolysis experiments were combined with GC-MS measurements to evaluate the efficiency of CO generation by **Ni₂L^Me (PF₆)₂**. To verify the nature of the reduction products, controlled potential electrolysis (CPE) was carried out under the same conditions as those in cyclic voltammetry and the head space of the electrochemical cell was sampled by gas chromatography.

CPE conducted at − 2.25 V for 60 min reveals a maximum current efficiency for CO production of 55.8 ± 7.3 % after 30 min, decreased then to 49.8 ± 7.1 % after 1 hour. The maximum calculated TON$_{CO}$ was 0.06. The other detected product was H₂, and the CO:H₂ ratio significantly decreases from 2:1 (30 min), to 1:4 (60 min), as the chart in **Figure 7.20** shows. The limited value of TON$_{CO}$ and the FE value higher than 100% for H₂ production (194 % after 60 min) corroborate the hypothesis that **Ni₂L^Me (PF₆)₂**, under the investigated conditions, undergoes to side phenomena, that seem to lead to the deposition of active catalytic species, moderately active towards HER. In fact, the rinse test performed with fresh electrolyte after the CPE, revealed moderate residuals signal in the CV trace, symptom of electroactive metallic species on the electrode surface. Under these conditions, the evaluation of the activity and selectivity of **Ni₂L^Me (PF₆)₂** as CRC appears everything but trivial, and it would require sophisticated solid-state technique (*e.g.,* XPS) to investigate the nature of the deposited species, as well as SEC measurement to monitor the decomposition of the starting catalyst.
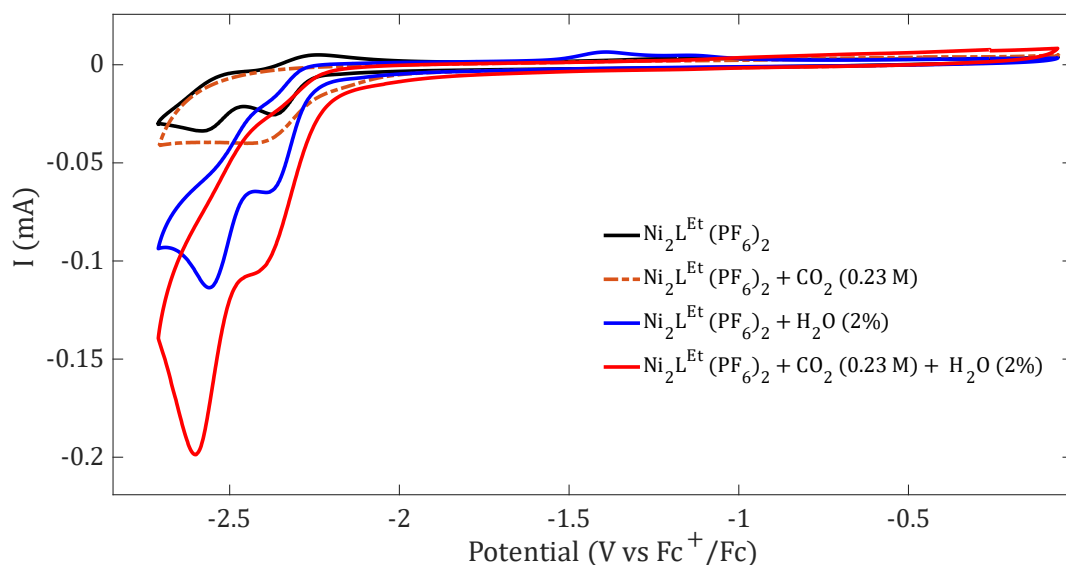
Figure 3.26 | CV of **Ni$_2$L^{Et} (PF$_6$)$_2$** under N$_2$ (black), CO$_2$ (dotted red), N$_2$ + 1.0 M H$_2$O (blue) and CO$_2$ + 1.0 M H$_2$O (red) in MeCN + 0.1 M TBAPF$_6$ scanning toward cathodic potentials at 0.1 V s^{-1} with a glassy carbon disk WE.

The ethylene-bridged complex shows a slightly different behaviour, since a reductive catalytic peak is observed at $E_{cat/2}$ = -2.38 V. This feature, which displays a pre-wave over the first reduction event of **Ni$_2$L^{Et} (PF$_6$)$_2$**, is characterized by an $i_{p,cat}$ / i_p^0 ratio of 5.9. Of note, the same complex showed activity towards HER, in presence of only H$_2$O, at the same $E_{p,cat}$ (blue trace, **Figure 3.26**), but the $i_{p,cat}$ / i_p^0 ratio of the detected H$_2$O reduction peak was only 3.4, suggesting that the activity of **Ni$_2$L^{Et} (PF$_6$)$_2$** towards CO$_2$RR is slightly higher than that for HER. The analysis of the onset potential corroborates this hypothesis, since the blue trace possesses an E_{onset} of -2.24 V, whereas the CO$_2$RR at -2.12 V.

As in the case of the methylene-bridged complex, one fundamental aspect to investigate when discussing electrocatalysis, is the stability of the metal complex upon several electrochemical scans, which reflects the robustness of the catalytic system. In **Figure 7.24** a multiscan CVs of **Ni$_2$L^{Et} (PF$_6$)$_2$** under CO$_2$-saturated conditions (+ 1 M H$_2$O) is reported, from which it can be noticed how the exchanged current decreases with consecutive scans. Even though the effect is not so pronounced as in the case of the methylene-bridged analogue, it denotes scarce electrochemical stability under the employed conditions. This is also the reason why no FOWA analysis for the catalyst's performance was performed. To shed light on the observed catalytic activity, CPE was conducted with **Ni$_2$L^{Et} (PF$_6$)$_2$** under the same conditions as those in CVs, at -2.60 V for 180 min. The evolution of the detected products is reported in **Figure 7.25**, in which an unexpected selectivity towards CO production was observed (maximum TON$_{CO}$ = 4.4 after 3 hours, CO:H$_2$ > 20). However, this chronoamperometric measurement was characterized by an intense turbidity of the solution inside the cell, accompanied by visible gas bubbling from the Freudenberg paper used as WE.
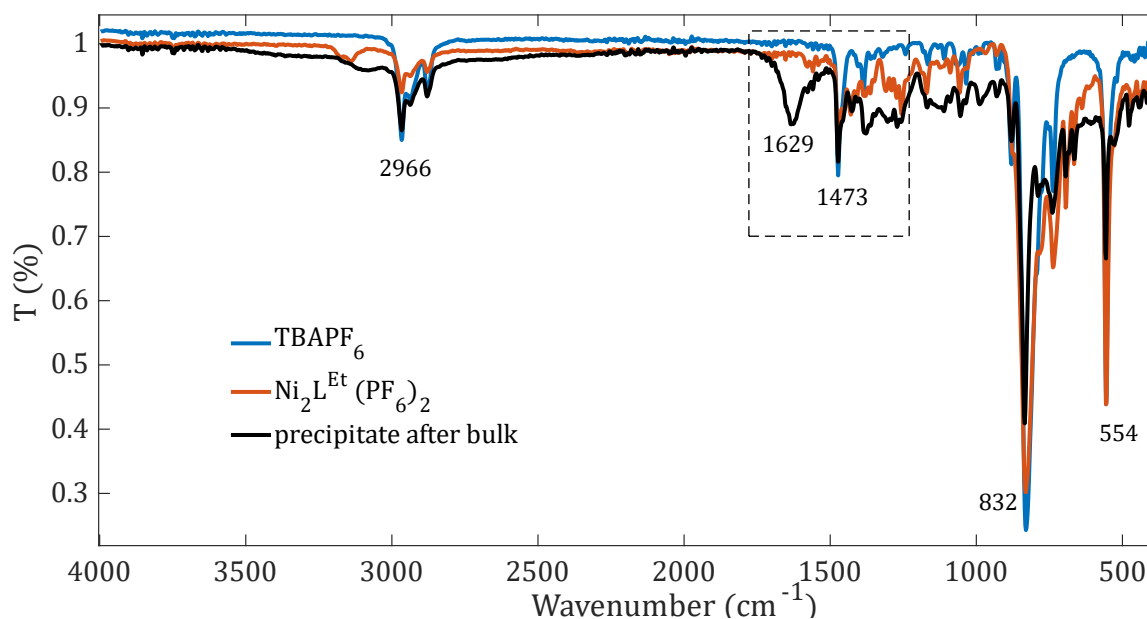
Figure 3.27 | ATR-FTIR spectra comparison between the supporting electrolyte (TBAPF$_6$, blue), **Ni$_2$L^{Et} (PF$_6$)$_2$** (red) and the precipitated obtained after CPE at -2.60 V for 180 min. The peak at 1629 cm^{-1} is indicative of a carbonyl-containing adduct.

The rinse test conducted to the WE (which was evidently covered by a yellowish layer), give positive results, with detectable residual catalytic activity. Furthermore, from the electrolyte solution, a yellowish precipitate was obtained after CPE, which has been washed, dried, and analysed with ATR-FTIR spectroscopy (**Figure 3.27**). Interestingly, the stretching vibration at 1629 cm^{-1}, present only in the spectrum of the insoluble species (and not in **Ni$_2$L^{Et} (PF$_6$)$_2$** and TBAPF$_6$), is indicative of the presence of a carbonyl species, whose nature was not fully elucidated. In fact, whereas according to Kubiak *et al.*, a Ni(II) coordinated bicarbonate species (formed by purging the solution containing the Ni-cyclam complex with CO$_2$) possesses IR activity in the 1660-1615 cm^{-1} region,[220] other authors suggest that free carbonates and hydrogencarbonates are found in the very same region ($\nu_a COO^-$).[221],[130]

Despite these considerations, it is clear how the chosen potential (-2.60 V) was probably too cathodic to protect the nickel complexes from unwanted reactions. Although the scarce reactivity of the complex towards CO$_2$ in aprotic solvents points towards the formation of a redox-inactive adduct rather than the establishment of a defined catalytic cycle (**Figure 3.23**). To minimize the deposition of electroactive species or decomposition, another CPE experiment at milder potentials could be potentially run.

Bearing in mind the electrochemical reversibility of **Ni$_2$L^{Pr} (PF$_6$)$_2$** (**Figure 3.21**), and its reactivity towards CO$_2$ in dry MeCN solution (**Figure 3.23**), the propylene-bridged complex is the most promising CRC of the series. In fact, when H$_2$O is added in 2 % (v/v) to a CO$_2$-saturated solution, an increase of reductive current is observed already over the catalytic peak of CO$_2$ reduction without proton source ($E_{p,cat}$= -2.05 V), followed by a more intense feature at $E_{cat/2}$ = -2.60 V. Nevertheless, when a multiscan CV is acquired,

a drastic reduction of the two redox events is observable from the second electrochemical cycle (**Figure 3.28**). This loss of reactivity is most likely caused by electrode deposition of chemical species originated by scanning towards negative potentials, as low as -2.8 V. As observed in **Figure 7.31**, the reactivity of the Ni-complex with CO_2 was maintained only if the scan was stopped after the catalytic peak (-2.05 V). Hence, it is reasonable to think, considered also the pronounced HER activity of **Ni_2L^{Pr} (PF$_6$)$_2$**, that simultaneous chemical (or electrochemical) reactions are competitive with the desired CO_2RR at more negative potentials. In fact, by stopping the potential at -2.6 V, the reactivity of the complex towards CO_2 (+1 M H_2O) is maintained upon several scans. Therefore, the most corroborated hypothesis is that one molecule of CO_2 binds at mild potentials to one reduced Ni(I)-centre via the electrophilic carbon atom (η^1-C coordination). Then, in presence of a proton source, a series of protonation and bonds cleavage reactions are promoted at more negative potentials, leading to the formation of the redox-inactive chemical species, which are responsible for the loss of reactivity seen in **Figure 3.28**.

The simultaneous presence of Ni Hydrides and Ni Hydroxo species, formed at potential lower than -2.7 V, cannot be discarded. The presence of small amount of H_2O, indeed, almost does not affect the intensity of the first reduction peak, whose $i_{p,cat}$ / i_p^0 ratio increases only from 1.6 to 2.1. Increasing the scan rate, instead, from 0.1 V s^{-1} to 1 V s^{-1}, has a pronounced effect on the cathodic current of that pre-peak, as **Figure 7.33** shows.
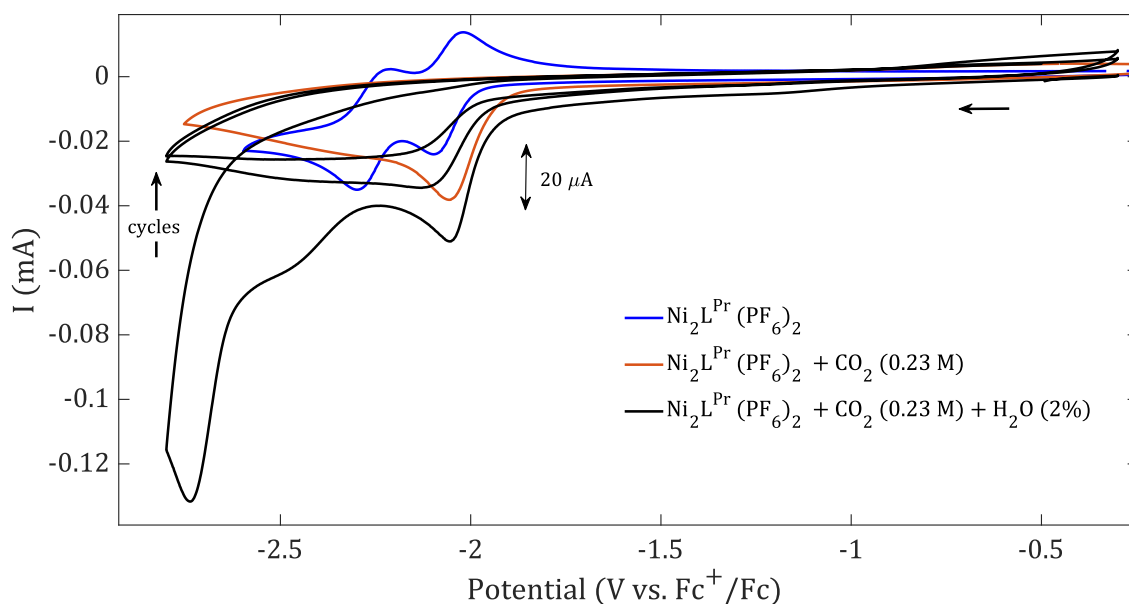
Figure 3.28 | CVs showing the reactivity of **Ni_2L^{Pr} (PF$_6$)$_2$** in a CO_2-saturated MeCN/0.1 M TBAPF$_6$ solution containing 2% H_2O. One can observe that the catalytic peak of the first cycle is disappears upon several electrochemical scans (black lines and arrow), suggesting competitive reactions at the electrode surface.

To further understand the role of H_2O in this process, increasing amounts of H_2O were added to a CO_2-saturated **Ni_2L^{Pr} (PF$_6$)$_2$** solution in MeCN (+0.1 M TBAPF$_6$) and the

resulting electrochemical behaviour (first cycle) was compared. Unexpectedly, a third cathodic peak appeared at $E_{p,cat}$ = -2.44 V, whose intensity follows the increase of H_2O concentration (1 - 3 M). Notably, the reductive peak currents of the other two redox features ($E_{p,cat}$ = -2.03 V and -2.78 V), are also enhanced when the amount of added H_2O rises (**Figure 3.29**).

With the purpose of comparing the activity of the propylene-bridged complex with that of the other Ni-analogues, CPE in a CO_2 saturated MeCN solution was conducted, maintaining the potential of -2.70 V for 3 hours. CO and H_2 were the only detected gaseous products, whose ratio (CO:H_2) slightly varies during the experiment; from 1 : 2.6 to 1 : 1.5 (**Figure 7.34**). The maximum TON_{CO} was 0.16, reached after 270 min of electrolysis. No turbidity was observed during the experiment, although yellowish crystals nucleated at the surface of the Freudenberg carbon paper employed as WE, which were washed with fresh MeCN and analysed by SC X-ray Diffraction. Regrettably, the quality of the crystals was not high enough to be properly refined, but some indications were obtained, which follow: no coordination to any Ni-centre was observed and, most importantly, only one PF_6^- counterion was co-crystallized with one molecule of complex, which would support the Ni^{II}/Ni^I MV species formation. However, lots of co-crystallized water was detected, which could also be hydroxide, hence the charge balance is somewhat speculative. The rinse test gave positive results, here too, even if the exchanged current was not so intense as in the case of **Ni₂L^{Et} (PF₆)₂**. Also in this case, to avoid catalyst decomposition, it would be interesting to repeat the CPE analysis by setting a less negative potential, *e.g.,* E_{appl} < -2.5 V (before the onset potential for HER, **Figure 3.24**), and to spectroscopically analyse the solution-phase products (HCOO⁻, HCO₃⁻, CO₃²⁻), which could have been formed at less negative potential. In addition, considering the reactivity of the complex towards CO_2RR in absence of a proton source, one CPE can also be run at $E_{p,cat}$ = -2.05 V without added H_2O, to isolate the potential disproportionation products and to validate the precedent hypothesis (*vide supra*).

Taken these results all together, the three Ni-complexes, despite possessing interesting electrochemical behaviours, dictated by their geometry and flexibility, are not the ideal candidate to develop stable and efficient CRCs. Their activity towards CO_2RR, although not entirely absent, is hampered by side phenomena occurring at the electrode which are boosted by the scarce reversibility of the methylene- and the ethylene-bridged complexes and by the negative potential necessary to their reduction. Between the series, when considering only the first electrochemical cycle in CO_2-saturated, H_2O containing (1.0 M) MeCN solution, the potential at half catalytic peak[222] shifts to more negative potentials when the alkylene-bridge is extended, which would imply, if one refers to a catalytic process with CO production, an overpotential that rises from 0.76 V of **Ni₂L^{Me} (PF₆)₂**, to 0.84 V and to 1.06 V for **Ni₂L^{Pr} (PF₆)₂**.
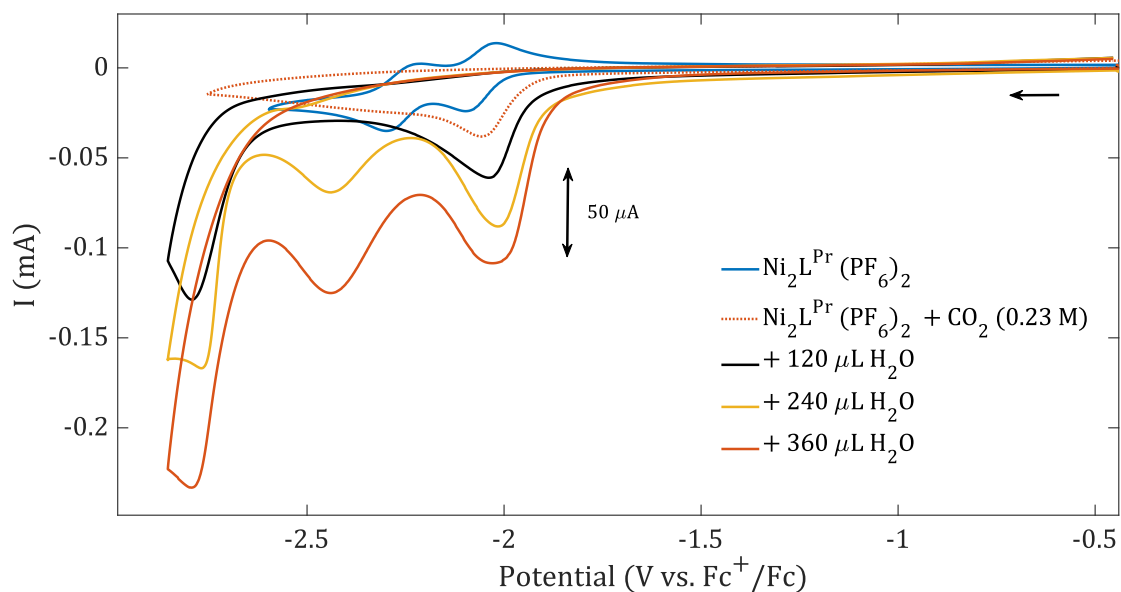
Figure 3.29 | CVs showing the reactivity of **Ni₂L^{Pr} (PF₆)₂** in a CO_2-saturated MeCN/0.1 M TBAPF₆ solution containing 2% H_2O (black), 4% H_2O (yellow) and 6% H_2O (red). The dotted red trace represents the reactivity towards CO_2 in without added H_2O. A new catalytic peak arises at $E_{p,cat}$= -2.44 V with H_2O conc. > 4% Only the first electrochemical cycle is reported.

When the stability of the catalysts is considered, instead, **Ni₂L^{Et} (PF₆)₂** seems to be less affected by degradation and/or inhibition processes, followed by the methylene-counterpart. **Ni₂L^{Pr} (PF₆)₂**, conversely, undergoes to drastic and irreversible chemical transformations when the potential is scanned as low as -2.75 V.

4 CONCLUSION AND PERSPECTIVES

The synthesis and electrochemical characterization of different alkylene-bridged Cu- and Ni homobimetallic calix[4]imidazolylidene[2]pyrazolate complexes is reported in this study. These bowl-shaped metal complexes, thanks to their unique structure and their ability to selectively recognize one halide ion (Cl- or Br-) are highly interesting for the activation of small molecules, such as CO_2. Hence, the CO_2RR ability of three Ni-complexes has been electrochemically investigated.

Adjusting the synthetic procedure reported by *Pöthig and coworkers*,[190] the propylene-version of the bridged NHC/pyrazolate Ni complexes was synthesized. The metalation of the macrocyclic tetraimidazolium ligand precursor was achieved with the employment of an excess of an external base, Cs_2CO_3, together with a stoichiometric amount of [$NiCl_2(PPh_3)_2$] as metal source. The three Ni-complexes were fully characterized using mono- and bidimensional NMR spectroscopy, UV-Vis, HR-ESI-MS and SC X-Ray diffraction. As for the methylene- and for the ethylene-bridged complexes, SC-XRD analysis for **Ni_2L^{Pr} (PF$_6$)$_2$** revealed a saddle-shaped conformation, but with a reduced cavity opening. Aiming to isolate the respective Cu-complexes, different halogen-free copper sources were tested. The most promising strategy consists in the employment of the *in situ* produced $Cu(PF_6)_2$, better described as {$Cu(NCCH_3)_4$} (PF$_6$)$_2$, which, together with the deprotonating Cs_2CO_3, leads to the synthesis of **Cu_2L^{Me} (PF$_6$)$_2$**. IR Spectroscopy, HR-ESI-MS, elementary analysis and SC-XRD were employed to assess its purity. The complex shows the presence of only one band in the UV-Vis spectrum, as expected for a d^9 electronic configuration, while the most stable ground-state spin multiplicity was computed to be the triplet state, with the two unpaired electrons lying in metal-based d orbitals. Notably, **Cu_2L^{Me} (PF$_6$)$_2$** is electrochemically active only scanning towards positive potentials, with the oxidized Cu^{III}/Cu^{III} state reached at mild potential (0.31 V). There is also a substantial through-ligand electronic communication between the two metal centres. Attempts to isolate the ethylene-bridged copper analogue leads to the formation of one supramolecular assembly in which two symmetry-equivalent cationic **[Cu_2L^{Et}]$^{2+}$** moieties encapsulate one chloride ion. The formation of this tennis-ball like aggregate, the so-called Capsoplex, was already reported by the group of *Pöthig* in 2016.[190] The electrostatic and H-bonding interactions that stabilize the host-guest **[(Cu_2L^{Et})$_2$Cl] (PF$_6$)$_3$** complex are that strong that even trace amount of Cl- is recognized and encapsulated. Future works should firstly consider robust Cl and Br-free routes to obtain the Crisp-shaped ethylene and propylene-bridged complexes, to then investigate their redox properties. In fact, it is particularly interesting to evaluate the versatility of such bimetallic pocket towards spin and electron density variation of the metal centres (going from a d^9 Cu^{II} to a d^8 Cu^{III}).

As the electrochemical behaviour of **Ni_2L^R (PF$_6$)$_2$** is concerned, the most striking difference was observed going from the ethylene- to the propylene-bridged complexes.
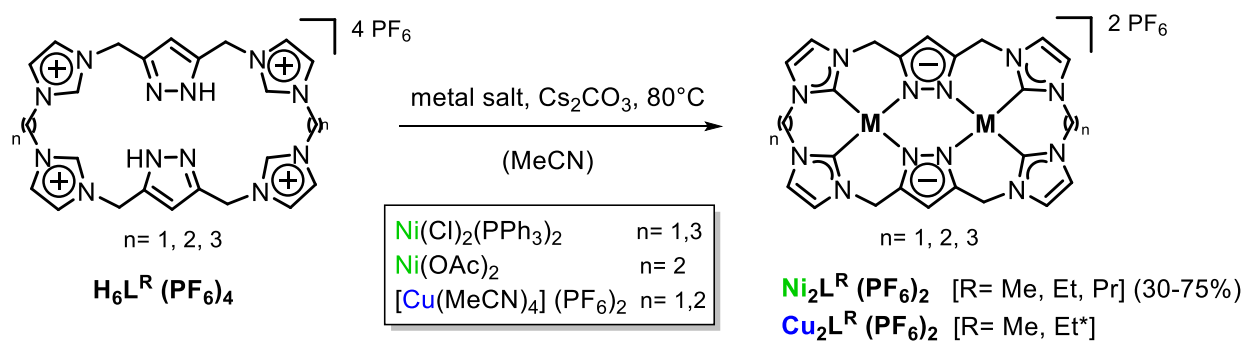
Scheme 4.1 | Successful synthesis of target nickel(II) and copper(II)–NHC complexes. *Trace amount of Cl⁻ led to the formation of the encapsulation **[(Cu₂L^Et)₂Cl] (PF₆)₃** complex.

If, on one side **Ni₂L^Me (PF₆)₂** and **Ni₂L^Et (PF₆)₂** are characterized almost by irreversible, very negative reductions, the propylene-bridged version displays quasi-reversible and less cathodic redox features. Hence, the Ni ions in **Ni₂L^Pr (PF₆)₂** are more prone to accept electrons and the resulting Ni^I,Ni^I species benefits from greater stability. In fact, from DFT studies, all the observed cathodic events are assigned to metal-centered reductions. The explanation of the greater reversibility and of the anodic shift of the redox events in **Ni₂L^Pr (PF₆)₂** can derive from structural consideration. In fact, the greater ligand flexibility that characterizes the compound can be associated to a more facile distortion of the first coordination sphere of the metal centres, resulting in more favored electron transfer kinetics. As a consequence, when CO_2 is purged into a solution with the propylene-bridged complex, a small catalytic peak is observable over the first redox couple, suggesting that a bimetallic, Ni^I,Ni^II promoted, CO_2 activation takes place. In the two other cases, only the addition of small amount of H_2O (1 M) leads to the detection of a catalytic wave. However, multiscan CVs and CPE measurements shows scarce stability of the catalyst over time, with electrodeposition and catalyst inhibition/degradation occurring already after the first scan. Complete loss of the catalytic current over time can be associated to lots of scenarios, including Ni Hydride formation and deposited electrochemically inactive Ni-CO or Ni-C(O)O-Ni species. In fact, electrochemical HER ability of the three Ni-complexes has been previously checked and shown to be not-absent, especially in **Ni₂L^Et (PF₆)₂** and **Ni₂L^Pr (PF₆)₂**. In order to evaluate the real catalytic potential of this class of compounds, further studies should be based on the investigation of the nature of these electrodeposited or insoluble adducts, (*e.g.* by solid state techniques for the WE surface, or by computationally approaches). Furthermore, to get a clear picture of the extension of the side reactions, different solvents or different proton sources should be screened, such as MeOH, PhOH or TFE, all possessing different mechanisms in promoting the C-O bond cleavage. CPE experiment can also be conducted at milder potential respect to what has been performed here, to maximize the CO_2RR selectivity over HER.

Another, more elegant approach, which should result in a greater robustness of the catalytic system, as well as in a minimization of side phenomena, is the immobilization of the catalyst in conductive supports. Heterogenization of molecular catalysts, in fact, is a field which is attracting increasing interest for the vast number of available immobilization strategies and for the unprecedent stability that certain systems show for long term studies. In order to immobilize the bimetallic complex investigated in this study, the additional backbone nitrogen atoms in the triazolate-based version of **Ni₂L^R (PF₆)₂** could be exploited to tether a proper linker. Linker, that has the role to connect the molecular catalyst to the chosen modified electrode surface (made of carbon allotropes or conductive metal oxides), through a specific anchoring group, whose nature must be compatible with the employed electrode (**Figure 4.1**). Furthermore, in heterogenized systems, the catalytic current is not limited by the mass transport of the catalyst.[144] The presence of an additional H-bonding acceptor in proximity to the metal centres, facilitating CO_2 binding and reduction,[215] can be considered another advantage of the triazolate-based series.
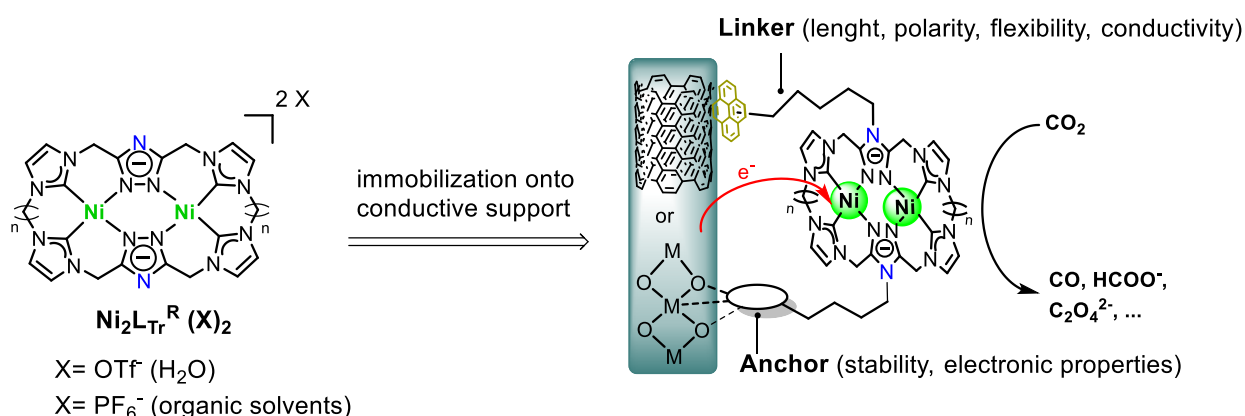
Figure 4.1 | Ni₂L$_{Tr}$^{R} (X)₂ complexes soluble either in H_2O or in organic solvents, and covalent/π-stacking anchoring strategies to immobilize the catalyst onto conductive electrodes, with the main features contributing to efficient electronic interaction between the catalyst and the surface highlighted.[144]

Despite the envisioned reductive dimerization of CO_2 promoted by selective recognition of two molecules of CO_2 and their encapsulation in a tennis-ball fashion has not been observed from gas phase-monitored CPE, the possibility of formation of some soluble products during the catalytic reaction cannot be ruled out. In fact, non-covalent dimerization has been observed by *Kubiak et al.* for Re- and Mn(bpy)-based catalyst,[168],[223] which led to the reductive disproportionation of CO_2 into CO and CO_3^{2-}, and liable bridging oxalate ligands have been reported to ligate bimetallic active centres in copper-based catalysts.[154],[155] As a consequence, in repeating CPE experiments, it would be worthwhile to detect also possible products formed in solution, employing dry CD_3CN as solvent and an internal standard for the quantification.

Electrochemical characterization of the Ni-and Cu Capsoplex would also be attractive, since the central halogen anion, being coordinated by all four metal centres (**Figure 3.16**), is susceptible to dissociation, even before the potential required to trigger the metal-based redox chemistry. This phenomenon is highly attractive, since the selectivity towards the *guest* species can be tuned by ligand modification, potentially rendering this class of *host* molecules selective for pharmaceutical/environmental relevant anions. The subsequent *guest* release (triggered by external stimuli) will, in this way, allow the sequestration/concentration of the anion, simultaneously regenerating two cationic, crisp-shaped metal complexes.

5 EXPERIMENTAL

5.1 GENERAL INFORMATION AND ANALYTIC TECHNIQUES

All reagents for the synthesis were commercially acquired (*Alfa Aesar*, *Thermo Fisher Scientific*, *Merck*, *Sigma-Aldrich*) and applied without further purification. Solvents (CH_2Cl_2, $CHCl_3$, MeOH, EtOH, Et_2O, pentane, hexane, THF) for the usage in water sensitive reactions were obtained from an *MBraun* MB-SPS solvent purification system and were used without further purification. Technical solvents (CH_2Cl_2, $CHCl_3$, MeOH, EtOH, Et_2O, pentane, hexane) were distilled prior to use. Deuterated solvents ($CDCl_3$, MeCN-d_3, DMSO-d_6, D_2O) were purchased from *Sigma-Aldrich* or *Eurisotop* and stored over activated molecular sieves (3Å). Anhydrous caesium carbonate was obtained by drying *in vacuo* at 120 °C for 72 h. Copper(II)acetate was dehydrated by heating a sample *in vacuo* at approximately 150 °C until it was of green colour entirely. Anhydrous nickel acetate was prepared by heating Ni(II) acetate tetrahydrate at 110 °C under vacuum for 2 h. Pure sodium hydride was obtained by washing a 60 wt-% suspension in mineral oil with dry *n*-hexane. $AgPF_6$ was stored under the exclusion of light. All experiments involving air- or moisture-sensitive reagents were carried out under an argon atmosphere in preheated flasks using standard Schlenk techniques or in an *MBraun* UNIlab glove box.

Thin-layer chromatography (TLC) were performed with TLC plates (*Merck*, Aluminium, silica gel 60, F_{254}), with visualization by short-wave UV light (λ=254 nm, 366 nm). Column chromatography was performed on silica gel (*Geduran* Si 60,40-63 μm, *Merck*).

NMR spectra were recorded on a *Bruker* AV-400US, AVHD-500, or AV-500C spectrometer. Chemical shifts δ are reported in parts per million (ppm) and, for ^{1}H NMR spectra, referenced to residual solvent peaks ($CDCl_3$: δ 7.26 ppm; CD_3CN: δ 1.94, DMSO-d_6: δ 2.50 ppm) with respect to $SiMe_4$ (δ = 0 ppm). ^{13}C NMR spectra were referenced to the ^{13}C‑D septets of CD_3CN (δ = 1.32 ppm), DMSO-d_6 (δ = 39.52 ppm), or the ^{13}C‑D triplet of $CDCl_3$ (δ = 77.16 ppm). Coupling constants ^nJ (where n is the number of chemical bonds between two nuclei) are reported in Hertz (Hz). Standard abbreviations indicating multiplicity were used as follows: m = multiplet, q = quartet, t = triplet, dt = double triplet, d = doublet, dd = double doublet, s = singlet, br = broad, *virt* = virtual. Correlation NMR experiments (^{1}H‑^{1}H COSY, ^{1}H‑^{1}H NOESY, ^{1}H‑^{13}C HSQC, ^{1}H‑^{13}C HMBC) were used for the assignment of the ^{1}H and ^{13}C NMR signals. All the spectra were processed with the *MestReNova 14.1.0* software package by *Mestrelab Research*.

Elemental Analyses were performed by the microanalytical laboratory at the Technical University of Munich using a *HEKAtech* Euro EA‑CHNS combustion analyser.

UV/vis spectra were recorded on an *Agilent* Cary 60 UV-Vis spectrophotometer.

101

HRESI-MS analyses were performed on a *Thermo Fisher* Exactive Plus Orbitrap mass spectrometer equipped with a *Thermo Fisher* ESI source.

SC-XRD data were collected on a *Bruker* D8 Venture Duo IMS single-crystal X-ray diffractometer equipped with a CPAD detector (*Bruker* Photon II), an IMS microfocus source with Mo K_α (λ = 0.71073 A) radiation, a *Helios* optic monochromator, and a four circle goniometer (kappa geometry). Measurements were performed at 100 K on single crystals coated with perfluorinated ether and fixed on top of a microsampler.

Cyclic Voltammetry and electrocatalysis experiments were recorded on a *BioLogic* (SP-200) potentiostat in a homemade gastight cell with a glassy carbon WE (3 mm diameter GC surface), glassy carbon CE, and silver wire pseudo reference electrode. The CV spectra were referenced to the $Fc^{+/0}$ couple that was recorded under exactly the same experimental conditions as an external reference. All electrochemical measurements were performed in a dry and degassed MeCN solution with 0.1 M TBAPF$_6$ (three times re-crystallized and dried at 120 °C under vacuum prior to use) under a N$_2$ or a CO$_2$ environment. Ohmic drop was carefully compensated during CV. Solutions (1 mM catalyst concentration in 5 mL electrolyte solution) were prepared in a glovebox and sealed in an air-tight cell and studied either under N$_2$ or by purging the cell with CO$_2$ for a minimum of 15 min (concentration of CO$_2$ in saturated MeCN solution = 0.23 M).[224]

Controlled Potential Electrolysis. Electrolysis reactions were performed using a *BioLogic* (SP-200) potentiostat. Experiments were carried out in a two-compartment cell with a Freudenberg carbon paper as working electrode (WE). The volume of the solution was 8 mL (MeCN + 0.1 M ^{n}Bu$_4$PF$_6$ + 2% H$_2$O), and active surface area was 1.0 cm^2. Ag-AgNO$_3$ electrode was used as reference (RE), composed by a Ag wire in a 3 M AgNO$_3$ solution (with 0.1 M ^{n}Bu$_4$PF$_6$), and the counter electrode was a platinum gauze positioned in a bridge separated from the cathodic compartment by a ceramic frit, containing a 2% H$_2$O + 0.1 M ^{n}Bu$_4$PF$_6$ MeCN solution (2mL). The electrolysis solution was purged with CO$_2$ during 15 min prior to electrolysis. The ohmic drop between WE and RE was minimized by dipping the former one directly in the solution and positioning it close to the working electrode. All CPE experiments have been performed under stirring. FE was calculated by dividing the determined number of moles of CO by Q/2F (the charge passed divided by 2 times the Faraday constant). The divisor 2 is used because two electrons are required to produce 1 mol of CO.

Gas Chromatography. Analyses from the gas evolved in the headspace during electrolysis were carried out with SRI 8610C Gas Chromatograph equipped with a thermal conductivity detector (TCD), for H$_2$ detection and FID-methanizer for CO detection. Temperature was held at 150 °C for the detector and 34 °C for the oven. The carrier gas was He for CO-detection (FID) and N$_2$ for H$_2$ detection (TCD). Since the employed detectors were different for the analysis of the two gaseous products, each sample was injected twice in the GC analyser. Injection was performed via a 20 mL gas-tight syringe. These conditions allowed for separation of both H$_2$, O$_2$, N$_2$, CO, and CO$_2$.

Calibration curves for H_2 and CO were determined separately by injecting known quantities of pure gas.

5.2 COMPUTATIONAL METHODS

All calculations were performed with GAUSSIAN-09 using the unrestricted density exchange/correlation functional ωB97x-D with the split valence double-ζ (DZ) basis set 6- 31G,[225] and the triple-ζ basis set 6- 311G, supplemented by polarized (+) and, when necessary, by diffuse functions, namely one set of d functions on heavy atoms, one set of p functions on hydrogens: 6-31(1)+G(d,p). The Grimme D3 dispersion correction is by default implemented in the employed functional. No symmetry or internal coordinate constraints were applied during optimizations. All reported intermediates were verified as being true minima by the absence of negative eigenvalues in the vibrational frequency analysis. The values for the partial atomic charges come from the atomic polar tensor (APT) derived charges reported in the Gaussian-09 outputs of the frequency calculations. These charges are more basis set independent than the pure Mulliken charges.[214]

To take into account the stabilization contribution arising from solvation (solvent: MeCN, ε= 37.50), quantomechanical calculation involving solution-properties, such as electrochemical studies and UV-Vis absorption, were conducted using the Conductor-like polarizable continuum model (CPCM),[195] or the Solvation Model based on Density approaches (SMD) [213]. These models are referred to be implicit solvation models, in which the solute molecule is placed in a cavity surrounded by a continuum polarizable media, which represent the solvent, that interacts with the charges in the cavity surface. Hence, the free energy of solvation is given by:
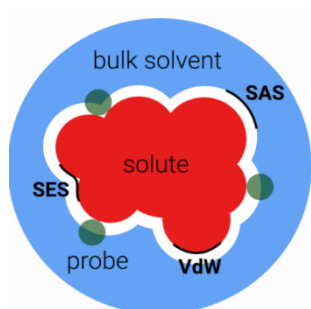
$$\Delta G^0_{solv} = \Delta G_{cav} + \Delta G_{disp} + \Delta G_{elec} + (\Delta G_{H-bond})$$

In which ΔG_{cav} is the free energy required to form the solute cavity; ΔG_{disp} is the term which takes into account for the VdW dispersion forces between solute and solvent, and ΔG_{elec} is the electrostatic component.

5.3 SYNTHETIC PROCEDURES AND ANALYTICAL DATA

5.3.1 Proligands Synthesis

Monopotassium pyrazole-3,5-dicarboxylate (1)
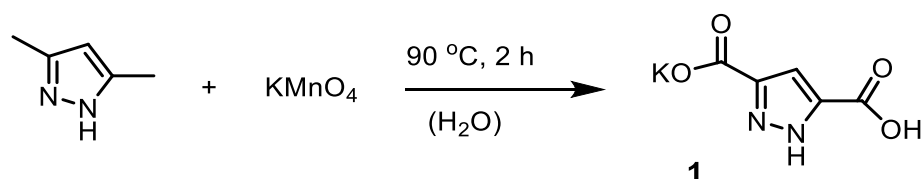
A solution of 3,5-dimethyl pyrazole (41.207 g, 428.66 mmol, 1 equiv.) in 2 L water was heated to 80 °C under stirring and a steady stream of CO2 was passed through the solution in order to provide a buffered medium. To this solution solid KMnO4 (288.00 g, 1.822 mol, 4.24 equiv.) was added in portions at a rate sufficient to maintain an internal temperature of approximately 90 °C. The resulting mixture was stirred for additional 2 h at 90 °C. The suspension was filtered, and the filtrate reduced to approximately 750 mL. A white solid was precipitated by slow addition of acetic acid (150 mL, 17 M). After stirring for 2 h, the precipitate was filtered off and washed with water, ethanol and diethyl ether. After drying *in vacuo* **1** was obtained as a white solid in a yield of 62.097 g (319.77 mmol, 75 %).

Elemental Analysis (%):

Calcd. for $C_5H_3KN_2O_4 \cdot 0.15\ H_2O$: C, 30.50; H, 1.69; N, 14.23

Found: C, 30.62; H, 1.83; N, 14.00

Dimethyl pyrazole-3,5-dicarboxylate (2)
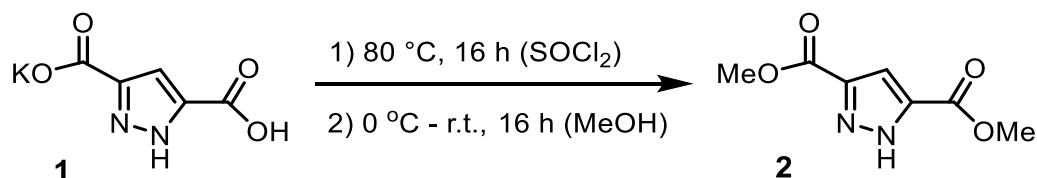
1 (62.097 g, 319.77 mmol, 1 equiv.) was suspended in thionyl chloride (460 mL, 760.81 g, 6.40 mol, 20 equiv.) and stirred at 80 °C under reflux conditions. After 16 h residual thionyl chloride was removed *in vacuo* and 850mL of methanol were added to the remaining solid at 0 °C under vigorous stirring. After stirring for additional 16 h at room

temperature the solvent was removed *in vacuo* and the crude product was dissolved in 1 L dichloromethane, filtered and extracted with $NaHCO_3$,(aq) and NaCl(aq). The solvent was removed and after drying *in vacuo* **2** was obtained as a shiny white solid in a yield of 45.0 g (244 mmol, 76 %).

1H NMR (400 MHz, CDCl3, 298 K): δ (ppm) = 12.21 (s, 1H, N*H*), 7.32 (s, 1H, HCCHC), 3.92 (s, 6H, 2x CH3).

3,5-Bis(hydroxymethyl)pyrazole hydrochloride (3)
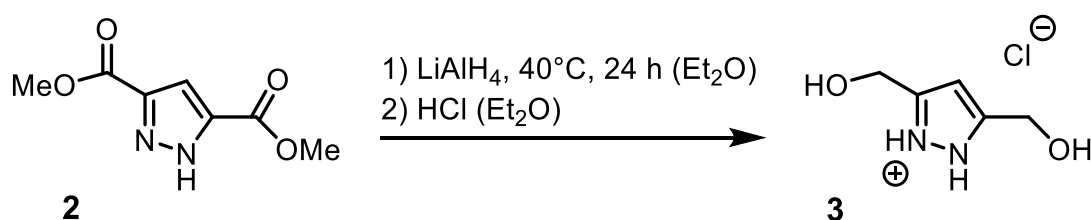
In an 1 L Schlenk flask LiAlH4 (10.25 g, 270 mmol, 4.1 equiv.) was suspended in 750mL dry diethyl ether. **2** (12.16 g, 65.83 mmol, 1 equiv.) was placed in a paper thimble of a Soxhlet apparatus that was fitted in the extractor. The solvent was refluxed for 24 h with a recycling time of approximately 15 min. The resulting suspension was cooled to room temperature and 50mL water were added dropwise over 30 min. The solvent was removed *in vacuo* and the remaining white solid was suspended in 700mL methanol. The mixture was treated with gaseous CO_2 for 30 min under stirring and then refluxed for additional 6 h. The suspension was filtered, and the filtrate evaporated. The residue was redissolved in 250mL ethanol, filtered and concentrated to approximately 100 mL. Under stirring hydrochloric acid (8.5 mL, 12 M) was added and a white solid was precipitated by addition of 1 L diethyl ether. The precipitate was filtered off and washed with diethyl ether twice. After drying *in vacuo* **3** was obtained as a white solid in a yield of 8.887 g (54.18 mmol, 82 %).

[1]**H NMR** (400 MHz, DMSO-*d*6, 298 K): δ (ppm) = 7.23 (br s, 2H, N*H*), 6.33 (s, 1H, HCCHC), 4.52 (s, 4H, CH2).

3,5-Bis(chloromethyl)-pyrazolium chloride (4)
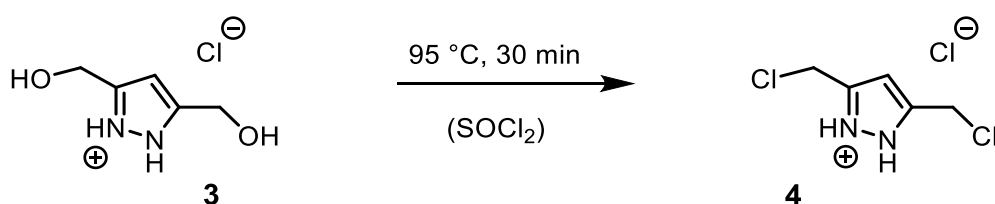
3 (8.887 g, 53.99 mmol, 1 equiv.) and thionyl chloride (60 mL, 827 mmol, 15.3 equiv.) were placed in a Schlenk flask equipped with a reflux condenser and a pressure valve under vigorous stirring. The mixture was heated to 95 °C and stirred at this temperature for 30 minutes. Subsequently, the excess thionyl chloride was removed *in vacuo* into an external cooling trap. The residue was dissolved in 150mL ethanol and filtered. The solution was concentrated *in vacuo* to approximately 30mL and 200mL diethyl ether were added. The resulting precipitate was collected via filtration. After drying *in vacuo* **4** was obtained as a glittery white solid in a yield of 8.030 g (39.86 mmol, 73.8 %).

[1]**H NMR** (400 MHz, DMSO-*d*6, 298 K): δ (ppm) = 6.69 (br s, 2H, N*H*), 6.38 (s, 1H, H$_{CCHC}$), 4.72 (s, 4H, CH$_2$).

3,5-Bis(chloromethyl)-1-(tetrahydropyran-2-yl)-1H-pyrazole (5)
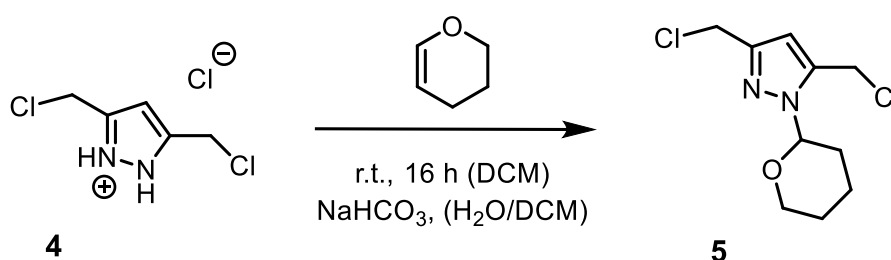
4 (8.030 g, 39.86 mmol, 1 equiv.) was suspended in 100mL dry dichloromethane. 3,4-dihydro- 2*H*-pyran (8.50 mL, 93.1 mmol, 2.34 equiv.) was added and the mixture was stirred at room temperature for 16 h. Subsequently, a solution of 5 g NaHCO$_3$ in 50mL water was added. The phases were separated, and the aqueous phase was extracted with dichloromethane (2x 50 mL). The combined organic phase was dried over MgSO4, filtered and evaporated *in vacuo*. The crude product was recrystallized from hexane and after drying *in vacuo* **5** was obtained as a white solid in a yield of 8.72 g (35.0 mmol, 88 %).
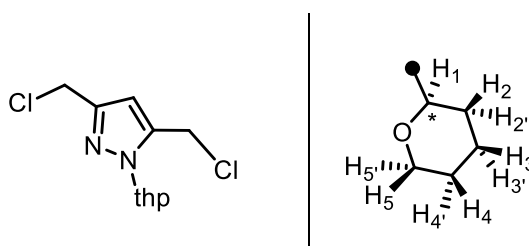
[1]**H NMR** (400 MHz, CDCl$_3$, 298 K): δ (ppm) = 6.40 (s, 1H, H$_{Pyr}$), 5.45 (dd, ^3J= 9.5/2.7 Hz, 1H, H$_1$), 4.67 (q, ^2J=12.8 Hz, 2H, H$_{CH2}$), 4.57 (d, ^2J=12.83 Hz, 2H, H$_{CH2}$), 4.05-4.01

(m, 1H, H$_5$), 3.67 (td, $^{2,3}J$=11.3/ 2.7 Hz, 1H, H$_{5'}$), 2.44-2.34 (m, 1H, H$_2$), 2.12-2.08 (m, 1H, H$_{2'}$), 2.04-2.00 (m, 1H, H$_3$), 1.75-1.55 (m, 3H, H$_{3',4,4'}$).

Sodium imidazolide (6)
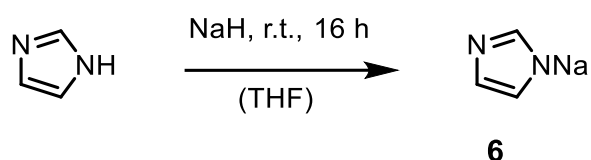
Imidazole (56.4 g, 0.828 mol, 1 equiv.) was dissolved in 300 mL dry tetrahydrofuran under inert atmosphere. Sodium hydride (33.13 g, 0.828 mol, 1 equiv., 60% suspension washed three times with hexane to remove oil) was added slowly and the mixture was stirred until evolution of gas ceased. The resulting suspension was filtered under inert conditions, and the residue washed with tetrahydrofuran three times. After drying *in vacuo* **6** was obtained as a white, crystalline solid in a yield of 20.44 g (0.227 mol, 27 %).

^{1}H NMR (400 MHz, D$_2$O, 298 K): δ (ppm) =7.76 (s, 1H, H$_{NCHN}$), 7.12 (s, 2H, H$_{NCHCHN}$).

*The ^{1}H NMR spectrum indicates approximately 0.5 equivalents of THF solvate. Sodium imidazolide was stored under argon atmosphere.

3,5-Bis(imidazol-1-ylmethyl)-1-(tetrahydropyran-2-yl)-1*H*-pyrazole (7)
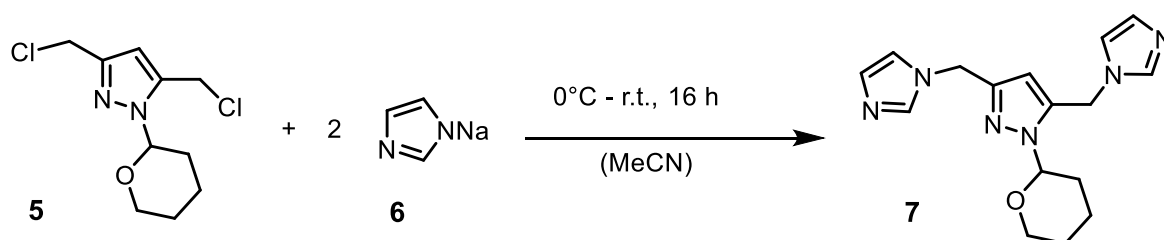
A Schlenk tube was charged with **6** (10.8 g, 109 mmol, 3.1 equiv.) and cooled to 0°C. A solution of **5** (8.72 g, 35.0 mmol, 1 equiv.) in 50mL dry acetonitrile was added under vigorous stirring. The resulting suspension was allowed to warm to room temperature overnight and filtered through a pad of Celite R. The solution was concentrated to dryness, the crude product dissolved in 50mL dichloromethane and extracted with water (2 x 50 mL). The aqueous extract was washed with 50mL dichloromethane and the combined organic phases were dried over MgSO4, filtered and concentrated to dryness. After drying *in vacuo* **18** was obtained as a colorless resin in a yield of 10.1 g (32.35 mmol, 92%).
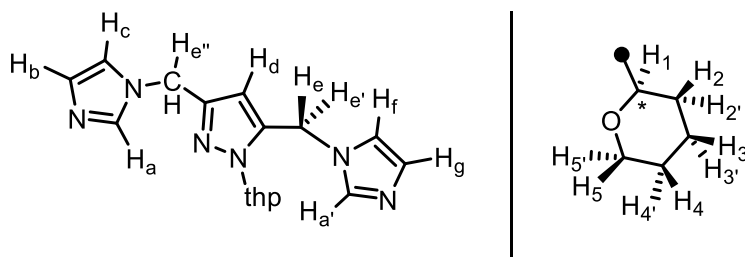
¹H NMR (400 MHz, CDCl₃, 298 K): δ (ppm) =7.52 (*virt.* t, ^4J=1.1 Hz, 1H, Ha), 7.49 (*virt.* t, ^4J=1.12 Hz, 1H, Ha'), 7.07 (*virt.* t, 1H, ^3J= ^4J= 1.1 Hz, 1H, Hb'), 7.04 (*virt.* t, 1H, ^3J= ^4J= 1.1 Hz, 1H, Hb), 6.93 (*virt.* t, 1H, ^3J= ^4J=1.3 Hz, 1H, Hc), 6.87 (*virt.* t, 1H, ^3J= ^4J= 1.3 Hz, 1H, Hc'), 5.96 (s, 1H, Hd), 5.23 (d, ^2J= 15.88 Hz, 1H, He'), 5.16 (d, ^2J=15.9 Hz, 1H, He), 5.14 (dd, ^3J=15.9,2.8 Hz, 1H, H₁), 5.05 (*virt.* d, ^4J=0.7 Hz, 2H, He''), 3.99-3.92 (m, 1H, H₅), 3.62- 3.54 (m, 1H, H₅'), 2.27-2.13 (m, 1H, H₂), 2.09-1.89 (m, 2H, H₂',₃), 1.68-1.52 (m, 3H, H₃',₄,₄').

¹³C NMR (101 MHz, CDCl₃, 298 K): δ (ppm) = 147.3, 139.4, 137.4, 137.3, 130.2, 129.8, 119.3,119.1, 106.5, 86.0, 67.6, 44.7, 41.8, 29.4, 24.9, 22.1.

Methylene-bis(trifluoromethanesulfonate) (8) SN_10
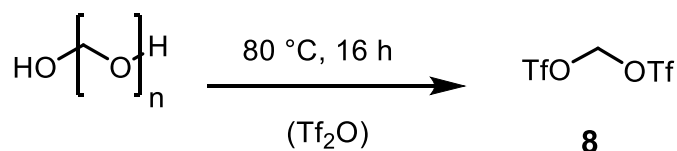
A mixture of paraformaldehyde (2.30 g, 76.0 mmol, 1 equiv.) and trifluoromethanesulfonic anhydride (13.0 mL, 21.8 g, 77.9 mmol, 1 equiv.) in a tightly sealed Schlenk tube was heated to 80°C for 16 h. Excess trifluoromethanesulfonic anhydride was removed *in vacuo* at room temperature, yielding a black residue. The crude product was purified by column chromatography using dichloromethane as eluent. After drying *in vacuo* **8** was obtained as a colorless oil in a yield of 3.38 g (10.83 mmol, 23 %).

¹H NMR (400 MHz, CDCl₃, 298 K): δ (ppm) = 6.06 (s, 2H, HCH₂).

¹³C NMR (101 MHz, CDCl₃, 298 K): δ (ppm) = 116.7 (s, CCH₃), 91.3 (s, CCH₂).

Ethylene-bis(trifluoromethanesulfonate) (9)
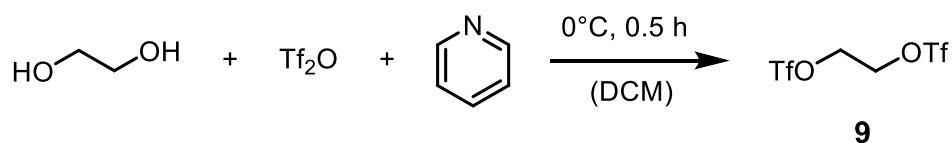
This synthesis was reproduce as reported in the literature.[226] To a mixture of CH_2Cl_2 (50 mL), triflic anhydride (8.48 g, 5.0 mL 30 mmol, 2), and pyridine (2.4 mL, 30 mmol, 2 eq) was added ethylene glycol (0.87 mL, 15 mmol, 1eq) at 0 ºC, and the whole mixture was stirred at 0 ºC for 0.5 h. The resulting solution was filtered and washed with ion-exchanged water (10 mL × 3). The CH_2Cl_2 layer was dried over Na_2SO_4 and filtered. The filtrate was concentrated under reduced pressure, and the residue was chromatographed (silica gel, CH_2Cl_2) to afford 1,2-bis{(trifluoromethylsulfonyl)oxy}ethane (3.64 g, 11.1 mmol, 74%) as a colorless liquid.

1H NMR (400 MHz, $CDCl_3$, 298 K): δ (ppm) = 4.77 (s, 2H, H_{CH2}).

Calix[4]imidazolylidene[2]pyrazole trifluoromethanesulfonate proligands
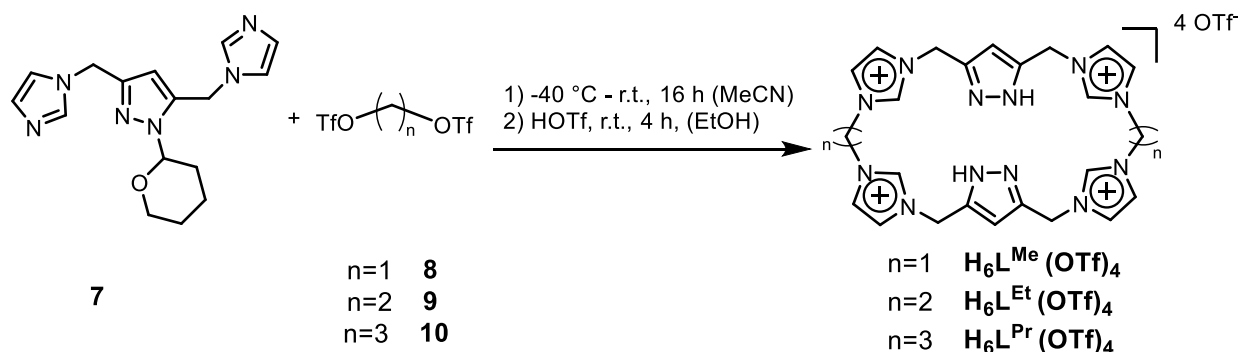
In a pre-heated 1 L Schlenk flask **7** (see following table for stoichiometry) was dissolved in 500 mL of dry MeCN and cooled to -40 °C. In a 20 mL syringe bistriflate (**8-10**) was dissolved in 15 mL MeCN (dry) and added to **7** at -40 °C over the course of 1 h *via* syringe pump. The mixture was allowed to reach room temperature and stirred for 16 h. The solvent was removed under reduced pressure and the resulting oil was dissolved in 20 mL EtOH. *In situ* generated TfOH (by mixing 1.5 mL of Tf_2O and 1.5 mL H_2O) was added dropwise to the filtrate and the mixture was stirred for 1 h. Et_2O (300 mL) was added to precipitate a white solid and the suspension was stirred overnight. The supernatant was removed by cannula filtration and the wet residue was treated with 20 mL acetone. The suspension was transferred into a 50 mL centrifugation tube and centrifuged. Removal of the supernatant and drying *in vacuo* afforded **H₆Lᴿ (OTf)₄** (R=

Me, Et, Pr) as a white solid (see table for yields). For **H₆LᴹᵉMe (OTf)₄** and **H₆LᴱᵗEt (OTf)₄**, the analytical data were in accordance with those reported in the literature.[78],[190]

Target compound	Amount **7**	Bis-OTf employed	Amount proligand	Yield (%)
H₆Lᴹᵉ (OTf)₄	1.14 g 3.65 mmol	**8:** 1.14 g 3.66 mmol	1.14 g 1.055 mmol	29
H₆Lᴱᵗ (OTf)₄	0.84 g 2.67 mmol	**9:** 0.870 g 2.67 mmol	0.64 g 0.579 mmol	22
H₆Lᴾʳ (OTf)₄	1.26 g 4.06 mmol	**10:** 1.38 g 4.06 mmol	0.83 g 0.729 mmol	18

Calix[4]imidazolylidene[2]pyrazole hexafluorophosphate proligands
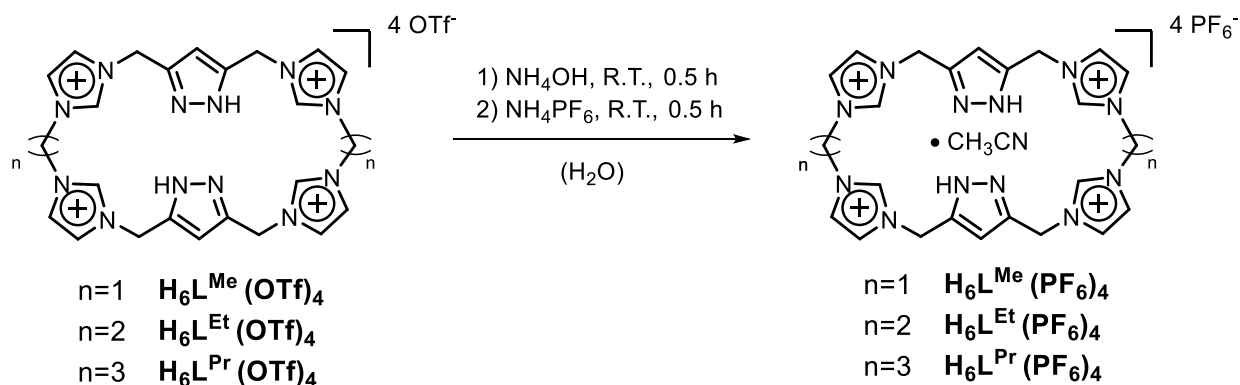
In a 50 mL conical tube **H₆Lᴿ (OTf)₄** (R= Me, Et, Pr, see following table) was dissolved in 3.2 mL H_2O. 0.8 mL NH₄OH (aq.) (25 wt-%) were added and the solution was stirred for approx. 10 min. Upon dropwise addition of the obtained solution to another conical tube containing NH₄PF₆ (see table) dissolved in 4 mL H_2O, a white solid immediately precipitated. The suspension was stirred for 30 min to complete the precipitation. Hence, it was centrifuged, and the supernatant was decanted off. The residue was washed with H_2O (2 × 10 mL) and dried under reduced pressure. To remove all the water traces for the compound, it was dissolved in the minimum amount of MeCN, precipitated with an excess of Et_2O, centrifugated and isolated from the supernatant. After washing with Et_2O (2x10 mL) and drying *in vacuo*, **H₆Lᴿ (OTf)₄** (R= Me, Et, Pr) was obtained as a white solid (see table for yields). For **H₆Lᴹᵉ (PF₆)₄** and **H₆Lᴱᵗ (PF₆)₄**, the analytical data were in accordance with those reported in the literature.[78, 190] One equivalent of MeCN was found to remain in the sample.

Target compound	From	Amount NH_4PF_6	Amount proligand obtained	Yield (%)
$H_6L^{Me}(PF_6)_4$	$H_6L^{Me}(OTf)_4$ 1.14 g - 1.06 mmol	0.890 g, 5.27 mmol, 5 eq.	0.504 g 0.473 mmol	45
$H_6L^{Et}(PF_6)_4$	$H_6L^{Et}(OTf)_4$ 0.600 g - 0.541 mmol	0.440 g, 2.70 mmol, 5 eq.	0.508 g 0.465 mmol	86
$H_6L^{Pr}(PF_6)_4$	$H_6L^{Pr}(OTf)_4$ 0.480 g - 0.407 mmol	0.440 g, 2.70 mmol, 5 eq.	0.420 g 0.375 mmol	92

$H_6L^{Pr}(PF_6)_4$
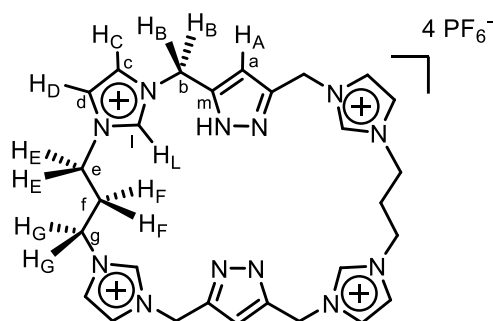
^{1}H NMR (400 MHz, CD$_3$CN): δ (ppm) = 11.41 (br s, 2 H, NH$_{Py}$), 8.43 (s, 4H, H$_L$), 7.43 (t, ^3J= 2.0 Hz, 4H, H$_C$), 7.39 (t, ^3J= 2.0 Hz, 4H, H$_D$), 6.43 (s, 2H, H$_A$), 5.35 (s, 4H, H$_B$), 4.15 (t, ^3J= 7.5 Hz, 8H, H$_E$ / H$_G$), 2.35 (*virt.* quint, ^3J= 7.5 Hz and ^3J= 1.2 Hz, 4H, H$_F$), 1.96 (s, 3H, CH$_3$CN).

^{13}C NMR (125.8 MHz, CD$_3$CN) δ (ppm)= 136.50, 123.90, 123.5, 118.26 (MeCN), 123.50, 106.73, 66.17, 47.22, 1.22 (MeCN).

HR-ESI(+)-MS (m/z): 269.33 (H_6L^{Pr})$^{2+}$, 415.29 ($H_6L^{Pr} \cdot 2PF_6$)$^{2+}$, 683.22 ($H_6L^{Pr} \cdot PF_6$)$^+$, 826.08 ($H_6L^{Pr} \cdot 2PF_6$)$^+$, 975.00 ($H_6L^{Pr} \cdot 3PF_6$)$^+$

5.3.2 Synthesis of Calix[4]imidazolium[2]pyrazole complexes

Ni₂L^R (PF₆)₂   R=Me, Et, Pr

H₆L^R (PF₆)₄
R= Me, Et, Pr

X= [Cl₂(PPh₃)₂]²⁻ for n=1, 3
X= [(OAc)₂]²⁻   for n=2

Ni₂L^R (PF₆)₂
R=Me, Et, Pr
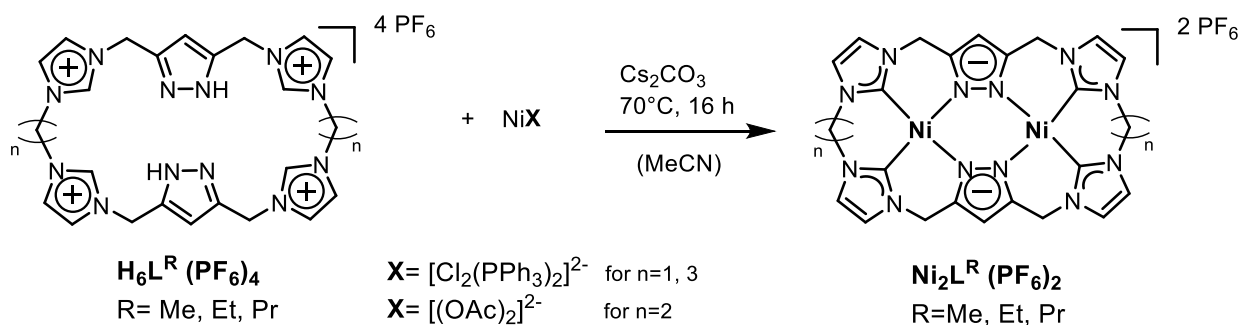
To a mixture of **H₆L^R (PF₆)₄** (see following table for amounts), the chose nickel(II) precursor (see table) and caesium carbonate (10 eq.), 5 mL dry acetonitrile were added under inert atmosphere and the resulting suspension was stirred at 70 °C for 16 h. The suspension was allowed to cool to room temperature and was concentrated to approximately 2 mL. Subsequently, 10 mL of water were added to precipitate a yellow solid which was isolated by centrifugation and washed three times with water. The residue was dissolved in acetonitrile, filtered and diethyl ether was added to the solution to precipitate a solid that was washed with diethyl ether three times. The crude product was purified by fractional precipitation (MeCN, Et₂O). After drying *in vacuo* **Ni₂L^R (PF₆)₂** (R=Me, Et, Pr) were obtained as pale yellow solids. (yields in the table below). The analytical data were in accordance with those reported in the literature.[78],[190]

From	Metal precursor used (2 eq.)	Amount Cs₂CO₃ (10 eq.)	Amount complex obtained	Yield (%)
H₆L^{Me} (PF₆)₄ 150 mg - 0.141 mmol	**NiCl₂(PPh₃)₂:** 184 mg, 0.282 mmol	459 mg, 1.409 mmol	**Ni₂L^{Me} (PF₆)₂** 35 mg - 0.040 mmol	*28*
H₆L^{Et} (PF₆)₄ 100 mg – 0.0822 mmol	**Ni(OAc)₂** 31.2 mg, 0.176 mmol	287 mg, 0.882 mmol	**Ni₂L^{Et} (PF₆)₂** 60 mg - 0.066 mmol	*74*
H₆L^{Pr} (PF₆)₄ 152 mg - 0.136 mmol	**NiCl₂(PPh₃)₂:** 223 mg, 0.340 mmol	431 mg, 1.32 mmol	**Ni₂L^{Pr} (PF₆)₂** 37 mg - 0.039 mmol	*29*

Ni₂L^Pr (PF₆)₂
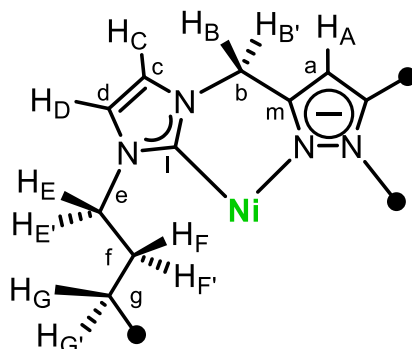
¹H NMR (400 MHz, CD₃CN): δ (ppm) = 7.22 (d, ^3J= 2.0 Hz, 4H, H_C), 7.07 (d, ^3J= 2.0 Hz, 4H, H_D), 6.30 (s, 2H, H_A), 5.47 (d, ^2J= 15.4 Hz, 4H, H_B'), 5.09 (d, ^2J= 15.4 Hz, 4H, H_B), 4.69-4.63 (m, 4H, H_E'/G'), 3.65 – 3.54 (dt, ^2J= 14.5, ^3J=5.5 Hz 4H, H_E/G), 2.27-2.20 (m, 4H, H_F/F').

¹³C{¹H} NMR (125.8 MHz, CD₃CN): δ (ppm) = 158.2 (C_NHC), 146.7 (C_m), 124.4 (C_c/d), 124.3 (C_c/d), 118.26 (MeCN), 103.9 (C_a), 47.5 (C_e/g), 47.4 (C_b), 29.8 (C_f).

ESI(+)-MS (m/z): 941.09 (Ni₂L^Pr · 2PF₆ + H)⁺, 796.13 (Ni₂L^Pr · PF₆ + H)⁺, 326.08 (Ni₂L^Pr)²⁺.

UV/vis (CH₃CN): λ_{max} = 217 nm, 297 nm.

EA (%): calcd. C 35.70, H 3.21, N 17.84; found C 32.52, H 2.99, N 15.85.

Cu₂L^Me (PF₆)₂
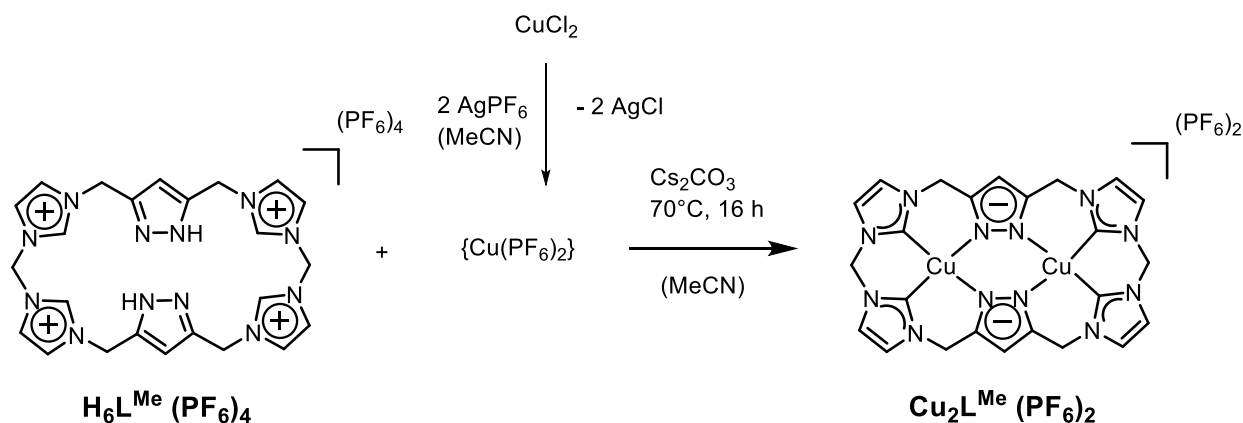
In a pre-heated 10 mL Schlenk tube, anhydrous CuCl₂ (31.5 mg, 0.234 mmol, 2.5 eq.) was dissolved in 3 mL of dry MeCN, to which a solution of AgPF₆ (235 mg, 0.930 mmol) in MeCN was dropwise added. A white solid (AgCl) immediately precipitated from a light blue solution, containing [Cu(MeCN)₄](PF₆)₂, which was filtered under inert conditions directly into a 20 mL Schlenk tube containing a mixture of **H₆L^Me (PF₆)₄** (100 mg, 0.0939

mmol, 1 eq.) and Cs_2CO_3 (305 mg, 0.939 mmol, 10 eq.). The resulting suspension was stirred at 80°C for 16 h, cooled down and transferred into a 50 mL centrifugation tube. An excess (40 mL) of Et_2O were added to the yellow solution to precipitate a yellow/orangish solid, which washed with H_2O (3x10 mL) and purified via fractional precipitation (DMF:Et_2O). After drying in vacuo, **Cu_2L^{Me} (PF_6)_2** was obtained as a yellow solid which was characterized via HR-ESI(+)MS, UV-Vis and SC X-ray crystallography.

HR-ESI(+)-MS (m/z): 893.63 ($Cu_2L^{Me} \cdot 2\ PF_6$)$^+$, 748.97 ($Cu_2L^{Me} \cdot PF_6$)$^+$, 649.07, 302.37 (Cu_2L^{Me})$^{2+}$

UV/vis (CH_3CN): λ_{max} = 232 nm

[(Cu₂L^{Et})₂Cl] (PF₆)₃

In a pre-heated 10 mL Schlenk tube, anhydrous $CuCl_2$ (29.0 mg, 0.216 mmol, 2.3 eq.) was dissolved in 7.2 mL of dry MeCN, to which a solution of $AgPF_6$ (109.2 mg, 0.432 mmol) in MeCN was dropwise added. A white solid (AgCl) immediately precipitated from a light blue solution, containing [Cu(MeCN)_4](PF_6)_2, which was filtered under inert conditions directly into a 20 mL Schlenk tube containing a mixture of **H_6L^{Et} (PF_6)_4** (102.5 mg, 0.0938 mmol, 1 eq.) and Cs_2CO_3 (298 mg, 0.915 mmol, 10 eq.). The resulting green suspension was stirred at 80°C for 16 h, cooled down and transferred into a 50 mL centrifugation tube. An excess (40 mL) of Et_2O were added to the solution to precipitate a brownish solid, which washed with H_2O (3x10 mL) and dried under reduced pressure. The obtained solid was hence redissolved in a small amount of MeCN and filtered through a Celite® pad, to remove the possible Ag contaminations. A fractional precipitation was also attempted (DMF:Et_2O), but no clear evidence of a defined chemical compound was obtained. Therefore, by slowly diffusion of Et_2O into a concentrated solution of DMF (at r.t.), orange-brown needles were obtained, which were analysed by SC X-ray crystallography. The obtained complex was **[(Cu₂L^{Et})₂Cl] (PF₆)₃**, in which one chloride ion (deriving from not fully reacted CuC_2) is encapsulated by two cationic bimetallic fragments.

In order to obtain the single **Cu_2L^{Et} (PF_6)_2** complex, this synthetic procedure needs to be optimized and performed with pure reagents, especially the photolabile AgPF6, whose main role (precipitate all Cl$^-$ as AgCl) is crucial to provide a highly reactive Cu(II) ion in a chloride-free environment.

6 REFERENCES

[1]   in *The New York Times*, **1959**.
[2]   in *The Wiley-Blackwell Encyclopedia of Globalization*.
[3]   https://www.esrl.noaa.gov/gmd/ccgg/trends/global.html.
[4]   in *Climate Change 2013 – The Physical Science Basis: Working Group I Contribution to the Fifth Assessment Report of the Intergovernmental Panel on Climate Change* (Ed.: C. Intergovernmental Panel on Climate), Cambridge University Press, Cambridge, **2014**, pp. 1-30.
[5]   T. A. Boden, G. Marland, and R.J. Andres, Information Analysis Center, Oak Ridge National Laboratory, U.S. Department of Energy, USA, **2014**.
[6]   http://www.esrl.noaa.gov/gmd/ccgg/trends/mlo.html.
[7]   M. C. Colin Baird, *ENVIRONMENTAL CHEMISTRY*, 5th Edition ed., W. H. Freeman and Company New York, **2012**.
[8]   A. Aruliah, energypost.eu, **July 10, 2019**
[9]   Z.-s. Hong, Y. Cao, J.-f. Deng, K.-n. Fan, *Catalysis Letters* **2002**, *82*, 37-44.
[10]   Z. Mohammad, M. Abdolsamad Zarringhalam, R. Abdolhosein, O. Mohammad Reza, *International Journal of Chemical Reactor Engineering* **2010**, *8*.
[11]   T. Riedel, H. Schulz, G. Schaub, K.-W. Jun, J.-S. Hwang, K.-W. Lee, *Topics in Catalysis* **2003**, *26*, 41-54.
[12]   M. Aresta, A. Dibenedetto, A. Angelini, *Chem Rev* **2014**, *114*, 1709-1742.
[13]   N. A. Tappe, R. M. Reich, V. D'Elia, F. E. Kühn, *Dalton Transactions* **2018**, *47*, 13281-13313.
[14]   C.-K. Ran, X.-W. Chen, Y.-Y. Gui, J. Liu, L. Song, K. Ren, D.-G. Yu, *Science China Chemistry* **2020**, *63*, 1336-1351.
[15]   M. Cokoja, C. Bruckmeier, B. Rieger, W. A. Herrmann, F. E. Kühn, *Angewandte Chemie International Edition* **2011**, *50*, 8510-8537.
[16]   Y. Kayaki, M. Yamamoto, T. Ikariya, *Angewandte Chemie* **2009**, *121*, 4258-4261.
[17]   G. Yuan, C. Qi, W. Wu, H. Jiang, *Current Opinion in Green and Sustainable Chemistry* **2017**, *3*, 22-27.
[18]   D. J. M. Snelders, G. van Koten, R. J. M. Klein Gebbink, *Journal of the American Chemical Society* **2009**, *131*, 11407-11416.
[19]   I. I. Boogaerts, S. P. Nolan, *Journal of the American Chemical Society* **2010**, *132*, 8858-8859.
[20]   S. Gaillard, A. M. Slawin, S. P. Nolan, *Chemical communications* **2010**, *46*, 2742-2744.
[21]   L. Zhang, J. Cheng, T. Ohishi, Z. Hou, *Angewandte Chemie International Edition* **2010**, *49*, 8670-8673.
[22]   P. Shao, S. Wang, C. Chen, C. Xi, *Organic letters* **2016**, *18*, 2050-2053.
[23]   X. Wang, M. Nakajima, R. Martin, *Journal of the American Chemical Society* **2015**, *137*, 8924-8927.
[24]   M. Ishii, F. Mori, K. Tanaka, *Chemistry–A European Journal* **2014**, *20*, 2169-2174.
[25]   X.-W. Chen, L. Zhu, Y.-Y. Gui, K. Jing, Y.-X. Jiang, Z.-Y. Bo, Y. Lan, J. Li, D.-G. Yu, *Journal of the American Chemical Society* **2019**, *141*, 18825-18835.
[26]   A. M. Appel, J. E. Bercaw, A. B. Bocarsly, H. Dobbek, D. L. DuBois, M. Dupuis, J. G. Ferry, E. Fujita, R. Hille, P. J. A. Kenis, C. A. Kerfeld, R. H. Morris, C. H. F.

Peden, A. R. Portis, S. W. Ragsdale, T. B. Rauchfuss, J. N. H. Reek, L. C. Seefeldt, R. K. Thauer, G. L. Waldrop, *Chemical Reviews* **2013**, *113*, 6621-6658.

[27] S. Bagherzadeh, N. P. Mankad, *Journal of the American Chemical Society* **2015**, *137*, 10898-10901.

[28] J.-H. Jeoung, H. Dobbek, *Science* **2007**, *318*, 1461.

[29] H. Dobbek, L. Gremer, R. Kiefersauer, R. Huber, O. Meyer, *Proceedings of the National Academy of Sciences* **2002**, *99*, 15971.

[30] M. Hofmann, J. K. Kassube, T. Graf, *JBIC Journal of Biological Inorganic Chemistry* **2005**, *10*, 490-495.

[31] N. P. Mankad, *Chemistry – A European Journal* **2016**, *22*, 5822-5829.

[32] S. Gambarotta, F. Arena, C. Floriani, P. F. Zanazzi, *Journal of the American Chemical Society* **1982**, *104*, 5082-5092.

[33] O. Cooper, C. Camp, J. Pécaut, C. E. Kefalidis, L. Maron, S. Gambarelli, M. Mazzanti, *Journal of the American Chemical Society* **2014**, *136*, 6716-6723.

[34] M. Hoppert, in *Encyclopedia of Geobiology* (Eds.: J. Reitner, V. Thiel), Springer Netherlands, Dordrecht, **2011**, pp. 558-563.

[35] D. Fregona, Università degli Studi di Padova, **2019**.

[36] J. L. Dreyer, *Experientia* **1984**, *40*, 653-675.

[37] K. Brown, M. Tegoni, M. Prudêncio, A. S. Pereira, S. Besson, J. J. Moura, I. Moura, C. Cambillau, *Nature Structural Biology* **2000**, *7*, 191-195.

[38] V. R. Kaila, M. P. Johansson, D. Sundholm, L. Laakkonen, M. Wistrom, *Biochim Biophys Acta* **2009**, *1787*, 221-233.

[39] G. Backes, Y. Mino, T. M. Loehr, T. E. Meyer, M. A. Cusanovich, W. V. Sweeney, E. T. Adman, J. Sanders-Loehr, *Journal of the American Chemical Society* **1991**, *113*, 2055-2064.

[40] R. Bonnett, in *The Porphyrins* (Ed.: D. Dolphin), Academic Press, **1978**, pp. 1-27.

[41] G. Melson, *Coordination chemistry of macrocyclic compounds*, Springer Science & Business Media, **2012**.

[42] S. Hiroto, Y. Miyake, H. Shinokubo, *Chemical reviews* **2017**, *117*, 2910-3043.

[43] K. Kadish, K. M. Smith, R. Guilard, *The Porphyrin Handbook: Chlorophylls and Bilins: Biosynthesis, Synthesis and Degradation, Vol. 13*, Elsevier, **2000**.

[44] D. K. Cabbiness, D. W. Margerum, *Journal of the American Chemical Society* **1969**, *91*, 6540-6541.

[45] A. W. Adamson, *Journal of the American Chemical Society* **1954**, *76*, 1578-1579.

[46] E. V. Anslyn, D. A. Dougherty, *Modern physical organic chemistry*, University science books, **2006**.

[47] G. P. MOSS, *European Journal of Biochemistry* **1988**, *178*, 277-328.

[48] M. M. Pereira, L. D. Dias, M. J. F. Calvete, *ACS Catalysis* **2018**, *8*, 10784-10808.

[49] R. Singh, A. Mukherjee, *ACS Catalysis* **2019**, *9*, 3604-3617.

[50] M. Hammouche, D. Lexa, J. M. Savéant, M. Momenteau, *Journal of Electroanalytical Chemistry and Interfacial Electrochemistry* **1988**, *249*, 347-351.

[51] C. Costentin, S. Drouet, M. Robert, J.-M. Savéant, *Science* **2012**, *338*, 90.

[52] I. Azcarate, C. Costentin, M. Robert, J.-M. Savéant, *Journal of the American Chemical Society* **2016**, *138*, 16639-16644.

[53] E. Vogel, M. Köcher, H. Schmickler, J. Lex, *Angewandte Chemie International Edition in English* **1986**, *25*, 257-259.

[54] J. L. Sessler, E. A. Brucker, S. J. Weghorn, M. Kisters, M. Schäfer, J. Lex, E. Vogel, *Angewandte Chemie International Edition in English* **1994**, *33*, 2308-2312.

[55] A. Srinivasan, H. Furuta, *Accounts of Chemical Research* **2005**, *38*, 10-20.

[56] E. Vogel, P. Scholz, R. Demuth, C. Erben, M. Bröring, H. Schmickler, J. Lex, G. Hohlneicher, D. Bremm, Y.-D. Wu, *Angewandte Chemie International Edition* **1999**, *38*, 2919-2923.

[57] H. Furuta, T. Asano, T. Ogawa, *Journal of the American Chemical Society* **1994**, *116*, 767-768.

[58] P. J. Chmielewski, L. Latos-Grażyński, K. Rachlewicz, T. Glowiak, *Angewandte Chemie International Edition in English* **1994**, *33*, 779-781.

[59] A. Srinivasan, T. Ishizuka, A. Osuka, H. Furuta, *Journal of the American Chemical Society* **2003**, *125*, 878-879.

[60] H. Rexhausen, A. Gossauer, *Journal of the Chemical Society, Chemical Communications* **1983**, 275-275.

[61] J. L. Sessler, D. Seidel, *Angewandte Chemie International Edition* **2003**, *42*, 5134-5175.

[62] R. Bonnett, *Chemical Society Reviews* **1995**, *24*, 19-33.

[63] J. L. Sessler, G. Hemmi, T. D. Mody, T. Murai, A. Burrell, S. W. Young, *Accounts of chemical research* **1994**, *27*, 43-50.

[64] H. Furuta, T. Ogawa, Y. Uwatoko, K. Araki, *Inorganic Chemistry* **1999**, *38*, 2676-2682.

[65] H. Furuta, H. Maeda, A. Osuka, *Journal of the American Chemical Society* **2000**, *122*, 803-807.

[66] M. Broadhurst, R. Grigg, A. Johnson, *Journal of the Chemical Society D: Chemical Communications* **1969**, 23-24.

[67] J. L. Sessler, R. A. Miller, *Biochem Pharmacol* **2000**, *59*, 733-739.

[68] R. Shimanovich, S. Hannah, V. Lynch, N. Gerasimchuk, T. D. Mody, D. Magda, J. Sessler, J. T. Groves, *J Am Chem Soc* **2001**, *123*, 3613-3614.

[69] S. J. Weghorn, J. L. Sessler, V. Lynch, T. F. Baumann, J. W. Sibert, *Inorganic chemistry* **1996**, *35*, 1089-1090.

[70] S. Mori, A. Osuka, *Journal of the American Chemical Society* **2005**, *127*, 8030-8031.

[71] L. K. Frensch, K. Pröpper, M. John, S. Demeshko, C. Brückner, F. Meyer, *Angewandte Chemie International Edition* **2011**, *50*, 1420-1424.

[72] T. D. Lash, A. M. Young, A. L. Von Ruden, G. M. Ferrence, *Chemical Communications* **2008**, 6309-6311.

[73] L. K. Blusch, K. E. Craigo, V. Martin-Diaconescu, A. B. McQuarters, E. Bill, S. Dechert, S. DeBeer, N. Lehnert, F. Meyer, *Journal of the American Chemical Society* **2013**, *135*, 13892-13899.

[74] A. Vogel, S. Dechert, C. Brückner, F. Meyer, *Inorganic Chemistry* **2017**, *56*, 2221-2232.

[75] S. J. Dorazio, A. Vogel, S. Dechert, D. E. Nevonen, V. N. Nemykin, C. Brückner, F. Meyer, *Inorganic Chemistry* **2020**, *59*, 7290-7305.

[76] L. K. Blusch, O. Mitevski, V. Martin-Diaconescu, K. Pröpper, S. DeBeer, S. Dechert, F. Meyer, *Inorganic Chemistry* **2014**, *53*, 7876-7885.

[77] K. Tatsumi, R. Hoffmann, *Journal of the American Chemical Society* **1981**, *103*, 3328-3341.

[78] P. J. Altmann, C. Jandl, A. Pöthig, *Dalton Transactions* **2015**, *44*, 11278-11281.

[79] T. Pickl, Technischen Universität München (Munich), **2020**.

[80] P. J. Altmann, A. Pöthig, *Angewandte Chemie International Edition* **2017**, *56*, 15733-15736.

[81] P. J. Altmann, A. Pöthig, *Journal of the American Chemical Society* **2016**, *138*, 13171-13174.

[82] Y. Zhou, Z. Xi, W. Chen, D. Wang, *Organometallics* **2008**, *27*, 5911-5920.

[83] B. Liu, B. Liu, Y. Zhou, W. Chen, *Organometallics* **2010**, *29*, 1457-1464.

[84] T. Guo, S. Dechert, F. Meyer, *Organometallics* **2014**, *33*, 5145-5155.

[85] Y. Zhou, W. Chen, *Organometallics* **2007**, *26*, 2742-2746.

[86] S. A. Reindl, A. Pöthig, M. Drees, B. Bechlars, E. Herdtweck, W. A. Herrmann, F. E. Kühn, *Organometallics* **2013**, *32*, 4082-4091.

[87] J. F. Hartwig, *Organotransition metal chemistry: from bonding to catalysis*, Univ Science Books, **2010**.

[88] M. N. Hopkinson, C. Richter, M. Schedler, F. Glorius, *Nature* **2014**, *510*, 485-496.

[89] P. de Frémont, N. Marion, S. P. Nolan, *Coordination Chemistry Reviews* **2009**, *253*, 862-892.

[90] E. A. Kantchev, C. J. O'Brien, M. G. Organ, *Angew Chem Int Ed Engl* **2007**, *46*, 2768-2813.

[91] C. Valente, S. Çalimsiz, K. H. Hoi, D. Mallik, M. Sayah, M. G. Organ, *Angewandte Chemie International Edition* **2012**, *51*, 3314-3332.

[92] aC. Samojłowicz, M. Bieniek, K. Grela, *Chemical Reviews* **2009**, *109*, 3708-3742; bG. C. Vougioukalakis, R. H. Grubbs, *Chemical Reviews* **2010**, *110*, 1746-1787.

[93] H. Stevens, P.-C. Duan, S. Dechert, F. Meyer, *Journal of the American Chemical Society* **2020**.

[94] N. Marion, S. P. Nolan, *Chemical Society Reviews* **2008**, *37*, 1776-1782.

[95] A. T. Normand, K. J. Cavell, *European Journal of Inorganic Chemistry* **2008**, *2008*, 2781-2800.

[96] aB. Marciniec, in *Hydrosilylation: A Comprehensive Review on Recent Advances* (Ed.: B. Marciniec), Springer Netherlands, Dordrecht, **2009**, pp. 87-123; bF. Wang, L.-j. Liu, W. Wang, S. Li, M. Shi, *Coordination Chemistry Reviews* **2012**, *256*, 804-853.

[97] L. Mercs, M. Albrecht, *Chemical Society Reviews* **2010**, *39*, 1903-1912.

[98] A. Biffis, M. Baron, C. Tubaro, in *Advances in Organometallic Chemistry, Vol. 63* (Ed.: P. J. Pérez), Academic Press, **2015**, pp. 203-288.

[99] D. Martin, M. Soleilhavoup, G. Bertrand, *Chemical Science* **2011**, *2*, 389-399.

[100] M. Fevre, J. Pinaud, Y. Gnanou, J. Vignolle, D. Taton, *Chem Soc Rev* **2013**, *42*, 2142-2172.

[101] G. A. Grasa, T. Güveli, R. Singh, S. P. Nolan, *The Journal of Organic Chemistry* **2003**, *68*, 2812-2819.

[102] H.-W. Wanzlick, H.-J. Schönherr, *Angewandte Chemie International Edition in English* **1968**, *7*, 141-142.

[103] K. Öfele, *Journal of Organometallic Chemistry* **1968**, *12*, P42-P43.

[104] A. J. Arduengo, R. L. Harlow, M. Kline, *Journal of the American Chemical Society* **1991**, *113*, 361-363.

[105] W. A. Herrmann, M. Elison, J. Fischer, C. Köcher, G. R. J. Artus, *Angewandte Chemie International Edition in English* **1995**, *34*, 2371-2374.

[106] F. E. Hahn, M. C. Jahnke, *Angewandte Chemie International Edition* **2008**, *47*, 3122-3172.

[107] C. A. Tolman, *Chemical Reviews* **1977**, *77*, 313-348.

[108] C. Köcher, W. A. Herrmann, *Journal of Organometallic Chemistry* **1997**, *532*, 261-265.

[109] E. L. Rosen, C. D. Varnado, A. G. Tennyson, D. M. Khramov, J. W. Kamplain, D. H. Sung, P. T. Cresswell, V. M. Lynch, C. W. Bielawski, *Organometallics* **2009**, *28*, 6695-6706.

[110] A. Poater, B. Cosenza, A. Correa, S. Giudice, F. Ragone, V. Scarano, L. Cavallo, *European Journal of Inorganic Chemistry* **2009**, *2009*, 1759-1766.

[111] M. Poyatos, J. A. Mata, E. Peris, *Chemical Reviews* **2009**, *109*, 3677-3707.

[112] X. Chi, W. Cen, J. A. Queenan, L. Long, V. M. Lynch, N. M. Khashab, J. L. Sessler, *Journal of the American Chemical Society* **2019**, *141*, 6468-6472.

[113] F. Zapata, A. Caballero, N. G. White, T. D. W. Claridge, P. J. Costa, V. t. Félix, P. D. Beer, *Journal of the American Chemical Society* **2012**, *134*, 11533-11541.

[114] J. Yoon, S. K. Kim, N. J. Singh, K. S. Kim, *Chemical Society Reviews* **2006**, *35*, 355-360.

[115] S. W. Robinson, C. L. Mustoe, N. G. White, A. Brown, A. L. Thompson, P. Kennepohl, P. D. Beer, *Journal of the American Chemical Society* **2015**, *137*, 499-507.

[116] B. M. Rambo, H.-Y. Gong, M. Oh, J. L. Sessler, *Accounts of Chemical Research* **2012**, *45*, 1390-1401.

[117] F. E. Hahn, V. Langenhahn, T. Lügger, T. Pape, D. Le Van, *Angew Chem Int Ed Engl* **2005**, *44*, 3759-3763.

[118] L. Zhang, Y.-F. Han, *Dalton Transactions* **2018**, *47*, 4267-4272.

[119] M.-M. Gan, J.-Q. Liu, L. Zhang, Y.-Y. Wang, F. E. Hahn, Y.-F. Han, *Chemical Reviews* **2018**, *118*, 9587-9641.

[120] M. V. Baker, B. W. Skelton, A. H. White, C. C. Williams, *Organometallics* **2002**, *21*, 2674-2678.

[121] I. Klawitter, M. R. Anneser, S. Dechert, S. Meyer, S. Demeshko, S. Haslinger, A. Pöthig, F. E. Kühn, F. Meyer, *Organometallics* **2015**, *34*, 2819-2825.

[122] Y. Liu, S. G. Resch, I. Klawitter, G. E. Cutsail III, S. Demeshko, S. Dechert, F. E. Kühn, S. DeBeer, F. Meyer, *Angewandte Chemie International Edition* **2020**, *59*, 5696-5705.

[123] P. J. Barnard, M. V. Baker, S. J. Berners-Price, B. W. Skelton, A. H. White, *Dalton Transactions* **2004**, 1038-1047.

[124] M. V. Baker, S. K. Brayshaw, B. W. Skelton, A. H. White, C. C. Williams, *Journal of Organometallic Chemistry* **2005**, *690*, 2312-2322.

[125] M. V. Baker, D. H. Brown, P. V. Simpson, B. W. Skelton, A. H. White, C. C. Williams, *Journal of Organometallic Chemistry* **2006**, *691*, 5845-5855.

[126] C. Schulte to Brinke, F. Ekkehardt Hahn, *Dalton Transactions* **2015**, *44*, 14315-14322.

[127] T. Lu, C.-F. Yang, L.-Y. Zhang, F. Fei, X.-T. Chen, Z.-L. Xue, *Inorganic Chemistry* **2017**, *56*, 11917-11928.

[128] H. M. Bass, S. A. Cramer, J. L. Price, D. M. Jenkins, *Organometallics* **2010**, *29*, 3235-3238.

[129] S. A. Cramer, D. M. Jenkins, *Journal of the American Chemical Society* **2011**, *133*, 19342-19345.

[130] A. A. Massie, C. Schremmer, I. Rüter, S. Dechert, I. Siewert, F. Meyer, *ACS Catalysis* **2021**, *11*, 3257-3267.

[131] P. J. Altmann, D. T. Weiss, C. Jandl, F. E. Kühn, *Chemistry – An Asian Journal* **2016**, *11*, 1597-1605.

[132] Z. S. Ghavami, M. R. Anneser, F. Kaiser, P. J. Altmann, B. J. Hofmann, J. F. Schlagintweit, G. Grivani, F. E. Kühn, *Chemical Science* **2018**, *9*, 8307-8314.

[133] E. B. Bauer, M. A. Bernd, M. Schütz, J. Oberkofler, A. Pöthig, R. M. Reich, F. E. Kühn, *Dalton Transactions* **2019**, *48*, 16615-16625.

[134] M. R. Anneser, S. Haslinger, A. Pöthig, M. Cokoja, V. D'Elia, M. P. Högerl, J.-M. Basset, F. E. Kühn, *Dalton Transactions* **2016**, *45*, 6449-6455.

[135] J. W. Kück, M. R. Anneser, B. Hofmann, A. Pöthig, M. Cokoja, F. E. Kühn, *ChemSusChem* **2015**, *8*, 4056-4063.

[136] J. F. Schlagintweit, P. J. Altmann, A. D. Böth, B. J. Hofmann, C. Jandl, C. Kaußler, L. Nguyen, R. M. Reich, A. Pöthig, F. E. Kühn, *Chemistry – A European Journal* **2021**, *27*, 1311-1315.

[137] R. Francke, B. Schille, M. Roemelt, *Chemical Reviews* **2018**, *118*, 4631-4701.

[138] L.-S. Wang, J. E. Reutt, Y. T. Lee, D. A. Shirley, *Journal of Electron Spectroscopy and Related Phenomena* **1988**, *47*, 167-186.

[139] G. L. Gutsev, R. J. Bartlett, R. N. Compton, *The Journal of Chemical Physics* **1998**, *108*, 6756-6762.

[140] T. M. T.-O. Klapötke, I. C.; Oetting, I. C. T., *Nichtmetallchemie*, Wiley VCH, Weinheim, **1994**.

[141] M. E. Vol'pin, I. S. Kolomnikov, *Pure and Applied Chemistry* **1973**, *33*, 567-582.

[142] A. D. Walsh, *Journal of the Chemical Society (Resumed)* **1953**, 2260-2266.

[143] R. Kortlever, I. Peters, S. Koper, M. T. M. Koper, *ACS Catalysis* **2015**, *5*, 3916-3923.

[144] K. E. Dalle, J. Warnan, J. J. Leung, B. Reuillard, I. S. Karmel, E. Reisner, *Chemical Reviews* **2019**, *119*, 2752-2875.

[145] M. Aresta, C. F. Nobile, V. G. Albano, E. Forni, M. Manassero, *Journal of the Chemical Society, Chemical Communications* **1975**, 636-637.

[146] P. Kang, C. Cheng, Z. Chen, C. K. Schauer, T. J. Meyer, M. Brookhart, *Journal of the American Chemical Society* **2012**, *134*, 5500-5503.

[147] A. J. Göttle, M. T. M. Koper, *Journal of the American Chemical Society* **2018**, *140*, 4826-4834.

[148] Y. Y. Birdja, PhD thesis, Leiden University **2018**.

[149] K. Tanaka, D. Ooyama, *Coordination Chemistry Reviews* **2002**, *226*, 211-218.

[150] B. H. Solis, A. G. Maher, D. K. Dogutan, D. G. Nocera, S. Hammes-Schiffer, *Proceedings of the National Academy of Sciences* **2016**, *113*, 485.

[151] J. Schneider, H. Jia, K. Kobiro, D. E. Cabelli, J. T. Muckerman, E. Fujita, *Energy & Environmental Science* **2012**, *5*, 9502-9510.

[152] Z. Weng, J. Jiang, Y. Wu, Z. Wu, X. Guo, K. L. Materna, W. Liu, V. S. Batista, G. W. Brudvig, H. Wang, *Journal of the American Chemical Society* **2016**, *138*, 8076-8079.

[153] E. E. Benson, C. P. Kubiak, A. J. Sathrum, J. M. Smieja, *Chemical Society Reviews* **2009**, *38*, 89-99.

[154] R. Angamuthu, P. Byers, M. Lutz, A. L. Spek, E. Bouwman, *Science* **2010**, *327*, 313-315.

[155] U. R. Pokharel, F. R. Fronczek, A. W. Maverick, *Nature Communications* **2014**, *5*, 5883.

[156] M. Beley, J.-P. Collin, R. Ruppert, J.-P. Sauvage, *Journal of the Chemical Society, Chemical Communications* **1984**, 1315-1316.

[157] J. P. Collin, A. Jouaiti, J. P. Sauvage, *Inorganic Chemistry* **1988**, *27*, 1986-1990.

[158] C. de Alwis, J. A. Crayston, T. Cromie, T. Eisenblätter, R. W. Hay, Y. D. Lampeka, L. V. Tsymbal, *Electrochimica acta* **2000**, *45*, 2061-2074.

[159] E. Y. Lee, D. Hong, H. W. Park, M. P. Suh, *European Journal of Inorganic Chemistry* **2003**, *2003*, 3242-3249.

[160] D. L. DuBois, A. Miedaner, R. C. Haltiwanger, *Journal of the American Chemical Society* **1991**, *113*, 8753-8764.

[161] J. W. Raebiger, J. W. Turner, B. C. Noll, C. J. Curtis, A. Miedaner, B. Cox, D. L. DuBois, *Organometallics* **2006**, *25*, 3345-3351.

[162] A. Miedaner, C. J. Curtis, R. M. Barkley, D. L. DuBois, *Inorganic Chemistry* **1994**, *33*, 5482-5490.

[163] B. D. Steffey, C. J. Curtis, D. L. DuBois, *Organometallics* **1995**, *14*, 4937-4943.

[164] Z. N. Zahran, E. A. Mohamed, Y. Naruta, *Scientific Reports* **2016**, *6*, 24533.

[165] I. Azcarate, C. Costentin, M. Robert, J.-M. Savéant, *The Journal of Physical Chemistry C* **2016**, *120*, 28951-28960.

[166] C. Costentin, S. Drouet, G. Passard, M. Robert, J.-M. Savéant, *Journal of the American Chemical Society* **2013**, *135*, 9023-9031.

[167] E. A. Mohamed, Z. N. Zahran, Y. Naruta, *Chemical Communications* **2015**, *51*, 16900-16903.

[168] C. W. Machan, S. A. Chabolla, J. Yin, M. K. Gilson, F. A. Tezcan, C. P. Kubiak, *Journal of the American Chemical Society* **2014**, *136*, 14598-14607.

[169] J. Hawecker, J.-M. Lehn, R. Ziessel, *Journal of the Chemical Society, Chemical Communications* **1984**, 328-330.

[170] J. M. Smieja, C. P. Kubiak, *Inorganic Chemistry* **2010**, *49*, 9283-9289.

[171] F. P. A. Johnson, M. W. George, F. Hartl, J. J. Turner, *Organometallics* **1996**, *15*, 3374-3387.

[172] B. P. Sullivan, C. M. Bolinger, D. Conrad, W. J. Vining, T. J. Meyer, *Journal of the Chemical Society, Chemical Communications* **1985**, 1414-1416.

[173] W. Yang, S. Sinha Roy, W. C. Pitts, R. L. Nelson, F. R. Fronczek, J. W. Jurss, *Inorganic Chemistry* **2018**, *57*, 9564-9575.

[174] H. Takeda, C. Cometto, O. Ishitani, M. Robert, *ACS Catalysis* **2017**, *7*, 70-88.

[175] M. D. Sampson, A. D. Nguyen, K. A. Grice, C. E. Moore, A. L. Rheingold, C. P. Kubiak, *Journal of the American Chemical Society* **2014**, *136*, 5460-5471.

[176] L. Chen, Z. Guo, X.-G. Wei, C. Gallenkamp, J. Bonin, E. Anxolabéhère-Mallart, K.-C. Lau, T.-C. Lau, M. Robert, *Journal of the American Chemical Society* **2015**, *137*, 10918-10921.

[177] M. Rudolph, S. Dautz, E.-G. Jäger, *Journal of the American Chemical Society* **2000**, *122*, 10821-10830.

[178] P. W. Jolly, K. Jonas, C. Krüger, Y. H. Tsay, *Journal of Organometallic Chemistry* **1971**, *33*, 109-122.

[179] I. S. Kolomnikov, T. S. Loveeva, V. V. Gorbachevskaya, G. G. Aleksandrov, Y. T. Struckhov, M. E. Vol'pin, *Journal of the Chemical Society D: Chemical Communications* **1971**, 972-973.

[180] F. Franco, M. F. Pinto, B. Royo, J. Lloret-Fillol, *Angewandte Chemie International Edition* **2018**, *57*, 4603-4606.

[181] C. Riplinger, M. D. Sampson, A. M. Ritzmann, C. P. Kubiak, E. A. Carter, *Journal of the American Chemical Society* **2014**, *136*, 16285-16298.

[182] V. S. Thoi, C. J. Chang, *Chemical Communications* **2011**, *47*, 6578-6580.

[183] V. S. Thoi, N. Kornienko, C. G. Margarit, P. Yang, C. J. Chang, *Journal of the American Chemical Society* **2013**, *135*, 14413-14424.

[184] M. Sheng, N. Jiang, S. Gustafson, B. You, D. H. Ess, Y. Sun, *Dalton Transactions* **2015**, *44*, 16247-16250.

[185] J. D. Cope, N. P. Liyanage, P. J. Kelley, J. A. Denny, E. J. Valente, C. E. Webster, J. H. Delcamp, T. K. Hollis, *Chemical Communications* **2017**, *53*, 9442-9445.

[186] J. A. Therrien, M. O. Wolf, B. O. Patrick, *Dalton Transactions* **2018**, *47*, 1827-1840.

[187] X. Su, K. M. McCardle, J. A. Panetier, J. W. Jurss, *Chemical Communications* **2018**, *54*, 3351-3354.

[188] X. Su, K. M. McCardle, L. Chen, J. A. Panetier, J. W. Jurss, *ACS Catalysis* **2019**, *9*, 7398-7408.

[189] A. J. B. a. L. R. Faulkner, *Electrochemical Methods: Fundamentals*

and Applications, 2nd edn ed., John Wiley and Sons, New York, **2001**.

[190] P. J. Altmann, A. Pöthig, *Chemical Communications* **2016**, *52*, 9089-9092.

[191] D. Mayer, Technischen Universität München (Garching bei Muenchen), **2016**.

[192] P. Altmann, Technischen Universität München (Garching bei München), **2014**.

[193] S. Mitra, A. K. Shukla, S. Sampath, *Journal of Power Sources* **2001**, *101*, 213-218.

[194] C. Schaller, **2020**.

[195] V. Barone, M. Cossi, *The Journal of Physical Chemistry A* **1998**, *102*, 1995-2001.

[196] C. Schulte to Brinke, T. Pape, F. E. Hahn, *Dalton Transactions* **2013**, *42*, 7330-7337.

[197] R. E. Andrew, C. M. Storey, A. B. Chaplin, *Dalton Transactions* **2016**, *45*, 8937-8944.

[198] Z. Lu, S. A. Cramer, D. M. Jenkins, *Chemical Science* **2012**, *3*, 3081-3087.

[199] A. Meyer, D. Abdullin, G. Schnakenburg, O. Schiemann, *Physical Chemistry Chemical Physics* **2016**, *18*, 9262-9271.

[200] M. J. Frisch, J. A. Pople, J. S. Binkley, *The Journal of Chemical Physics* **1984**, *80*, 3265-3269.

[201] M. B. Robin, P. Day, in *Advances in Inorganic Chemistry and Radiochemistry, Vol. 10* (Eds.: H. J. Emeléus, A. G. Sharpe), Academic Press, **1968**, pp. 247-422.

[202] J.-L. Chou, J.-P. Chyn, F. L. Urbach, D. F. Gervasio, *Polyhedron* **2000**, *19*, 2215-2223.

[203] P. Aguirre-Etcheverry, D. O'Hare, *Chemical Reviews* **2010**, *110*, 4839-4864.

[204] F. Meyer, A. Jacobi, L. Zsolnai, *Chemische Berichte* **1997**, *130*, 1441-1447.

[205] G.-F. Zhang, Q.-P. Zhou, Y.-L. Dou, M.-H. Yin, Y. Wang, *Applied Organometallic Chemistry* **2007**, *21*, 1059-1065.

[206] H. Stevens, P.-C. Duan, S. Dechert, F. Meyer, *Journal of the American Chemical Society* **2020**, *142*, 6717-6728.

[207] C. K. Jørgensen, *Coordination Chemistry Reviews* **1966**, *1*, 164-178.

[208] D.-H. Manz, P.-C. Duan, S. Dechert, S. Demeshko, R. Oswald, M. John, R. A. Mata, F. Meyer, *Journal of the American Chemical Society* **2017**, *139*, 16720-16731.

[209] N. Elgrishi, K. J. Rountree, B. D. McCarthy, E. S. Rountree, T. T. Eisenhart, J. L. Dempsey, *Journal of Chemical Education* **2018**, *95*, 197-206.

[210] D. M. D'Alessandro, F. R. Keene, *Chemical Society Reviews* **2006**, *35*, 424-440.

[211] A. Okuniewski, D. Rosiak, J. Chojnacki, B. Becker, *Polyhedron* **2015**, *90*, 47-57.

[212] Hendoa are the -CH2 methylene groups that point towards the bimetallic Ni-Ni core in the bowl-shaped complexes

[213] A. V. Marenich, C. J. Cramer, D. G. Truhlar, *The Journal of Physical Chemistry B* **2009**, *113*, 6378-6396.

[214] J. Cioslowski, *Journal of the American Chemical Society* **1989**, *111*, 8333-8336.

[215] A. Chapovetsky, T. H. Do, R. Haiges, M. K. Takase, S. C. Marinescu, *Journal of the American Chemical Society* **2016**, *138*, 5765-5768.

[216] C. Costentin, S. Drouet, M. Robert, J.-M. Savéant, *Journal of the American Chemical Society* **2012**, *134*, 11235-11242.

[217] J.-W. Wang, W.-J. Liu, D.-C. Zhong, T.-B. Lu, *Coordination Chemistry Reviews* **2019**, *378*, 237-261.

[218] W. A. Hoffert, J. A. S. Roberts, R. Morris Bullock, M. L. Helm, *Chemical Communications* **2013**, *49*, 7767-7769.

[219] M. Wang, L. Chen, L. Sun, *Energy & Environmental Science* **2012**, *5*, 6763-6778.

[220] J. D. Froehlich, C. P. Kubiak, *Journal of the American Chemical Society* **2015**, *137*, 3565-3573.

[221] K. Föttinger, R. Schlögl, G. Rupprechter, *Chemical Communications* **2008**, 320-322.

[222] A. M. Appel, M. L. Helm, *ACS Catalysis* **2014**, *4*, 630-633.

[223] C. W. Machan, C. P. Kubiak, *Dalton Transactions* **2016**, *45*, 15942-15950.

[224] J. E. Heimann, W. H. Bernskoetter, N. Hazari, James M. Mayer, *Chemical Science* **2018**, *9*, 6629-6638.

[225] M. M. Francl, W. J. Pietro, W. J. Hehre, J. S. Binkley, M. S. Gordon, D. J. DeFrees, J. A. Pople, *The Journal of Chemical Physics* **1982**, *77*, 3654-3665.

[226] E. Lindner, G. von Au, H.-J. Eberle, *Chemische Berichte* **1981**, *114*, 810-813.

7 Appendix

Geometrical Parameters
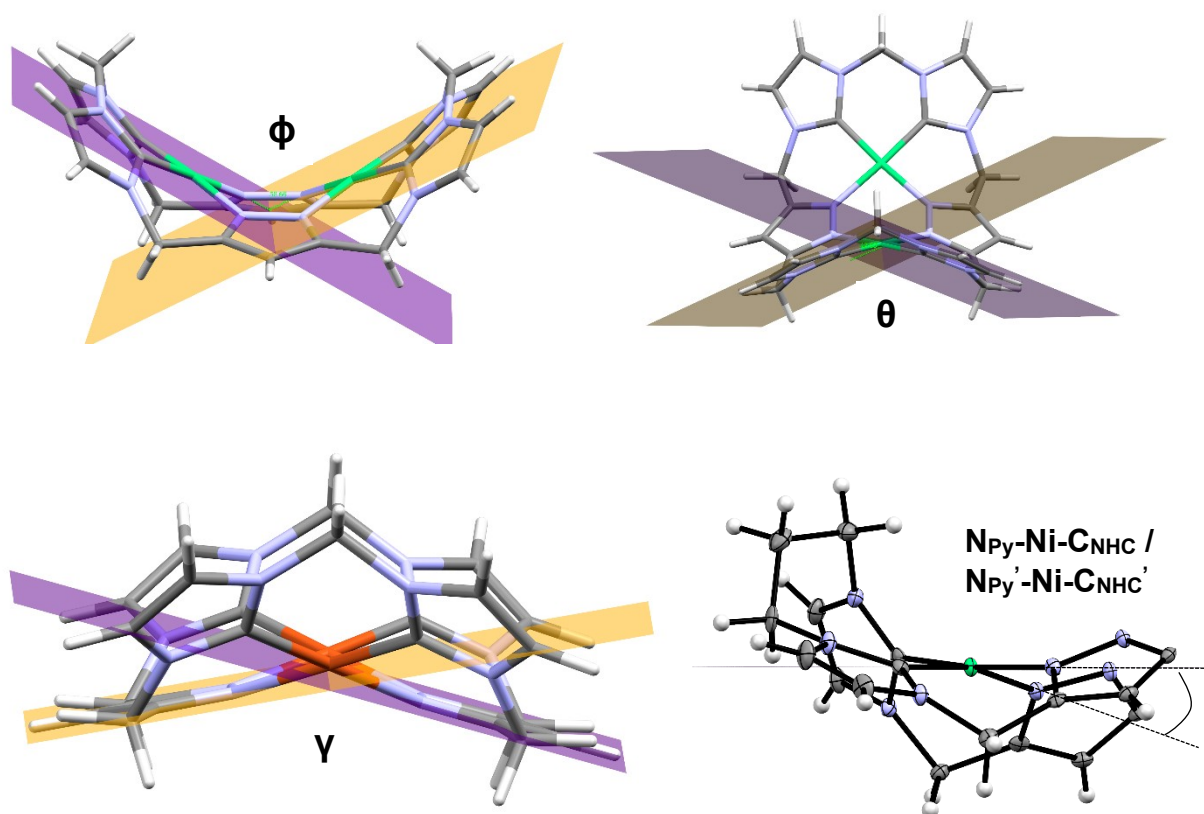
Figure 7.1 | Structural angles ϕ, θ and γ employed to compare the SC structures of the analysed complexes in **Table 3.1** and **Table 3.2**, as well as the N_{Py}-Ni-C_{NHC} / N_{Py}'-Ni-C_{NHC}' angle, used in **Table 3.5** to quantify the distortion from the ideal SP geometry.

The distortion from the perfect SP geometry has been evaluated with the τ_4' parameter, introduced by *Okuniewski et al.*, which has the following expression:[211]

$$\tau_4' = \frac{\beta - \alpha}{360° - \theta} + \frac{180° - \beta}{180 - \theta}$$

In which β, α ($\beta > \alpha$), are the two greatest valence angles, and θ is the tetrahedral angle.
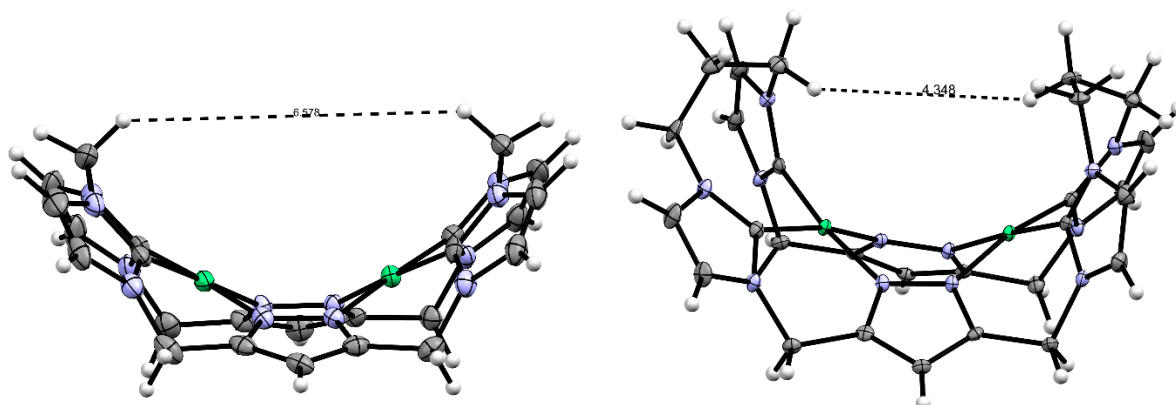
Figure 7.2 | Differences in cavity width in **Ni$_2$L^{Me}(PF$_6$)$_2$** (left, 6.578 Å) and **Ni$_2$L^{Pr}(PF$_6$)$_2$** (right, 4.348 Å).

CRYSTALLOGRAPHIC DATA

Cu$_2$L^{Me}(PF$_6$)$_2$

Identification Code	NeuSa2
Chemical formula	$C_{24}H_{22}F_{12}N_{12}P_2Cu_2$
Formula weight	895.55
Temperature	100(2) K
Wavelength	0.71073 Å
Crystal size	0.041 × 0.103 × 0.154 mm
Crystal system	orthorhombic
Space group	P n m a
Unit cell dimensions	a = 28.036 (8) Å α= 90°
	b = 14.833(4) Å β= 90°
	c = 8.057(2) Å γ= 90°
Volume	3350.6(16) Å^3
Z	4
Density (calculated)	1.775 g/cm^3
Absorption coefficient	1.471 mm^{-1}
F(000)	1784
Diffractometer	Bruker D8 Venture Duo IMS
Radiation source	TXS rotating anode, Mo
Theta range for data collection	2.63 to 25.02°
Index ranges	$-33 \leq h \leq 33, -17 \leq k \leq 17, -9 \leq l \leq 9$
Reflections collected	36412
Independent reflections	3087 R(int) = 0.1209
Coverage of independent reflections	99.9%
Absorption correction	Multi-Scan
Max. and min. transmission	0.9420 and 0.8050
Structure solution technique	direct methods
Structure solution program	SHELXT 2014/5 (Sheldrick, 2014)
Refinement method	Full-matrix least-squares on F^2
Refinement program	SHELXL-2018/3 (Sheldrick, 2018)
Function minimized	$\Sigma\ w(F_o^2 - F_c^2)^2$

Data / restraints / parameters	3087 / 696 / 432
Goodness-of-fit on F^2	1.153
Δ / σ max	0.001
Final R indices	2303 data; I>2o(I) R_1 = 0.0825, wR_2 = 0.1586
	all data R_1 = 0.1138, wR_2 = 0.1737
Weighting scheme	$w = 1/[\sigma^2(F_o)^2 + (0.0280P)^2 + 34.0555P]$
Largest diff. peak and hole	0.924 and -0.852 eÅ^3
R.M.S. deviation from mean	0.120 eÅ^3

$[(Cu_2L^{Et})_2Cl](PF_6)_3$

Identification Code	NeuSa3_1
Chemical formula	$C_{32}H_{40}Cl_{0.5}Cu_2F_9N_{14}O_2P_{1.5}$
Formula weight	1015.04
Temperature	100(2) K
Wavelength	0.71073 Å
Crystal size	0.162 × 0.170 × 0.253 mm
Crystal system	monoclinic
Space group	C 1 2/c 1
Unit cell dimensions	a = 16.0726 (15) Å α= 90°
	b = 31.749(4) Å β= 93.355(3)°
	c = 15.4759(2) Å γ= 90°
Volume	7883.6 (14) Å^3
Z	8
Density (calculated)	1.710 g/cm^3
Absorption coefficient	1.269 mm^{-1}
F(000)	4128
Diffractometer	Bruker D8 Venture Duo IMS
Radiation source	IMS microsource, Mo
Theta range for data collection	1.89 to 26.39°
Index ranges	$-20 \leq h \leq 20, -39 \leq k \leq 39, -19 \leq l \leq 19$
Reflections collected	199124
Independent reflections	8082 R(int) = 0.0307
Coverage of independent reflections	100.0%
Absorption correction	Multi-Scan
Max. and min. transmission	0.8210 and 0.7390
Structure solution technique	direct methods
Structure solution program	SHELXT 2014/5 (Sheldrick, 2014)
Refinement method	Full-matrix least-squares on F^2
Refinement program	SHELXL-2018/3 (Sheldrick, 2018)
Function minimized	$\Sigma\, w(F_o^2 - F_c^2)^2$
Data / restraints / parameters	8082 / 660 / 735
Goodness-of-fit on F^2	1.031
Δ / σ max	0.002
Final R indices	2303 data; I>2o(I) R_1 = 0.0235, wR_2 = 0.0597
	all data R_1 = 0.0253, wR_2 = 0.0609
Weighting scheme	$w = 1/[\sigma^2(F_o)^2 + (0.0264P)^2 + 15.1250P]$
Largest diff. peak and hole	0.671 and -0.281 eÅ^3
R.M.S. deviation from mean	0.050 eÅ^3

SPECTRA

For the ^{1}H-NMR spectra of compound **2-4** (**Errore. L'origine riferimento non è stata trovata.**), as well for that of **H₆L^Me (OTf)₄**, the interested reader could refer to the Supporting information of [78]. For the characterization of **H₆L^Et (OTf)₄**, instead, the reference paper is [190].

3,5-Bis(chloromethyl)-1-(tetrahydropyran-2-yl)-1H-pyrazole (5)
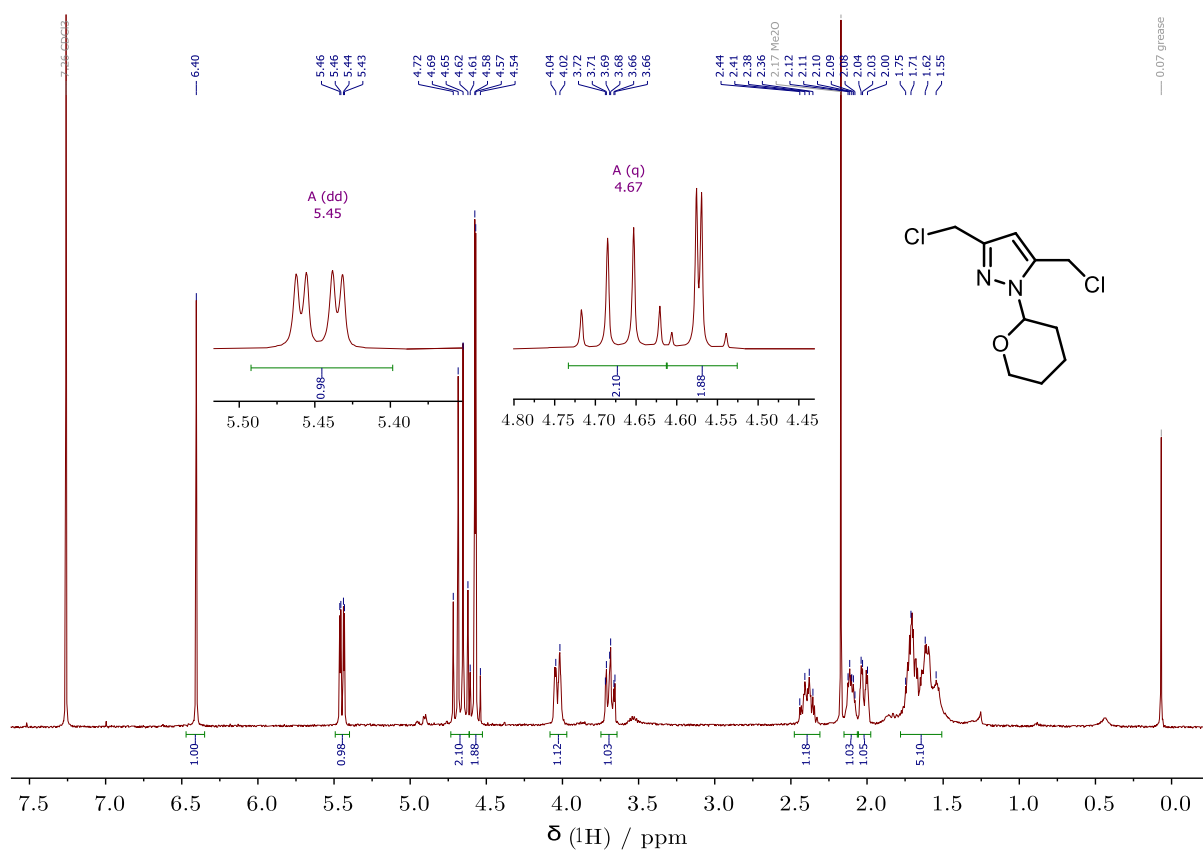
Sodium imidazolide (6)
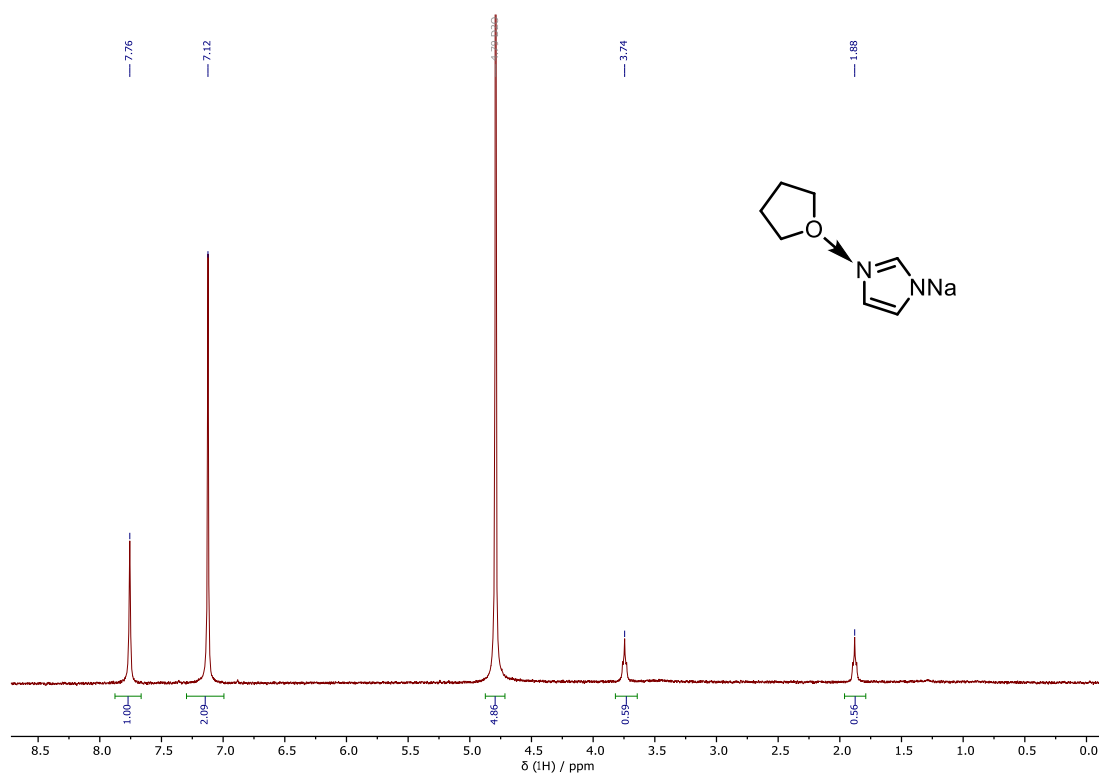
3,5-Bis(imidazol-1-ylmethyl)-1-(tetrahydropyran-2-yl)-1*H*-pyrazole (7)
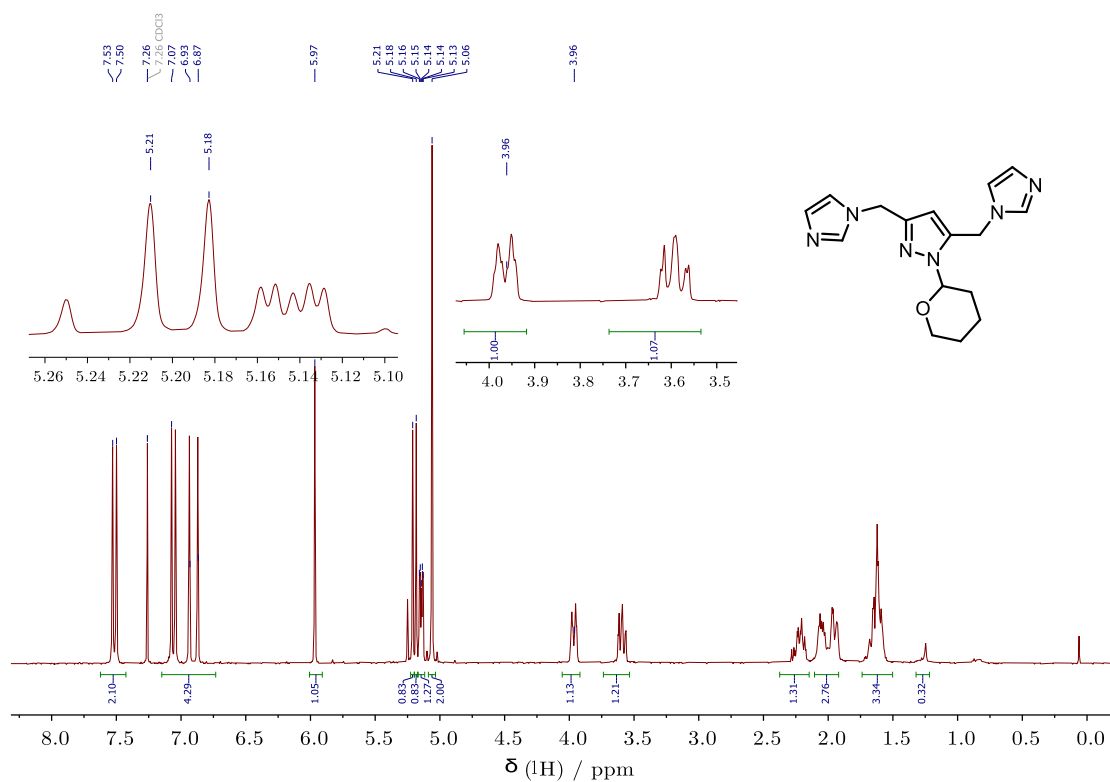
H6LMe (PF6)4
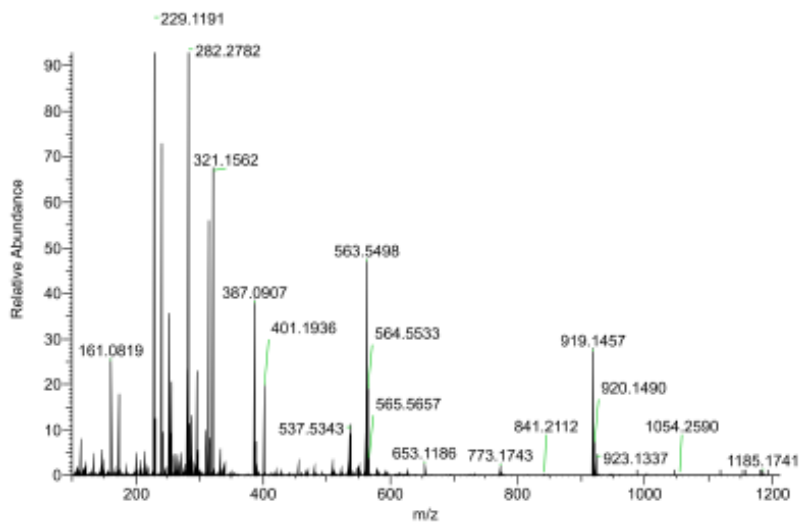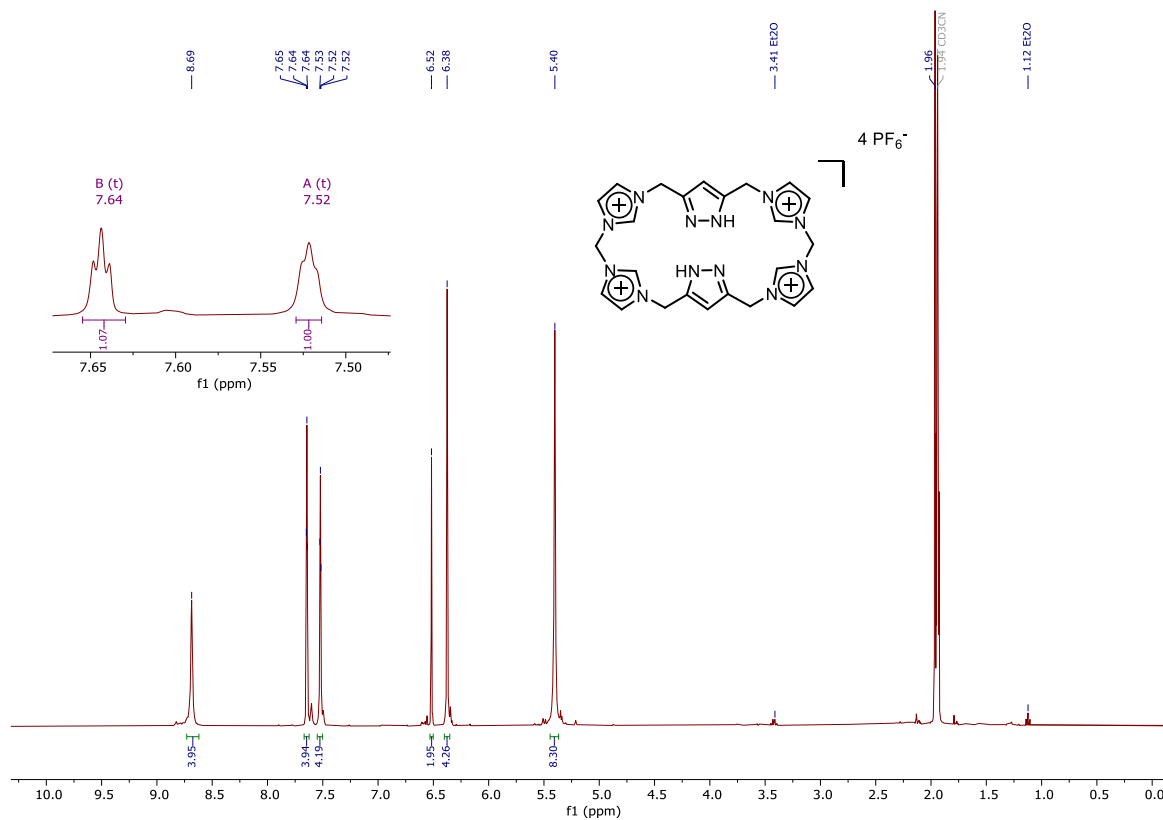
H₆L^{Et} (PF₆)₄

$H_6L^{Et} (PF_6)_4$

H6L^Pr (PF6)4

4 PF6^-

A (t) 7.43   B (t) 7.39

A (t) 4.15

A (p) 2.35
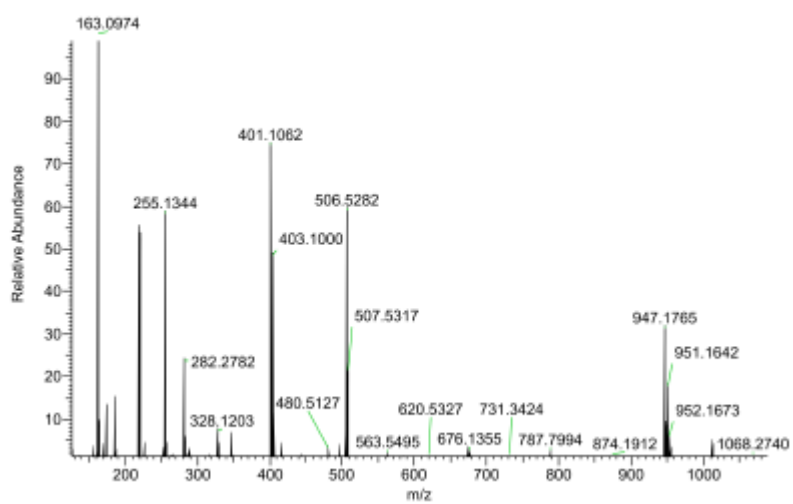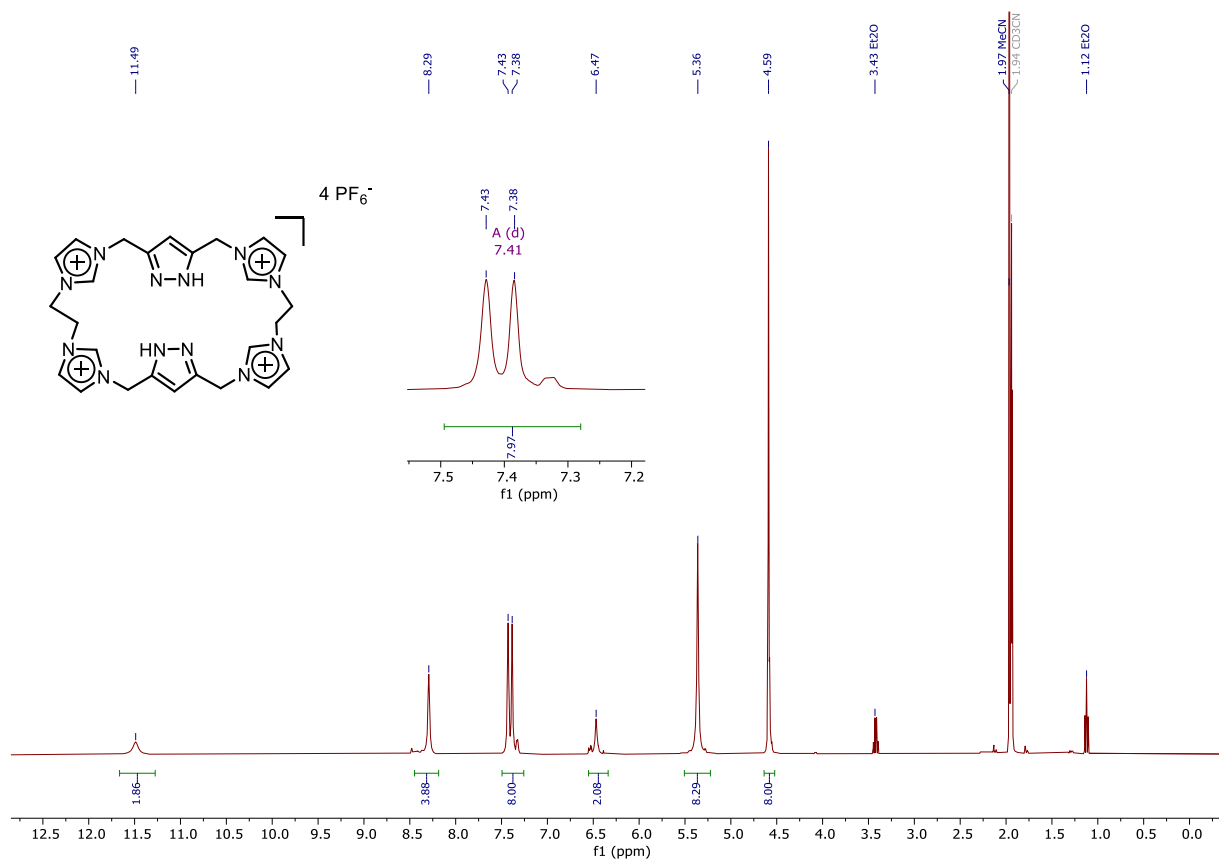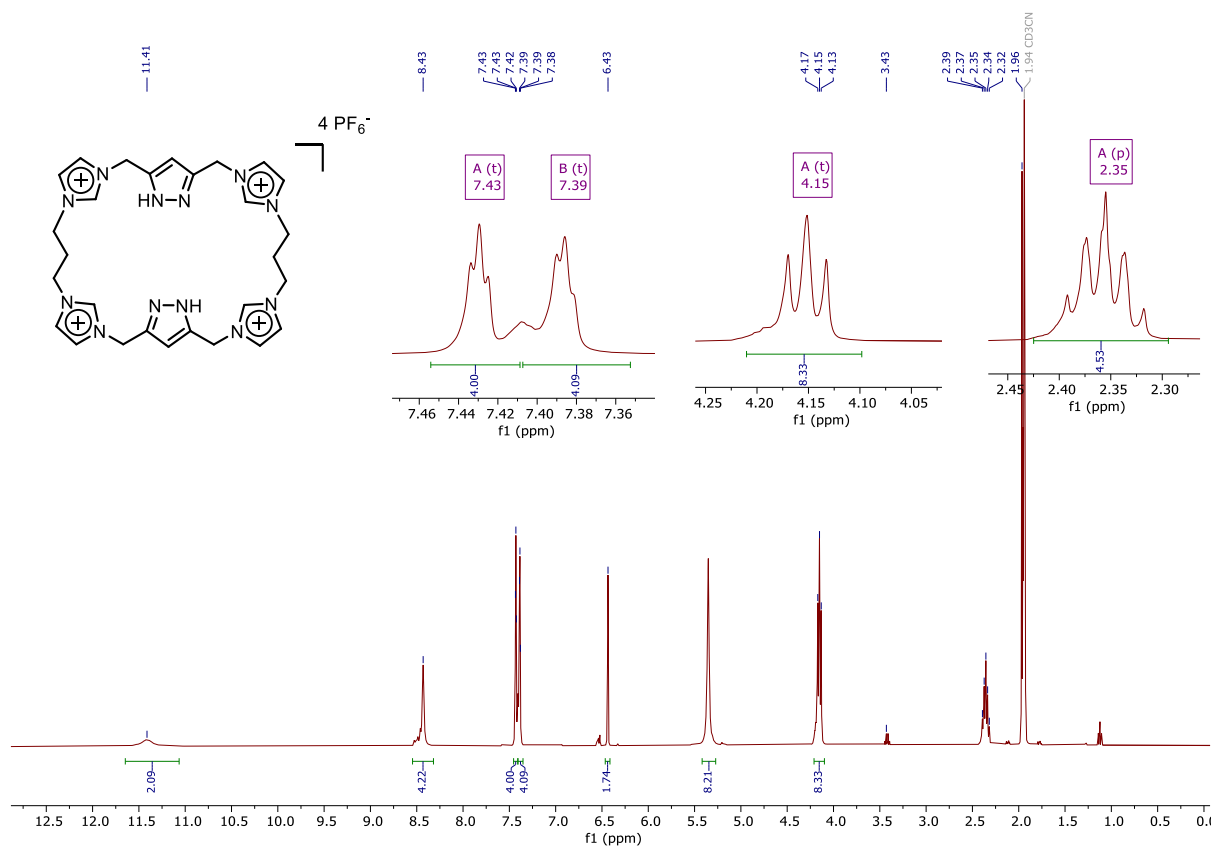
^13C{^1H} NMR
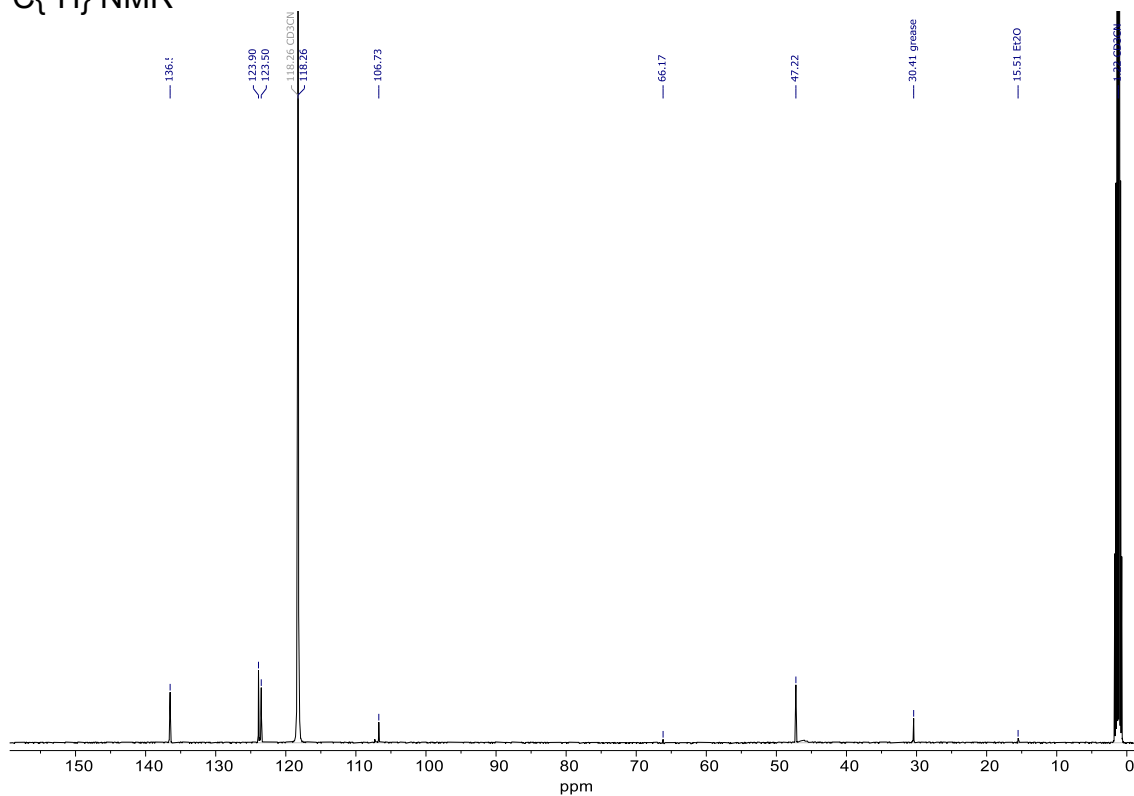
Ni₂L^{Me} (PF₆)₂

Ni₂L^Me (PF₆)₂
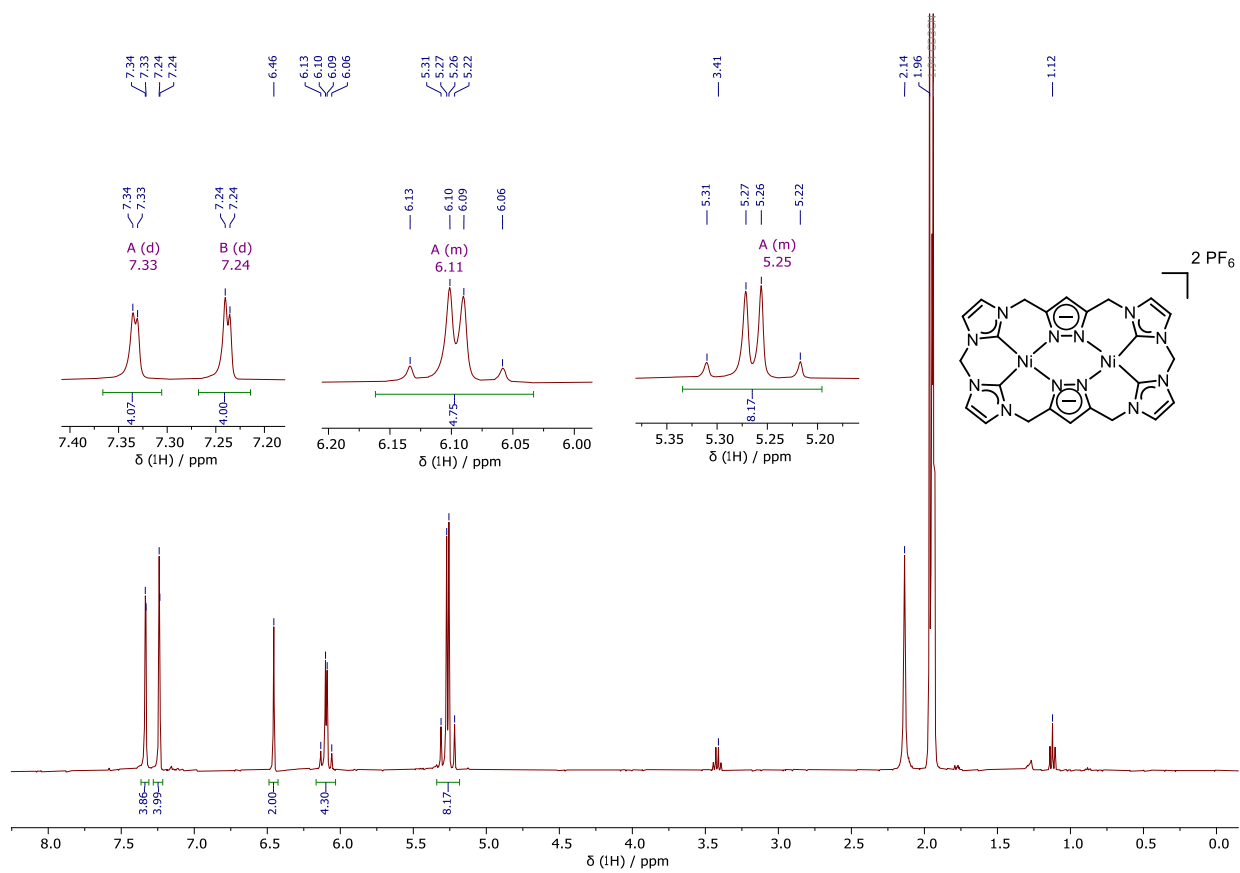
¹³C{¹H} NMR
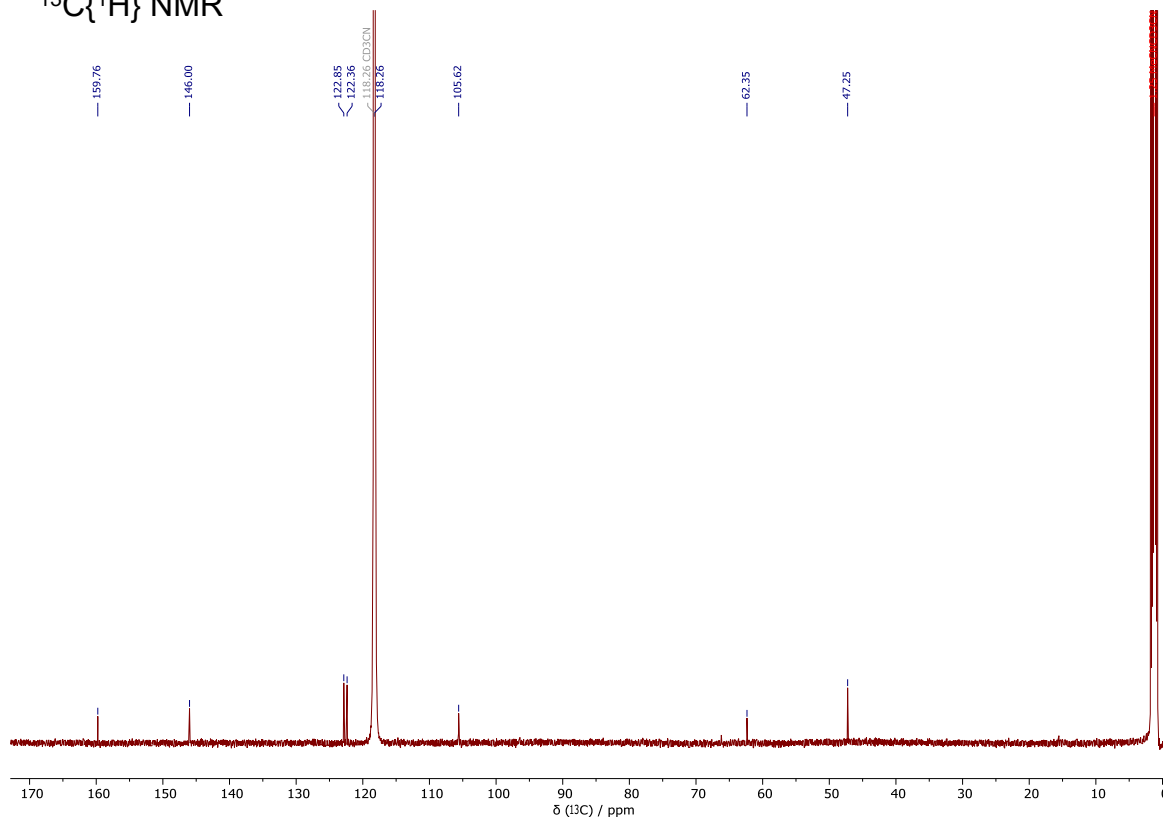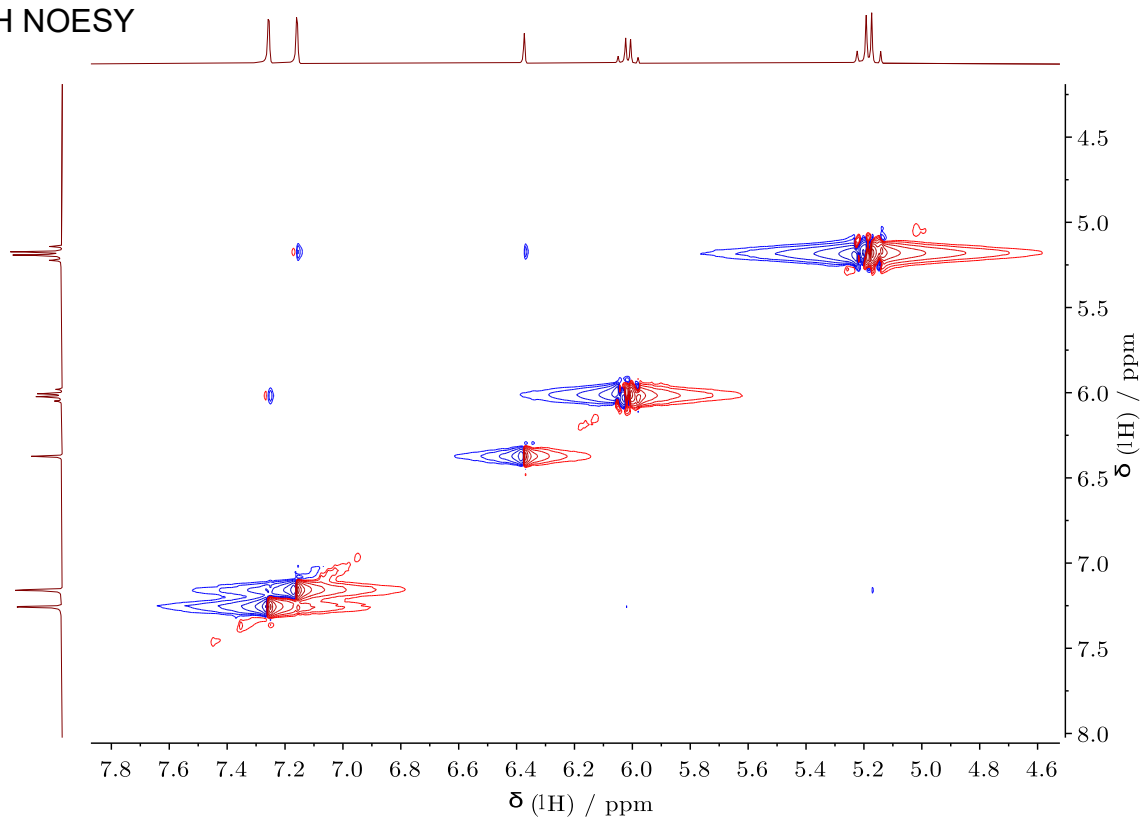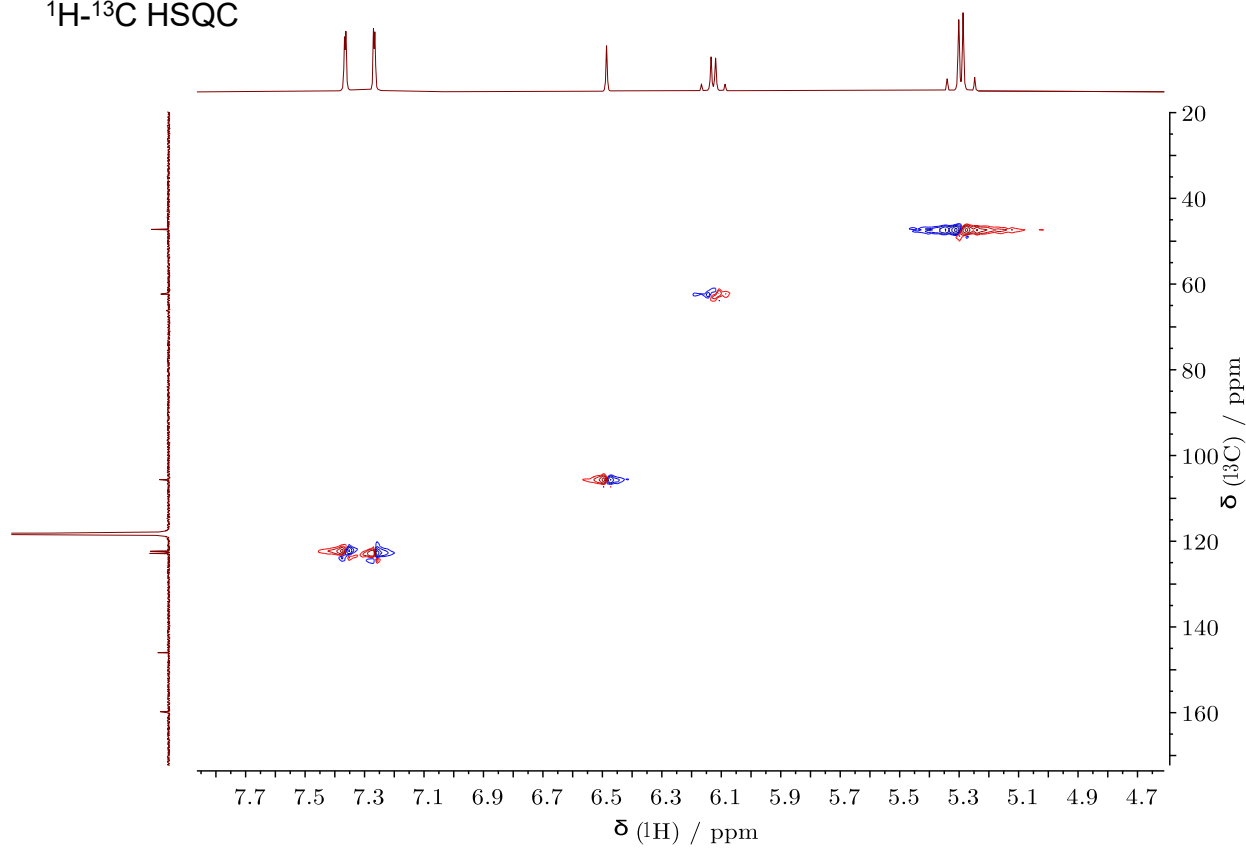
^{1}H-^{13}C HMBC

Ni$_2$L^{Et} (PF$_6$)$_2$

^{13}C{^{1}H} NMR

158.43
145.72
124.04
123.66
118.26 CD3CN
103.38
48.68
47.46
1.24 MeCNCD3CN

δ (1H) / ppm

170 160 150 140 130 120 110 100 90 80 70 60 50 40 30 20 10 0

^{1}H-^{13}C HSQC

δ (13C) / ppm

30 40 50 60 70 80 90 100 110 120 130 140 150 160 170

δ (1H) / ppm

7.8 7.6 7.4 7.2 7.0 6.8 6.6 6.4 6.2 6.0 5.8 5.6 5.4 5.2 5.0 4.8 4.6 4.4 4.2 4.0 3.8

136
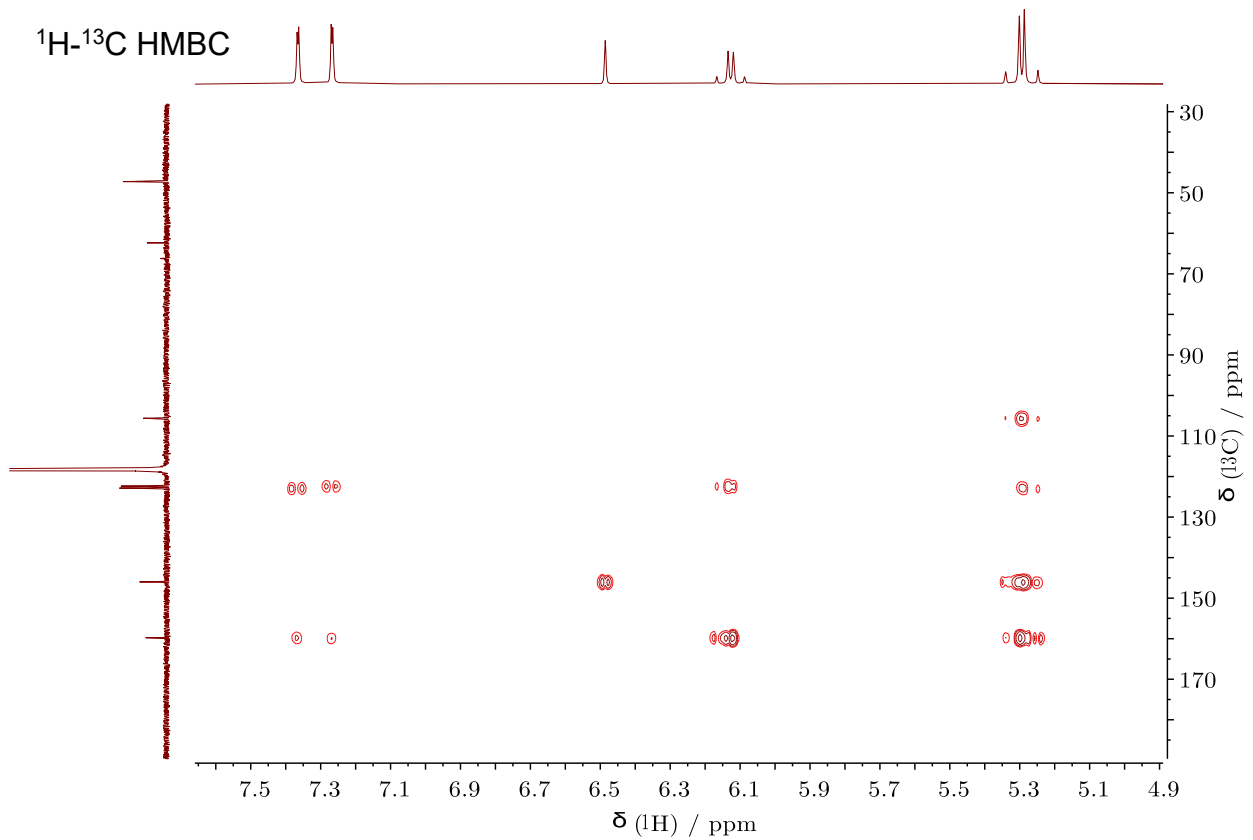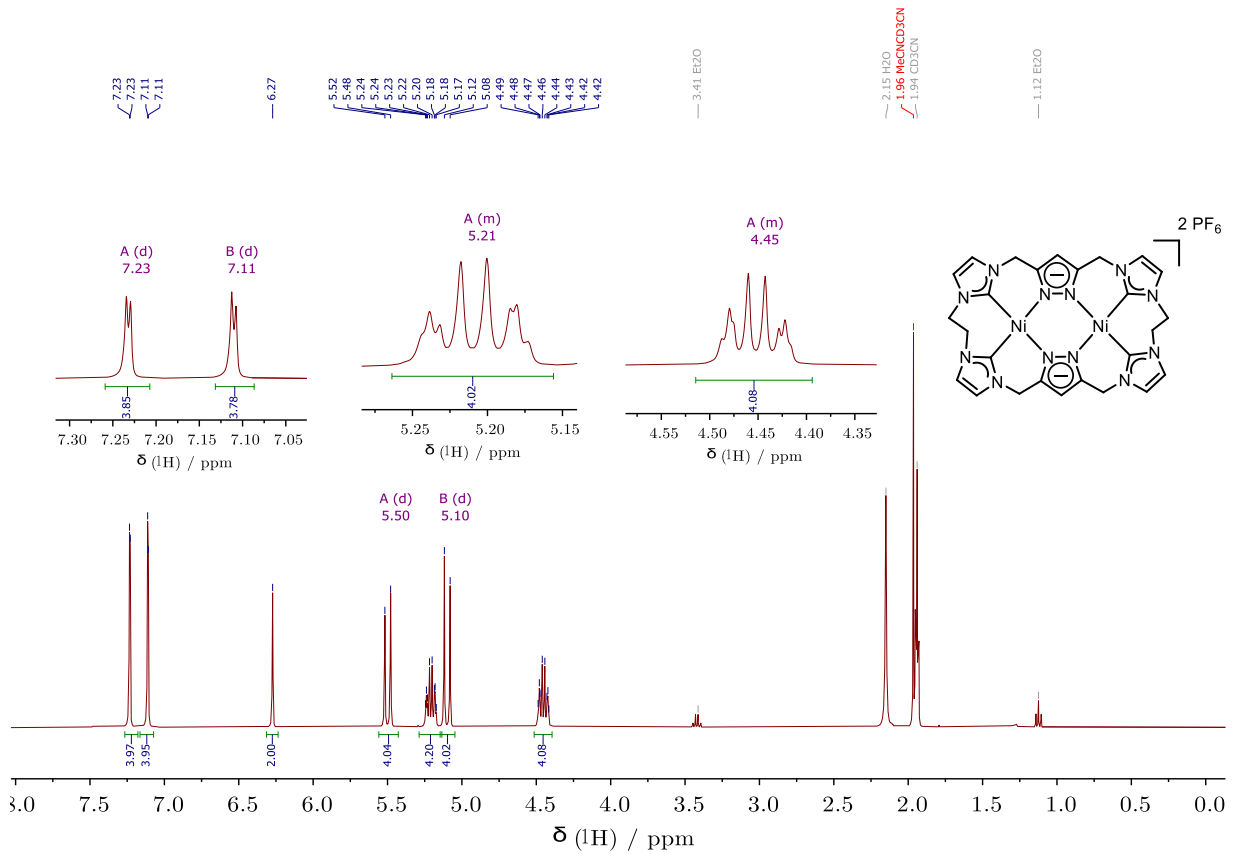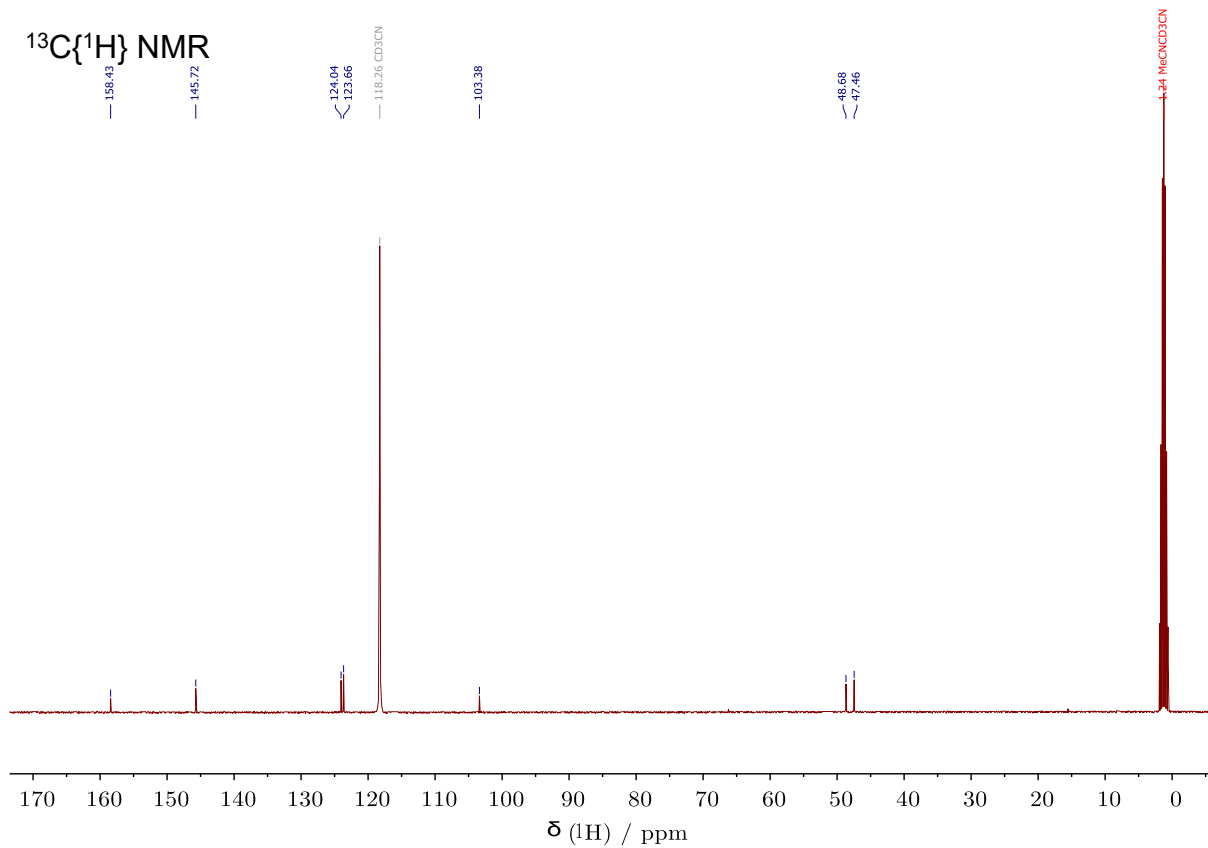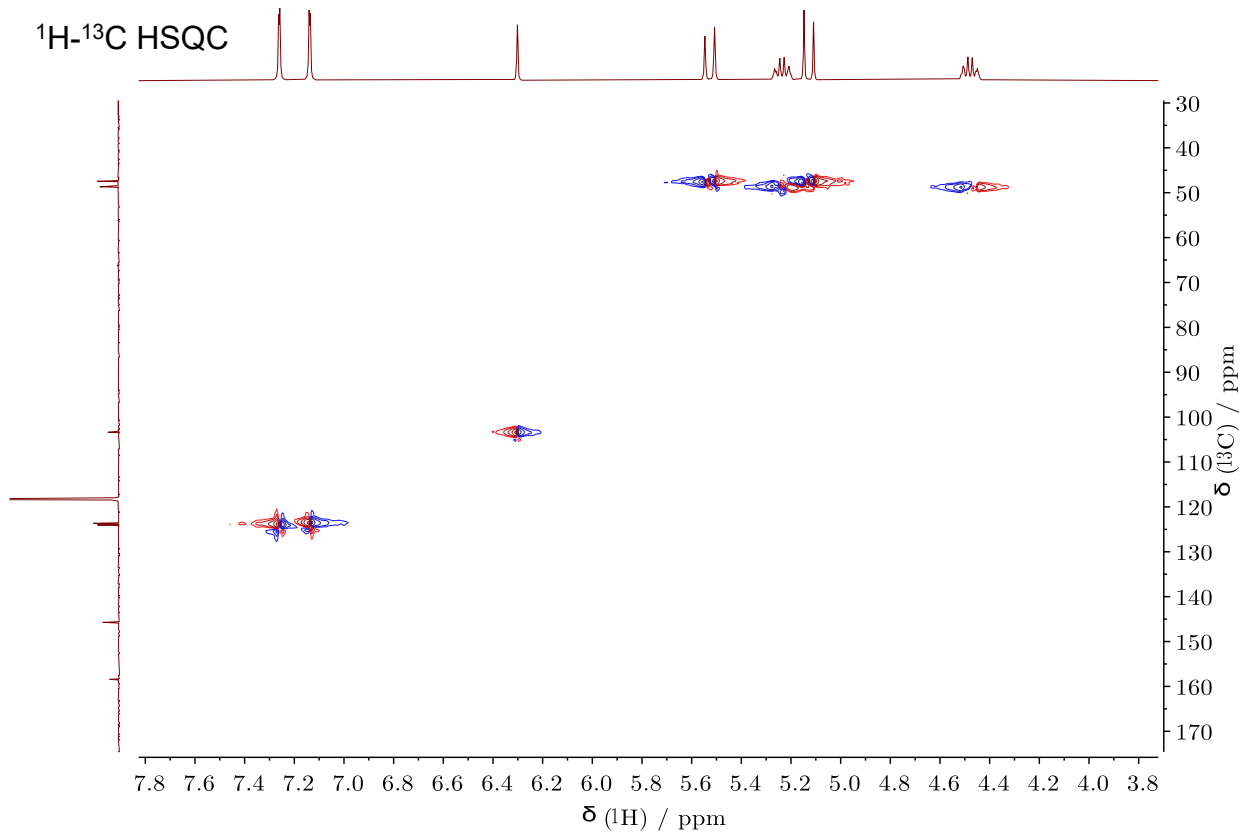
^{1}H-^{13}C HMBC

Ni$_2$L^{Pr} (PF$_6$)$_2$

^1H-^1H NOESY

^1H-^{13}C HSQC

Cu$_2$L^{Me} (PF$_6$)$_2$
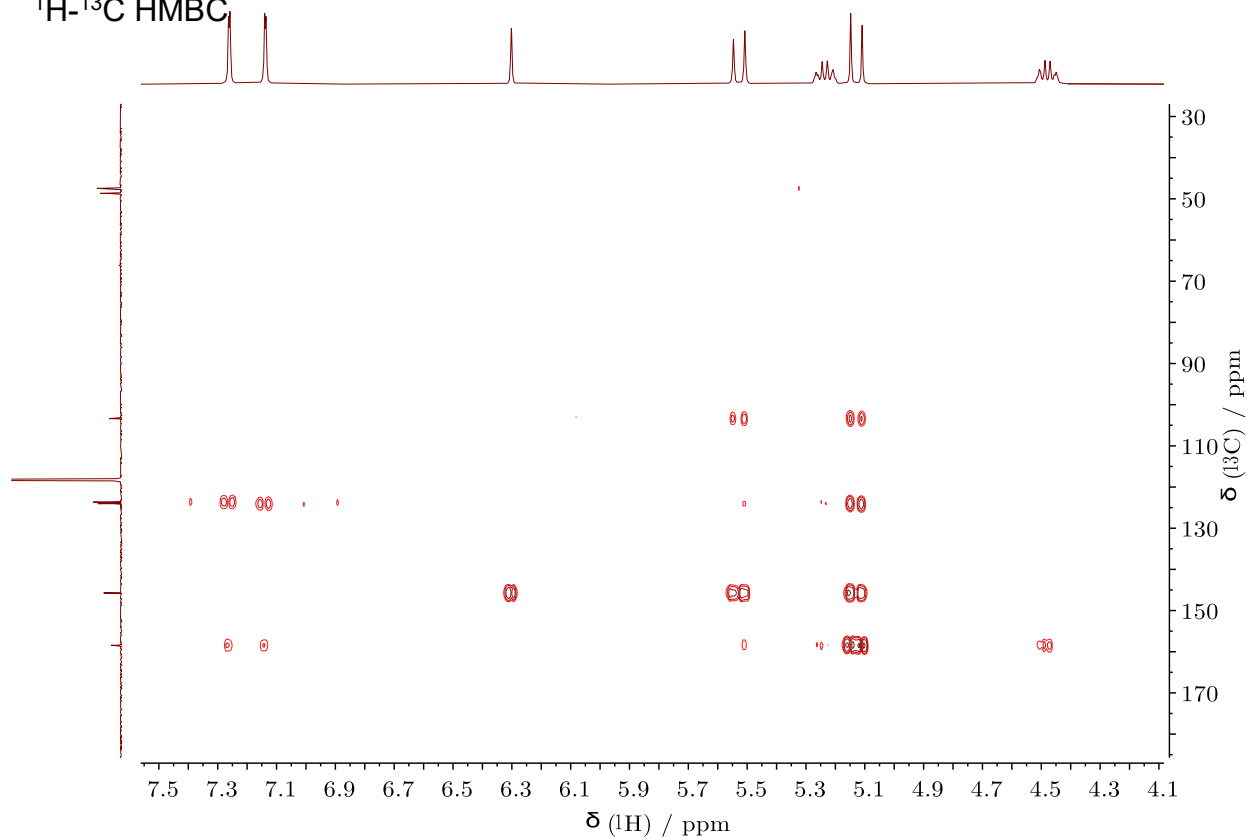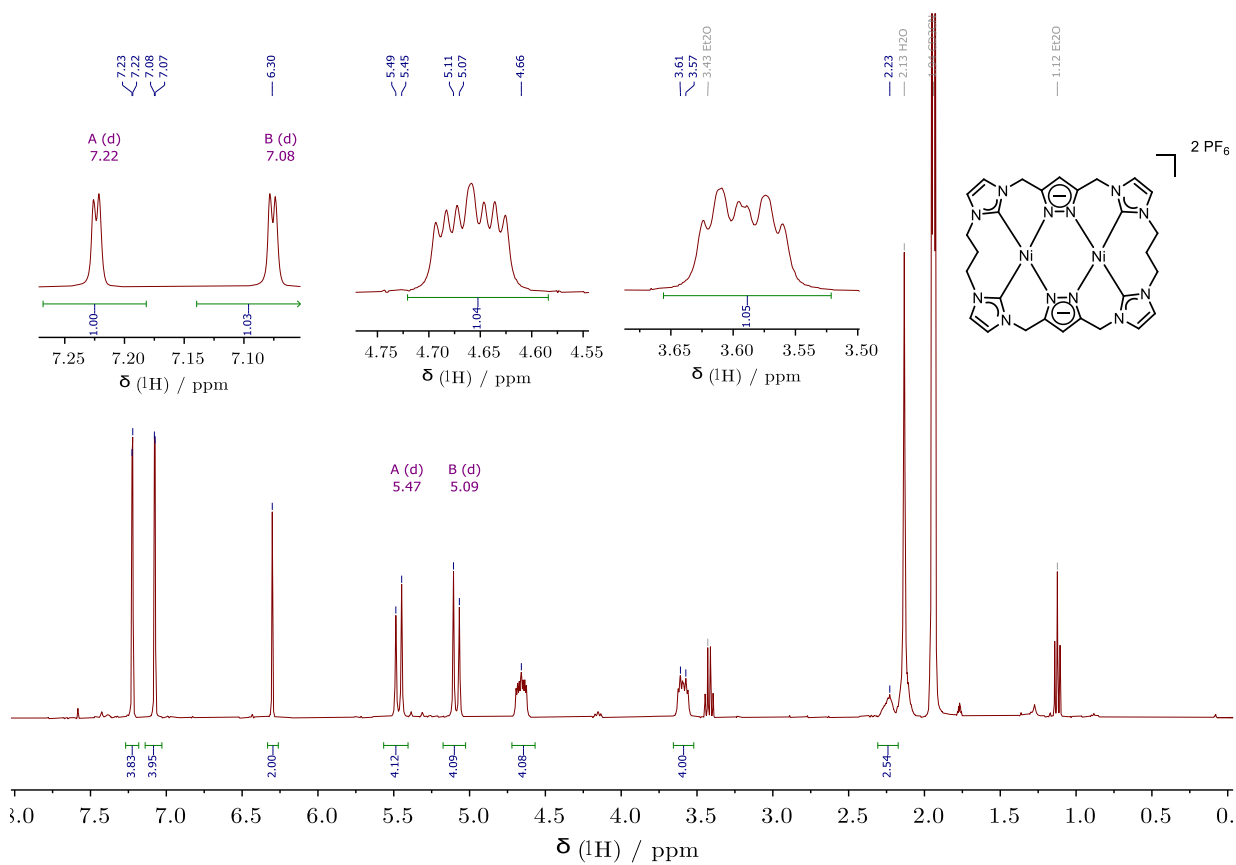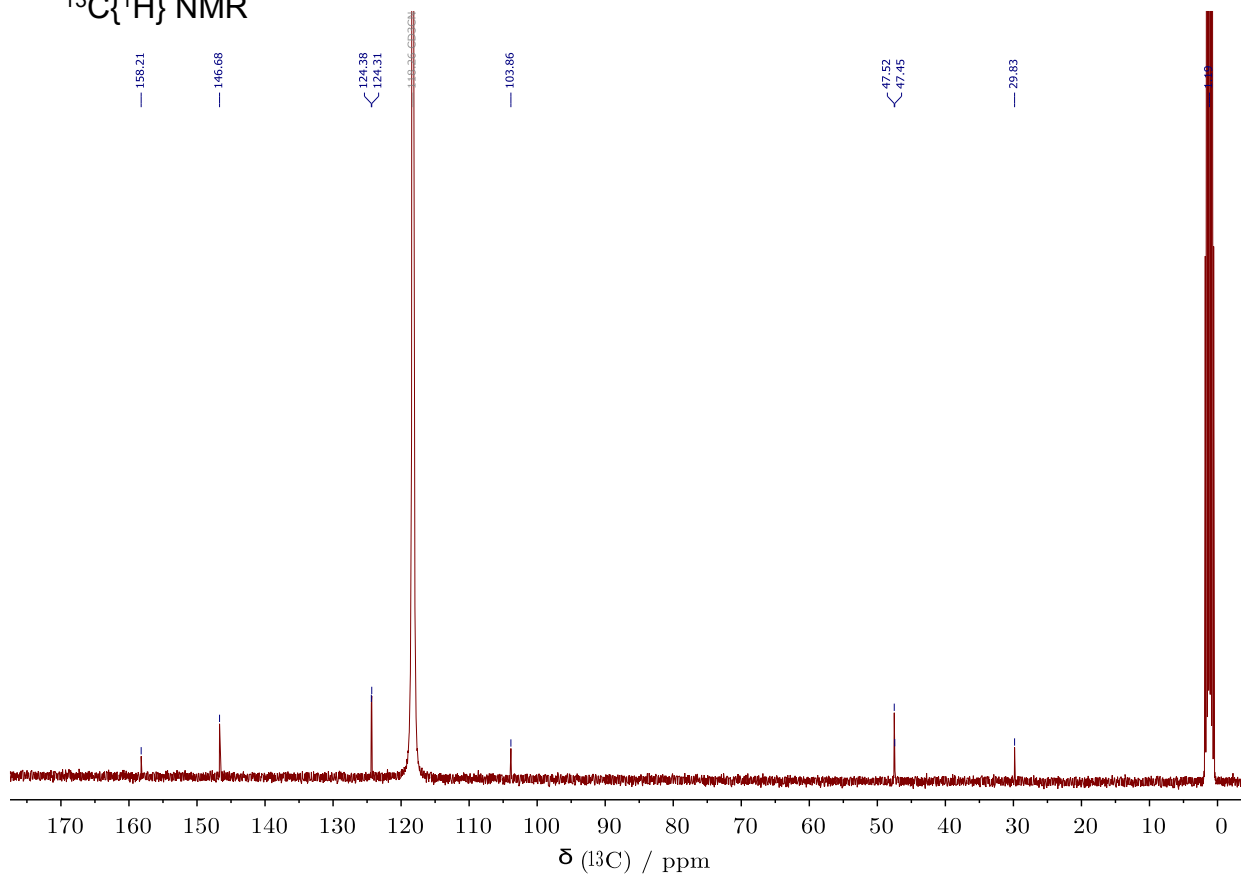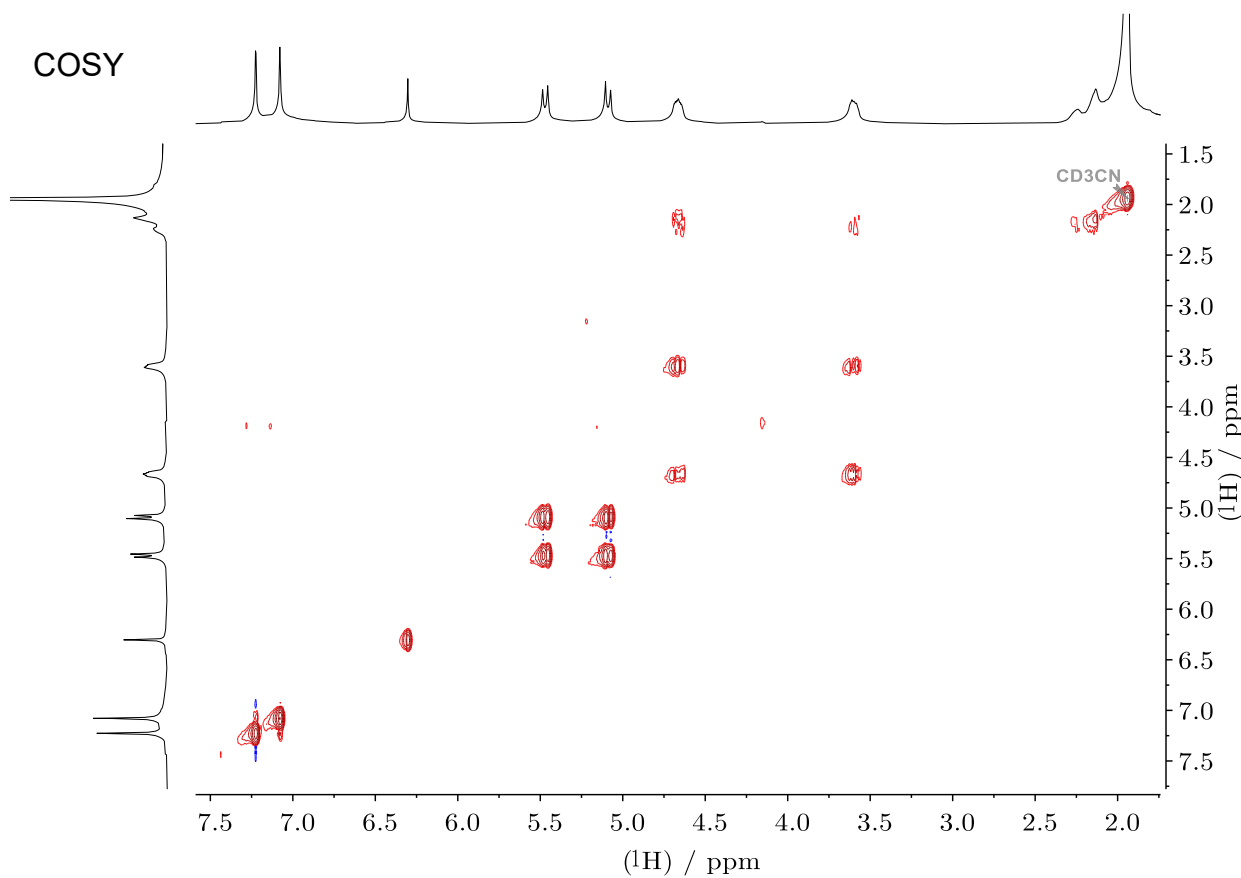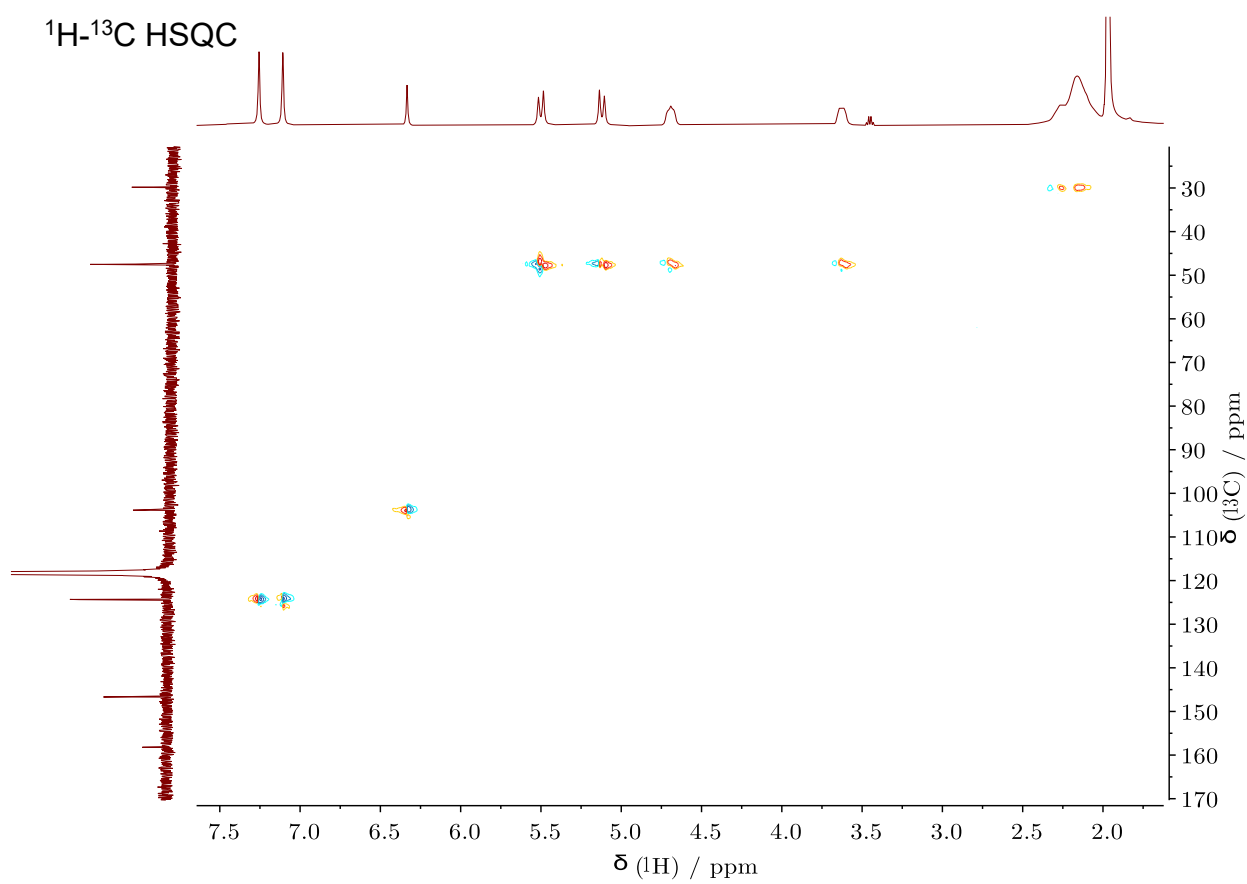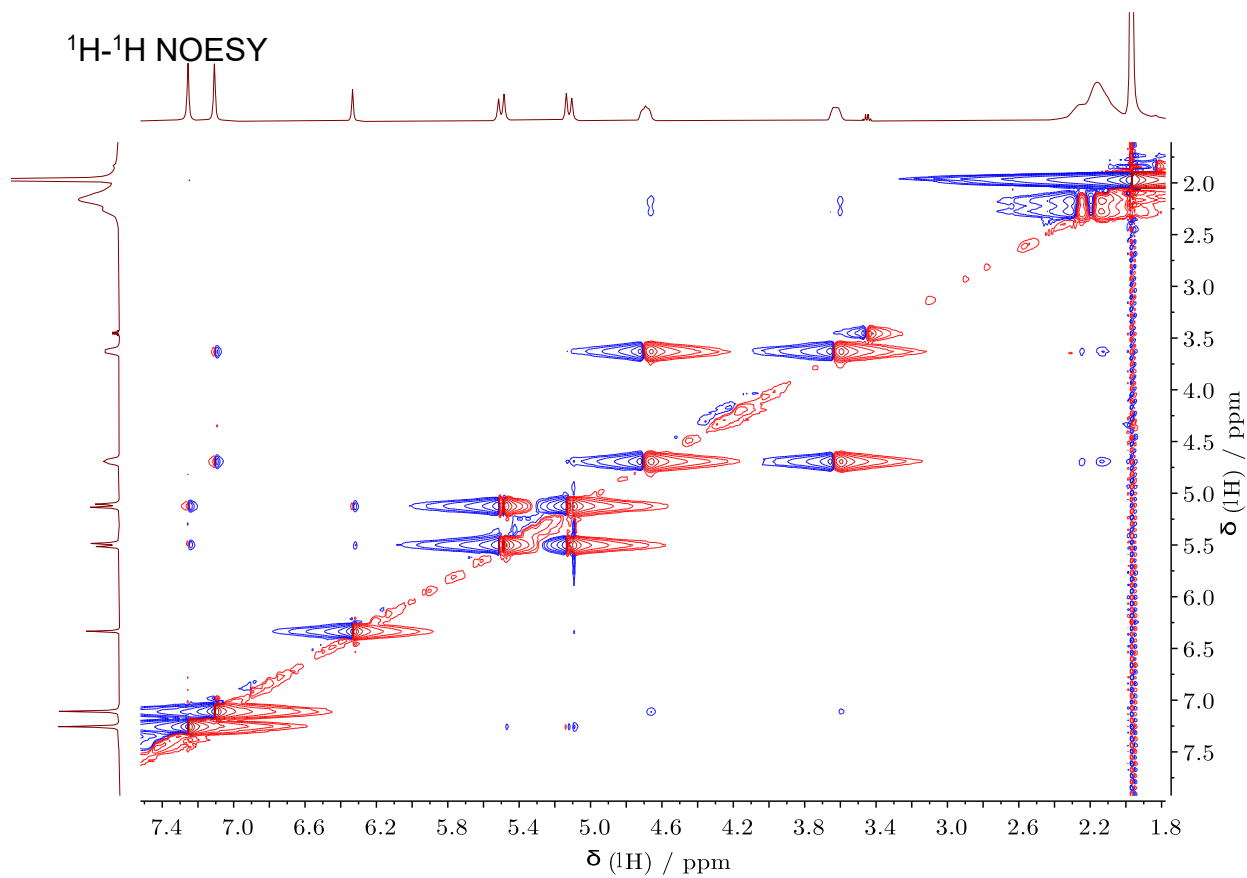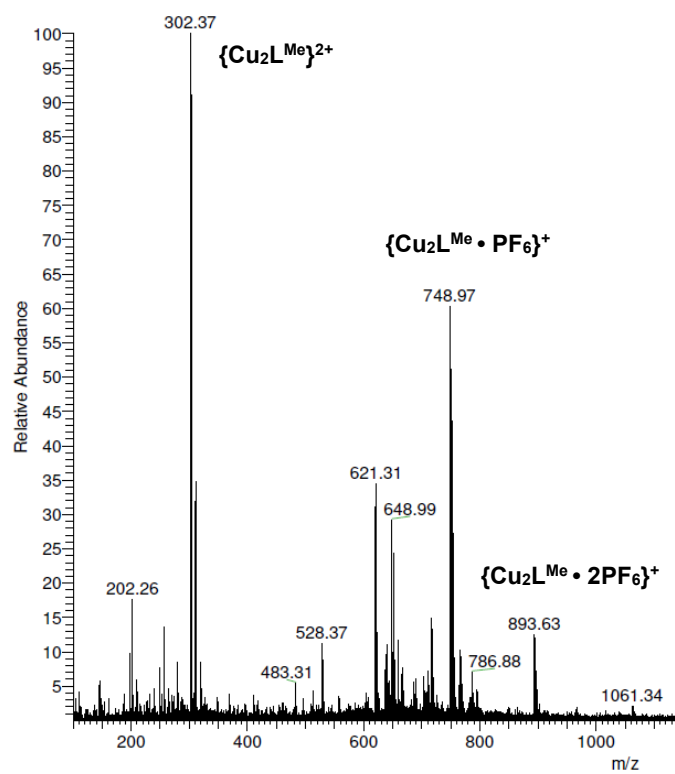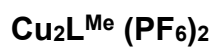
DFT Figures
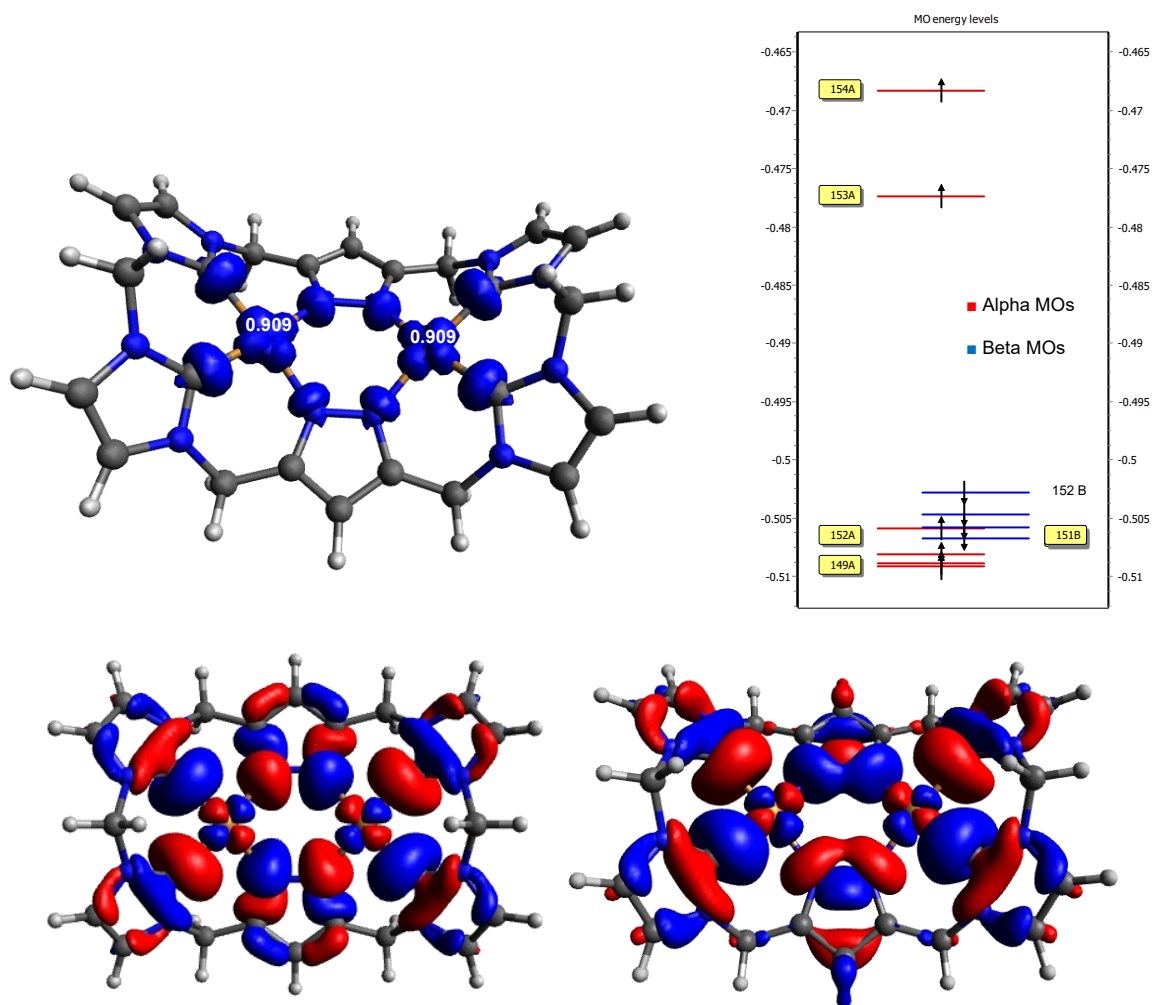
Figure 7.3 | Plot of the spin density (top left), the MOs energy diagram (top right) and of the two single-occupied MOs (bottom left: HOMO; right: HOMO-1) (bottom) in $^3[Cu_2L^{Me}]^{2+}$. Calculation conducted in gas phase, with ωB97xD/6-31+G(d,p) theory level. Isosurface: 0.007 for Spin density and 0.02 for MOs.
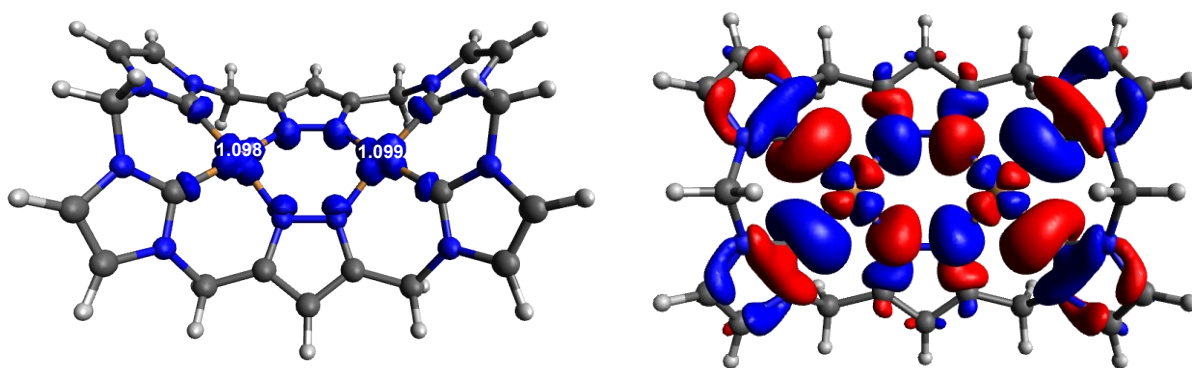
Figure 7.4 | Plot of the spin density (left) and of the SOMO (right) in ^{2}[Cu$_2$L^{Me}]$^{3+}$. Calculation conducted in gas phase, with ωB97xD/6-31+G(d,p) theory level. Isosurface: 0.007 for Spin density and 0.02 for MOs.
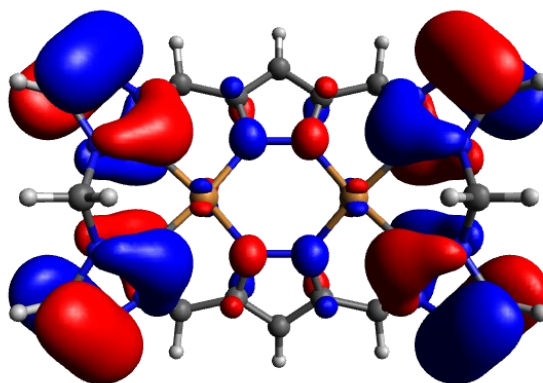
Figure 7.5 | Plot of the HOMO in ^{1}[Cu$_2$L^{Me}]$^{4+}$. Calculation conducted in gas phase, with ωB97xD/6-31+G(d,p) theory level. Isosurface: 0.007 for Spin density and 0.02 for MOs.
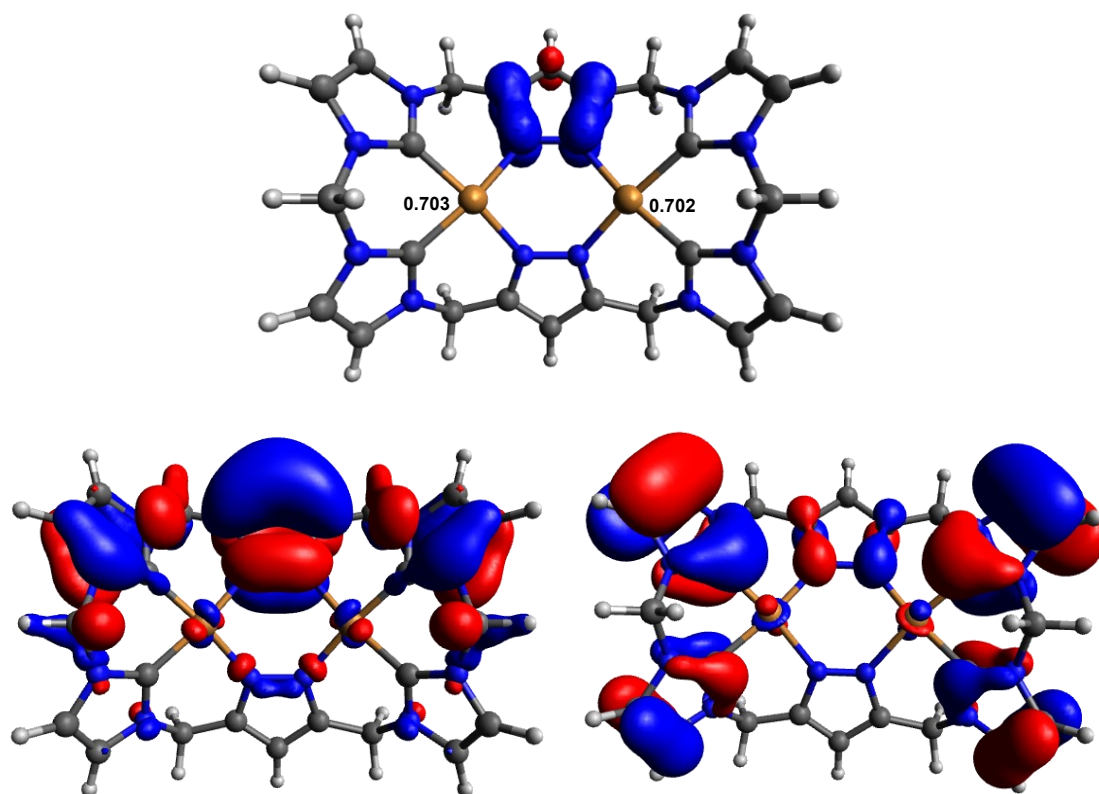
Figure 7.6 | Plot of the spin density (top), SOMO (HOMO-11, bottom left) and HOMO (bottom, right) in ^{2}**[Cu$_2$L^{Me}]$^{5+}$**. Calculation conducted in gas phase, with ωB97xD/6-31+G(d,p) theory level. Isosurface: 0.007 for Spin density and 0.02 for MOs.
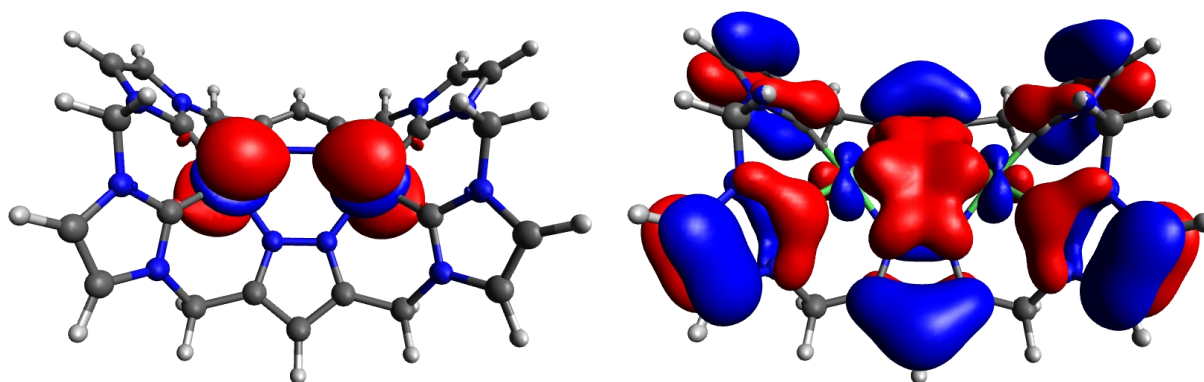
Figure 7.7 | Plot of HOMO‒7 (left) HOMO-8 (right) of **[Ni$_2$L^{Me}]$^{2+}$.** Whereas HOMO-7 gives only some indications that the two metal-centred d_{z^2} lobes may be directed at each other, HOMO-8 suggests extended electronic delocalization between the Ni centres and the pyrazolate-π orbitals due to linear combination of the d-type orbital lobes of the metals and of the p-type of the donor nitrogen atoms (plotted in *Avogadro* with an isosurface value of 0.02).
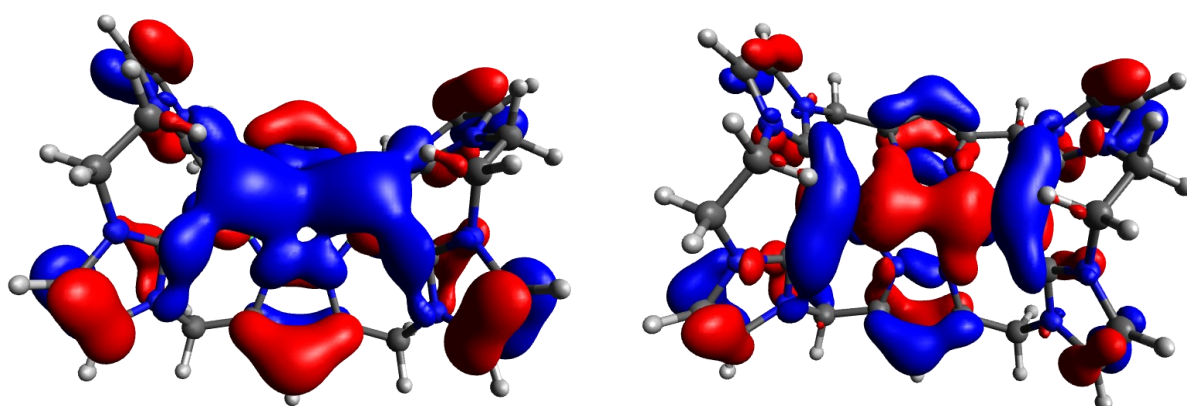
Figure 7.8 | Plot of HOMO‑7 (left) and HOMO-10 (right) of **[Ni₂L^{Et}]^{2+}**. The shape and the extension of HOMO-7 and, to a lower extent, of HOMO-10, which are linear combination of d-type metal orbitals with the pyrazole π-systems corroborate the assumption that in the ethylene-bridged complex the magnitude of electronic coupling between the two Ni-centres is higher than in **Ni₂L^{Me} (PF₆)₂**. Plotted in *Avogadro* with an isosurface value of 0.02.
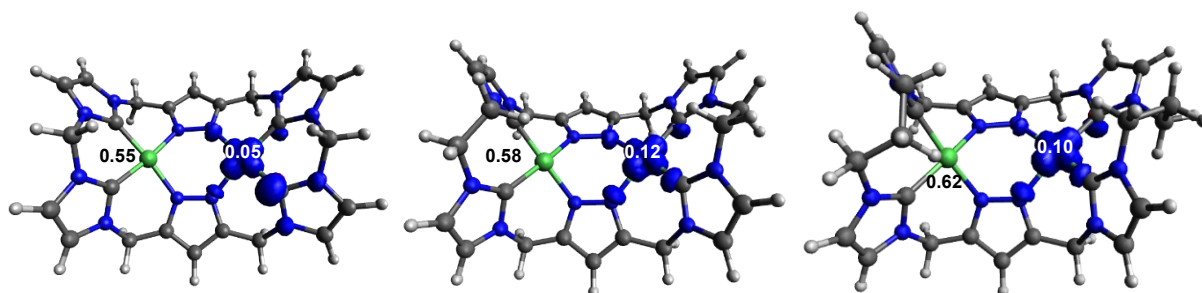
Figure 7.9 | Plot of the Mulliken spin density of **²[Ni₂L^{Me}]⁺** (left), **²[Ni₂L^{Et}]⁺** (middle) and **²[Ni₂L^{Pr}]⁺** (right). Calculation conducted in solvation mode (SMD), with uωB97x-D/6-31+G theory level. Isosurface: 0.005.
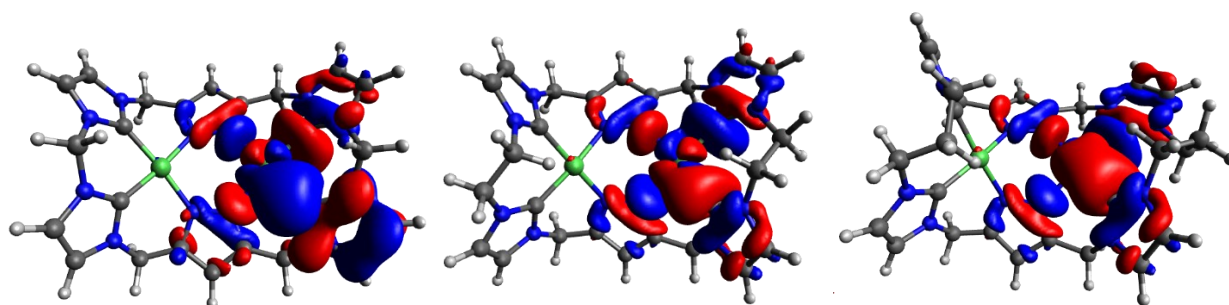
Figure 7.10 | Plot of the SOMO in of **²[Ni₂L^{Me}]⁺** (left), **²[Ni₂L^{Et}]⁺** (middle) and **²[Ni₂L^{Pr}]⁺** (right). Calculation conducted in solvation mode (SMD), with uωB97x-D/6-31+G theory level. Isosurface: 0.02.

144
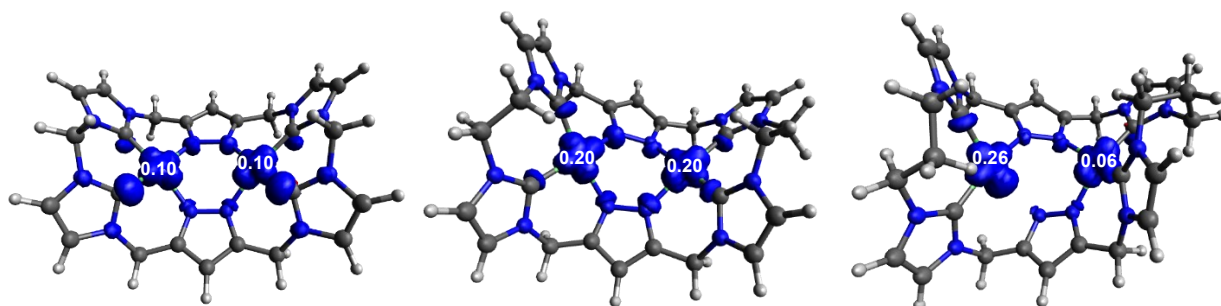
Figure 7.11 | Plot of the Mulliken spin density of $^3[Ni_2L^{Me}]^0$ (left), $^3[Ni_2L^{Et}]^0$ (middle) and $^3[Ni_2L^{Pr}]^0$ (right). Calculation conducted in solvation mode (SMD), with uωB97x-D/6-31+G theory level. Isosurface: 0.005.
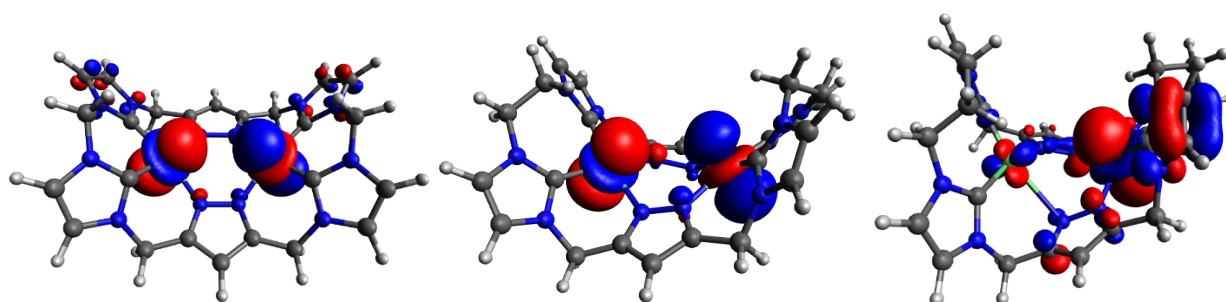
Figure 7.12 | Plot of the HOMO-2 in of $^3[Ni_2L^{Me}]^0$ (left), HOMO-2 of $^3[Ni_2L^{Et}]^0$ (middle) and HOMO-4 of $^3[Ni_2L^{Pr}]^0$ (right). These d_{z^2}-based orbitals of the formal Ni^I/Ni^I active site can facilitate the activation of CO_2. Calculation conducted in solvation mode (SMD), with uωB97x-D/6-31+G theory level. Isosurface: 0.02.

CYCLIC VOLTAMMOGRAMS DATA
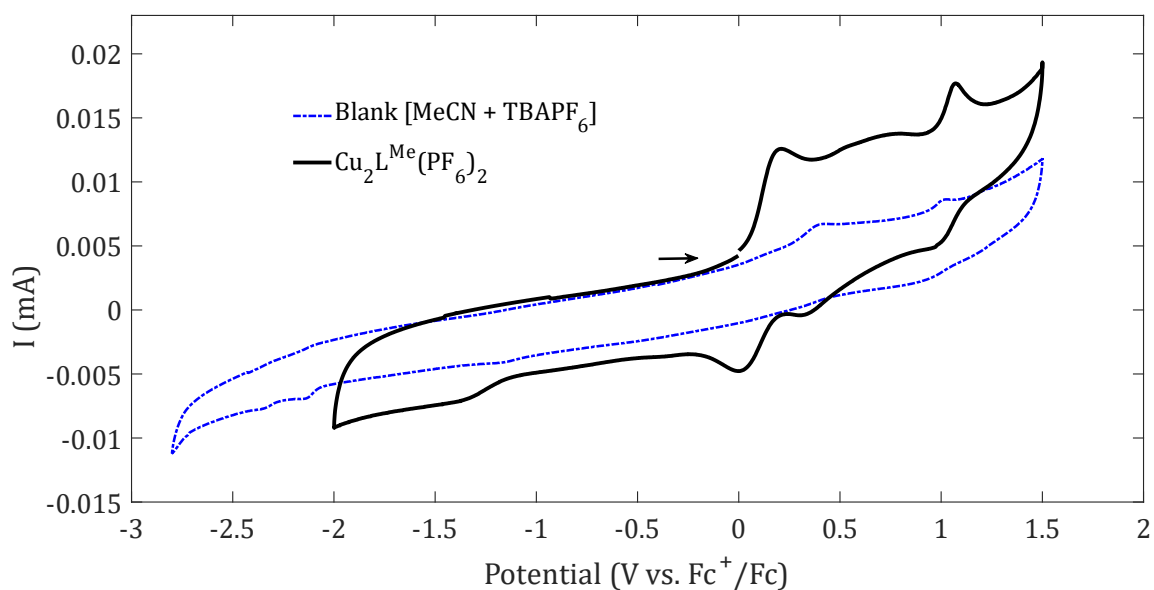
Figure 7.13 | CV of **Cu₂L^Me (PF₆)₂** in the whole stability window of the solvent (MeCN); scan rate: 100 mV s^-1. The direction of the scan is reported by the small arrow.
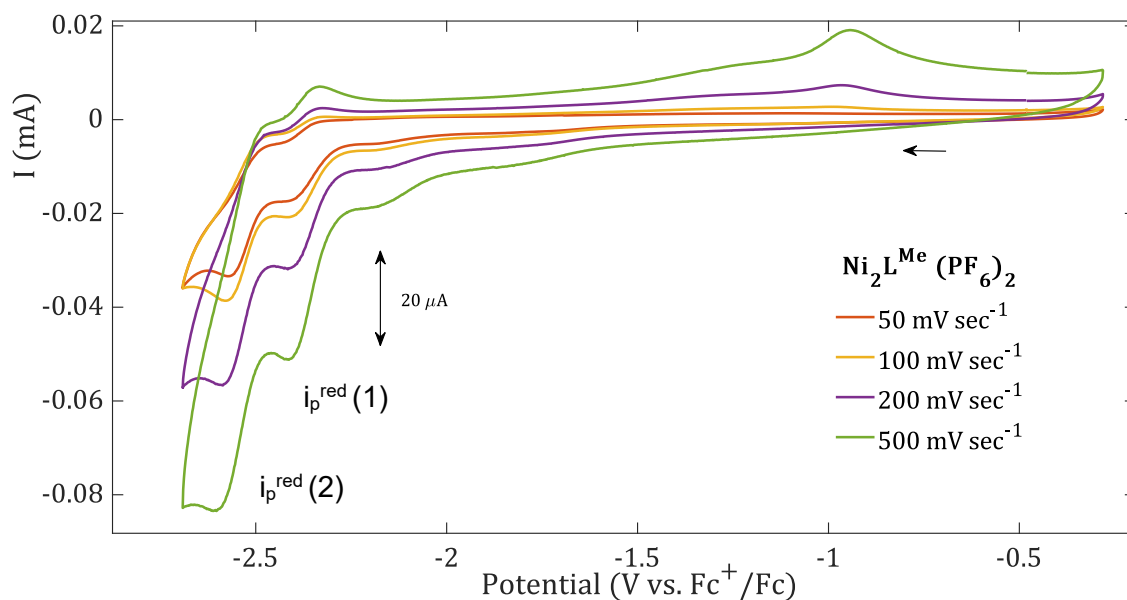
Figure 7.14 | CVs at different scan rates with 1 mM **Ni₂L^Me (PF₆)₂** in MeCN/0.1 M TBAPF₆ solution under Ar, GC WE. One can observe the increased reversibility of the first reduction peak and the appearance of one oxidation peak, pronounced at 500 mV s^-1, at -0.944 V.
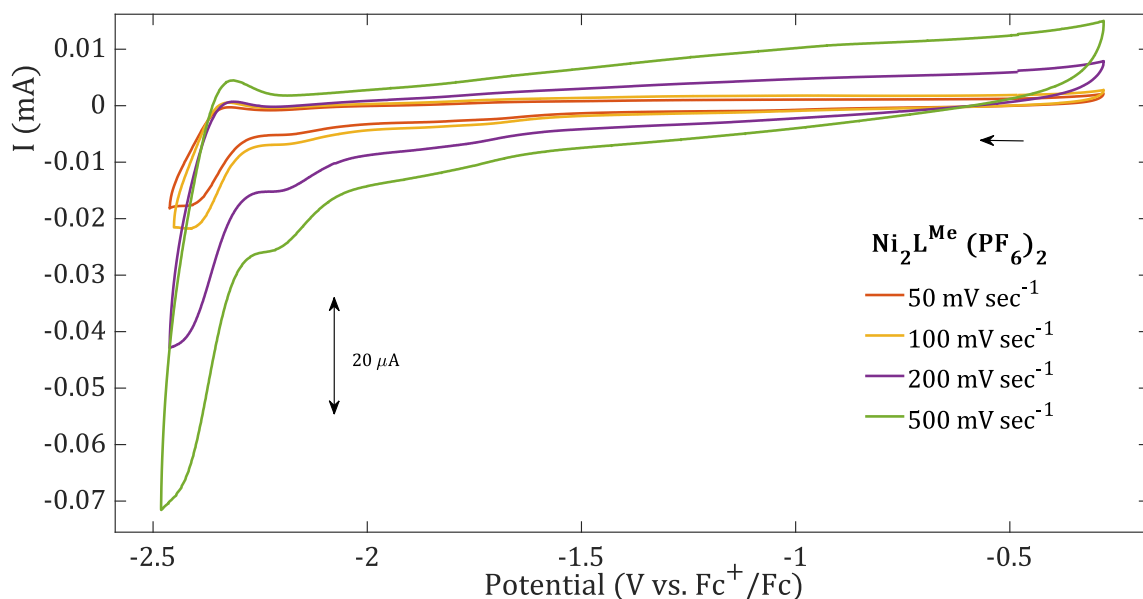
Figure 7.15 | CVs at different scan rates with 1 mM **Ni$_2$L^{Me} (PF$_6$)$_2$** in MeCN/0.1 M TBAPF$_6$ solution under Ar, GC WE. The reversibility of the anodic peak related to the first reduction event, i$_p$^{red}(1), is not enhanced upon stopping the scan right after $E_p{}^a$ (1): -2.41 V. In addition, the oxidation feature at -0.944 (**Figure 7.14**) is no longer observable.
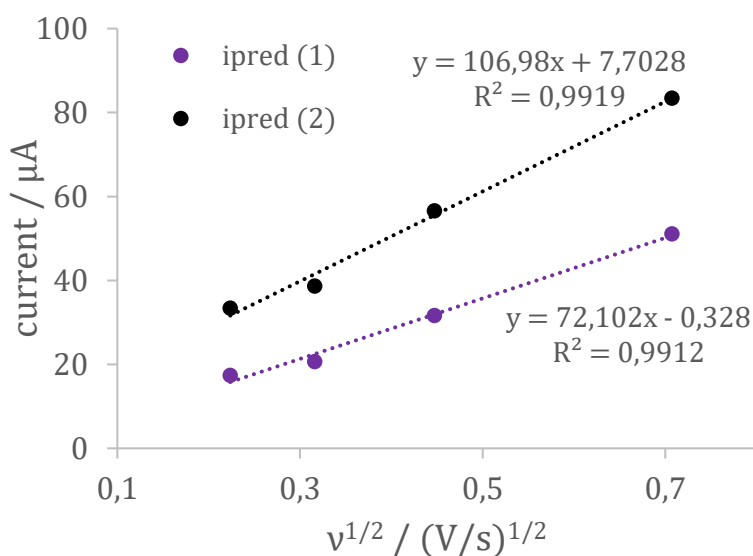
Figure 7.16 | Scan rate dependence for **Ni$_2$L^{Me} (PF$_6$)$_2$**: reductive peak current *vs* the square root of scan rate (v$^{1/2}$). The given line equations correspond to the linear fit of the first, i$_p$^{red} (1) and the second, i$_p$^{red} (2) reduction events at respectively -2.41 V and -2.57 V.
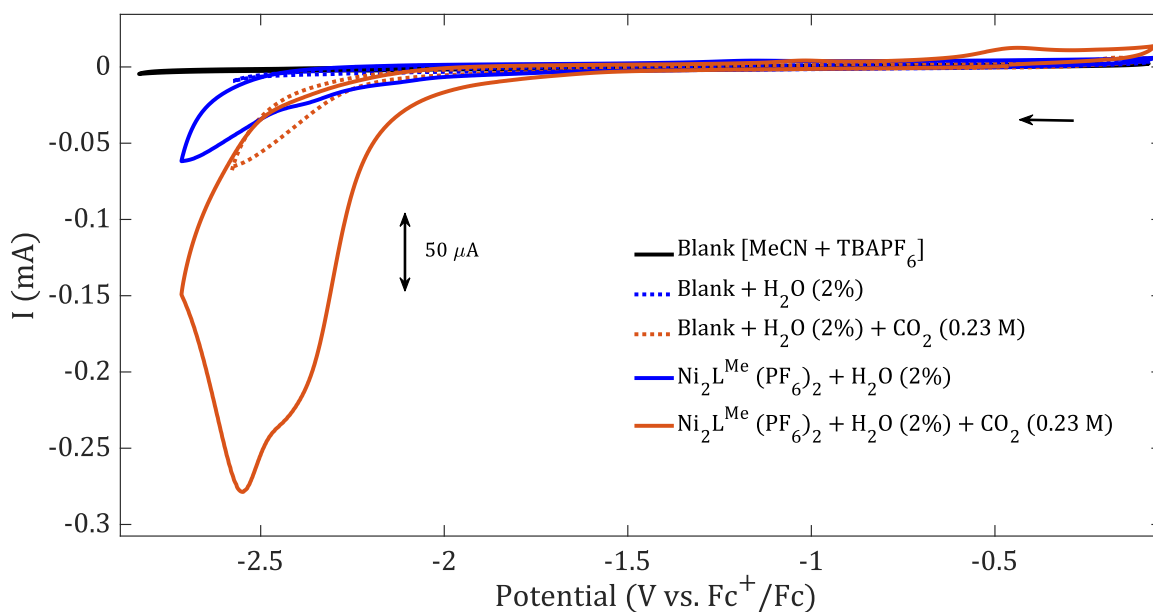
Figure 7.17 | CVs showing the reactivity of the employed electrolyte solution (MeCN + 0.1 M $^{n}Bu_4\, PF_6$) towards the addition of 100 μL H_2O (light blue) and saturation of CO_2 (yellow), to realise a concentration of 0.23 M. The catalytic waves observed in presence of **Ni_2L^{Me} ($PF_6)_2$** with 2% H_2O (blue line) and upon saturation with CO_2 (red line) are also reported.
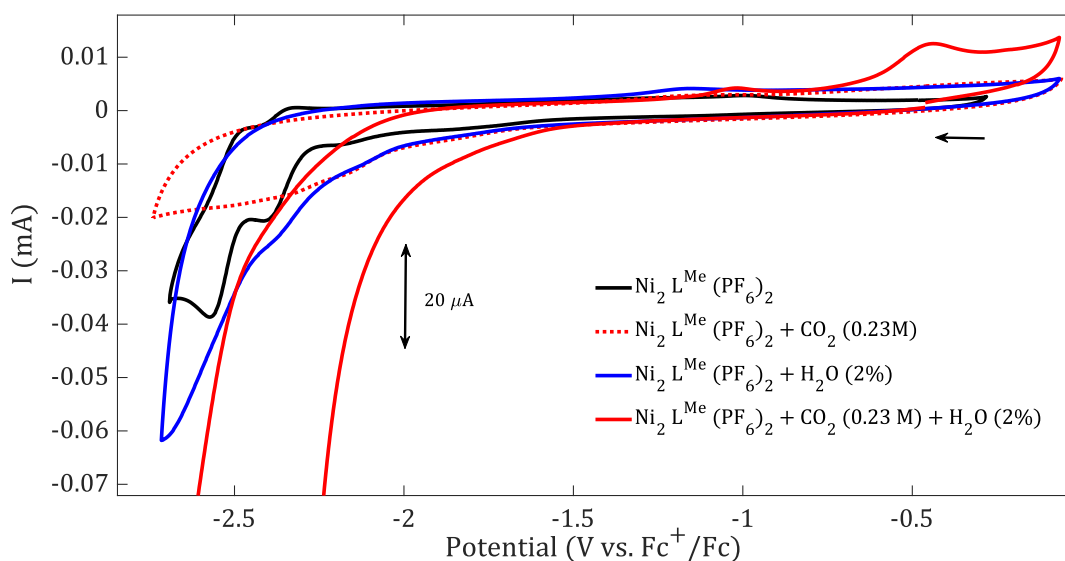
Figure 7.18 | CV of **Ni_2L^{Me} ($PF_6)_2$** under N_2 (black), CO_2 (dotted red), N_2 + 1.0 M H_2O (blue) and CO_2 + 1.0 M H_2O (red) in MeCN + 0.1 M TBAPF$_6$ scanning toward cathodic potentials at 0.1 V s^{-1} with a GC disk WE. The catalytic wave ($E_{cat/2}$ = - 2.30 V; E_{onset} = -1.60 V) is fully reported in **Figure 3.25**. That peak is not constant upon several cycles (see next CV).
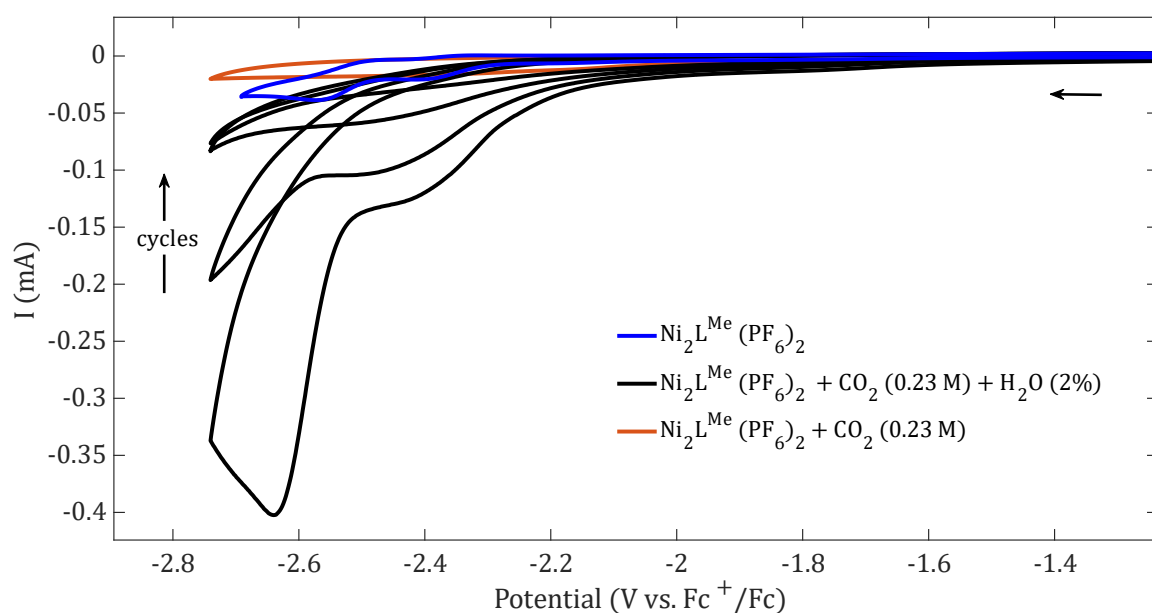
Figure 7.19 | CVs showing the reactivity of **Ni₂Lᴹᵉ (PF₆)₂** in a CO_2-saturated MeCN/0.1 M TBAPF₆ solution containing 2% H_2O. One can observe that the exchanged current decreases upon several electrochemical cycles (black lines and arrow), suggesting competitive reaction at the electrode surface.
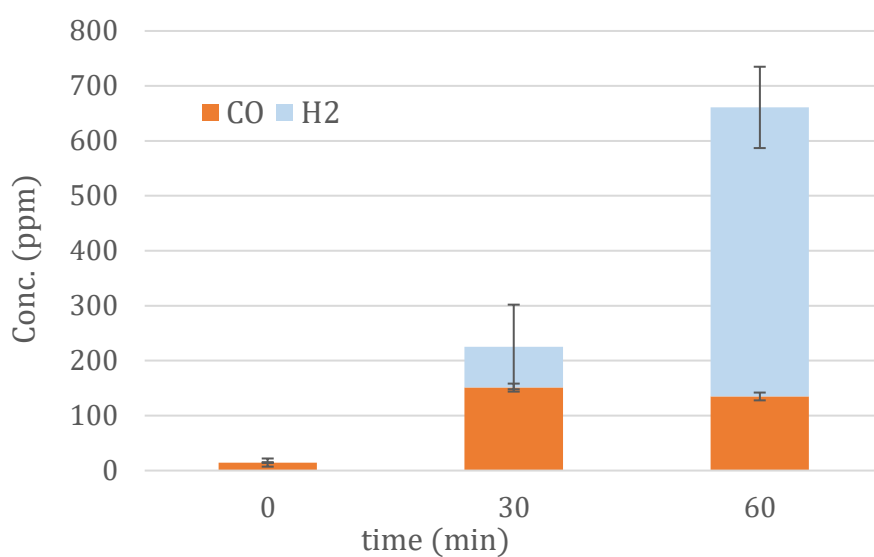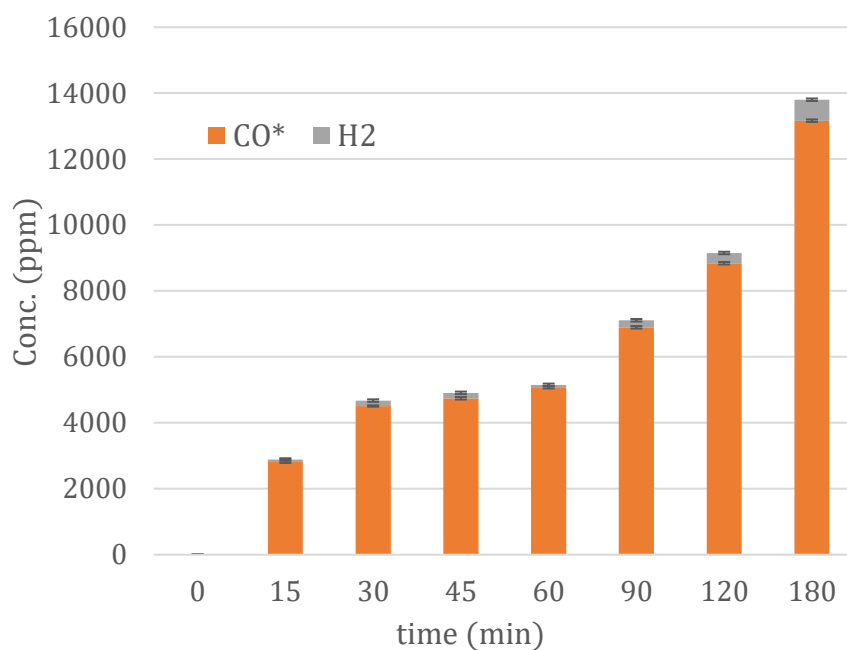

Figure 7.20 | Detected gaseous product from CPE conducted with 1mM of **Ni₂Lᴹᵉ(PF₆)₂** at -2.25 V in a CO_2-saturated MeCN/0.1 M TBAPF₆ solution containing 2% H_2O at a Freudenberg carbon paper WE.
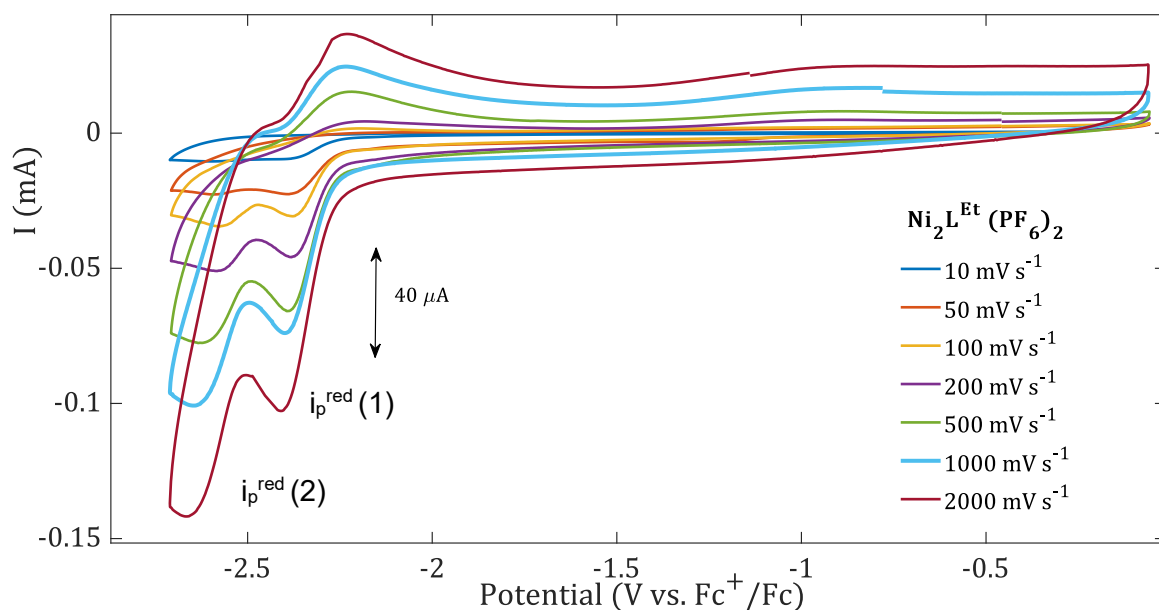
Figure 7.21 | CVs at different scan rates with 1 mM **Ni₂L^{Et} (PF₆)₂** in MeCN/0.1 M TBAPF₆ solution under Ar, GC WE. Of note, increasing the scan rate leads to an increase of the oxidation peak at -2.23 V, coupled with the first reduction event.
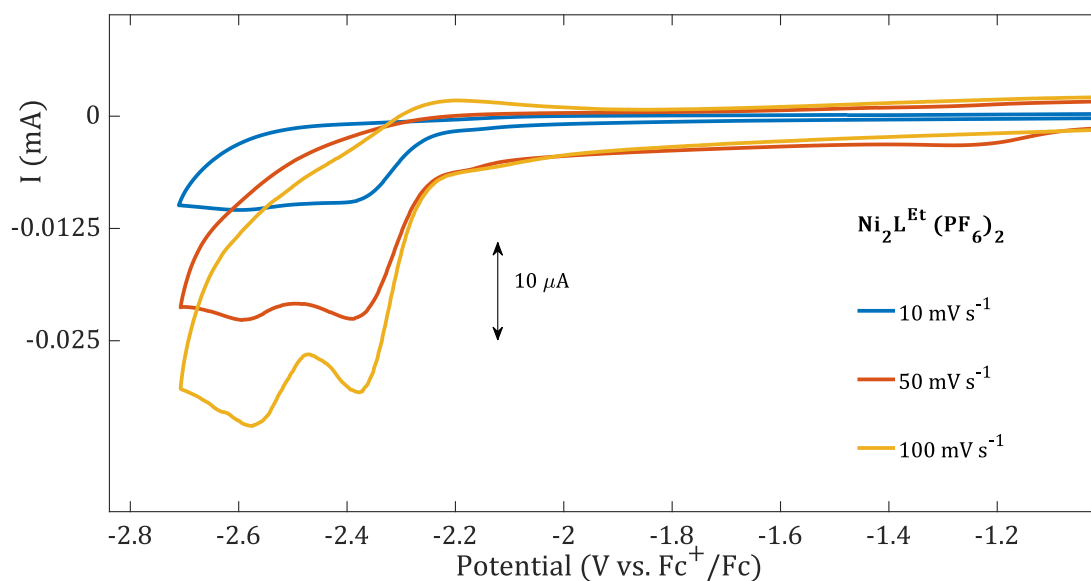
Figure 7.22 | CVs of 1 mM **Ni₂L^{Et} (PF₆)₂** in MeCN/0.1 M TBAPF₆ solution under Ar, GC WE. Scan rate 10, 50 and 100 mV s⁻¹. One can note how the weak coupled oxidation peak at -2.24 V is completely lost at 50 mV s⁻¹ and that the second reduction event is hardly detectable with the slower scan rate (blue line).
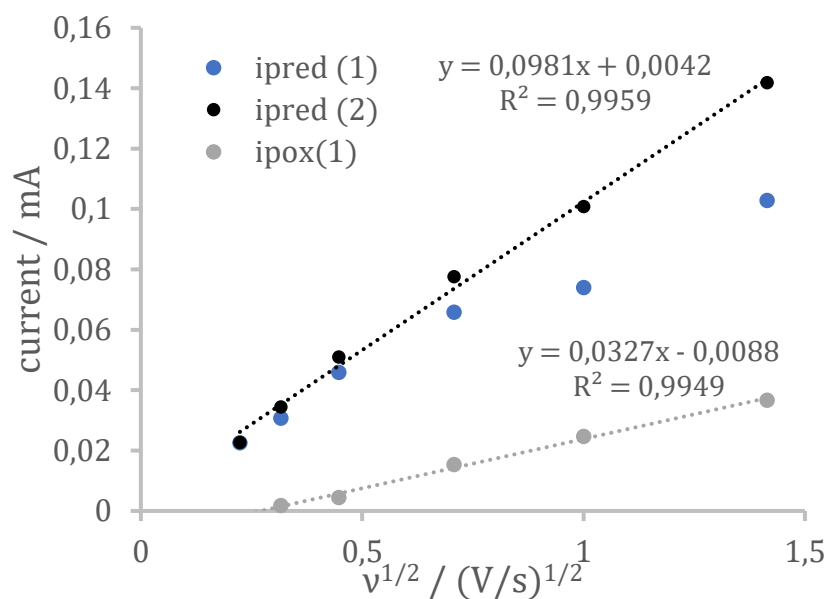
Figure 7.23 | Scan rate dependence for **Ni$_2$L^{Et} (PF$_6$)$_2$**: reductive peak current *vs* the square root of scan rate ($v^{1/2}$). The given line equations (dotted black line) correspond to the linear fit of the most cathodic reduction event, i_p^{red} (2); whereas, for the first redox feature, the peak current does not linearly relate with $v^{1/2}$ at scan rate higher than 500 mV s^{-1}. The coupled oxidation of the first reduction possesses instead a linear response to scan rate (dotted grey line).
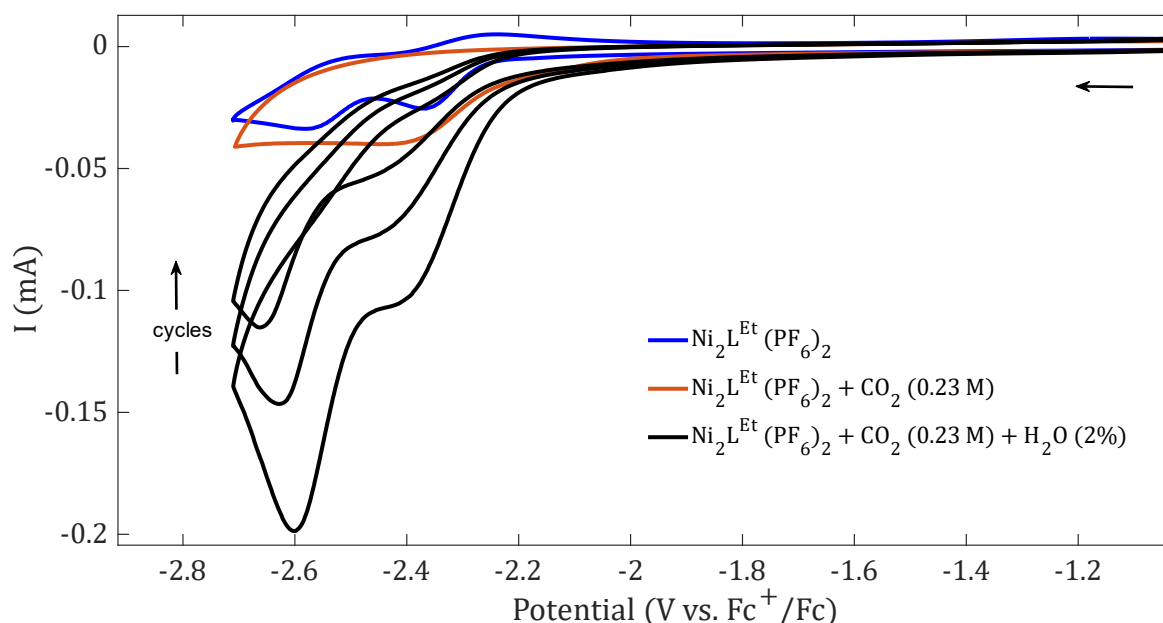
Figure 7.24 | CVs showing the reactivity of **Ni$_2$L^{Et} (PF$_6$)$_2$** in a CO$_2$-saturated MeCN/0.1 M TBAPF$_6$ solution containing 2% H$_2$O. One can observe that the exchanged current decreases upon several electrochemical cycles (black lines and arrow), suggesting competitive reaction at the electrode surface.

Figure 7.25 | Detected gaseous product from CPE conducted with 1mM of **Ni₂Lᴱᵗ (PF₆)₂** at -2.60 V in a CO₂-saturated MeCN/0.1 M TBAPF₆ solution containing 2% H₂O at a Freudenberg carbon paper WE.
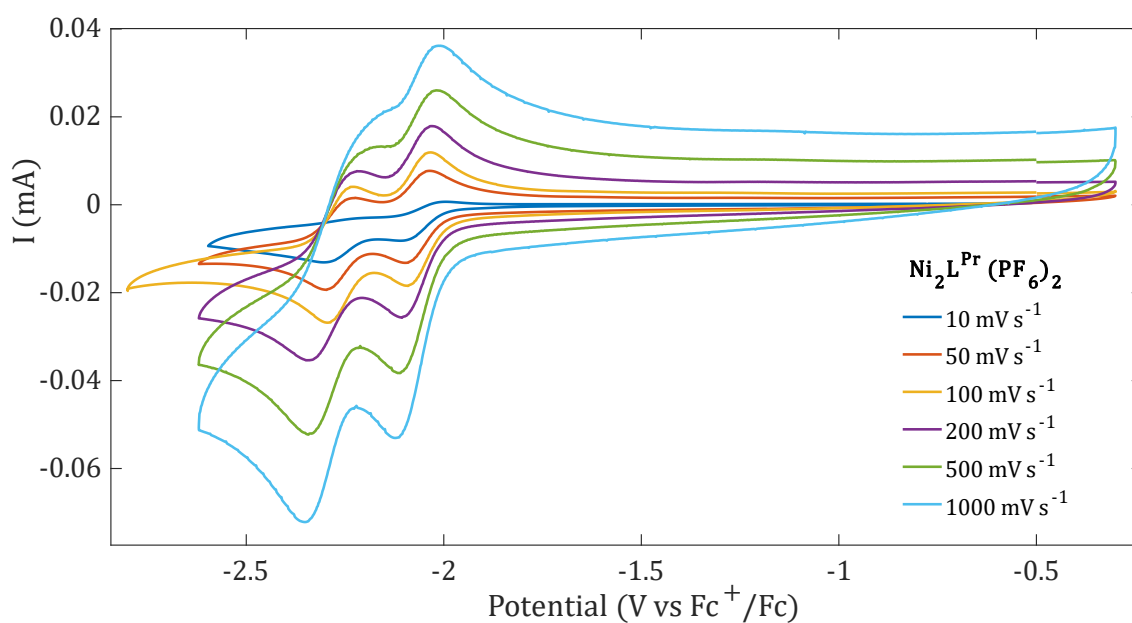
Figure 7.26 | CVs at different scan rates with 1 mM **Ni₂Lᴾʳ (PF₆)₂** in MeCN/0.1 M TBAPF₆ solution under Ar, GC WE.
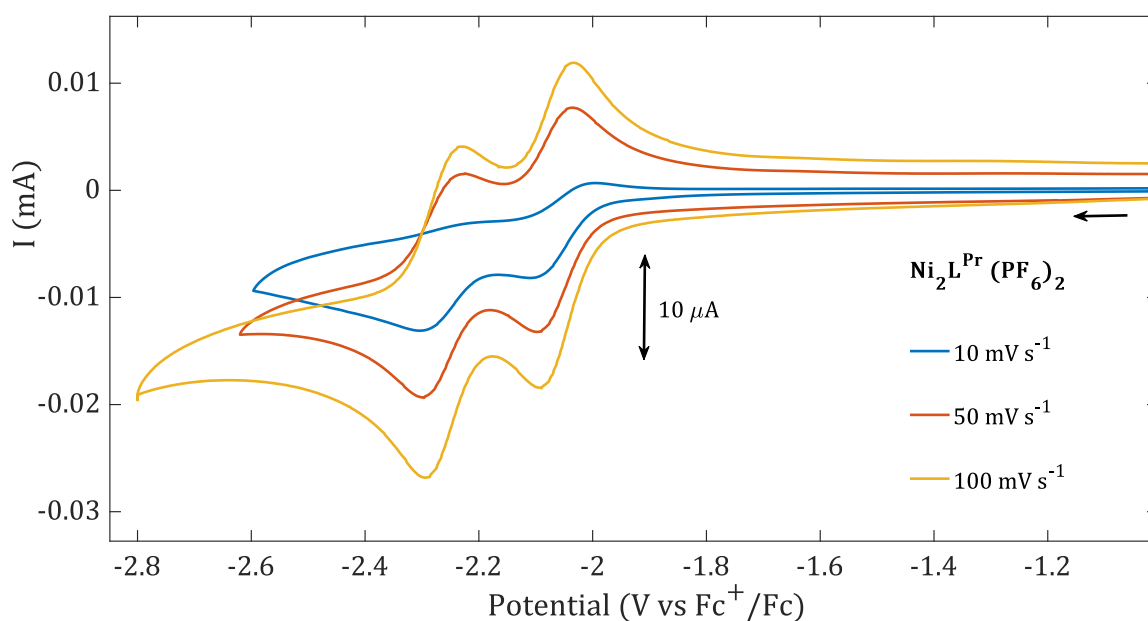
Figure 7.27 | CVs of 1 mM **Ni₂Lᴾʳ (PF₆)₂** in MeCN/0.1 M TBAPF₆ solution under Ar, GC WE. Scan rate 10, 50 and 100 mV s⁻¹. One can note how the quasi-reversibility of the two reduction features is lost at 10 mV s⁻¹ (blue line).
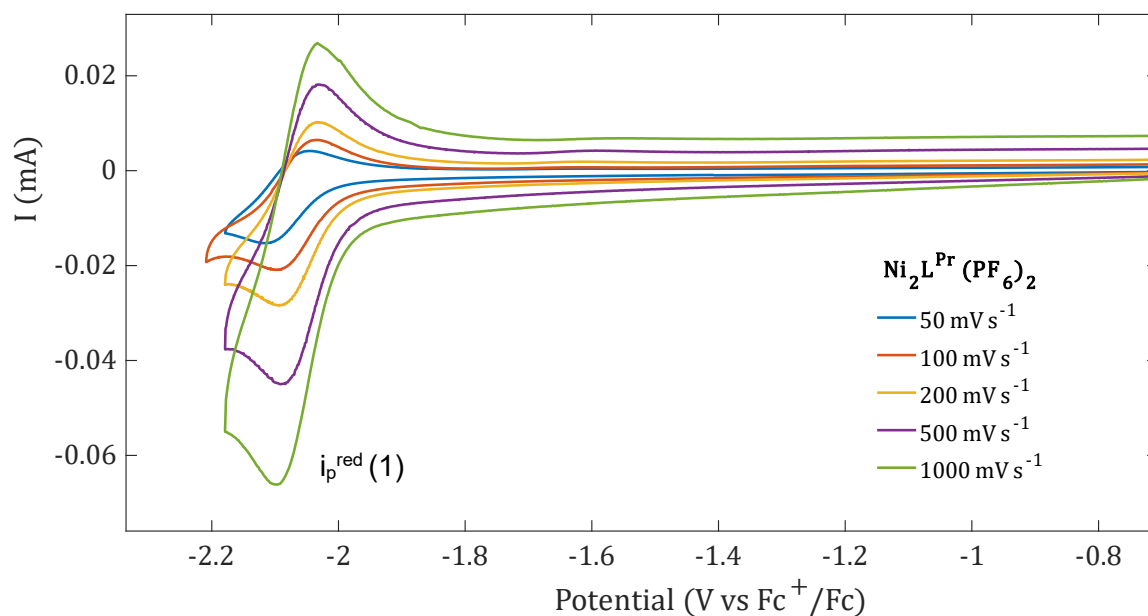
Figure 7.28 | CVs at different scan rates with 1 mM **Ni₂Lᴾʳ (PF₆)₂** in MeCN/0.1 M TBAPF₆ solution under Ar, GC WE. The reversibility of the anodic peak coupled with i_p^c (1), is slightly enhanced upon stopping the scan right after E_p^a (1): -2.03 V.
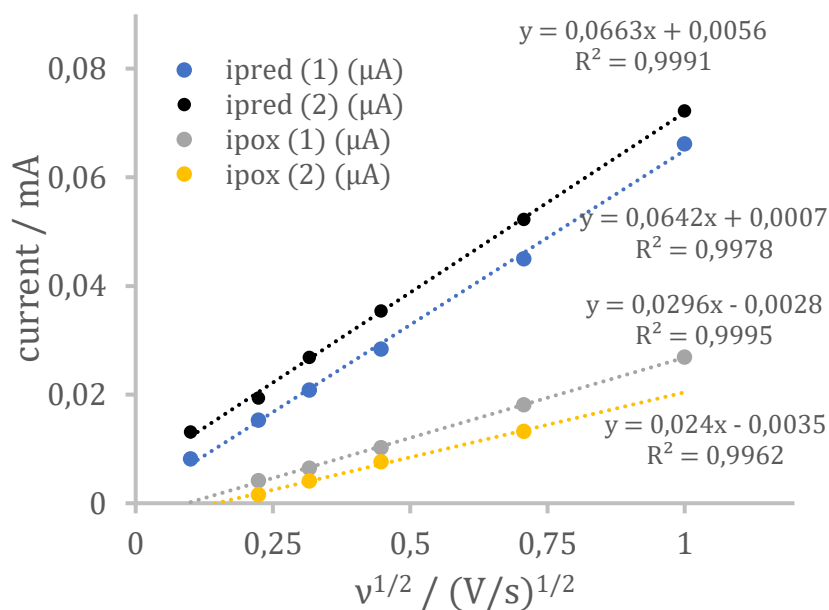
Figure 7.29 | Scan rate dependence for **Ni₂L^Pr (PF₆)₂**: reductive (and oxidative) peak current *vs* the square root of scan rate ($v^{1/2}$). The given line equations correspond to the linear fit of the first (blue, i_p^{red} (1)) and second (black, i_p^{red} (2)) reduction event, as well to the coupled oxidations (grey, i_p^{ox} (1) and yellow, i_p^{ox} (2)). All the traces have good correlation with a linear fit ($R^2 > 0.996$), suggesting freely diffusing species in solution.
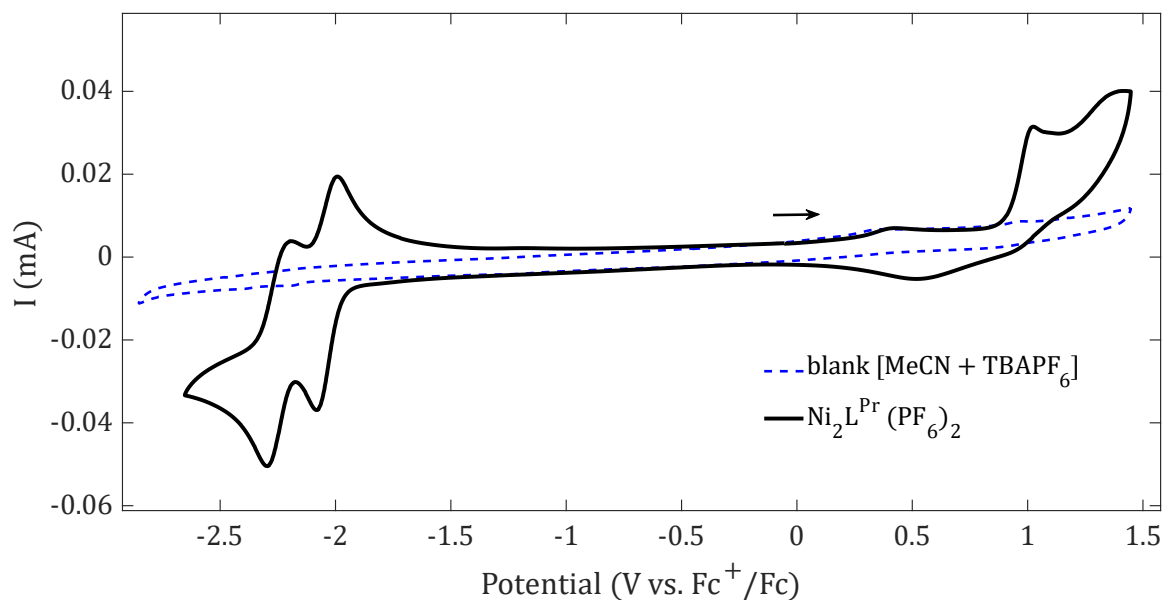

Figure 7.30 | CV of **Ni₂L^Pr (PF₆)₂** in the whole stability window of the solvent (MeCN); scan rate 100 mV s⁻¹. The direction of the scan is reported by the small arrow.
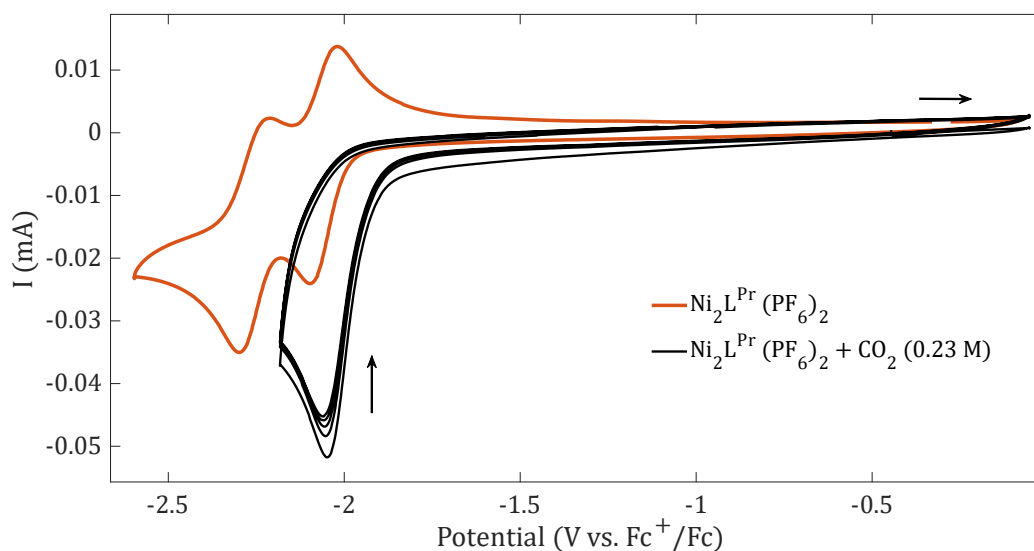
Figure 7.31 | CV of **Ni₂L^Pr (PF₆)₂** under a N₂ (red) or CO₂ (black) atmosphere in MeCN + 0.1 M TBAPF₆ scanning toward cathodic potentials at 0.1 V s⁻¹ with a glassy carbon disk WE. By stopping the scan at -2.2 V, $i_{p,cat}$ is constant upon several cycle: $E_{cat/2}$ = -1.97; E_{onset} = -1,87 V $i_{p,cat}$ / i_p^0 = 2.0.
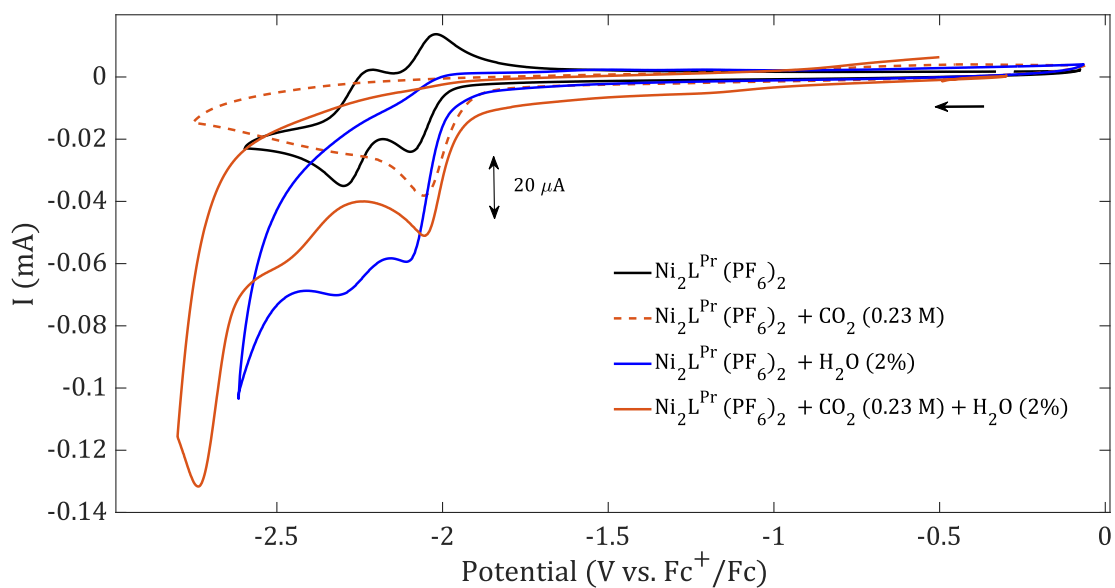
Figure 7.32 | CV of **Ni₂L^Pr (PF₆)₂** under N₂ (black), CO₂ (dotted red), N₂ + 1.0 M H₂O (blue) and CO₂ + 1.0 M H₂O (red) in MeCN + 0.1 M TBAPF₆ scanning toward cathodic potentials at 0.1 V s⁻¹ with a GC disk WE.
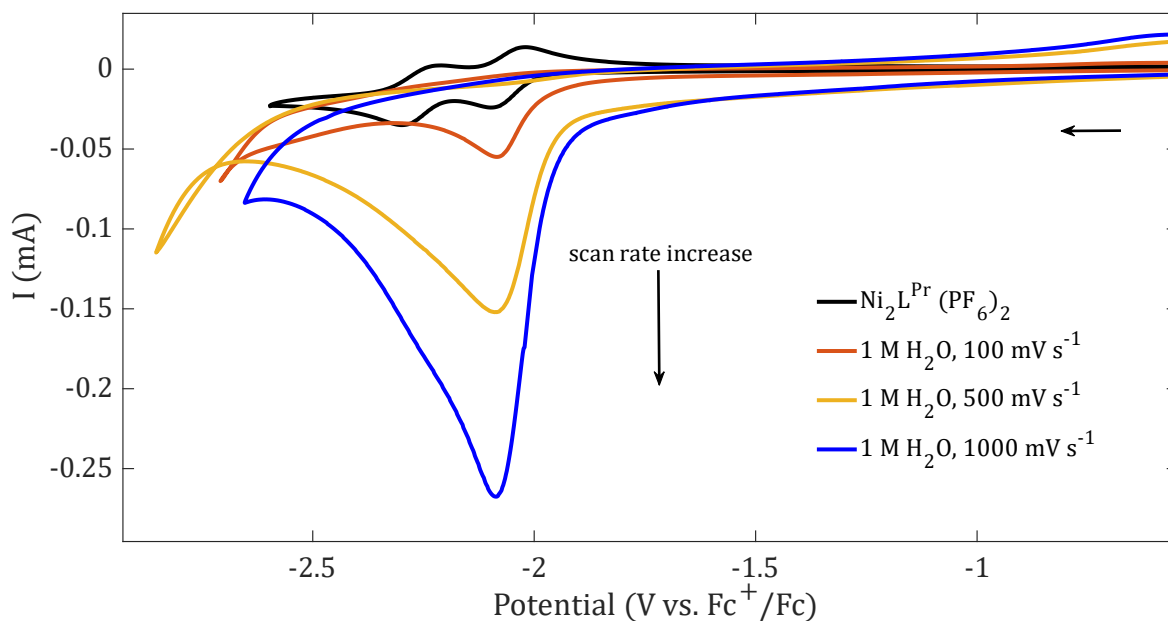
Figure 7.33 | CVs showing the reactivity of **Ni₂L^{Pr} (PF₆)₂** in a CO$_2$-saturated MeCN/0.1 M TBAPF$_6$ solution containing 2% H$_2$O with scan rate 0.1 V s^{-1} (red), 0.5 V s^{-1} (yellow) and 1 V s^{-1} (red). The scans are stopped at -2.6 V to avoid electrode deposition.
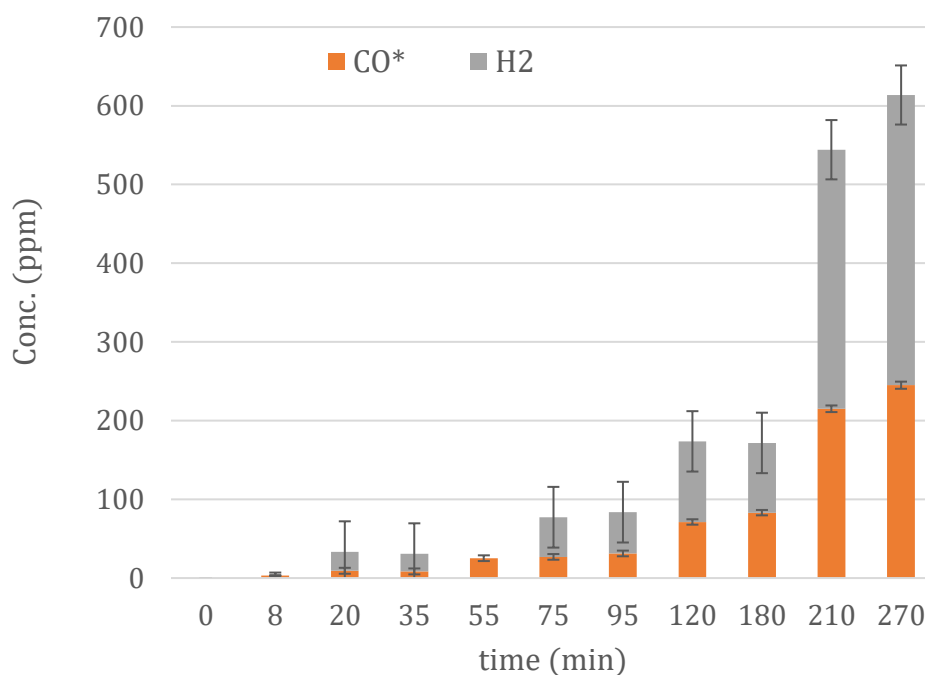

Figure 7.34 | Detected gaseous product from CPE conducted with 1mM of **Ni₂L^{Pr} (PF₆)₂** at -2.70 V in a CO$_2$-saturated MeCN/0.1 M TBAPF$_6$ solution containing 2% H$_2$O at a Freudenberg carbon paper WE.